THÈSE

Pour obtenir le grade de

DOCTEUR DE L'UNIVERSITE GRENOBLE ALPES

Spécialité : **Signal, Image, Parole, Télécoms**

Arrêté ministériel : 25 mai 2016

Présentée par

Pierre-Amaury GRUMIAUX

Thèse dirigée par **Laurent GIRIN,** Professeur, Univ. Grenoble Alpes, Grenoble-INP, GIPSA-lab, et
Co-encadré par **Srđan KITIĆ,** Ingénieur de Recherche, Orange Labs,
Et **Alexandre GUÉRIN,** Ingénieur de Recherche, Orange Labs

préparée au sein du **Laboratoire Grenoble Images Parole Signal Automatique (GIPSA-lab)** et **Orange Labs**
dans **l'École Doctorale Electronique, Electrotechnique, Automatique, Traitement du Signal (EEATS)**

Deep learning pour le comptage et la localisation de sources de parole avec des signaux ambisoniques

Thèse soutenue publiquement le **15 décembre 2021**,
devant le jury composé de :

Monsieur Sharon GANNOT
Full Professor, Bar-Ilan University, Israël, Rapporteur
Monsieur Alexey OZEROV
Ingénieur de Recherche, InterDigital, France, Rapporteur
Madame Christine EVERS
Lecturer, University of Southampton, Royaume-Uni, Examinatrice
Monsieur Roland BADEAU
Professeur, Télécom ParisTech, Examinateur
Monsieur Romain SERIZEL
Maître de Conférences, Université de Lorraine, Examinateur
Monsieur Laurent GIRIN
Professeur, Univ. Grenoble Alpes, Grenoble-INP, GIPSA-lab, Directeur de thèse
Monsieur Srđan KITIĆ
Ingénieur de Recherche, Orange Labs, Co-encadrant de thèse, Invité
Monsieur Alexandre GUÉRIN
Ingénieur de Recherche, Orange Labs, Co-encadrant de thèse, Invité

Abstract

Sound source localization (SSL) is a subtask of audio scene analysis that has challenged researchers for more than four decades. Traditional methods (e.g., MUSIC or GCC-PHAT) impose strong assumptions on the sound propagation, number of active sources and/or signal content, which makes them vulnerable to adverse acoustic phenomena, such as reverberation and noise. Recently, data-driven models – and particularly deep neural networks – have shown increased robustness in noisy and reverberant environments. However, their performance is still seriously degraded in the presence of multiple sound sources, especially when their number is unknown. Moreover, source detection and localization in real-life use-cases, where the latency is an important criterion, is still an open research problem.

In this thesis, we focus on speaker detection and localisation in office/domestic indoor environments, using multichannel Ambisonics recordings, with the emphasis on low-latency performance. First, we propose to use deep neural networks (DNNs) to estimate the number of speakers (NoS) in a multichannel mixture. We propose a model that is capable to count up to five speakers, with a relatively high accuracy, at the short-term-frame resolution. We also provide a performance analysis of this model depending on several hyperparameters, which gives interesting insights on its behavior. Second, we explore the capabilities of a multichannel audio signal representation called time-domain velocity vector (TDVV), akin to relative impulse response in the present spherical harmonics domain, as a novel type of input features of DNNs for detection/localization tasks. Next, we address multi-speaker localization, by first improving upon a state-of-the-art convolutional recurrent neural network (CRNN) with a substantial gain in accuracy. We also examine the potential of self-attention-based neural networks for multi-speaker localization, as these models are known to be suitable for other audio processing tasks due to their capability to capture both short- and long-term dependencies in the input signal. Furthermore, we investigate the use of the estimated NoS, provided by our speaker counting neural network, to improve our speaker localization CRNN. We show experimentally that using the estimated NoS leads to more robust multi-speaker localization than the classical threshold-based direction of arrival (DoA) estimation. Moreover, we show the interest of injecting the NoS information as an additional input feature for the localization neural network. Finally, we explore multi-task neural architectures to estimate both the NoS and speaker DoAs at the same time.

Résumé

La localisation de sources sonores est une sous-tâche de l'analyse de scènes sonores qui a défié les chercheurs pendant plus de quatre décennies. Les méthodes traditionnelles (e.g., MUSIC ou GCC-PHAT) imposent des hypothèses fortes sur la propagation du son, le nombre de sources actives et/ou le contenu du signal, ce qui les rend vulnérables à des phénomènes acoustiques adverses tels que la réverbération ou le bruit. Récemment, les méthodes basées sur les données – et particulièrement les réseaux de neurones profonds – ont montré une plus grande robustesse dans les environnements réverbérants et bruités. Cependant, leur performance est toujours sensiblement dégradée en présence de plusieurs sources sonores, notamment quand leur nombre est inconnu. De plus, la détection et la localisation de sources pour des usages pratiques, où la latence joue un rôle important, est toujours un sujet de recherche ouvert.

Dans cette thèse, nous nous intéressons à la détection et à la localisation de locuteurs dans des environnements domestiques, en utilisant des enregistrements ambisoniques multicanaux, avec un accent sur une performance à basse latence. Tout d'abord, nous proposons d'utiliser des réseaux de neurones profonds (DNN, pour deep neural network) pour estimer le nombre de locuteurs (NoS, number of sources) dans un mélange multicanal. Notre modèle est capable de compter jusqu'à cinq locuteurs, avec une précision relativement grande, pour une résolution à la trame. Nous proposons également une analyse de la performance du modèle en fonction de certains hyperparamètres, ce qui fournit des informations intéressantes sur son comportement. Ensuite, nous explorons les capacités d'une représentation d'un signal audio multicanal appelée vecteur vélocité dans le domaine temporel (TDVV, time-domain velocity vector), qui est analogue à la réponse impulsionnelle relative dans le domaine des harmoniques sphériques, en tant que nouvelle représentation d'entrée de DNNs pour la localisation/détection. Par la suite, nous nous penchons sur la localisation de plusieurs locuteurs en commençant par améliorer un réseau de neurones convolutif et récurrent (CRNN, convolutional recurrent neural network) de l'état de l'art avec un gain important en précision. Puis nous examinons le potentiel des mécanismes de self-attention pour la localisation de plusieurs locuteurs, alors que ces modèles sont connus pour être adaptés à d'autres tâches de traitement audio étant donnée leur capacité à capter les dépendances à court et long terme dans le signal d'entrée. En outre, nous investiguons l'utilisation du NoS estimé, fourni par notre réseau de neurones de comptage, pour améliorer le CRNN de localisation. Nous montrons expérimentalement qu'utiliser le NoS estimé donne plus de robustesse à la localisation multi-locuteur que la méthode de seuillage classiquement utilisée dans l'estimation de direction d'arrivée (DoA, direction of arrival). De plus, nous montrons l'intérêt d'injecter l'information du NoS en tant qu'entrée additionnelle pour le réseau de neurones de localisation. Finalement, nous explorons les architectures neuronales multi-tâches pour estimer le NoS et la DoA des locuteurs dans le même temps.

Acknowledgements

First, I would like to thank my academic supervisor Laurent Girin. I have really appreciated all your advice and recommendations which I believe have taught me precious principles on the research work. Although the distance were not our ally, you always took your time to attend the meetings, answer my questions and review my works. I also thank Srđan Kitić and Alexandre Guérin, my industry supervisors, with whom I spent most of my time when we were at the office. I think you have guided on the right path during this thesis, by suggesting me a lot of food for thought and being very helpful when I had some doubts over technical considerations. With you three, I have learned a lot, on the technical, the methodological and ethical aspects, so again, thank you.

I also thank my other colleagues at Orange Labs, with whom I spent more or less time at the office: Arnaud, Clément, Gil, Grégory, Lauréline, Marc, Michel, Thomas. I spent many pleasing moments, around a coffee, a drink or at the restaurant. Thank you to my colleagues at Lannion as well, I greatly enjoyed the few times we met, with a special thanks to Jérôme who provided me with his expertise during part of my experiments. Also, thanks to Prerak, Jérémi and Théodoric who delved into considerations I did not have time to explore during my thesis.

This thesis has been evaluated by a jury of which I would like to thank all the members: Sharon Gannot et Alexey Ozerov who took the time to review this manuscript, and Roland Badeau, Christine Evers and Romain Serizel for being present at my PhD defense. Special thanks for the latter, as well as Nancy Bertin, who took an interest in my thesis from the beginning by being a member of the thesis follow-up committee.

Thanks to the members of the GIPSA-lab, my academic laboratory, whom I had the chance to met for only a couple of weeks during the first year of my PhD. I have good memories of our few discussions.

Finally, thanks to my family and friends, for their support during these three years, even though most of you were without a clue of what I was doing. Thanks a lot to Manon, with whom I have spent most of my everyday life and who supported me throughout this period. You helped me escape from my thesis work from time to time, notably with amazing trips around Bretagne.

P.S.: Special thanks to Covid-19, without whom I would have not spent so many hours on the piano or producing music instead of playing volley-ball.

"*The composer of the past has been like the chemist or alchemist of ancient time, who could use in his combinations some few compound bodies only. The composer of the future will have in the sinusoidal vibrations of electrical music those pure elements out of which all tone-compounds can be built; not merely the known and approved tones of the orchestra, but many shades and nuances heretofore unattainable.*"

Thaddeus Cahill, 1907

Contents

List of Figures

List of Tables

List of Acronyms

ANN	**A**rtificial **N**eural **N**etwork
ASR	**A**utomatic **S**peech **R**ecognition
BiLSTM	**Bi**directional **L**ong **S**hort-**T**erm **M**emory
BPTT	**B**ack**P**ropagation **T**hrough **T**ime
CMH	**C**ross-**M**ulti-**H**ead
CNN	**C**onvolutional **N**eural **N**etwork
CRNN	**C**onvolutional **R**ecurrent **N**eural **N**etwork
DAW	**D**igital **A**udio **W**orkstation
DL	**D**eep **L**earning
DoA	**D**irectional **o**f **A**rrival
ESPRIT	**E**stimation of **S**ignal **P**arameters via **R**otational **I**nvariance **T**echniques
FDVV	**F**requency-**D**omain **V**elocity **V**ector
FF	**F**eed**F**orward
FOA	**F**irst-**O**rder **A**mbisonics
GCC	**G**eneralized **C**ross-**C**orrelation
GPU	**G**raphical **P**rocessing **U**nit
GRU	**G**ated **R**ecurrent **U**nit
HOA	**H**igher-**O**rder **A**mbisonics
IFT	**I**nverse **F**ourier **T**ransform
IPD	**I**nteraural **P**hase **D**ifference
ISM	**I**mage-**S**ource **M**ethod
LSTM	**L**ong **S**hort-**T**erm **M**emory
MFCC	**M**el **F**requency **C**epstral **C**oefficients
MH	**M**ulti-**H**ead
MLP	**M**ulti**L**ayer **P**erceptron
MSE	**M**ean **S**quared **E**rror
MUSIC	**MU**ltiple **SI**gnal **C**lassification
NLP	**N**atural **L**anguage **P**rocessing
NoS	**N**umber **o**f **S**ources
PHAT	**PHA**se **T**ransform
PIV	**P**seudo**I**ntensity **V**ector
ReLU	**Re**ctified **L**inear **U**nit
RIR	**R**oom **I**mpulse **R**esponse
RNN	**R**ecurrent **N**eural **N**etwork
RTF	**R**elative **T**ransfer **F**unction

RT60	**R**everberation **T**ime **60** dB
SA	**S**elf-**A**ttention
SCM	**S**patial **C**ovariance **M**atrix
SHD	**S**pherical **H**armonics **D**ecomposition
SIR	**S**ignal-to-**I**nterference **R**atio
SNR	**S**ignal-to-**N**oise **R**atio
SPL	**S**ound **P**ressure **L**evel
SRP	**S**teered **R**esponse **P**ower
SSL	**S**ound **S**ource **L**ocalization
STFT	**S**hort-**T**erm **F**ourier **T**ransform
TCN	**T**emporal **C**onvolutional **N**etwork
TDoA	**T**ime-**D**ifference **o**f **A**rrival
TDVV	**T**ime-**D**omain **V**elocity **V**ector
TF	**T**ime-**F**requency
VAD	**V**oice **A**ctivity **D**etection
VR	**V**irtual **R**eality

Notations

Linear algebra

x	scalar
$\mathbf{x}$	vector
$\mathbf{X}$	tensor
$\mathbf{x}^T$	transpose of $\mathbf{x}$
x^*	complex conjugate of x
$\Re(x)$	real part of x
$\Im(x)$	imaginary part of x

Indexes

I	number of microphones
i	microphone index
J	total number of sources
$\bar{J}$	maximum number of sources
$J(t)$	instantaneous number of sources
j	source index
T	number of frames
t	time or frame index
τ	alternative time index
F	number of frequency bins
f	frequency bin index
ω	angular frequency

Geometry

$\mathbf{r}_j$	position of source j
x_j, y_j, z_j	cartesian coordinates of source j
r_j	distance of source j from the array origin
θ_j	azimuth of source j
ϕ_j	elevation of source j

Signal

$\mathbf{x}$	$I \times 1$ multi-channel input signal
x_i	input signal recorded at microphone i
c_{ij}	signal from source j recorded at microphone i
a_{ij}	room impulse response from source j to microphone i
n_i	noise signal recorded at microphone i

Acoustics

p	acoustic pressure
c	speed of sound
Y_n^m	complex spherical harmonic at order n and degree m
$\tilde{Y}_n^m$	real spherical harmonic at order n and degree m
N	Ambisonics order
B_n^m	Ambisonics coefficient at order n and degree m
W	Ambisonics coefficient B_0^0
X, Y, Z	Ambisonics coefficients B_1^1, B_1^{-1} and B_1^0, respectively
$\mathbf{I}$	complex intensity or pseudointensity vector (at order 1)
$\mathbf{I}^N$	complex pseudointensity vector at order N
$\mathbf{I}_a$	complex active intensity or pseudointensity vector
$\mathbf{I}_r$	complex reactive intensity or pseudointensity vector
$\mathbf{V}(t)$	time-domain velocity vector
$\mathbf{V}(f)$	frequency-domain velocity vector

Metrics

A_{ij}	Entry of the confusion matrix $\mathbf{A}$ for ground-truth NoS i and predicted NoS j
$A(\tau)$	Overall classification accuracy for predictions at frame τ
M_i	Mean absolute error for class i

Chapter 1

Introduction

1.1 General context

1.1.1 Human hearing

We, as humans, have been granted a couple of ears capable of reacting to surrounding sound and processing the vibrations through our brain. From even before our birth, we have learned to use them properly, and we have impressive capabilities of dealing with a complex sound environment.

Imagine yourself at a friend's party. Many guests are present, you are in the middle of a discussion with two friends, surrounded with other small groups of chatting people. A few meters from you, one of the guest performs an entertaining dub music DJ set, while someone is ringing at the door. A lot of audio information arrive at the same time to your ears. Yet, you are still able to understand what your two friends are debating, and you can handle the conversation, maybe at the cost of speaking louder. Also, you can shift your attention at any time by indiscreetly listening the next group's conversation, or enjoying the music coming from the DJ booth, while being aware that a new guest is arriving at the door. This phenomenon is called the *cocktail party effect* [Aro92]. It refers to the brain's ability to let us focus on any sound stimulus among many other stimuli. In other words, the fact that all sounds are mixed together when incoming to our ears is not an obstacle for us to understand the surrounding sound space.

The cocktail party effect is partially due to our great ability for sound source localization. Because our ears do not receive the exact same sound signal at a given instant, the brain can sense small differences in intensity, spectral content and timing cues between the two signals in order to locate the sound sources [Bre94]. Except if a sound source location is equidistant to both ears, the signals arrive time-shifted from each other and the difference is a localization cue. The shapes of our head, torso and pinna causes diffraction which also helps to locate sound sources [Bla97]. Consequently, all human beings perceive sound differently, and we have learned to hear based on the characteristics of the body parts around our ears. We are also capable of estimating the source distance based on the loss of amplitude and the ratio between the direct path and the reverberated part. Thus, our localization ability is

greatly responsible for our capacity to extract meaningful information from a complex sound environment.

1.1.2 What is sound ?

Sound is a vibration travelling through a medium. It propagates, as a wave, in any medium allowing local oscillations: gases, fluids and solids. On Earth, silence almost does not exist. Any vibrating object, like flowers, tree leaves, fleas, fish, wind, icebergs, underwater volcanoes, loudspeaker, guitar string, emits a sound wave and acts as a sound source. The resulting vibration then freely travels through the surrounding medium, if no obstacle is encountered, at a speed c depending on the medium properties (in the air, $c = 343\,\mathrm{m\,s^{-1}}$ at 20 °C). When a sound wave passes through a fixed point in space, local pressure and velocity vary in time, a little shifted from the equilibrium state. The changes are generally very small. On Earth, the average atmospheric pressure at the surface is around 100 000 Pa, while the just audible pressure deviation for human hearing is 0.00002 Pa (corresponding to 0 dB in sound pressure level, SPL), and the threshold of pain is between 20 and 200 Pa (corresponding to 120-140 dB SPL).

In such a vibrating phenomenon, frequency is defined as the number of vibrations per second, or *Hertz* (Hz). In nature, most sound waves are propagating vibrations containing multiple frequencies, which characterize its aspect, commonly referred as *timbre*. For example, a guitar bass sound is mainly made of *low* frequencies, whereas a singing bird mostly emits *high* frequencies. We can describe a complex wave (*i.e.*, containing many frequencies) in terms of a superposition of sinusoidal plane waves, each one containing only one frequency. As a sound source vibration evolves with time (for instance, it can attenuate), its frequency content also evolves. Thus, the time and frequency dimensions are two important characteristics of a sound wave.

When a sound wave encounters an obstacle, several phenomena can occur. *Specular reflections* happen when the wave arrives at a smooth surface, like a wall. In this case, the incoming sound wave is reflected in the opposite direction from the wall, at an angle equal to the incoming angle. When the surface irregularities of a surface are smaller than the wavelength – the distance over which a wave's shape is repeated - we witness *scattering*, whose consequence is a propagation of the incoming wave into directions deviated from a straight trajectory. Another phenomenon, *diffraction*, can occur when the wave passes across a surface edge.

As sound waves cause local displacements of matter (vibrations) when travelling through a medium, they obey the superposition principle. That is, when two sound waves incoming from two separated sound sources pass through the same point in space, the vibrations are added, resulting in a combination of the propagated information, as illustrated in Fig. 1.1. This property makes the analysis of sound complicated: when recording the surround sound scene with one or several microphones, it is not straightforward to decompose the different incoming sound waves according to their respective sound source.

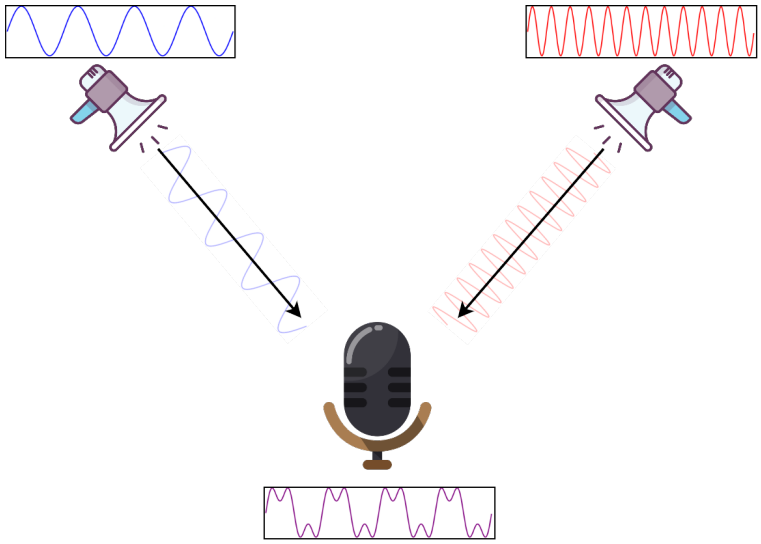

Figure 1.1: Superposition of two sound waves arriving simultaneously at the same point in space. The signal in purple, recorded by the microphone, is the sum of the two incoming sound signals, in blue and red. The black arrows illustrate the propagation of the waves from the sound sources to the microphone.

This phenomenon is even more accentuated when a sound wave propagates in an environment with walls and furniture. As illustrated in Fig. 1.2, the sound wave can reflect successively multiple times onto the walls, following a determined path. Moreover, as most sound sources generate spherical waves, leading to a spherical wavefront, the wave propagates in many directions at the same time (illustrated by the multiple arrows coming from the loudspeaker in Fig. 1.2). Because of the many resulting reflections, several delayed copies of the same wave arrive simultaneously at the recording point. Due to the superposition principle, they are added together to the *direct path*, which is the wavefront going directly from the sound source to the receiver. The resulting recorded signal is thus not an exact copy of the original source signal, but rather a combination of delayed and attenuated versions of the original signal. The phenomenon of a signal coming to a receiver from several paths is called *multipath propagation*. The first reflections form what is called *early reflections*, which generally lasts a few milliseconds, until there are "too many" of them, which is referred as *reverberation*. Reverberation happens in every closed space, and is more or less accentuated depending on several parameters, such as wall materials or room dimensions. Typically, high reverberation can be heard in churches and cathedrals, while special rooms called *anechoic chambers* have been designed to minimize the effect of reverberation.

As we can see, the superposition principle makes it difficult to retrieve a clean version of the original sound source signal in a real-world environment. When several sources occur, or when there are reflections in a room, the fact that different sound waves arrive at the recording point makes it very difficult to retrieve the original signals without prior information.

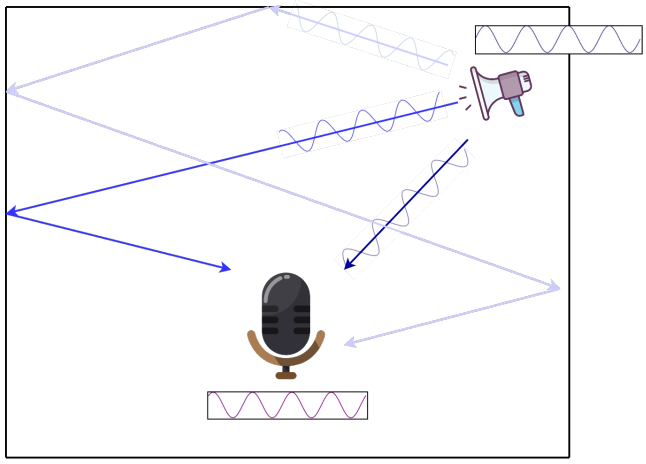

Figure 1.2: Illustration of a multipath propagation, which occurs in the presence of walls where the wavefront of a single sound wave reflects several times onto. The dark blue arrow exhibits the *direct path* from the source to the receiver, and the two other arrows show two different paths that do not arrive at the same time as the direct path. The resulting recorded signal is a combination of all the received waves, delayed from each other because of a different path lengths.

1.1.3 Audio signal processing

For decades, researchers have been trying to reproduce the human hearing abilities using machines. The general motivation of this research effort is to build systems capable of understanding the surrounding sound scene. Such systems require one or more microphones, mimicking the human ears, and signal processing algorithms replacing the brain activity. To accomplish certain goals, usually several algorithms are interconnected into a processing chain, such that each one performs a specific subtask, in order to form a fully-working system. Let us take the example of a system capable of decoding human speech, commonly named automatic speech recognition (ASR) [Nas+19]. If one can record a perfectly clean speech signal, directly applying an effective ASR algorithm might be sufficient. But in a real-world context, a lot of interference makes the task more complicated. For example, in a domestic environment, other sources (dog barks, TV sound, vacuum cleaning, etc.) could interfere with the target speech signal, as well as surrounding noise coming for example from the outside of an open window. Reverberation is also an important factor that blurs the original speech signal.

To cope with this challenging conditions, several audio signal processing algorithms can be used to clean the recorded speech signal beforehand. As their names refer, *denoising* and *dereverberation* algorithms, often encapsulated as *speech enhancement* [VVG18], aim to remove or at least reduce noise interference and reverberant parts of a signal, respectively. When several sound sources are captured, *source separation* [WC18] aims to separate a mixture signal into several component signals, each one containing the information coming from a single particular source. Source separation

techniques can rely on frequency contents, or be obtained by spatial filtering when multiple microphones are used. In the latter type of methods, assuming the knowledge of the target source location, one can spatially filter out the unwanted part of the sound field and extract the sound coming from the target location. However such methods rely on the knowledge of the source location(s), which can be estimated using *sound source localization* (SSL). To estimate the source(s) location, one needs at least two microphones, as we humans possess two ears. SSL algorithms can estimate the directions of one or more overlapping sound sources, and a *source counting* method might be handy to apply beforehand, to ensure that the right number of sources are located in the analyzed signal. Note that when we deal with speech signals, source counting (thus named *speech counting)* is a subtask of *speaker diarization* [Ang+12; TR06; Par+21], which is the task aiming to answer the question *who speaks and when ?* in a signal.

1.1.4 Thesis focus

Speaker counting and localization

In this thesis, we addressed two of the previously mentioned audio tasks: sound source localization and source counting. More precisely, we dealt with speech sources. As stated above, knowing the number of speakers in a signal is a very useful piece of information to extract beforehand. It could prevent the localization algorithm focus onto more sources than the sound really contains, and thus avoid the inclusion of interfering sources, such as noise. Part of this thesis work was thus to design an algorithm capable of counting the number of speakers in challenging acoustic conditions, *i.e.*, in noisy and reverberant environments. The other focus of this thesis was to explore speaker localization in the same kind of challenging environments. Following our interest in counting speakers, we aimed to localize several overlapping speech sources. In order to design robust systems for counting and localizing multiple speakers, our research exploited several tools.

Ambisonics format

Throughout this thesis, we took benefit of the Ambisonics format to represent the sound signal. Such a format is obtained from a spherical microphone array, leading to a multi-channel signal. This more and more adopted audio format presents several great advantages. It is agnostic to the choice of microphone array, that is the encoded signal does not depend on the arrangement of microphones within an array. It can also render the recorded sound scene given any disposition of loudspeakers, but this aspect was not of interest in this thesis. Also, it is an isotropic format, meaning that the recording process does not favor any direction. We detail this format in Chapter 2.

Artificial neural networks

We explored the potential of artificial neural networks to design robust sound source counting and localization systems. This family of models is part of *deep learning* (DL) [GBC16], which is a class of algorithms behind most recent artificial intelligence systems. Their success is due to the ability of neural networks to model complex functions by adjusting their parameters through a learning phase based on a dataset of many examples. They are more and more used today, due to the amount of available data and the increasing computational power to train the algorithms. The basics of artificial neural networks are presented in Chapter 3.

1.2 Problem formulation

In this section, we formulate the problems of counting and localizing sources (regardless whether they are speech or not) in a mathematical framework. The goal is to formally describe the problem we address in this thesis, as well as set the notations we use throughout the chapters.

1.2.1 Mixture model

We adopt the same mixture model formalization as in [VVG18]. Let us assume an environment with J point sources, in which we place a microphone array consisting of I microphones. Each microphone records the sound scene in terms of pressure change from a different position in space, resulting in a multi-channel mixture signal $\mathbf{x}(t)$ containing the recorded signal $x_i(t)$ from each microphone i:

$$\mathbf{x}(t) = \begin{bmatrix} x_1(t) \\ x_2(t) \\ \vdots \\ x_I(t) \end{bmatrix}, \tag{1.1}$$

where t denotes time.

As multiple sound sources are present in the environment, according to the superposition principle, each microphone signal is a sum of the signals arriving at the microphone position from each sound source j:

$$x_i(t) = \sum_{j=1}^{J} c_{ij}(t). \tag{1.2}$$

Here, $c_{ij}(t)$ is the signal arriving at microphone i resulting from the emission of a signal $s_j(t)$ from sound source j. The propagation of the source signal and the reverberation of the room has to be taken into account. This can be modeled using a linear time-invariant filter $a_{ij}(\tau)$ if the sources and microphones are static. As all

the microphones and sources are at different positions, all filters a_{ij} are distinct. The signal arriving at microphone i can then be expressed as:

$$c_{ij}(t) = \sum_{\tau=0}^{+\infty} a_{ij}(\tau) s_j(t-\tau), \tag{1.3}$$

considering a causal filter (*i.e.*, depending only on past and present inputs). The filters $a_{ij}(\tau)$ are called *room impulse responses* (RIRs) and model the propagation of the source signal from the sound source position to the microphone position, including the reverberation phenomena. The reverberation components are dependent of the source and microphone positions, as well as the room properties (geometry and dimensions, material properties, etc.). Theoretically, a room impulse response is the signal recorded by a perfect microphone (without any noise), coming from a point source emitting an impulse (Dirac distribution), hence the name *room impulse response*.

In real-world environment, noise is an important component which has to be included in the model of the multi-channel mixture signal. Two types of noise can be present in such a recording. On the one hand, we have to take into account the ambient noise which almost always exists in any sound scene. Such a noise is generally considered as a *diffuse source*, which is a source emitting from a whole region in space, as if it was composed of an infinite number of point sources. Examples of diffuse sources include surrounding musical ambience, outside construction works, incomprehensible background conversations (usually referred to as *babble noise*), or even small fluctuations of air. Such diffuse noise can be considered independent of the position in the room, thus common to all microphones. On the other hand, noise modelling the imperfection of each microphone also constitutes an important artifact. Practically, the microphones do not record the world perfectly as it is, and they are not rigorously identical to each other. Therefore, we can incorporate a noise signal $n_i(t)$ for each microphone, including both diffuse noise and microphone-wise noise, to complete the multi-channel mixture signal model:

$$x_i(t) = \sum_{j=1}^{J} \sum_{\tau=-\infty}^{+\infty} a_{ij}(\tau) s_j(t-\tau) + n_i(t). \tag{1.4}$$

1.2.2 Room impulse responses

The room impulse responses $a_{ij}(\tau)$ represent the acoustic behavior of the sound according to the emitting and recording positions, as well as the propagation effects induced by the presence of walls or furniture.

Fig. 1.3 shows an illustration of a typical RIR. The first and highest peak (in red) represents the *direct path*, which is the straight propagation between the point source and the microphone. The following peaks (in green) are referred to as *early echoes* and encode the beginning of multipath propagation which includes the main reflections from the obstacles. The last part features the *reverberation* phenomenon and results from the superposition of the many late reflections.

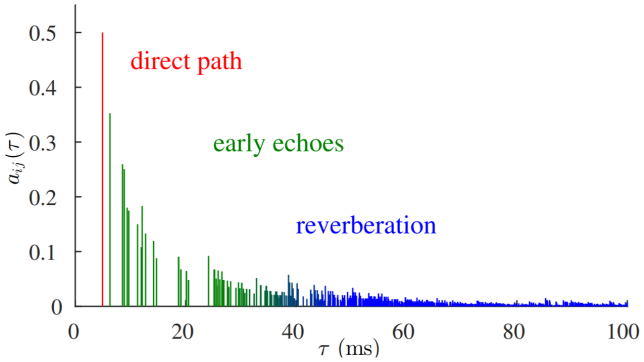

Figure 1.3: Illustration of an room impulse response. Three noticeable parts in an RIR: the direct path (in red), the early echoes (in green) and the reverberation (in blue). Borrowed from [VVG18].

The *reverberation time* (RT60) is a quantity measuring the duration for the impulse response envelop to decrease by 60 dB. It depends on the room size and the obstacle materials. Typical values of RT60 is between 0.2 and 0.8 s for small domestic rooms, and can be higher that 1 s for larger rooms such as restaurant rooms.

1.2.3 Source counting

The number of sources (NoS) $J \in \mathbb{N}$ is an important piece of information which can be very useful to several audio processing tasks such as source separation or source localization. For instance, knowing J can improve the performance of separation or localization systems since it can help avoiding "unwanted" sound sources (interference). However estimating the number of sources is not straightforward, mainly due to the superposition principle. Fig. 1.4 illustrates the profile over time of the number of active sources in a 3-source mixture.

Source counting refers to the problem of estimating the number of sources given a single- or multi-channel mixture signal $\mathbf{x}(t)$. However this problem can be defined according to different levels of temporal resolution. The following NoS quantities can be estimated:

- the instantaneous number of sources $J(t)$. The goal is to estimate the NoS at each timestep t, depending on the considered temporal resolution (audio sample, time frame). It is at most equal to the total NoS J, but it is often lower than J since in general not all sources overlap at the same time;
- the maximum number of simultaneous sources $\bar{J}$. It is defined as $\bar{J} = \max_t J(t)$, which is the maximum of number of sources which were simultaneously active through the whole analyzed signal;
- the total number of sources J, which is, as previously defined, the total number of sources involved in the mixture (*i.e.*, they have been active at least once

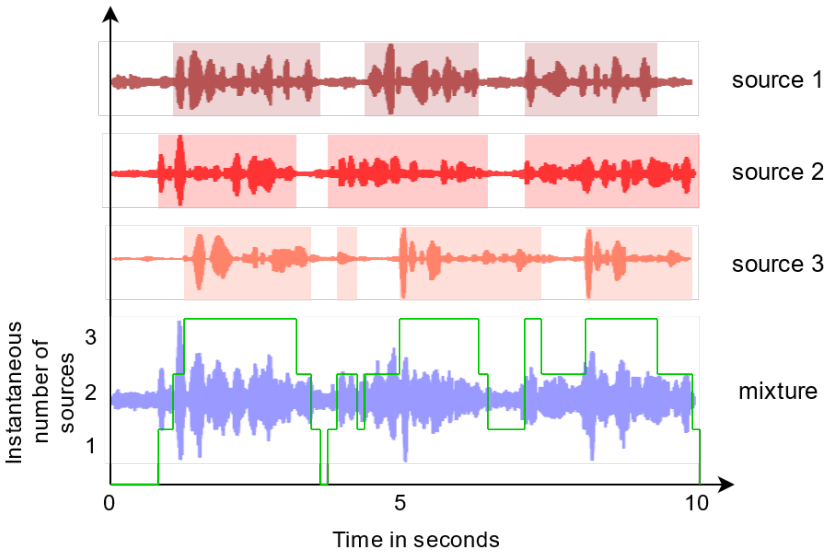

Figure 1.4: Time profile of the number of active sources in a 3-source mixture. The activity of each individual source is represented with rectangles (top). The instantaneous number of active sources in the mixture $J(t)$, resulting from the superposition of each source's activity, is depicted with the green line (bottom).

during the analysis). It can be retrieved from $J(t)$ if we are able to identify the sources.

In this thesis, we were interested in estimating the instantaneous number of sources. The motivation was to provide a succeeding block in the processing chain (*e.g.*, a localization or tracking algorithm) with an NoS estimate $\tilde{J}(t)$ at any time index t. In practice, this necessitates a source counting method operating at high temporal resolution.

Note that when $J = 1$, source counting simplifies to the problem of source detection, which is predicting whether a particular source is active ($J(t) = 1$) or not ($J(t) = 0$) at any time t.

When the sources are human speakers (as it is the case in this thesis), source counting is referred to as *speaker counting*, except for $J = 1$ for which it is commonly named *voice activity detection* (VAD). When the speech sources need to be identified in addition to counting, this problem is equivalent to *speaker diarization*.

1.2.4 Source localization

The goal of SSL is to derive the spatial positions of the target source(s) based on the recorded multi-channel signal. While multiple microphone arrays can be employed to localize sources, most systems assume the use of only one microphone array, as it is a more practical solution. This problem is not trivial, notably due to the presence of noise as well as reverberation in enclosed spaces. Looking back at Fig. 1.2, we see that several signals originating from the same source arrive at the microphone

from different directions. Thus, estimating the actual source direction, and even interpreting the different incoming sound waves as coming from the same point source is not a straightforward task.

Assuming an environment with J emitting sources, the goal of a SSL algorithm is to estimate the position $\mathbf{r}_j(t)$ of each source j, given a certain coordinate system, from a multi-channel signal $\mathbf{x}(t)$. Using Euclidian coordinates, $\mathbf{r}_j(t) = (x_j(t), y_j(t), z_j(t))$, while in a spherical domain, $\mathbf{r}_j(t) = (r_j(t), \theta_j(t), \phi_j(t))$, where r_j is the distance, θ_j the azimuth angle and ϕ_j the elevation angle. When only θ_j and ϕ_j are estimated, it is referred to direction-of-arrival (DoA) estimation. Spherical coordinates are especially handy when the microphone is taken as the origin. Cylindrical coordinates are used less often.

Note that the source positions $\mathbf{r}_j(t)$ are functions of time, as in a general framework the source can be mobile in the surrounding area. In that case, sound source localization can be done with the help of a target tracking system, whose goal is to associate the multiple position estimates and the target sources over time.

1.3 Main contributions

During three thesis years, our research was focused on speaker counting and localization. Through many experiments, we explored new ways of addressing these tasks in order to improve the existing methods, and tried to analyze their behaviors. Several of these methods led to a published/submitted papers:

- P.-.A Grumiaux, S. Kitić, L. Girin, A. Guérin, High-resolution speaker counting in reverberant rooms using CRNN with Ambisonics features, *European Signal Processing Conference (EUSIPCO)*, Amsterdam, Netherlands, 2020.
- P.-.A Grumiaux, S. Kitić, L. Girin, A. Guérin, Multichannel CRNN for speaker counting: an analysis of performance, *Forum Acusticum (FA2020)*, Lyon, France, 2020.
- P.-.A Grumiaux, S. Kitić, L. Girin, A. Guérin, Improved feature extraction for CRNN-based multiple sound source localization, *European Signal Processing Conference (EUSIPCO)*, Dublin, Ireland, 2021.
- P.-.A Grumiaux, S. Kitić, P. Srivastava, L. Girin, A. Guérin, SALADnet: Self-Attentive multisource Localization in the Ambisonics Domain, *IEEE Workshop on Applications of Signal Processing to Audio and Acoustics (WASPAA)*, Mohonk Mountain House, New Paltz, NY, 2021.
- P.-.A Grumiaux, S. Kitić, L. Girin, A. Guérin, A survey of sound source localization with deep learning methods, Submitted, 2021.

1.3.1 Speech counting

We explored several neural network architectures in order to improve existing methods for speech counting. We showed that relying on multi-channel features (in the Ambisonics format) we could obtain improved speaker counting compared to using single-channel signals. Our method showed great performance to count up to 5 simultaneous speakers in noisy and reverberant environments, at a short-term frame-wise resolution. This work was presented at the European Conference on Signal Processing in 2020 [Gru+20a]. We also conducted several analyses on the performance of neural network architectures according to different hyperparameters, leading to a presentation [Gru+20b] at the conference Forum Acusticum 2020.

1.3.2 Sound source localization literature review

During our literature review on SSL, which was especially geared towards neural-based methods, a great amount of interesting papers was gathered, annotated and classified. We thoroughly kept collecting more and more deep-learning-based SSL papers, as more and more methods were proposed throughout the years. We finally decided to share this intensive literature review by writing a survey paper on SSL techniques using deep learning [Gru+21c]. This paper proposes a classification of neural-based SSL methods according to neural network architectures, types of input features, output paradigms, and learning strategies. It also provides an overview of datasets used for such systems, as well as two summary tables which allow to easily find papers according to specific criteria.

1.3.3 Multi-source localization

We spent several months to address speaker localization with multiple sources in challenging conditions. Using a classification paradigm, we experimented several neural network architectures to improve the localization performance. First, we managed to notably improve the performance of a state-of-the-art system [Per+19] and extended it up to 3 speakers, by rethinking the feature extraction[1] part of the network. This work was presented at the European Conference on Signal Processing in 2021 [Gru+21a]. We also improved this work by extending the Ambisonics order of the multi-channel recording. We then explored the benefit of self-attention models for an attempt to remove the recurrent layers, known to be computationally cumbersome. Not only did we successfully manage to replace the recurrent part with self-attention, but we also slightly improved the localization performance. This work has been accepted for presentation at the Workshop on Applications of Signal Processing to Audio and Acoustics [Gru+21b]. We finally assessed the benefit of using more microphones to record the analyzed signal, *i.e.*, increasing the Ambisonics order (see Chapter 2). The

[1] Note that throughout all this thesis, we refer as feature extraction the first network components which allows to compute a more *high-level* representation of the input features for the remaining part of the network.

results clearly demonstrated the improvement of the localization performance in this configuration, at the cost of more recorded data.

1.3.4 Exploration of a new type of input features for localization

Based on a pioneering work [DK20] introducing a new type of Ambisonics representation called time-domain velocity vector (TDVV), we carried out a lot of experiments to take benefit of this new feature for SSL. As it was an exploratory idea, we limited our experiments to single-source configuration, with the intention to extend the models to multi-source signals when reaching conclusive results. We tried many neural networks architectures, including dilated convolutions, residual connections, self-attention mechanisms. We also explored several approaches to estimate the TDVV as it is not a straightforward feature to derive.

While the models trained with this new representation were able to localize one source at a fair precision, we never managed to improve the single-source baseline we used to compare our models, which was developed using intensity-based features. Although this series of experiments was not conclusive, we nevertheless present all our results in this document, and try to find out what was missing to take the most out of this new idea.

1.3.5 Combination of speech counting and localization

After exploring new ideas regarding speaker counting and localization, we proposed several systems combining both tasks, either sequentially or jointly. First, we showed that estimating the number of speakers with a neural network allows better localization performance than if it is derived solely from the localization output. We also observed that the performance is still satisfactory compared to the use of a ground-truth NoS. Next, we evaluated the benefit of using the estimated NoS as an additional input feature for the localization network. Finally, we proved that it is possible to train a neural network to jointly estimate the number of sources and their positions, with high counting and localization accuracies.

1.4 Manuscript outline

The remainder of this document is organized as follows. Chapter 2 introduces the concept of spherical harmonics and the Ambisonics representation. The intensity features, frequency-domain and time-domain velocity vectors are also derived. In Chapter 3, we quickly present the different neural network architectures used in our experiments, with an emphasis on less common mechanisms, such as residual connections or multi-head self-attention. We then provide a literature review on source counting and sound source localization, focused on neural-based methods, in Chapter 4. The following chapters detail the experiments conducted during the three years of this thesis. Our models and their analyses for speaker counting are explained in

Chapter 5. In Chapter 6 we present our attempts to improve single-source localization using the TDVV, while in Chapter 7 we describe our work on multi-source localization using more usual features. Next, Chapter 8 presents our investigations towards a neural model for joint speaker counting and localization. Finally, we conclude this thesis in Chapter 9.

Chapter 2

Ambisonics

The Ambisonics format is an audio format capable of efficiently representing the spatial aspect of a sound field. Hence, it has become a popular format for 3D spatial audio coding [PDMP18], as a *de facto* standard in both professional and consumer domains [Her+14] (see also the Facebook 360[1] and the Google360[2] systems available online). Ambisonics finds its roots in the 1930s, when Blumlein's original work [Blu31] on coincident stereo recordings proposed to place two figure-of-eight microphones in a orthogonal manner. Gerzon [Ger73] extended this idea in the 1970s by theorizing what we call the first-order Ambisonics (FOA) format, originally known as B-format, which paved the path to high-order Ambisonics (HOA) [Dan01].

While the term Ambisonics arose from the design of the corresponding microphones, we also often encounter terms related to the spherical harmonics theory in the literature. In fact, the Ambisonics representation consists of the coefficient of the spherical harmonics decomposition of the signal. In this thesis, we will use the term Ambisonics because of the past of the laboratory we conducted our research in, but in this chapter we show how both theories are linked together.

In this chapter, we establish the theoretical foundations of the Ambisonics format, which we adopted to represent audio signals in this thesis. After briefly explaining why this format is of interest, we derive the spherical harmonics decomposition of the solution of the wave equation. This decomposition leads us to the definition of first-order and higher-order Ambisonics. We finally discuss several representations derived from the Ambisonics format, useful for sound scene analysis: the pseudointensity vector, the frequency-domain velocity vector, and the time-domain velocity vector.

An interesting reader may find more in-depth details in diverse references, *e.g.*, theses [Dan01; Mer06; Baq17; Mor06], or books [ZF19; Raf19; JHN17; WM00].

2.1 Interest of the Ambisonics format

One of the main benefits of the Ambisonics lies in its capability of compactly encoding the surrounding sound scene in a format that is theoretically agnostic regarding the configuration of the recording microphone array. Likewise, the Ambisonics format

[1] https://facebook360.fb.com/spatial-workstation/
[2] https://support.google.com/youtube/answer/6395969

Figure 2.1: Examples of microphone arrays suitable for the encoding of the recorded sound field into the Ambisonics format. **Left**: Zoom's H3-VR (4 capsules, Ambisonics format up to order 1); **middle**: Zylia's ZM-1 (19 capsules, up to order 3); **right**: mh acoustics' EigenMike (32 capsules, up to order 4).

is flexible with respect to the setup of an audio system used for reproduction, as its decoding can be adapted to match the given layout, *e.g.*, to headphones, stereo monitors, 5.1 audio systems, or even a setup with many loudspeakers [ZF19]. The Ambisonics format is an isotropic representation of the sound field, *i.e.*, the encoding takes equally into account all spatial directions. It contains the directional information of the sound sources, due to the microphones nature and orientation. A particularity of this characteristics is that it becomes very handy to perform some transformations of the encoded sound recording: for instance, one can easily rotate the sound field by multiplying the multi-channel recording by the appropriate matrix. One typical application of such a property is to take into account the movement of a robot's head when localizing surrounding sounds.

Due to these advantages, more and more commercial applications opt for this sound representation to handle audio signals. As we have seen above, internet giants such as Google or Facebook use the Ambisonics format for their spatial audio applications, especially in virtual reality (VR) environments. Recently, we have witnessed an increase of available easy-to-use devices that can be used to record spatial audio in the Ambisonics format (see Fig. 2.1): mh acoustics' EigenMike,[3] Zoom's H3-VR recorder,[4] Zylia's ZM-1.[5] Decoding tools are also largely available nowadays, especially to be used in digital audio workstations (DAW): IEM plug-in suite,[6] b<>com plug-ins,[7] IRCAM's Panoramix,[8] or Noise Makers' Ambi Head HD[9] to name a few.

[3] https://mhacoustics.com/products#eigenmike1
[4] https://zoomcorp.com/fr/fr/enregistreurs-portatifs/handheld-recorders/h3-vr-360-audio-recorder/
[5] https://www.zylia.co/zylia-zm-1-microphone.html
[6] https://plugins.iem.at/
[7] https://b-com.com/en/process/spatial-audio-family
[8] https://forum.ircam.fr/projects/detail/panoramix/
[9] https://www.noisemakers.fr/ambi-head-hd/

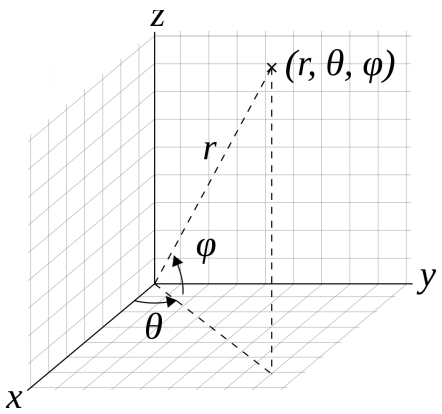

Figure 2.2: Spherical coordinate system. Any position in space can be described with three numbers: the distance r, the azimuth angle θ and the elevation angle (or polar angle) ϕ. The relation between spherical coordinates r, θ, ϕ and cartesian coordinates x, y, z is given by (2.2). Borrowed from Dmcq, CC BY-SA 3.0.

2.2 Wave equation and spherical harmonics decomposition

In this section, we derive the solution of the wave equation in the spherical domain and exhibit the spherical harmonics decomposition of the sound signal, which will lead to the definition of the Ambisonics format in the following section.

2.2.1 Wave equation solution in the spherical domain

A sound signal is the evolution of the sound pressure $p(\mathbf{r}, t)$ with time t at the recording point $\mathbf{r}$, which is measured in Pascals (Pa). The recorded signal is due to the sound source which produces a sound wave, *i.e.*, the solution of the famous *acoustic wave equation* :

$$\nabla^2 p(\mathbf{r}, t) - \frac{1}{c^2} \frac{\partial^2}{\partial t^2} p(\mathbf{r}, t) = 0, \tag{2.1}$$

where ∇^2 denotes the Laplacian operator and c is the speed of sound in the considered fluid (in the air, $c = 343\,\mathrm{m\,s^{-1}}$ at $20\,^\circ\mathrm{C}$).

We want to find the general solution of the wave equation in the three-dimensional space. To do that, we represent the 3D space using spherical coordinates, *i.e.*, $\mathbf{r} = (r, \theta, \phi)$, where θ is the azimuth angle and ϕ the elevation angle, as illustrated in Fig. 2.2. The following equations describe the relationship between cartesian and spherical coordinates:

$$\begin{cases} x = r \cos\theta \cos\phi \\ y = r \sin\theta \cos\phi. \\ z = r \sin\phi \end{cases} \tag{2.2}$$

In three dimensions, using spherical coordinates, the Laplacian operator for a function $f(r, \theta, \phi)$ is given by:

$$\nabla^2_{\mathbf{r}} f = \frac{1}{r^2}\frac{\partial}{\partial r}\left(r^2 \frac{\partial f}{\partial r}\right) + \frac{1}{r^2 \sin\theta}\frac{\partial}{\partial \theta}\left(\sin\theta \frac{\partial f}{\partial \theta}\right) + \frac{1}{r^2 \sin^2\theta}\frac{\partial^2 f}{\partial \phi^2}. \tag{2.3}$$

To derive a solution for the wave equation in the spherical domain, one can proceed to a separation of variables, *i.e.*, we assume that p takes the form:

$$p(r, \theta, \phi, t) = R(r)\Theta(\theta)\Phi(\phi)T(t). \tag{2.4}$$

Then, by injecting (2.4) in (2.1) using (2.3), we obtain one separate partial equation for each variable r, θ, ϕ and t [Raf19, p. 35]:

$$r^2 \frac{d^2}{dr^2}R + 2r\frac{d}{dr}R + \left[(kr)^2 - n(n+1)\right]R = 0, \tag{2.5}$$

with $k = \frac{\omega}{c}$ being the wave number of the sound wave ($\omega = 2\pi f$ is the angular frequency),

$$\frac{d}{d\mu}\left[(1-\mu^2)\frac{d}{d\mu}\Theta\right] + \left[n(n+1) - \frac{m^2}{1-\mu^2}\right]\Theta = 0, \tag{2.6}$$

with $\mu = \cos^2\theta$ and $|m| \leq n, m \in \mathbb{Z},\ n \in \mathbb{N}$,

$$\frac{d^2\Phi}{d\phi^2} + m^2\Phi = 0, \tag{2.7}$$

and

$$\frac{d^2T}{dt^2} + \omega^2 T = 0, \quad \omega \in \mathbb{R}. \tag{2.8}$$

(2.7) and (2.8) immediately lead to the following exponential solutions, valid for an harmonic wave, *i.e.*, with a single frequency ω :

$$T(t) = e^{i\omega t}, \tag{2.9}$$

and

$$\Phi(\phi) = e^{im\phi}, \tag{2.10}$$

where $i = \sqrt{-1}$. Note that m is an integer because Φ is 2π-periodic. (2.6) is known as the associated *Legendre differential equation*, whose non-singular solutions are given by the associated *Legendre functions of the first kind* [AWH13, p. 715]:

$$\Theta(\theta) = P_n^m(\cos\theta), \quad m \in \mathbb{Z}, n \in \mathbb{N}. \tag{2.11}$$

(2.5) is referred as the *spherical Bessel equation*, whose solutions are a weighted combination of the *spherical Bessel functions of the first kind* $j_n(kr)$ or the *spherical Hankel functions of the first kind* $h_n(kr)$:

$$R(r) = R_1 j_n(kr) + R_2 h_n(kr), \tag{2.12}$$

with R_1, $R_2 \in \mathbb{R}$. In fact, in our case, we have necessarily $R_2 = 0$ since the functions h_n diverge at $r = 0$ and we suppose that no infinite sound pressure occurs at the recording point.

Finally, combining these variable-wise equations leads to the set of fundamental solutions for the wave equation in the spherical domain :

$$p(\mathbf{r}, t) = R_1 j_n(kr) P_n^m(\cos\theta) e^{im\phi} e^{iwt}, \tag{2.13}$$

with $n \in \mathbb{N}$, $m \in \mathbb{Z}$ and $|m| \leq n$. The general solution is a weighted sum of these fundamental solutions. The products formed by the angular factors $P_n^m(\cos\theta)$ and $e^{im\phi}$ are known to be the (scaled) *spherical harmonics*, which brings us to the next subsection.

2.2.2 Spherical harmonics

Complex spherical harmonics

The terms depending on θ and ϕ on the wave equation solutions (2.13) are grouped together to define the complex spherical harmonics. This set of complex functions, indexed by n and m, are defined on the unit sphere by [Raf19, p. 4]:

$$Y_n^m(\theta, \phi) = \sqrt{\frac{2n+1}{4\pi} \frac{(n-m)!}{(n+m)!}} P_n^m(\cos\theta) e^{im\phi}, \tag{2.14}$$

where $n \in \mathbb{N}$ is the order, and $m \in \{-n, -n+1, ..., n-1, n\}$ is the degree of the spherical harmonic. We recognize the associated Legendre functions as well as the exponential function of the elevation ϕ.

An interesting property of these complex spherical harmonics is that they form an orthonormal basis of the Hilbert space $L_2(S^2)$ (*i.e.*, the set of all square-integrable complex functions of the unit sphere), with the following inner product:

$$\langle f \mid g \rangle = \frac{1}{4\pi} \int_{\theta=0}^{2\pi} \int_{\phi=-\frac{\pi}{2}}^{\frac{\pi}{2}} f(\theta, \phi) g(\theta, \phi)^* \cos\phi d\phi d\theta, \tag{2.15}$$

where $*$ denotes the complex conjugates. This property involves that any function $f(\theta, \phi) \in L_2(S^2)$ can be decomposed as a weighted sum of spherical harmonics:

$$f(\theta, \phi) = \sum_{n=0}^{\infty} \sum_{m=-n}^{n} f_{nm} Y_n^m(\theta, \phi), \tag{2.16}$$

with f_{nm} denoting the coefficients of $f(\theta, \phi)$ on this basis. This representation is known as the *spherical harmonics decomposition* (SHD) of $f(\theta, \phi)$. The coefficients

f_{nm} can be computed as:

$$\begin{aligned} f_{nm} &= \langle f(\theta,\phi) \mid Y_n^m(\theta,\phi)\rangle \\ &= \int_{\theta=0}^{2\pi}\int_{\phi=-\frac{\pi}{2}}^{\frac{\pi}{2}} f(\theta,\phi)Y_n^m(\theta,\phi)^* \cos\phi d\phi d\theta. \end{aligned} \tag{2.17}$$

From (2.13), we can express the general solution (linear sum of fundamental solutions) of the wave equation on the basis of spherical harmonics:

$$p(\theta,\phi,r,t) = \sum_{n=0}^{\infty}\sum_{m=-n}^{n} \alpha_{nm} j_n(kr) Y_n^m(\theta,\phi) e^{i\omega t}, \tag{2.18}$$

where $\alpha_{nm} \in \mathbb{R}$ are the weights of each fundamental solution.

Real spherical harmonics

Real spherical harmonics $\tilde{Y}_n^m$ also exist and are defined by [JHN17, p. 28]:

$$\tilde{Y}_n^m(\theta,\phi) = (-1)^{|m|}\sqrt{\frac{2n+1}{4\pi}\frac{(l-|m|)!}{(l+|m|)!}}P_n^{|m|}(\cos\theta)\begin{cases}\sqrt{2}\sin(|m|\phi), & \text{if } m<0\\ 1, & \text{if } m=0.\\ \sqrt{2}\cos(m\phi), & \text{if } m>0\end{cases} \tag{2.19}$$

The real spherical harmonics $\tilde{Y}_n^m$ can be derived from the complex spherical harmonics by:

$$\tilde{Y}_n^m(\theta,\phi) = \begin{cases}\sqrt{2}(-1)^m\Im(Y_n^{-m}(\theta,\phi)), & \text{if } m<0\\ Y_n^0(\theta,\phi), & \text{if } m=0,\\ \sqrt{2}(-1)^m\Re(Y_n^m(\theta,\phi)), & \text{if } m>0\end{cases} \tag{2.20}$$

where $\Re(\cdot)$ and $\Im(\cdot)$ denote the real and imaginary parts of the argument, respectively. Inversely, the complex spherical harmonics Y_n^m can be obtained from the real spherical harmonics:

$$Y_n^m(\theta,\phi) = \begin{cases}\frac{1}{\sqrt{2}}(\tilde{Y}_n^{-m}(\theta,\phi) - i\tilde{Y}_n^m(\theta,\phi)), & \text{if } m<0\\ \tilde{Y}_n^0(\theta,\phi), & \text{if } m=0.\\ \frac{1}{\sqrt{2}}(-1)^m(\tilde{Y}_n^m(\theta,\phi) + i\tilde{Y}_n^{-m}(\theta,\phi)), & \text{if } m>0\end{cases} \tag{2.21}$$

The real-valued spherical harmonics also form an orthogonal basis of the set of real functions on the unit sphere, using the inner product [Dan01, p. 302]:

$$\langle f \mid g\rangle = \frac{1}{4\pi}\int_{\theta=0}^{2\pi}\int_{\phi=-\frac{\pi}{2}}^{\frac{\pi}{2}} f(\theta,\phi)g(\theta,\phi)\sin\phi d\phi d\theta. \tag{2.22}$$

An orthonormal basis can be defined by scaling each real spherical harmonic $\tilde{Y}_n^m$ by $\sqrt{2n+1}$ [Dan01], and similarly to the complex spherical harmonics, we can decompose

any real function $f(\theta, \phi)$ on the unit sphere on this basis:

$$f(\theta, \phi) = \sum_{n=0}^{\infty} \sum_{m=-n}^{n} f_{nm} \tilde{Y}_n^m(\theta, \phi), \tag{2.23}$$

where f_{nm} are the coefficients of the decomposition.

2.2.3 Wave equation solution for a single plane wave

To define the Ambisonics components from the wave equation solution, we focus on deriving the solution for a single plane wave, and then we deduce the expression in the general case. We consider a single-frequency plane wave arriving from direction (θ_k, ϕ_k), with amplitude B and wave number $k = \frac{\omega}{c}$, $\omega = 2\pi f$ where f is the frequency of the wave. This plane wave also satisfies the general solution of the wave equation, and it can be shown that in this case the solution can be written as [WM00, p. 227]:

$$p(r, \theta, \phi, t) = 4\pi B e^{i\omega t} \sum_{n=0}^{\infty} i^n j_n(kr) \sum_{m=-n}^{n} Y_n^m(\theta, \phi) Y_n^m(\theta_k, \phi_k)^*. \tag{2.24}$$

Using the relation between real and complex spherical harmonics in (2.21), we can express the sum containing complex spherical harmonics in terms of real spherical harmonics:

$$\sum_{m=-n}^{n} Y_n^m(\theta, \phi) Y_n^m(\theta_k, \phi_k)^* = \sum_{m=-n}^{n} \tilde{Y}_n^m(\theta, \phi) \tilde{Y}_n^m(\theta_k, \phi_k), \tag{2.25}$$

leading to the expression of the pressure for the single plane wave, using real spherical harmonics:

$$p(r, \theta, \phi, t) = B e^{i\omega t} \sum_{n=0}^{\infty} i^n j_n(kr) \sum_{m=-n}^{n} \tilde{Y}_n^m(\theta, \phi) \tilde{Y}_n^m(\theta_k, \phi_k), \tag{2.26}$$

where the constant term 4π has been incorporated in the amplitude term A. This last expression for the solution of the wave equation in the spherical domain (for a single plane wave) brings us to the definition of the Ambisonics coefficients.

2.3 First-order and higher-order Ambisonics

2.3.1 Definition of Ambisonics coefficients

(2.26) exhibits a solution of the wave equation for a single-frequency plane wave of amplitude A, angular frequency ω and coming from direction (θ_k, ϕ_k). The Ambisonics coefficients are defined as the coefficients of the decomposition of the pressure p on the basis of real spherical harmonics [Dan01]:

$$B_n^m(t) = B e^{i\omega t} \tilde{Y}_n^m(\theta_k, \phi_k). \tag{2.27}$$

As we can see, the propagation term $i^n j_n(kr)$ is not taken into account when deriving the Ambisonics components. In fact, this term can be computed for all r, so a sound field can be completely recreated based on the Ambisonics coefficients only.

Finally, the definition of Ambisonics coefficients can be extended to the general case of a composite point source signal $s(t)$ with different frequencies (*i.e.*, not only a single-frequency wave):

$$B_n^m(t) = s(t)\tilde{Y}_n^m(\theta_k, \phi_k). \tag{2.28}$$

(2.26) and (2.18) state that we can represent the sound field at any given point in space using the infinite number of Ambisonics coefficients. In practice, the number of available Ambisonics coefficients is limited (we explain why in subsection 2.3.4). Hence, the infinite summation over n is truncated up to the *Ambisonics order* N :

$$p(r, \theta, \phi, t) \approx \sum_{n=0}^{N} i^n j_n(kr) \sum_{m=-n}^{n} B_n^m(t)\tilde{Y}_n^m(\theta, \phi). \tag{2.29}$$

The truncation above restricts the set of functions p that can be faithfully represented by such a reduced set of coefficients. Therefore, we assume that p is "order-limited", *i.e.*, that its expansion coefficients for the orders higher than N are negligible [Raf19] (this is analogous to band-limited functions in classical Fourier analysis). Such functions can be spatially sampled, and perfectly reconstructed, from $(N+1)^2$ nearly-uniform measurements on the sphere [JHN17].

2.3.2 First-order Ambisonics

When $N = 1$, the truncated representation of p is called *first-order Ambisonics*. It has been originally proposed by Gerzon [Ger73] in the 1970s, who referred to it as the *B-format*. This representation includes four components: B_0^0 for $n = 0$, usually written as W, and B_1^1, B_1^{-1} and B_1^0 for $n = 1$, usually written as X, Y and Z, respectively. The choice of designation for X, Y and Z follows the directivity of the spherical harmonics according to the usual axes x, y, z of an Euclidean space. For a plane wave coming from (θ_k, ϕ_k) and carrying a signal $s(t)$, the FOA representation is obtained using (2.19):[10]

$$\mathbf{x}(t) = \begin{bmatrix} W(t) \\ X(t) \\ Y(t) \\ Z(t) \end{bmatrix} = \begin{bmatrix} s(t)\tilde{Y}_0^0(\theta_k, \phi_k) \\ s(t)\tilde{Y}_1^1(\theta_k, \phi_k) \\ s(t)\tilde{Y}_1^{-1}(\theta_k, \phi_k) \\ s(t)\tilde{Y}_1^0(\theta_k, \phi_k) \end{bmatrix} = \begin{bmatrix} 1 \\ \sqrt{3}\cos\theta_k \cos\phi_k \\ \sqrt{3}\sin\theta_k \cos\phi_k \\ \sqrt{3}\sin\phi_k \end{bmatrix} s(t). \tag{2.30}$$

The directivities of the FOA components are illustrated on Fig. 2.3. We can interpret these four components as the recordings of four spatially coincident microphones: W represents the recording of an omnidirectional microphone, and X, Y and Z represent the recordings of three bidirectional microphones, each oriented on the corresponding

[10] In this thesis we use the N3D normalization standard [Dan01], which makes use of the real spherical harmonics normalized with $\sqrt{2n+1}$ as introduced in Sec. 2.2.2.

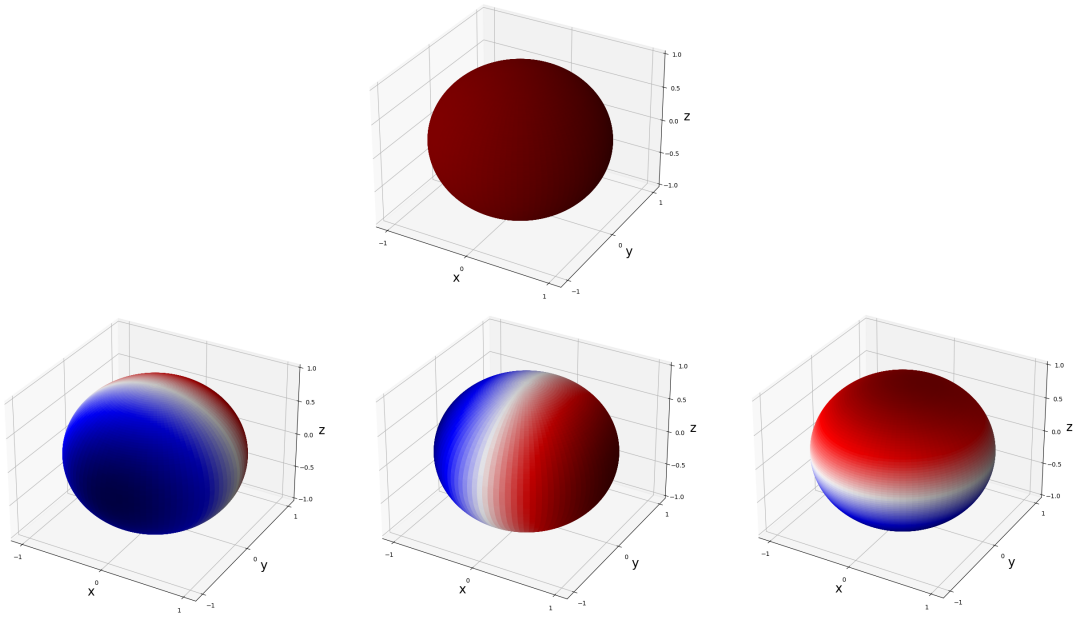

Figure 2.3: First-order Ambisonics directivities. Top: $\tilde{Y}_0^0$ normalized, corresponding to W. Bottom, from left to right: $\tilde{Y}_1^1$, $\tilde{Y}_1^{-1}$, $\tilde{Y}_1^0$ normalized, corresponding to X, Y, Z, respectively. The red regions correspond to positive values and the blue regions correspond to negative values.

axis. The channels X, Y and Z are assimilated to pressure gradients, which will be a useful propriety later in this chapter.

As a consequence of its low number of channels, which is a practical advantage here, the FOA format suffers from a low spatial resolution when representing the sound field [Raf05]. One consequence is the reduction of the *sweet spot* size: it is the spatial region between the loudspeakers in which the restitution of the original sound field is the most accurate.

Note that the Ambisonics format can be transposed directly into the short-time Fourier transform (STFT) domain, *i.e.*, for each STFT time frame index t and frequency bin f [11], we have:

$$\mathbf{x}(t,f) = \begin{bmatrix} W(t,f) \\ X(t,f) \\ Y(t,f) \\ Z(t,f) \end{bmatrix} = \begin{bmatrix} 1 \\ \sqrt{3}\cos\theta_k \cos\phi_k \\ \sqrt{3}\sin\theta_k \cos\phi_k \\ \sqrt{3}\sin\phi_k \end{bmatrix} s(t,f). \tag{2.31}$$

2.3.3 Higher-order Ambisonics

To improve the spatial resolution of the Ambisonics representation, we can increase the order N, leading to more components. When $N > 1$, we call it the higher-order

[11] Note that in this thesis we use the notations t and f for the frame index and frequency bin in the STFT domain, as it is usually employed. Those notations are also used to express the physical frequency f and time t only for some preliminary discussions as in this chapter.

Ambisonics representation. For an order N, there are $(N+1)^2$ channels to represent the original signal. Table 2.1 sums up the directivities of the HOA components up to order 3, also illustrated in Fig 2.4. Using HOA components notably increases the size of the sweet spot and the resolution of the spatial characteristics of the encoded sound field, but at the cost of more channels to handle.

n	m	$\tilde{Y}_n^m$	$\tilde{Y}_n^m(\theta,\phi)$
0	0	$\tilde{Y}_0^0$	1
1	-1	$\tilde{Y}_1^{-1}$	$\sqrt{3}\cos\theta\cos\phi$
	0	$\tilde{Y}_1^0$	$\sqrt{3}\sin\theta\cos\phi$
	1	$\tilde{Y}_1^1$	$\sqrt{3}\sin\phi$
2	-2	$\tilde{Y}_2^{-2}$	$\frac{\sqrt{15}}{2}\sin 2\theta\cos^2\phi$
	-1	$\tilde{Y}_2^{-1}$	$\frac{\sqrt{15}}{2}\sin\theta\sin 2\phi$
	0	$\tilde{Y}_2^0$	$\frac{\sqrt{5}}{2}(3\sin^2\phi-1)$
	1	$\tilde{Y}_2^1$	$\frac{\sqrt{15}}{2}\cos\theta\sin 2\phi$
	2	$\tilde{Y}_2^2$	$\frac{\sqrt{15}}{2}\cos 2\theta\cos^2\phi$
3	-3	$\tilde{Y}_3^{-3}$	$\sqrt{\frac{35}{8}}\sin 3\theta\cos^3\phi$
	-2	$\tilde{Y}_3^{-2}$	$\sqrt{\frac{105}{2}}\sin 2\theta\sin\phi\cos^2\phi$
	-1	$\tilde{Y}_3^{-1}$	$\sqrt{\frac{21}{8}}\sin\theta\cos\phi(5\sin^2\phi-1)$
	0	$\tilde{Y}_3^0$	$\frac{1}{2}\sin\phi(5\sin^2\phi-3)$
	1	$\tilde{Y}_3^1$	$\sqrt{\frac{21}{8}}\cos\theta\cos\phi(5\sin^2\phi-1)$
	2	$\tilde{Y}_3^2$	$\sqrt{\frac{105}{2}}\cos 2\theta\sin\phi\cos^2\phi$
	3	$\tilde{Y}_3^3$	$\sqrt{\frac{35}{8}}\cos 3\theta\cos^3\phi$

Table 2.1: Directivities of HOA components up to order 3, with the N3D normalization standard [Dan01].

2.3.4 Ambisonic encoding

In practice, Ambisonic signals (FOA or HOA respresentations) are computed from the finite number of acoustic pressure observations $\{p_i\}_{i\in[1,I]}$, measured by a microphone array. Denoting by $\mathbf{p}\in\mathbb{R}^I$ and $\mathbf{b}\in\mathbb{C}^{(N+1)^2}$ the vectors of concatenated observations $p(r,\theta_i,\phi_i,t)$, $q\in[1,I]$, and coefficients B_n^m, respectively, the expression (2.29) can be compactly written as

$$\mathbf{p}\approx\mathbf{Y}\mathbf{W}\mathbf{b}, \tag{2.32}$$

where $\mathbf{Y}\in\mathbb{R}^{I\times(N+1)^2}$ is the matrix whose rows contain spherical harmonic functions $\tilde{Y}_n^m(\theta_k,\phi_k)$, evaluated at the directions (θ_i,ϕ_i), and $\mathbf{W}\in\mathbb{C}^{(N+1)^2\times(N+1)^2}$ is the diagonal weight matrix whose entries contain a sum of $i^n j_n(kr)$ and a regularization term [Nic10]. Without additional information, one would need a microphone array containing $I\geq(N+1)^2$ channels to obtain the coefficients $\mathbf{b}$ of the order N, which imposes practical limitation for the design of an Ambisonics microphone.

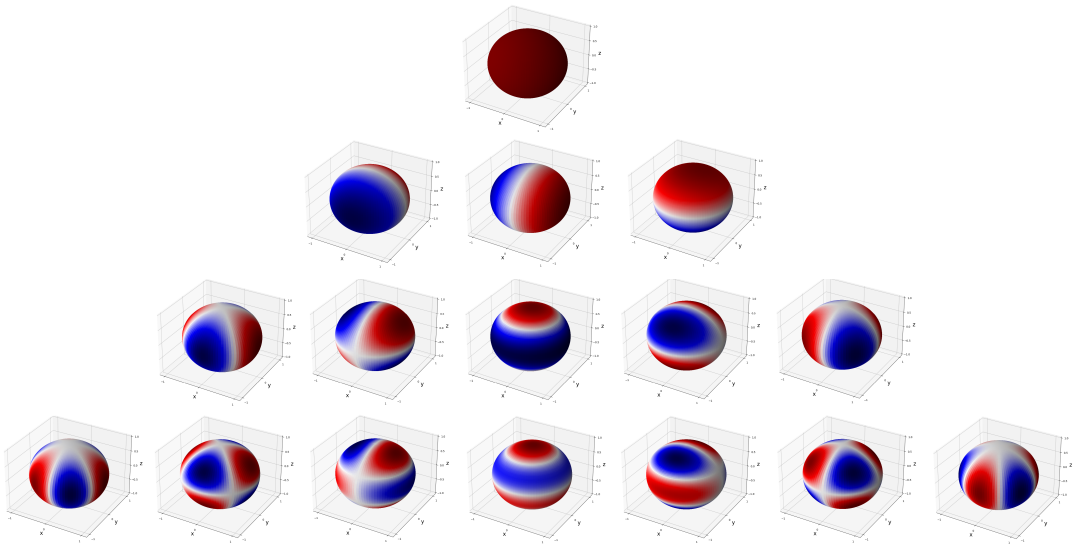

Figure 2.4: Higher-order Ambisonics directivities, with the spherical harmonics degree n increasing from top to bottom and the order m increasing from left to right. Red regions correspond to positive values and blue regions correspond to negative values.

2.4 Sound intensity and velocity vector

In the previous section, we introduced the definition of the Ambisonics coefficients, which are sufficient to entirely represent the sound field at any recording point. In this section, we present several representations based on the Ambisonics format which will be useful in the remainder of this thesis.

2.4.1 Sound intensity vector

Definition

Sound intensity is a fundamental acoustic quantity that is often used to characterize the distribution of energy of a sound field [WM00]. Often expressed as a time-averaged quantity over certain temporal segment, it describes the magnitude and direction of the flow of sound energy per unit area [JJ13]. For narrowband signals, one can define the complex "steady state" sound intensity vector as [Jac91; WM00]:

$$\mathbf{I} = p\mathbf{u}^*, \tag{2.33}$$

where p is the sound pressure, $\mathbf{u}$ is the particle velocity vector, which is the physical velocity of the particles in motion which transmit the wave [Kin00].

It can be shown that the sound pressure p and the particle velocity vector $\mathbf{u}$ are related by the *linearized fluid momentum equation* [Mer06, p. 27]:

$$-\nabla p = \rho_0 \frac{\partial \mathbf{u}}{\partial t}, \tag{2.34}$$

with ∇ being the gradient operator and ρ_0 denoting the air density.

The omnidirectional channel W can be considered an estimate of the acoustic pressure at the microphone position, while the FOA channels X, Y and Z approximate the spatial derivatives of pressure p along the Cartesian coordinate axes [Mer06, p. 50]. Therefore, one can approximate the particle velocity vector relatively to these channels with [PDMP18, p. 90] (the factor $1/\sqrt{3}$ is due to the presumed N3D normalization):

$$\mathbf{u}(t) = -\frac{1}{\rho_0 c\sqrt{3}} \begin{bmatrix} X(t) \\ Y(t) \\ Z(t) \end{bmatrix}. \tag{2.35}$$

As we will see later, we are mainly interested in the *direction* of the vector $\mathbf{u}(t)$, hence, by an abuse of notation, we also denote by $\mathbf{u}$ the normalized particle velocity vector.

Since the previous equation is an approximation, injecting it into (2.33) leads to an approximation of the intensity vector, which we call the *pseudointensity* vector (PIV). To simplify the notation, we use the same symbol $\mathbf{I}$ to refer to the pseudointensity vector, which is now expressed using only the FOA components (in the STFT domain) as:

$$\mathbf{I}(t,f) = \alpha \begin{bmatrix} W(t,f)X^*(t,f) \\ W(t,f)Y^*(t,f) \\ W(t,f)Z^*(t,f) \end{bmatrix}, \tag{2.36}$$

with $\alpha = -\frac{1}{\rho_0 c\sqrt{3}}$ a factor that will be dropped thereafter. As for the remaining of this thesis, we will refer to the pseudointensity vector based on FOA components as the *first-order-pseudointensity vector* (FO-PIV).

Active first-order-pseudointensity vector

We define the *active first-order-pseudointensity vector* as the real part of the complex FO-PIV:

$$\mathbf{I}_a = \begin{bmatrix} \Re\big(W(t,f)X^*(t,f)\big) \\ \Re\big(W(t,f)Y^*(t,f)\big) \\ \Re\big(W(t,f)Z^*(t,f)\big) \end{bmatrix}. \tag{2.37}$$

This quantity physically represents the transport of sound energy in the fluid, and it can be shown to be proportional to the gradient of the phase of sound pressure [JJ13]. In other words, assuming free-field propagation, active intensity is orthogonal to the propagating wavefront.

Reactive first-order-pseudointensity vector

The *reactive first-order-pseudointensity vector* is defined as the imaginary part of the complex FO-PIV:

$$\mathbf{I}_r = \begin{bmatrix} \Im\big(W(t,f)X^*(t,f)\big) \\ \Im\big(W(t,f)Y^*(t,f)\big) \\ \Im\big(W(t,f)Z^*(t,f)\big) \end{bmatrix}. \tag{2.38}$$

Physically, the reactive FO-PIV represents the dissipative local energy transfers [Dan01], and is orthogonal to the surfaces of equal energy of sound pressure [JJ13; Dan01]. While being negligible under the far/free field assumptions, reactive intensity becomes important in reverberant conditions.

Higher-order pseudointensity vector

We extend the previously introduced FO-PIV by using HOA components. The general expression for this *higher-order-pseudointensity vector* (HO-PIV) is, at order N:

$$\mathbf{I}^N(t,f) = B_0^0(t,f)\mathbf{B}_{1:N}^*(t,f), \tag{2.39}$$

where $\mathbf{B}_{1:N}$ is the vector containing all HOA channels for $n = 1$ to N (there are $(N+1)^2 - 1$ channels in total). We can see that $\mathbf{I}^1$ corresponds to the FO-PIV.

The definition of the active and reactive HO-PIV using HOA components ($\mathbf{I}_a^N$ and $\mathbf{I}_r^N$) is similar to the first-order case, *i.e.*, they correspond to the real and imaginary part of the HO-PIV $\mathbf{I}^N$, respectively.

Pseudointensity vector normalization

A normalized version of the FO-PIV is obtained as follows:

$$\bar{\mathbf{I}}(t,f) = \frac{\mathbf{I}(t,f)}{|W(t,f)|^2 + \frac{1}{3}\big(|X(t,f)|^2 + |Y(t,f)|^2 + |Z(t,f)|^2\big)}. \tag{2.40}$$

Note that the norm of $\bar{\mathbf{I}}(t,f)$ is upper bounded by 1.

More generally, the normalized HO-PIV[12] is given by:

$$\bar{\mathbf{I}}^N(t,f) = \frac{\mathbf{I}^N(t,f)}{\sum_{n=0}^{N} \frac{1}{2n+1} \sum_{m=-n}^{n} |B_n^m|^2}. \tag{2.41}$$

Assuming that the time-frequency bin (t,f) is dominated by a single source, the normalized (FO-/HO-)PIV is independent of the source signal "content" $s(t,f)$, and mainly encodes the spatial footprint of sound propagation. This is easily observed for the plane wave propagation, since (according to (2.27)), we have $B_0^0 B_n^{m*} \propto |B|^2$. The latter term cancels out in (2.41), and the remaining part depends only on the corresponding spherical harmonics of different orders.

[12] Again, assuming the N3D normalization standard.

2.4.2 Frequency-domain velocity vector

The sound PIV was defined as the product between the first Ambisonics channel $W := B_0^0$ and the other channels (X, Y and Z for FO-PIV, and all channels except W for HO-PIV). We also showed a way to normalize the PIV to bound its values. A related representation, termed Frequency-Domain Velocity vector (FDVV) in [Dan01], is obtained by dividing the complex conjugate of FO-PIV by $|W(t,f)|^2$:

$$\mathbf{V}(t,f) = \frac{\mathbf{I}(t,f)^*}{|W(t,f)|^2} = \frac{1}{W(t,f)} \begin{bmatrix} X(t,f) \\ Y(t,f) \\ Z(t,f) \end{bmatrix}. \tag{2.42}$$

Analogously to $\bar{\mathbf{I}}(t,f)$, due to the division by $|W(t,f)|^2$, the FDVV has the advantage of being less dependent on the energy and therefore on the content of the signal. As for the complex PIV, we can separate the FDVV into the real and imaginary parts.

2.4.3 Time-domain velocity vector

In this section, we will define the *time-domain velocity vector* as the inverse Fourier transform (IFT) of the FDVV[13] [DK20], but we modify the expression of the FDVV a bit beforehand.

We place ourselves in a single-source environment in which the Ambisonics recording captures the multipath signal. For a single timestep, due to the superposition principle (1.3), each recorded FOA channel will be a sum of delayed and attenuated copies of the source signal $s(t)$ (with an attenuation depending on the incoming wavefront direction and channel directivity). Under the far field assumption, the n^{th} such wavefront $\mathbf{x}_n(t)$ may be represented by a plane wave. According to (2.30), the FOA components of the plane wave propagating from the direction (θ_n, ϕ_n), in frequency domain, are compactly expressed by

$$\mathbf{x}_n(f) = \begin{bmatrix} 1 \\ \sqrt{3}\mathbf{u}_n, \end{bmatrix} s(f),$$

where $\mathbf{u}_n$ is the corresponding normalized particle velocity defined in (2.35).

The recorded signal, in the noiseless case, is then a sum of FOA-encoded plane waves:

$$\mathbf{x}(f) = s(f) \sum_n a_n(f) \mathbf{x}_n(f),$$

with $a_n(f)$ being the complex magnitude (incorporating both the common attenuation factor and phase shift) of the sound wave at frequency f.

[13] Note that FDVV and TDVV are also known as *Relative Transfer Function* and *Relative Impulse Response* (in the spherical harmonic domain), respectively [JHN17].

Plugging these expressions into the definition of FDVV (2.42), we can now decompose the FDVV at frequency f into the different reflections[14]:

$$\mathbf{V}(f) \simeq \frac{\sum_n a_n(f)\mathbf{u}_n}{\sum_n a_n(f)} = \frac{\mathbf{u}_0 + \sum_{n\geq 1}\gamma_n(f)\mathbf{u}_n}{1 + \sum_{n\geq 1}\gamma_n(f)}, \tag{2.43}$$

where $\gamma_n(f) = \frac{a_n(f)}{a_0(f)} = g_n(f)e^{-2i\pi f\tau_n}$ is the relative *gain* of the n^{th} reflection with respect to the direct path (without losing generality we assume that n follows the order of reflections). Assuming that $|\sum_{n\geq 1}\gamma_n(f)| < 1$, we can express $\mathbf{V}(f)$ using the Taylor series of the function $f(x) = \frac{1}{1+x}$:

$$\mathbf{V}(f) = \Big(\mathbf{u}_0 + \sum_{n\geq 1}\gamma_n(f)\mathbf{u}_n\Big)\sum_{k=0}^{\infty}\Big(\sum_{n=1}^{\infty} -\gamma_n(f)\Big)^k, \tag{2.44}$$

which we can rearrange by separating the terms from the primary reflections and the terms coming from the interactions between reflections:

$$\begin{aligned}
\mathbf{V}(f) &= \mathbf{u}_0 + \mathbf{u}_0\sum_{k=1}^{\infty}\Big(\sum_{n=1}^{\infty} -g_n(f)e^{-2i\pi f\tau_n}\Big)^k \\
&+ \sum_{k=0}^{\infty}\sum_{n=1}^{\infty}\Big(g_n(f)e^{-2i\pi f\tau_n}\mathbf{u}_n\Big)\Big(\sum_{n=1}^{\infty} -g_n(f)e^{-2i\pi f\tau_n}\Big)^k \\
&= \mathbf{u}_0 + \mathbf{u}_0\sum_{k=1}^{\infty}\sum_{n=1}^{\infty}\Big(-g_n(f)e^{-2i\pi f\tau_n}\Big)^k \\
&+ \sum_{k=0}^{\infty}\sum_{n=1}^{\infty} -\mathbf{u}_n\Big(-g_n(f)e^{-2i\pi f\tau_n}\Big)^k + \Lambda(f),
\end{aligned} \tag{2.45}$$

where $\Lambda(f)$ contains the cross terms of the interactions between reflections. Finally we obtain:

$$\mathbf{V}(f) = \mathbf{u}_0 + \sum_{k=0}^{\infty}\sum_{n=1}^{\infty}\Big(\mathbf{u}_0 - \mathbf{u}_n\Big)\Big(-g_n(f)\Big)^k e^{-2i\pi fk\tau_n} + \Lambda(f). \tag{2.46}$$

Assuming now that $g_n(f) = g_n$ is frequency-independent, we now apply the IFT of $\mathbf{V}$ to define the *time-domain velocity vector* (TDVV) :

$$\mathbf{V}(t) = \delta(t)\mathbf{u}_0 + \sum_{k=0}^{\infty}\sum_{n=1}^{\infty}\Big(\mathbf{u}_0 - \mathbf{u}_n\Big)(-g_n)^k\delta(t - k\tau_n) + \lambda(t), \tag{2.47}$$

with δ denoting the Dirac delta function and $\lambda(t)$ the IFT of $\Lambda(f)$.

[14]Here we use the symbol "$\simeq$" instead of equality due to the N3D encoding factor $\sqrt{3}$ in the denominator. Without loss of generality, we drop this value in the ensuing expressions.

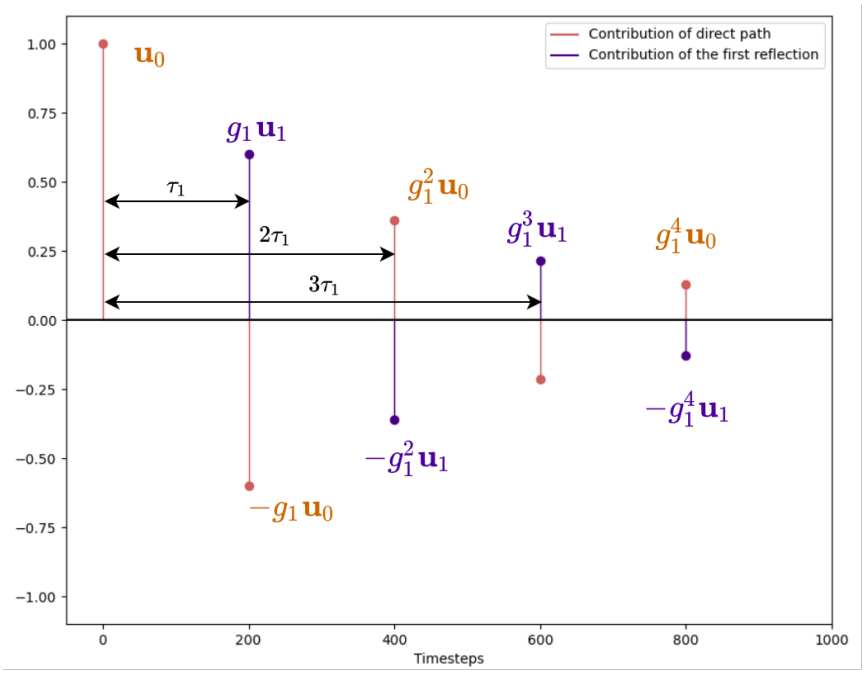

Figure 2.5: Theoretical time-domain velocity vector considering only one reflection. The first orange peak at $t = 0$ contains the coordinates of a vector colinear to the source DoA, representing the direct path between the source and the microphone array. The other orange peaks represent the contribution of the direct path to the value of the TDVV for different timesteps, while the purple peaks represent the contribution of the first reflection. All the peaks are equally spaced by an interval equal to τ_1, and the peak amplitudes exponentially decay by a factor $-g_1$, with alternating sign.

In order to better appreciate the information contained in the TDVV, let us first assume that there is only one reflection in the considered environment:

$$\mathbf{V}(t) = \delta(t)\mathbf{u}_0 + \sum_{k=0}^{\infty} \Big(\mathbf{u}_0 - \mathbf{u}_1\Big)(-g_1)^k \delta(t - k\tau_1) + \lambda(t). \tag{2.48}$$

Fig. 2.5 illustrates what the TDVV looks like when considering only one reflection. As the TDVV is a vector with three coordinates (considering only the FOA domain), the coordinate in y-axis actually encodes the vector coordinates (the x-axis represents time). At $t = 0$, we have $\mathbf{u}(0) = \mathbf{u}_0$ which is a vector colinear to the signal DoA. Then when t increases we have a series of exponentially decaying peaks which are colinear to $\mathbf{u}_0 - \mathbf{u}_1$ at all time values which are multiples of τ_1. Therefore we can theoretically retrieve the DoA, the first reflection direction, delay and relative gain with the TDVV under the assumptions of a single sound source with only one reflection and without noise.

Now let us consider the general form of the TDVV with more than one reflection, leading to interaction between them. On Fig. 2.6 we can see what the TDVV looks like by illustrating the contributions of the direct path and the first two reflections,

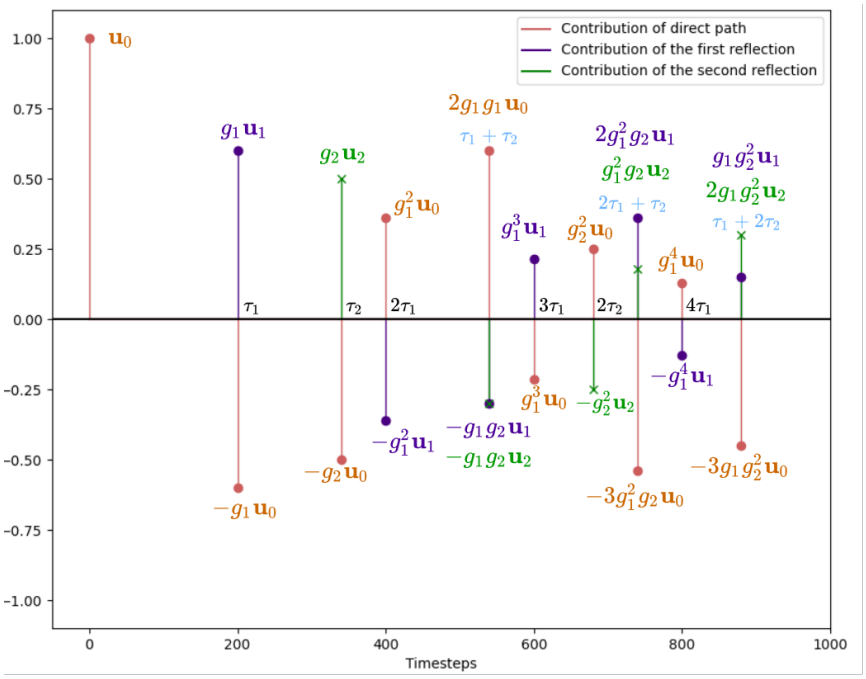

Figure 2.6: Theoretical time-domain velocity vector considering several reflections. The contributions of the direct path is represented in orange, those of the first reflection in purple and those of the second reflection in green. As in the case of only one reflection, the contributions corresponding to one reflection are equally spaced by τ_n. In blue are indicated times for which the peaks contain the contributions of the interactions between the different reflections.

including the interactions (in blue in the figure). We can see that the peaks involving the contribution of only one of the reflections are still equally spaced by τ_n. But now we see the appearance of some of the cross terms which were included in $\lambda(t)$ in (2.47). Another phenomenon not represented in the figure can occur: theoretically, the different contributions of the reflections alone or those of the interaction between the reflections can overlap at the same time (related to the least common multiple of τ_n) so it can be more difficult to separate the different contributions when analyzing the TDVV.

The TDVV thus provides an interesting representation to retrace the multipath propagation of a sound source. However, strong assumptions have been made to obtain an analytical expression for the TDVV: a single-source configuration without noise, frequency-independent gains, and the hypothesis that $|\sum_{n\geq 1}\gamma_n(f)| < 1, \forall f$ which is not fulfilled in practice. We do not push further the analysis of the TDVV in this thesis, since it is a relatively new idea in the literature. However, a certain number of experiments, discussed in Chapter 6, has been conducted to exploit such a representation.

2.5 Conclusion

In this chapter, we introduced the framework we relied on in this thesis, based on the Ambisonics format. The main advantage of Ambisonics lies in the fact that it is capable of encoding a sound scene independently of the microphone array configuration, and without emphasizing any particular direction. We have shown the definition of the Ambisonics coefficients based on the spherical harmonics decomposition of the signal, which emerged from solving the wave equation in the spherical domain. These coefficients, considered at order 1 (FOA) or higher (HOA), have been employed to define several physical quantities such as the FO- and HO-PIV, and the frequency-domain or time-domain velocity vector. All these sound representations have been used in our thesis work, generally as an input feature for neural networks, which are introduced in the next chapter.

Chapter 3

Artificial Neural Networks

Artificial neural networks (ANN) are a set of algorithms designed to mimic biological neural networks. They are the core components of deep learning [GBC16], which itself can be defined as a part of machine learning. Machine learning refers to the capabilities of certain systems to learn how to perform a specific task, having been provided with an appropriate data for training. At the time of this thesis writing, in 2021, more and more applications have proven how much deep learning has improved the performance of machines in many various tasks, *e.g.*, in image recognition [He+16], machine translation [Vas+17], speech recognition [Hin+12], sound source separation [Hen+20], board game playing [Sil+17], protein structure prediction [Jum+21], or music generation [HPN17]. While it is theoretically possible to learn any task with a three-layer neural network [HSW89], neural systems generally consist of many layers connected together, resulting in deep neural architectures, hence the term *deep learning*.

Many neural network architectures have been proposed in the past, and many of them were initially designed for a specific task, *e.g.*, convolutional neural networks (CNN) for image recognition [LeC+89] or attention mechanism for machine translation [He+16]. Due to their success, it is common to encounter adaptations of these architectures to address problems other than the original one: for example, CNNs have been widely used for audio related tasks [Pur+19], while attention-based neural networks are commonly applied for computer vision [Dos+21].

In this chapter, we provide a short overview of deep learning, and more precisely of different types of neural networks which were used throughout this thesis. Although the exploitation of artificial neural networks (ANN) is relatively new in the SSL literature (see Section 4.2), deep learning is widely established in the audio research community, so this section is written assuming that the reader has some basic background on ANNs. We describe the different neural network architectures and mechanisms we exploited in this thesis. We assume this short introduction will be sufficient to help the reader to easily follow the experiments described in the next chapters. If needed, more in-depth description of deep learning can be found in [GBC16].

This chapter is organized as follows. The first section introduces the basis of ANNs and the multilayer perceptron. The second section explains the inner workings of a CNN, while the third section deals with recurrent neural networks (RNNs). The

fourth section proposes a quick summary of residual connections. The fifth section describes the attention mechanism.

3.1 Multilayer perceptron and backpropagation algorithm

3.1.1 Multilayer perceptron or feedforward neural network

A *multilayer perceptron* (MLP) is a particular kind of artificial neural network in which all the connections are made forward, hence its name. In this section, we describe how an MLP can approximate a function using layers of artificial neurons and activation functions. We also explain how such a neural network can be trained with the backpropagation algorithm, with a review of loss functions and output units used throughout this thesis.

Artificial neurons

The fundations of artificial neural networks have been proposed as early as 1943 when McCulloch and Pitts [MP43] established a computational model of biological neurons. An artificial neuron is the building block of an ANN, and is composed of two stages :

- A linear combination of its entries, using a set of weights specific to this neuron, as in (3.1)
- The addition of a bias b
- An activation function σ applied after the linear combination

$$y = \sigma\Big(\sum_{i=1}^{I} \theta_i x_i + b\Big), \tag{3.1}$$

where $\{\theta_i\}_i$ and b form the weights of the neurons, x_i are the entries of the input $\mathbf{x}$ and y is the (scalar) output. We often set $b = \theta_0$ and append 1 to the input vector so that $\{\theta_i\}_i$ is the entire set of weights.

Generally, multiple neurons are assembled to form a *layer*, in which all the neurons are input with the same vector $\mathbf{x}$, thus each neuron of the same layer contains the same number of weights. An *artificial neural network* is then defined to be a succession of H layers of artificial neurons (H is known as the *depth* of the network), each layer being fed with the vector formed by the output of all neurons from the previous layer. If the layer h is composed of I_h neurons with input $\mathbf{x}^{h-1}$ (with I_{h-1} components), then the entries of the output vector $\mathbf{x}^h$ are:

$$x_j^h = \sigma\Big(\sum_{i=1}^{I_{h-1}} \theta_{j,i}^h x_i^{h-1} + b_j^h\Big), \tag{3.2}$$

for all $j \in \{1, ..., I_h\}$. This type of layer is called a *fully-connected* layer or a *feedforward* (FF) layer. The layer at $h = 1$ is known as the *input* layer, which directly receives the

input features to its entries, and the last layer at $h = H$ is known as the *output* layer. We generally name the output vector $\mathbf{y}$. The other layers are termed *hidden* layers.

We can rewrite (3.2) in a more compact manner as:

$$\mathbf{x}^h = \sigma(\mathbf{b}^h + \mathbf{W}^h \mathbf{x}^{h-1}), \tag{3.3}$$

where $\mathbf{b}^h$ is the *bias* vector of layer h and $\mathbf{W}^h$ is the weight matrix in $\mathbb{R}^{I_h \times I_{h-1}}$. This computation is known as a *forward pass*.

The universal approximation theorem [HSW89] states that a MLP with two layers and a non-polynomial activation function at the first layer can approximate any function f with an arbitrary accuracy.

Activation functions

There is a number of non-polynomial activation functions commonly used in the DL literature, as well as in this thesis. Linear activation functions are mostly used at the output layer, when the network is used in regression mode (see Section 4.2.2).

The *rectified linear unit* (ReLU) is one of the most used activation function:

$$\sigma(x) = max(0, x), \quad \forall x \in \mathbb{R}. \tag{3.4}$$

This function has the advantage to preserving some of the properties that make linear models generalize well [GBC16].

The *sigmoid* function is defined by:

$$\sigma(x) = \frac{1}{1 + e^{-x}}, \quad \forall x \in \mathbb{R}. \tag{3.5}$$

Its values are always in $[0, 1]$, and it converts large negative values to 0 and large positive values to 1. It is often used as an output activation function with its output value seen as a probability, which is particularly suitable for binary classification problems. Sometimes, the *hard sigmoid* is preferred for its sharper contour:

$$\sigma(x) = max\Big(0, min\big(1, \frac{x+1}{2}\big)\Big), \quad \forall x \in \mathbb{R}. \tag{3.6}$$

The *hyperbolic tangent (tanh)* function is defined by:

$$\sigma(x) = \frac{e^{2x} - 1}{e^{2x} + 1}, \quad \forall x \in \mathbb{R}. \tag{3.7}$$

The shape of tanh ressembles the shape of the sigmoid but it takes values within $[-1, 1]$. Finally, the *softmax* function is a generalization of the sigmoid function and produce a set of values within $[0, 1]$:

$$\sigma(y_i) = \frac{e^{x_i}}{\sum_{i=0}^{I} e^{x_i}}, \tag{3.8}$$

where x_i and y_i are the components of vectors $\mathbf{x}$ and $\mathbf{y}$, respectively. This function ensures that $\mathbf{y}$ can be seen as a probability distribution since its entries sum to 1, which is particularly suitable for multi-class classification problems.

3.1.2 The backpropagation algorithm

During the training stage, a neural network can adjust its weights with an algorithm called *backpropagation* – other algorithms exist - each time it is fed with a training example. To do that, the neural network performs a forward pass with training example $\mathbf{x}$, which gives an output value $\hat{\mathbf{y}}$. After choosing a *loss* (or *cost*) function $\mathcal{L}$, the knowledge of the target value $\mathbf{y}$ (which is known as the *label* or *ground-truth* of data $\mathbf{x}$) leads to the computation of the error made by the neural network for input $\mathbf{x}$, $\mathcal{L}(\mathbf{y}, \hat{\mathbf{y}})$. The backpropagation algorithm uses this value $\mathcal{L}(\mathbf{y}, \hat{\mathbf{y}})$ to adjust the weights of the neurons with a gradient descent. If at iteration t of the backpropagation algorithm the weights are $\mathbf{w}^t$ (we drop the index h for better visualization), the new value $\mathbf{w}^{t+1}$ at iteration $t+1$ is:

$$\mathbf{w}^{t+1} = \mathbf{w}^t - \eta \frac{\partial \mathcal{L}(\mathbf{y}, \hat{\mathbf{y}})}{\partial \mathbf{w}^t}, \tag{3.9}$$

where η is known as the *learning rate*. This operation is done for all weights and for all training examples, until some convergence criterion is met. In practice, the neural network is fed with the whole training set (which is called an *epoch*) for a certain number of times. The learning rate is often reduced when the loss has not decreased enough during a certain number of epochs.

Loss functions

The choice for the loss function $\mathcal{L}$ depends on the output strategy. The idea is to opt for a function that penalizes the difference between the ground-truth $\mathbf{y}$ and the estimated value $\hat{\mathbf{y}}$ with a sufficiently large value so that the change in weights due to gradient descent is significant. Moreover, loss functions are generally applied "simultaneously" on subsets of training examples called *training batches*. In the following, we define the loss functions only for one training example, while for training batches the loss is obtained by summing the losses of all batch examples. Throughout this thesis, several loss functions were exploited:

- Mean squared error (MSE) : $\mathcal{L}(\mathbf{y}, \hat{\mathbf{y}}) = \frac{1}{I} \sum_i^I (y_i - \hat{y}_i)^2$. When computing the loss for a training batch, the sum of all losses is divided by the number of examples in the batch, hence the term *mean*. It is often used with a regression paradigm.
- Categorical cross-entropy : $\mathcal{L}(\mathbf{y}, \hat{\mathbf{y}}) = -\sum_{i=1}^I y_i log(\hat{y}_i)$. This cross-entropy can be used for a classification problem, for which $\mathbf{y}$ is a one-hot vector (all entries are set to 0 except the one corresponding to the class which is set to 1). The softmax activation function suits well to this loss function.

- Binary cross-entropy : a particular case of the categorical cross-entropy when $I = 2$. It is generally used when $\mathbf{y}$ has a binary value (0 or 1) and in conjonction with the sigmoid function which bounds the values of $\hat{\mathbf{y}}$ in $[0, 1]$. If $\mathbf{y}$ and $\hat{\mathbf{y}}$ are vectors with binary values, the loss is obtained by summing the binary cross-entropy for each vector entry.

3.1.3 Avoiding overfitting

A major problem in neural networks is that the model can lack generalization when it is applied on data unseen during the training stage. This phenomenon is called overfitting, and part of deep learning research has been dedicated to avoid it and make the neural network to generalize better on unseen data. One strategy to control the learning of a neural network is to make use of a *validation* dataset, which does not contain common data with the training dataset. During the training phase, the performance of the neural network is evaluated on the validation dataset (hence unseen data), and the training is stopped when the performance starts decreasing, meaning that the model starts overfitting on the training data. This monitoring method is known as *early stopping*.

Another common regularization method is *dropout* [Sri+14]. It relies on bypassing random neurons (except for those in the output layer) based on a user-adjustable probability so that the output of these neurons are fixed to zero. This enforces the neural network not to overuse some specific neurons, and consequently prevents overfitting. Finally, batch normalization is a technique which can make a neural network more stable by rescaling and recentering the data in-between layers.

These methods were regularly used all along the experiments in this thesis.

3.2 Convolutional neural networks

Convolutional neural networks (CNN) are neural networks including convolutional layers which are specifically well-designed for processing data presented as a grid, for instance images represented by pixels. It has been pioneered in the end of the 1980s by LeCun et al. [LeC+89] to recognize handwritten digits in images. Since then, other new ideas around convolutional layers have been proposed in the literature. This section aims to provide a quick overview of CNNs, since they were used in our experiments.

3.2.1 Convolutional layers

As its name indicates, a convolutional layer applies a convolution on its input to produce an output, using a convolution kernel (or filter) k which contains the learnable weights. In the 1D discrete domain (*e.g.*, discrete time), this convolution is expressed by:

$$y(n) = (x * k)(n) = \sum_i x(n - i)k(i), \tag{3.10}$$

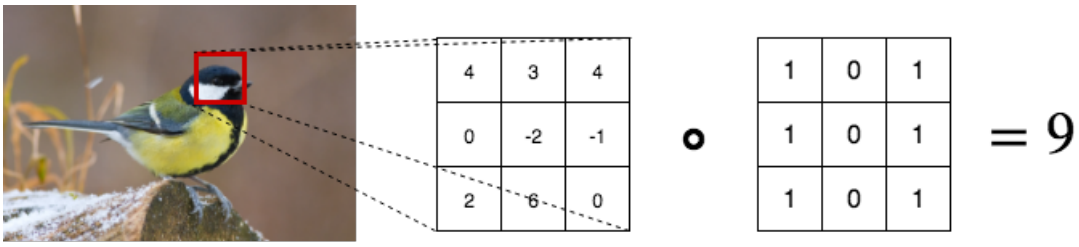

Figure 3.1: 2D convolution operation with a 3×3 kernel. Each 3×3 region on the image is multiplied with the kernel (right matrix), which is a 2D convolution operation, resulting in a scalar value associated to the region in the output. Zero-padding can optionally be used for regions on the edges. Note that the illustrated kernel is an example of how we can detect vertical contours with convolutions.

where x and y are the input and output, respectively, and n is the discrete sample index. In practice, the kernel k is a vector with a fixed size, so the sum is in a finite corresponding range.

In the 2D domain, the convolution is applied in both dimensions:

$$y(m,n) = (x * k)(m,n) = \sum_i \sum_j x(m-i, m-j)k(m,n). \tag{3.11}$$

In this case, the kernel is a 2D matrix, and the same consideration applies regarding the range of the summation. Fig. 3.1 illustrates how a single 2D kernel of size 3×3 would be applied for each pixel of an input image.

This convolution operation has also been extended to higher dimension, but this will be not used in this thesis. Zero-padding, *i.e.*, automatic completion of input image edges with zeros, can be used so that the output dimension is exactly the same as the input dimension. In contrast, one can use a *stride*, *i.e.*, a shift of the kernel operator in between two successive convolutions, greater than one so as to limit the size of the output and somehow "compress" the data representation, at the price of lower resolution.

During the training phase, the kernel matrix is learnt so that it provides the most meaningful convolution operation for the neural network to perform a task. In a convolutional layer, a bank of (possibly many) different kernels are generally instantiated, so that each one can perform a specific operation, leading to different higher-level outputs, which are commonly called *feature maps*. These outputs are then stacked, as illustrated in Fig. 3.2, and can become the input for another convolutional layer.

One major advantage of convolutional layers is that the operations are translation equivariant [Bro+21]. In that way, each kernel can be learnt to highlight specific contours in the input feature, which is why several kernels are assembled in each convolutional layer. The obtained feature maps provide a somehow higher-level representation of the input signal, and stacking several convolutional layers one after

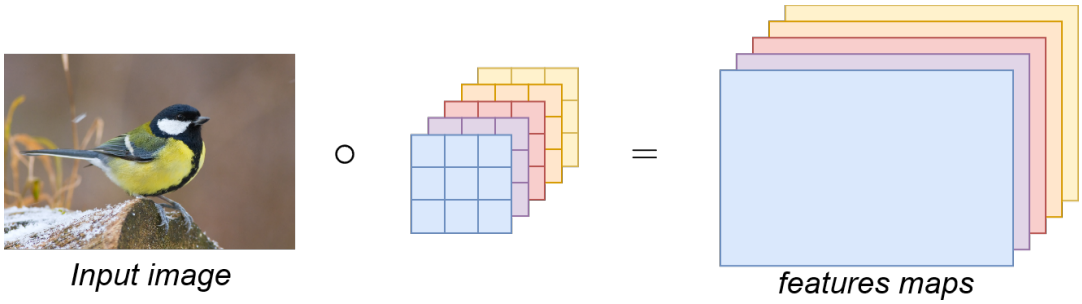

Figure 3.2: Application of multiple convolution kernels on a input image. Each kernel has its own set of learnable weights, and results in specific outputs, which are stacked in what is called feature maps.

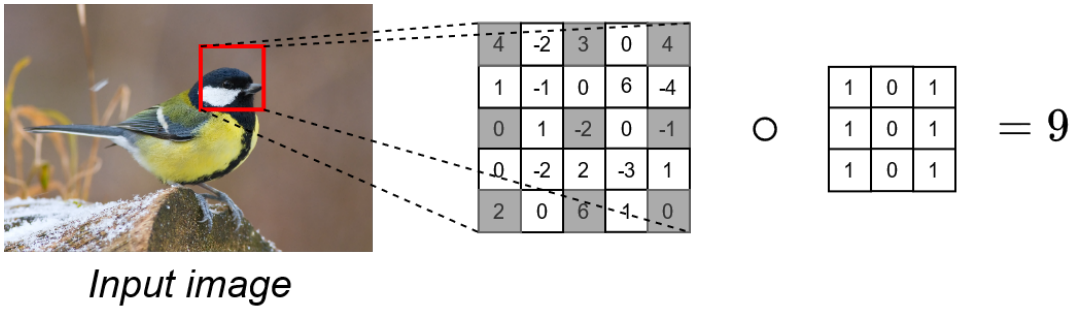

Figure 3.3: Visualization of dilated convolutions with a dilation factor $l = 2$.

another is often employed to perform *feature extractions* in practice.

3.2.2 Dilated convolutions

A generalization of the convolution kernels presented above has been proposed in [YK16], under the name *dilated convolution*. The idea is to apply the kernel on a downsampled version of the data, so that the convolution operation span is increased while keeping the same amount of learnable weights. This dilated convolution can be expressed by [YK16]:

$$(x * k)(n) = \sum_i x(n - li)k(i), \tag{3.12}$$

where l is the *dilation factor*. For $l = 1$, this operation is equivalent to the classical convolution. The idea can be extended to higher dimensions. Fig. 3.3 illustrates how these dilated convolutions operate on input data, showing how it increases the convolution operation span. Dilated convolutions are also called *atrous* convolutions, since we can see them as classical kernels with zeros inserted in between the actual weights.

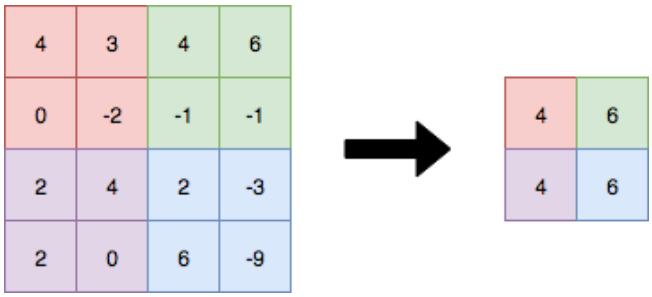

Figure 3.4: Max-pooling operation. The operation is downsampling the data by keeping only the highest value of a considered region., In this example, the pooling size is 2×2 and the stride is 2.

3.2.3 Pooling operation

Pooling layers are also very common when using convolutional layers in neural networks. The goal of these layers is to downsample the data to reduce its dimensionality. The pooling size indicates the region shape in which only one value is extracted. If max-pooling is used, the highest value is kept, while if average pooling is used, the extracted value is the mean of all values in the corresponding region. As with convolutional layers, one can opt for a stride value, *i.e.*, a shift that will skip data when applying the pooling operation. Fig. 3.4 illustrates the max-pooling operation with a pooling size of 2×2 and a stride of 2.

3.3 Recurrent neural networks

Recurrent neural networks (RNN) are a family of neural networks that are suitable for processing sequential data, in which the ordering of successive data vectors bears importance. With MLPs or CNNs, data are processed one layer after another, without memorizing the operations within the network. The idea behind RNNs is to keep in memory some values (called *states*) that contain a summary of past data information and which are used for further computation of the present output vector, thus giving more flexibility to the neural model.

3.3.1 Basic recurrent neural networks

We consider a sequence of data vectors $\mathbf{x}^t$ where $t \in \{1, ..., T\}$ is analog to a time index (although it could be any sequential index). In a basic recurrent layer, at each timestep t, a hidden vector $\mathbf{h}^t$ is considered in addition to the input vector $\mathbf{x}^t$. First, the hidden vector $\mathbf{h}^t$ is computed from the previous hidden vector $\mathbf{h}^{t-1}$ and the current input vector $\mathbf{x}^t$:

$$\mathbf{h}^t = \sigma_h(\mathbf{W}_h\mathbf{h}^{t-1} + \mathbf{W}_x\mathbf{x}^t + \mathbf{b}), \tag{3.13}$$

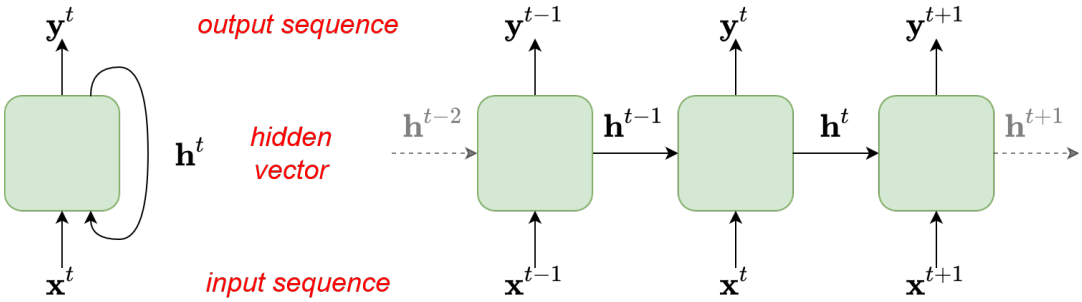

Figure 3.5: Compact (left) and unrolled (right) visualization of a basic recurrent layer.

where $\mathbf{W}_h$ and $\mathbf{W}_x$ are weight matrices and $\mathbf{b}$ is the bias weight vector. Then, the output vector is computed as :

$$\mathbf{y}^t = \sigma_y(\mathbf{W}_y\mathbf{h}^t), \tag{3.14}$$

with $\mathbf{W}_y$ being the layer output weight matrix. Note that the activation functions σ_h and σ_y are not necessarily the same. Fig. 3.5 illustrates how a basic recurrent layer processes data.

Note that recurrent layers are often employed besides convolutional layers to form a convolutional recurrent neural network (CRNN).

3.3.2 Backpropagation through time and vanishing gradient

With the way a recurrent neural network is defined, one has to turn the usual backpropagation algorithm presented in Section 3.1.2 into what is referred as backpropagation through time (BPTT). Without giving all details which can be found, *e.g.*, in [GBC16], the idea is to unfold the recurrent layer and consider the weights to be shared by each step. BPTT first relies on computing the loss for all timesteps of all sequences in the training batch. Then the gradient of the total loss for a specific weight is obtained as the sum of the gradients for each timestep. However the gradients for timesteps $t > 0$ depends on the gradients for previous timesteps $t' < t$, so one needs to iterate backwards through time in order to compute all the gradients (hence the name BPTT).

One well-known limitation of this algorithm is the so-called *vanishing gradient problem*. As the gradients are computed in an iterative way, some gradient values can become very small thus preventing the weight from changing its value. The more iterations are considered the more pronounced is this phenomenon.

3.3.3 Long short-term memory

The long short-term memory (LSTM) is a recurrent architecture proposed in 1997 by Hochreiter and Schmidhuber [HS97], as a means to cope with the vanishing gradient

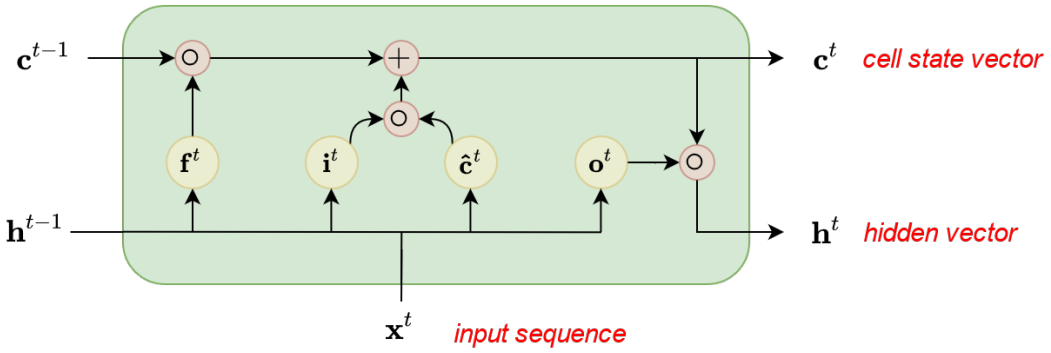

Figure 3.6: Long short-term memory cell mechanism. In this diagram the activation functions are not showed for the sake of clarity. The gates are displayed in yellow whereas the operations are in red, with $\circ$ denoting the Hadamard (element-wise) product.

problem. Fig. 3.6 illustrates the mechanism behind an LSTM cell. In addition to the input vector $\mathbf{x}^t$ and the hidden vector $\mathbf{h}^t$, this model introduces new vectors which are used as *gates* to control the flow of information inside the LSTM cell. The first four vectors, which are all computed in a similar way with their own weights, are:

- a forget gate vector $\mathbf{f}^t$ obtained by:

$$\mathbf{f}^t = \sigma_s(\mathbf{W}_{f,x}\mathbf{x}^t + \mathbf{W}_{f,h}\mathbf{h}^{t-1} + \mathbf{b}_f), \tag{3.15}$$

- an input gate vector $\mathbf{i}^t$ computed with:

$$\mathbf{i}^t = \sigma_s(\mathbf{W}_{i,x}\mathbf{x}^t + \mathbf{W}_{i,h}\mathbf{h}^{t-1} + \mathbf{b}_i), \tag{3.16}$$

- an output gate vector $\mathbf{o}^t$ expressed by:

$$\mathbf{o}^t = \sigma_s(\mathbf{W}_{o,x}\mathbf{x}^t + \mathbf{W}_{o,h}\mathbf{h}^{t-1} + \mathbf{b}_o), \tag{3.17}$$

- a cell input activation vector $\hat{\mathbf{c}}^t$ calculated from

$$\hat{\mathbf{c}}^t = \sigma_h(\mathbf{W}_{c,x}\mathbf{x}^t + \mathbf{W}_{c,h}\mathbf{h}^{t-1} + \mathbf{b}_c), \tag{3.18}$$

where σ_s and σ_h are the sigmoid and hyperbolic tangent activation functions, respectively.

Using the $\mathbf{x}^t$, $\mathbf{i}^t$, $\mathbf{f}^t$ and $\hat{\mathbf{c}}^t$, the cell state vector $\mathbf{c}^t$ (acting like a memory cell), can be obtained by:

$$\mathbf{c}^t = \mathbf{f} \circ \mathbf{c}^{t-1} + \mathbf{i}^t \circ \hat{\mathbf{c}}^t, \tag{3.19}$$

where $\circ$ denotes the element-wise product. Finally, the hidden vector $\mathbf{h}_t$ is computed with:

$$\mathbf{h}_t = \mathbf{o}^t \circ \sigma_h(\mathbf{c}^t). \tag{3.20}$$

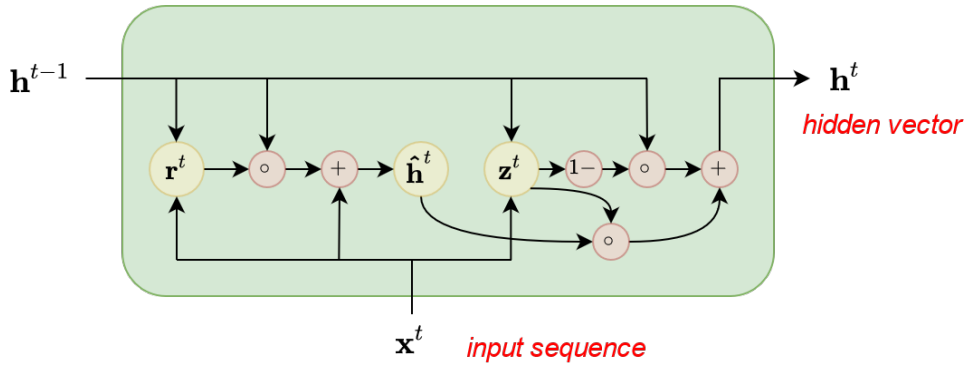

Figure 3.7: Gated recurrent unit mechanism.

In an LSTM cell, the hidden vector $\mathbf{h}^t$ actually acts as the output vector at each timestep t.[1]

3.3.4 Gated recurrent units

In the same vein as LSTMs, gated recurrent units (GRU) [Cho+14] have an internal mechanism which can circumvent the vanishing gradient problem. A GRU is composed of two gate vectors, as illustrated in Fig. 3.7:

- an update gate vector $\mathbf{z}^t$ obtained by:

$$\mathbf{z}^t = \sigma_s(\mathbf{W}_{z,x}\mathbf{x}^t + \mathbf{W}_{z,h}\mathbf{h}^{t-1} + \mathbf{b}_z), \tag{3.21}$$

- a reset gate vector $\mathbf{r}^t$ computed with:

$$\mathbf{r}^t = \sigma_s(\mathbf{W}_{r,x}\mathbf{x}^t + \mathbf{W}_{r,h}\mathbf{h}^{t-1} + \mathbf{b}_r). \tag{3.22}$$

A candidate activation vector is then calculated with:

$$\hat{\mathbf{h}}^t = \sigma_h\big(\mathbf{W}_{h,x}\mathbf{x}^t + \mathbf{W}_{r,h}(\mathbf{r}^t \circ \mathbf{h}^{t-1} + \mathbf{b}_h)\big). \tag{3.23}$$

Finally the hidden vector (also acting as the output vector) is obtained with:

$$\mathbf{h}^t = (1 - \mathbf{z}^t) \circ \mathbf{h}^{t-1} + \mathbf{z}^t \circ \hat{\mathbf{h}}^t. \tag{3.24}$$

In summary, a GRU is similar to an LSTM, with the main difference that a single gate performs both the forgetting and updating actions.

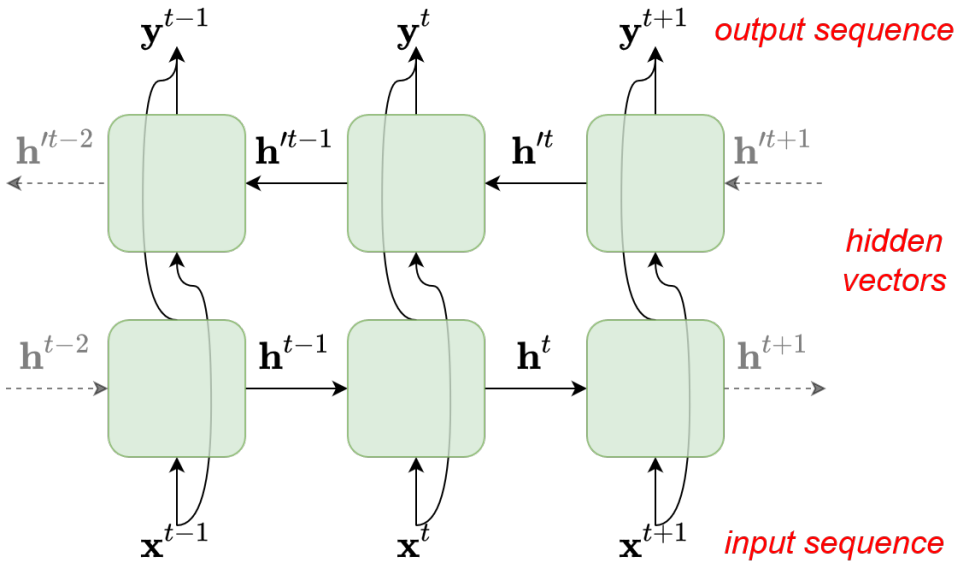

Figure 3.8: Bidirectional recurrent neural networks. A sequence is processed in both directions: from past to future and from future to past. This scheme can be applied for any recurrent mechanism, *i.e.*, the green cells can be basic recurrent units, LSTMs or GRUs.

3.3.5 Bidirectional recurrent layers

The different types of recurrent mechanism presented above (basic recurrent layer, LSTM and GRU) are capable of processing the sequential data in a causal way. However, depending on the learning task, it could be meaningful to process the data in the other direction as well, from future to current input (*e.g.*, when looking for a music tempo, or when a whole data sequence is analyzed to obtain an overall prediction). In other words, it can be interesting to exploit information from both past and future data when processing the data at the current timestep. Bidirectional recurrent neural networks [SP97] have been introduced to address this problem. They combine recurrent layers processing the sequence from beginning to the end with recurrent layers processing the sequence the other way around. Fig 3.8 illustrates how such a combination is done within the network. An input vector is fed separately into a forward layer and a backward layer, each one producing an independent output internal state vector. Thus, the next layer can benefit from two input vectors, one relying on the past and another relying on the future. Such bidirectional layers can also be applied with LSTMs or GRUs.

[1] Although this seems to contrast with the definition of an RNN, it is actually the way the LSTMs are implemented in most deep learning frameworks such as *Tensorflow* or *PyTorch*.

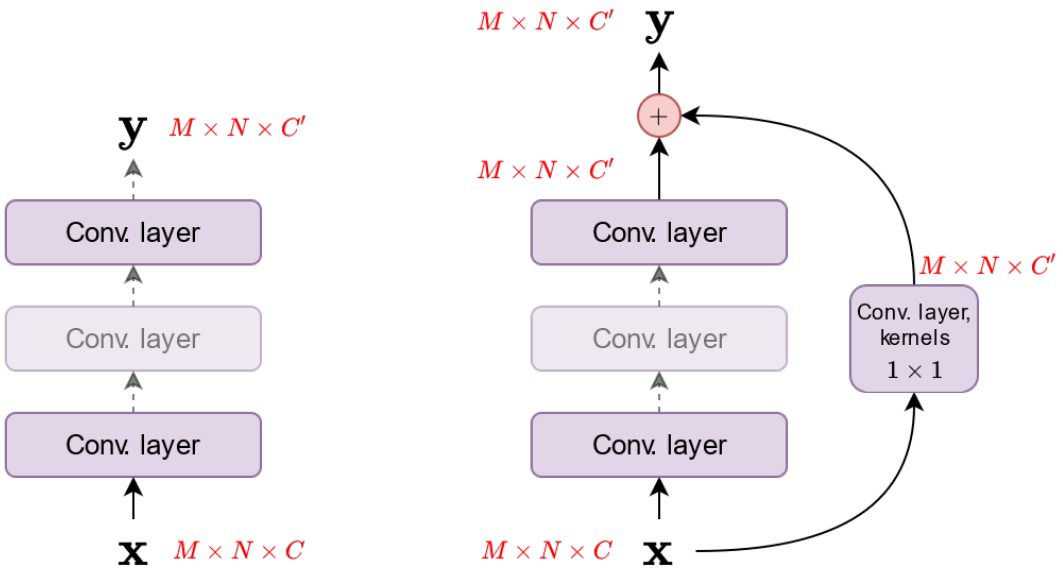

Figure 3.9: Comparison of a residual block (right) and a classical convolutional block (left). In a residual block, the input is added to the output of the last convolutional layer, eventually after its shape is adjusted using an additional convolutional layer to match the shapes.

3.4 Residual neural networks

In this section we briefly present what residual neural networks consist of, and why are they useful in deep learning models.

Residual neural networks have been proposed in 2016 by He et al. [He+16] to address two common training problems encountered with very deep convolutional neural networks: the vanishing gradient problem which we presented in Section 3.3, and the loss of accuracy resulting from the large number of layers. Their idea actually improved the performance of convolutional neural networks because it allowed for deeper architectures.

Residual neural networks are based on the desire of preserving the input features of a given layer, in addition to the output of this layer. Indeed, numerous successive transformations, applied by the multilayer structure of a deep neural network, can result in the loss of meaningful information contained in the layer's input features. By adding *residual connections* between the input of a layer and its output, one can make this input feature flow through this layer unaltered (or almost, as we will see) so that it can be used further in the network.

Fig. 3.9 illustrates how a residual block, *i.e.*, a series of layers including a residual connection, differs from a similar neural network segment without such connections. As we can see, the input of this block flows through the residual connection and is added to the output of the residual block. This residual block transforms the input using several layers, as a classical convolutional neural network usually does. However, in order to be able to add the input with the residual block output, we need to make

sure to match their shapes. One trick to do this relies on inserting a convolutional layer with kernels of size 1×1 to adapt the dimensions of the input feature.

An extension of this idea has been proposed in [Hua+17], where the authors propose to concatenate the input of one block with its output, instead of adding them. Their goal is to have every feature map propagated in each subsequent layer.

3.5 Attention mechanisms

In this section we explain the attention and self-attention mechanisms. Attention models were introduced by Badhanau et al. [BCB15] in 2014 and refined by Luong et al. [LPM15] in 2015 to improve sequence-to-sequence models. It granted neural networks with the capability to cope with long input sequences, especially in machine translation. Another great leap in natural language processing (NLP) was made with the Transformer architecture [Vas+17], which includes the concept of *self-attention*. This neural network based on an encoder-decoder scheme is very powerful to exploit the context of each word in a sentence, and has led to state-of-the-art language models such as BERT [Dev+19] or GPT [Bro+20].

3.5.1 Encoder-decoder scheme

A sequence-to-sequence model is an architecture that takes a sequence of items (words, frames, images, etc.) as input, and process it to output another sequence of items. Such models are often constituted of two components: an encoder and a decoder. As illustrated in Fig. 3.10, an encoder is a neural network which processes the entire input sequence and computes an output vector called the *context* vector. This context vector is then sent to the decoder, which is also a neural network, to output the final sequence. Before the advent of attention models, encoder and decoder were usually made of recurrent neural networks, where the context vector is actually the hidden vector of the last recurrent layer of the encoder network. The output sequence is generated item by item by the decoder, at each timestep, using the context vector to initialize its first hidden vector.

3.5.2 Concept of attention

As we have seen, the context vector contains all information available to the decoder to generate the output sequence. This is an issue when dealing with long input sequences, since it becomes more and more difficult to encode all relevant information from such a sequence in a single vector. Attention has been conceived to circumvent this limitation.

The first addition to the previously explained encoder-decoder scheme is that all encoder hidden vectors are passed to the decoder, instead of passing only the last hidden vector. In that way, information from each input sequence item is available to the decoder. The second novelty is the so-called attention step. The intuition is that,

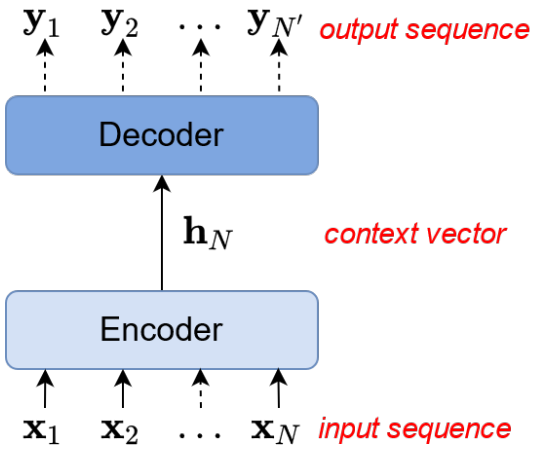

Figure 3.10: Encoder-decoder scheme. The encoder processes the entire input sequence and produces a context vector, which is then used as input for the decoder part to generate the output sequence. The input and output sequences are not necessarily of the same length.

with regards to a particular output item, there are some items in the input sequence which are more relevant than the others. Assuming the decoder is at timestep t, meaning it has already output $t-1$ items, and the current hidden vector is $\mathbf{h}_{t-1}$, the attention mechanism works as follows:

- a so-called *attention score* is computed between all encoder hidden vectors and the current decoder hidden vector $\mathbf{h}_{t-1}$, by the means of learnable weights matrices;
- a softmax function is applied to all obtained attention scores so that their sum is 1;
- a weighted sum of all encoder hidden vectors is calculated, using their respective softmaxed attention scores, leading to the "current" *context* vector relevant to $\mathbf{h}_{t-1}$.

This context vector thus contains all the information about the input sequence items that is useful for the processing of the current timestep. In [BCB15], the attention scores are obtained with a feedforward neural network, trained altogether with the other neural network parts. After this attention stage, the context vector is concatenated with $\mathbf{h}_{t-1}$ and is fed into another feedforward neural network, whose output is taken as the next output sequence item.

As we can see, the idea behind the attention mechanism is to provide a way for the decoding neural network to emphasize some of the input sequence items, regarding the current decoding timestep.

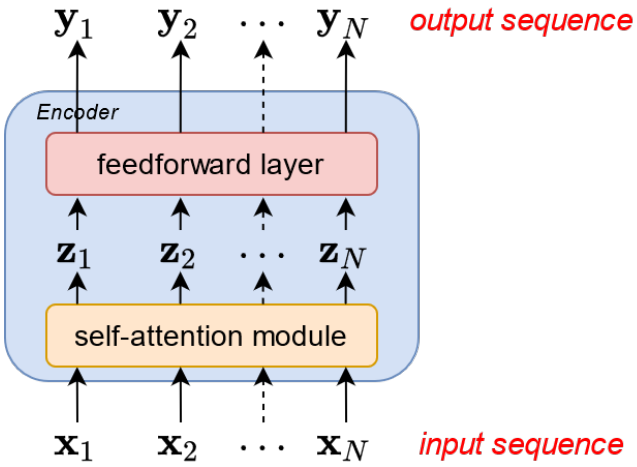

Figure 3.11: Transformer's encoder components. A self-attention module creates an intermediate vector $\mathbf{z}_i$ for each vector $\mathbf{x}_i$ of the input sequence. Each vector $\mathbf{z}_i$ then passed independently in a feedforward layer which produces an output sequence of the same size as the input sequence. The output sequence usually becomes the input sequence of another encoder as several encoders are stacked one after another in a typical Transformer architecture.

3.5.3 Self-attention in the Transformer architecture

The Transformer architecture is a model solely relying on the attention mechanisms, whereas previously presented models were designed as a mix of RNNs and attention. It has been proposed in 2017 by Vaswani et al. [Vas+17], outperforming the previous models, while being more parallelizable and requiring less training time. The Transformer model is also made of encoding and decoding modules, but here each one includes several (internal) encoders and decoders, respectively. All such encoders are identical and process the input sequence items one after another.

Fig. 3.11 shows the components included in one encoder. It is composed of a self-attention module, which is an attention block that compares the input sequence with itself, *i.e.*, it compares each item $\mathbf{x}_i$ with the other items in the same sequence, and outputs a new corresponding vector $\mathbf{z}_i$. Then each vector $\mathbf{z}_i$ is passed independently through the same feedforward layer. The output of the encoder is therefore a new sequence of the same size as the input sequence, which can then used as the input sequence of the next encoder.

The self-attention module is illustrated in Fig. 3.12. First, a self-attention layer actually performs the self-attention mechanism on the input sequence. For each item of the sequence $\mathbf{x}_i$, three vectors usually named *query*, *key*, and *value* are computed. They are obtained by multiplying $\mathbf{x}_i$ with three independent weight matrices that are

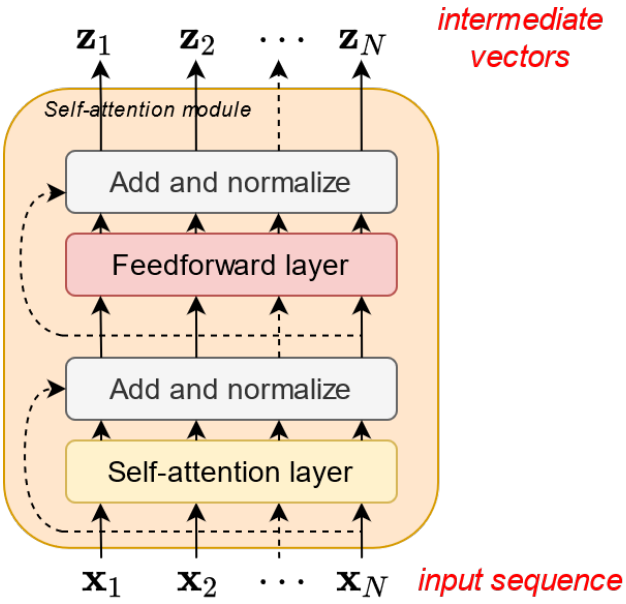

Figure 3.12: Self-attention module. In a self-attention module, the input sequence is first processed by a self-attention layer, of which the output is added to the input (using a residual connection) and the result is normalized. Then, each item of the obtained sequence goes independently through the same feedfoward layer, and the new sequence is again added to the forward layer's input sequence using a residual connection, then is normalized. Note that positional encoding, which is usually used in such encoder architecture, is not shown here as it was not used in this thesis work.

learnt during the training:

$$\begin{aligned} \mathbf{q}_i &= \mathbf{x}_i^T \mathbf{W}^Q \\ \mathbf{k}_i &= \mathbf{x}_i^T \mathbf{W}^K \\ \mathbf{v}_i &= \mathbf{x}_i^T \mathbf{W}^V \end{aligned}. \tag{3.25}$$

Then, when encoding the item $\mathbf{x}_i$, a score s_{ij} is computed with respect to every other item $\mathbf{x}_j$ as [Vas+17]:

$$s_{ij} = softmax\left(\frac{\mathbf{q}_i \cdot \mathbf{k}_j}{\sqrt{G}}\right), \tag{3.26}$$

where G is the dimension of the key vectors. Finally, a new vector $\mathbf{z}_i$ is calculated as the weighted sum of the value vectors $\mathbf{v}_i$, using the computed scores as weights:

$$\mathbf{z}_i = \sum_{j=1}^{N} s_{ij} \mathbf{v}_i, \tag{3.27}$$

with N being the sequence length. For each input sequence item $\mathbf{x}_i$ we thus obtain a new vector $\mathbf{z}_i$ that takes into account the dependencies between $\mathbf{x}_i$ and the other items (past and future) in the sequence.

The remaining components of the self-attention module shown in Fig. 3.12 are the

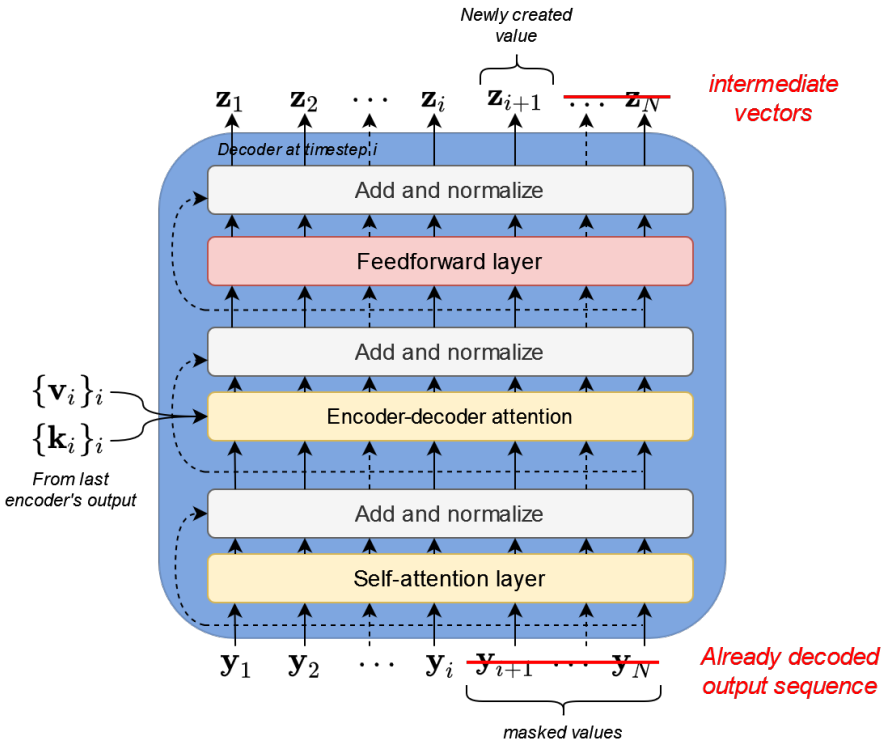

Figure 3.13: Transformer's decoder module at timestep i. After a self-attention module followed by an add and normalize layer, a encoder-decoder attention module is used, and followed by another add and normalize layer. This encoder-decoder attention actually uses the key and value vectors obtained from the last encoder. Then a feedforward layer followed by an add and normalize layer is used as in en encoder module. As for the encoders, several decoders are employed and stacked one after another. As timestep i (*i.e.*, when decoding item i of the output sequence), the previous items $1, ..., i-1$ are already decoded, and are used in the input sequence of the first decoder. The other items $i+1, ..., N$, not yet decoded, are masked in the input sequence. The newly created output item $i+1$ of the last decoder is finally used through a final layer which projects it into the target embedding space.

following: a layer adds the input of the encoder to the output of the self-attention layer (sequence-wise) using a residual connection, and then normalization is applied; then each item of the obtained sequence goes independently through the same feedfoward layer, is added with the corresponding input item of this layer, with another residual connection, and is also normalized.

A last particularity for the encoder is proposed in the original paper [Vas+17], and is called *positional encoding*. The authors propose to encode the position of each input vector within the sequence using a vector $\mathbf{p}_i$ (we do not detail such encoding here, *c.f.*, [Vas+17]), and append this position vector to the corresponding item $\mathbf{x}_i$, before going through the encoder.

Let us now briefly detail how the Transformer decoder part works, without going

too much into details since in this thesis we only adopted the encoder in our experiments. A decoder module, illustrated in Fig. 3.13, is made of a self-attention layer, which receives the already encoded output items (the future items, not created yet, are masked during the process), followed by an add and normalize layer with residual connection. The obtained sequence is fed into another similar attention block called *encoder-decoder attention* because its key and value vectors are those obtained from the output sequence of the last encoder. Finally, as in a encoder module, each obtained sequence item goes through the same feedforward layer, and then another add and normalize layer with residual connection is used. At the end, each item of the output sequence of the last decoder is projected into the target embedding space using a linear feedforward neural network, leading to the final output sequence.

3.5.4 Multi-head self-attention

In [Vas+17], the authors actually used an extended version of the self-attention mechanism presented above. In *multi-head* self-attention (MHSA), several instances of the query, key and value vectors are computed in parallel, with corresponding weights matrices $\mathbf{W}^Q$, $\mathbf{W}^K$ and $\mathbf{W}^V$. This allows a self-attention module to learn several representations for the three vectors of each item in the sequence, leading to more flexibility. When considering H heads, for each item $\mathbf{x}_i$ in the input sequence we obtain H vectors $\mathbf{z}_{ih}$ ($h \in [1, H]$) which are concatenated along the head dimension to give $\tilde{\mathbf{z}}_i$, and a new weight matrix $\mathbf{W}^O$ is used to obtain the final output vector $\mathbf{z}_i$:

$$\mathbf{z}_i = \tilde{\mathbf{z}}_i \mathbf{W}^O. \tag{3.28}$$

In the original paper [Vas+17], the operations to compute the self-attention scores consider the query and key vectors independently per head, *i.e.*, the score for pair of item (i, j) and for head h is obtained by :

$$s_{ijh} = \text{softmax}\Big(\frac{\mathbf{q}_{ih} \cdot \mathbf{k}_{jh}}{\sqrt{G}}\Big), \tag{3.29}$$

where q_{ih} is the query vector of item $\mathbf{x}_i$ for head h, and k_{jh} is the key vector of item $\mathbf{x}_j$ for the same head h. A more general way of calculating the scores is to consider the query and key vectors across different heads h and h':

$$s_{ijhh'} = \text{softmax}\Big(\frac{\mathbf{q}_{ih} \cdot \mathbf{k}_{jh'}}{\sqrt{G}}\Big). \tag{3.30}$$

We call this more general computation *cross multi-head* self-attention (CMHSA), however we did not find any literature reference considering such a mechanism. [2]

[2] As we will explain in a series of experiments in Sec. 7, we actually performed cross-multi-head self-attention by accident while tuning our models. After investigations we understood that the scores were computed as in (3.30) whereas we never encountered this in the literature.

Mathematically, we can interpret a cross-multi-head mechanism with H as a classical multi-head self-attention with H^2 heads where the query and key matrices share weights.

3.6 Conclusion

In this chapter, we provided a quick overview on different deep learning architectures that were used for designing neural models in this thesis. After presenting the basics of neuron mechanisms, we showed how feedforward neural networks, recurrent neural networks and convolutional neural networks can perform some particular tasks. We also briefly explained how residual connections work and why they are of interest. Finally, we described the basics of attention mechanism and Transformer architecture with self-attention, which are quite recent neural methods in the audio literature. Convolutional recurrent neural networks and attention mechanisms have been particularly considered in our experiments on sound source localization.

Chapter 4

State-of-the-art on speaker counting and localization

In this chapter, we provide a literature survey addressing speaker counting and localization. We limit the scope of the survey to methods evaluated on speech signals as it was the focus of this thesis. In the first section, we describe the relatively scarce literature on speaker counting, including parametric, clustering and deep learning methods. In the second section, we address the literature on sound source localization, by first quickly presenting conventional[1] methods, and then providing a short survey of SSL systems using deep learning techniques. As a more exhaustive survey of these neural-based SSL methods has been submitted at the time of this thesis writing [Gru+21c], in this section we limit our description on methods in relation with our research.

4.1 Speaker counting

Speaker counting is the task of estimating the number of people that are speaking in an audio signal. It can be seen as a subtask of speaker diarization, whose objective is to detect which speaker is chatting at any time. Most approaches actually focus on predicting the total number of speakers in the analyzed signals, but we found some works considering the instantaneous NoS or the maximum number of simultaneous speakers (see Section 1.2.3 for a mathematical definition). Note that in a lot of system, the total and maximum NoS are actually identical since they supposed a constant NoS through the whoel analyzed signal.

Speaker counting has not often been addressed in the speech processing literature as a separate task, although it is a useful information for other more complex speech-related tasks such as speaker diarization or speech signals separation. Many such systems actually assume the knowledge of the number of speakers, even though we do not have it at hand in practice.

[1] We define as "conventional" the methods based on traditional signal processing techniques, without deep learning.

4.1.1 Parametric methods

Early methods for speaker counting attempted to correlate the number of speakers to some features extracted from the audio signal. In [Ara03], the authors proposed to exploit the modulation characteristics of the human voice to correlate the modulation index calculated from the input signal, and the total number of speakers. They computed a function of the modulation index which outputs the number of speakers based on several multi-speaker signals constructed from TIMIT excerpts [Gar+93], containing up to 8 simultaneous speakers. Another parameter, derived from the statistics of a particular mel filter coefficient, has been proposed in [SO10] to estimate the total number of speakers in a single-channel mixture. The authors related these statistics directly with the number of speakers via a polynomial function. In [Pas+17], a parametric method has been derived for speaker counting, which relies on coherent-to-diffuse ratio estimation over several time frames. The maximum number of speakers $\bar{J}$ is then estimated by thresholding this computed parameter.

4.1.2 Clustering methods

A few counting methods based on clustering algorithms have been proposed in the literature to address source counting along with other tasks, such as source localization or separation. In [AGB10], an algorithm named DEMIX is derived to jointly count, locate and separate up to 6 sources in a multi-channel recording. This method has been applied for speech signals and works in an underdetermined setting, but is however limited to an anechoic environment. Another clustering scheme can be found in [YLP17] in which the principal eigenvectors of the covariance matrix of a multi-channel signal are extracted to estimate the total number of sources. It showed to be quite robust for speech recordings with signal-to-noise ratios (SNR) between 0 and 20 dB, in environments with low reverberation (TR60 = 250 ms). In [Xu+13], the authors use a clustering algorithm to aggregate the mel-frequency cepstrum coefficients (MFCC) computed from successive speech segments extracted from a single-channel audio mixture. Using a cosine similarity, the clustering algorithm compare pairs of MFCC features to aggregate them into a certain number of classes, which corresponds to the estimated total number of speakers.

4.1.3 Deep learning methods

Several recent works have used neural networks to estimate the number of speakers. To the best of our knowledge, the first deep-learning-based method for speaking counting has been proposed in [St18]. The authors aim to estimate the maximum number of concurrent speakers $\bar{J}$ in a 5-s single-channel audio mixture, containing at most 10 speakers. The classification strategy and the regression strategy (see Section 4.2.2 for more details) are compared, using a neural network consisting of bidirectional LSTM layers. The article further evaluates the use of different input features. The presented results indicate the superiority of classification over regression for speaker counting,

and that STFT features yield the best performance. The authors extended this work in [St19] by evaluating more neural network architectures, including CNN, RNN and CRNN. They compare the use of usual 3×3 convolutional kernels with full-band convolutional filters of size $1 \times F$, with F the number of frequency bins. The results indicate that a CRNN with 3×3 filters leads to the best performance. Their study also includes the use of different datasets, the evaluation of several reverberation time values, and a comparison of their system against human capabilities.

In the same vein, a speaker counting CNN is proposed in [WK18], capable of categorizing the input signal as containing 1, 2 or 3 and more speakers. In [ACB19], an interesting comparison on the human abilities for speaker counting and their machine counterpart is proposed. The authors show that machine algorithms can surpass human level performance, especially when the analysis time is short. Temporal convolutional networks (TCN) have been applied in [Cor+20] to count the maximum number of overlapping speakers in a single-channel mixture, as in [St18]. They show that TCN improves the counting accuracy compared to CRNNs and LSTM-based networks on real data. In [Wan+20], a neural-based speaker counting system is trained using transfer learning based on SincNet [RB18], a speaker recognition network. The output of a truncated version of the already trained SincNet is used as an input feature of their speaker counting system, along with the zero-crossing rate, the spectral spread and the spectral entropy of the input signal. All these features are fed in a feedforward neural network to estimate up to 10 speakers. Peng *et al.* [PWQ20] proposed to train a recurrent neural network to project the input features, composed of log-spectra and interaural phase differences (IPDs), extracted from multi-channel signals, into an embedding space. The number of speakers can be obtained as the rank of the covariance matrix of the embedded vectors. An attention-based network is explored in [YH21] for speaker counting. After a series of convolutional layers for feature extraction, an attention mechanism is trained to aggregate temporal information in a new feature vector. This vector is then fed into a feedforward layer for the final estimation of the number of speakers.

As estimating the number of speakers is generally done to provide another speech-related task with a precious piece of information, a few works has been proposed to jointly tackle the considered speech processing task and the speaker counting problem. Several speaker diarization/separation systems are trained to simultaneously count and separate speech signals [Neu+19; Kin+20]. These systems do not explicitly estimate the number of speakers, but rather extract the speech signals in a recursive manner. Another joint speaker counting and separation system is proposed in [XZ20], relying on an encoder-decoder architecture. The vector obtained at the bottleneck of the encoder-decoder network is projected into a embedding space, giving a set of embedded vectors whose covariance matrix rank gives the number of sources in the mixture, as in [PWQ20]. In [Ngu+20], the authors jointly estimate the number of sources and their respective direction-of-arrivals (DoAs, see Section 4.2) by designing

a CNN which separates into two distinct branches after a series of convolutional layers: one branch is trained to output the number of sources and another estimate the DoAs. They evaluate their system on speech signals and sound events showing better counting accuracy than DoA-based methods.

4.1.4 Thesis position

All the above-mentioned and recently proposed DL-based counting methods have shown promising results over conventional methods. Our research for estimating the number of speakers followed this trend. When the present PhD research work was carried out, in the beginning of 2019, the use of neural networks for speech source counting was a pioneering idea and all the related works were limited to single-channel signals. This motivated our effort to improve speaker counting with multi-channel signals in the hope of taking benefit of spatial information in addition to spectral content. Moreover, most systems considered the estimation of the total number of sources J, sometimes over audio segments of several seconds, although the instantaneous NoS $J(t)$ often varies along the signal. In our research, we rather focused on this instantaneous NoS $J(t)$. Another aspect that we address was the temporal resolution of the counting system, as most of the speech/audio source counting literature, at the time of our experiments, considered a quite large temporal context, which could be insufficient for online systems or for applications that require a good temporal resolution, such as speech signals separation. Finally, we made use of Ambisonics features, as for all the remaining of this thesis, which had never been proposed in the counting literature. The interest of such signal representation has been discussed in Chapter 2 and we assumed that it would be also appropriate for the speaker counting task since spatial information can help to detect spatially distinct speakers.

4.2 Sound source localization

The sound source localization problem has been thoroughly studied for decades, often with a focus on speech signals. A large variety of methods have been designed to address SSL in different scenarios, in anechoic and reverberant conditions, considering one or more sources, static or moving in the environment. In this section, after first presenting a short description of conventional SSL methods based on signal processing, we focus on deep-learning-based SSL techniques, as these have recently become a hot topic in the literature. We put an emphasis on neural SSL systems related to this thesis research.

4.2.1 Traditional signal processing methods

Time difference of arrival

When multiple microphones are used to record a sound field, the signal incoming from a point source arrives at different instants at each microphone. The time difference

of arrival (TDoA), between pairs of microphones, contains information about the direction of the source if the arrangement of the microphones is known. The TDoA can be estimated as the time lag corresponding to the maximum of the cross-correlation function between a pair of microphones. However, in real conditions it is blurred by noise and reverberation. To improve the robustness of this technique, Knapp and Carter [KC76] introduced in 1976 *generalized cross-correlation with phase transform* (GCC-PHAT), which is computed by dividing the cross-correlation by its amplitude. This latter can be computed using the signals of a microphone pair (i, i'), for a time frame t and a lag τ, by summing over all frequencies f:

$$\Psi_{ii'}(t,\tau) = \frac{1}{F}\sum_{f=0}^{F-1} \frac{x_i(t,f)x_{i'}^*(t,f)}{\mid x_i(t,f) \mid\mid x_{i'}(t,f) \mid} e^{2i\pi\tau\frac{f}{F}}, \tag{4.1}$$

where F is the total number of frequencies, and $x_i(t,f)$ and $x_{i'}(t,f)$ are the signals in the STFT domain from microphones i and i', respectively. Then the corresponding TDoA $\Delta_{ii'}(t)$ can be deduced as:

$$\Delta_{ii'}(t) = \arg\max_{\tau} \Psi_{ii'}(t,\tau). \tag{4.2}$$

Because of the demoninator in (4.1), the GCC-PHAT method is quite sensitive to noise, and besides is poorly robust in the presence of multiple sources [BOV12].

Many neural-based SSL methods rely on GCC-PHAT features as input for a localization neural network [Xia+15; Ves+16; LZL18; Com+20; VDPMG21] (see Section 4.2.2 for a more detailed survey of SSL with neural networks).

Acoustic maps

Another way to localize sound sources is to generate *acoustic maps*, which relate the energy or power of acoustic signals to predefined search directions (*e.g.*, on a discrete grid). The steered response power (SRP) can be used to generate such maps, and similarly to GCC-PHAT, it has also been adapted with the phase transform, resulting into the SRP-PHAT algorithm [DBA07]. Such an acoustic map can be obtained by scanning the whole space with a beamformer and computing the signal energy or power for each considered direction.

Because of the amplitude normalization and the averaging across all microphone pairs, this method is more robust to reverberation, however it has the undesired effect of emphasizing time-frequency bins containing only noise.

Neural networks have been used to improve the robustness of the SRP-PHAT algorithm. In [PC17], a CNN has been trained to estimate a time-frequency (TF) mask for each microphone signal. These are applied to corresponding STFT representations, prior to computing the GCC-PHAT quantity of each microphone pair. This method shows to be more robust to strong interfering sources and reverberation. Another system, proposed by Diaz-Guerra et al. [DGMB21], relies on a CNN to directly

estimate the Cartesian coordinates of a sound source from an SRP-PHAT acoustic map, again improving the performance in reverberant and noisy conditions.

Subspace methods

Subspace methods are based on the eigendecomposition of the spatial covariance matrix (SCM) calculated from the observation vectors. In the narrowband *multiple signal classification* (MUSIC) algorithm [Sch86], a subset of eigenvectors obtained from the decomposition is attributed to the sources, while the complementary set of eigenvectors is the basis of the noise subspace. The latter are used to compute an acoustic map:

$$\mathcal{M}(t, f, \theta, \phi) = \frac{1}{\mathbf{a}^H_{\theta,\phi}(f)\mathbf{U}_N(t, f)\mathbf{U}^H_N(t, f)\mathbf{a}_{\theta,\phi}(f)}, \tag{4.3}$$

where $\mathbf{U}_N$ is a matrix that contains the noise-related eigenvectors, and $\mathbf{a}_{\theta,\phi}(f)$ is the *steering* vector in direction (θ, ϕ), which represents the delays of the different captures of a plane wave recording at a microphone array. The estimated DoA is obtained with the angles (θ, ϕ) that maximize this acoustic map, thus one needs to probe all considered directions. This time-demanding search can be avoided with another well-known subspace algorithm for source localization, called the estimation of signal parameters via rotational invariance techniques (ESPRIT) [RK89], which relies on the source subspace to directly estimate the DoA.

4.2.2 Deep learning techniques

In this subsection, we describe the different approaches taken by neural-based SSL system. We categorize these systems with regards to several aspects: number of sources to localize, network architecture, type of input features, output scheme, learning strategies and training/test datasets. This part of the manuscript is a shortened version of the comprehensive survey of the neural-based literature that we have written and submitted for publication (a preprint version is available [Gru+21c]).

Number of sources

Many neural-based SSL systems consider only one source to localize, as it is already a very complex problem in real-world environments, due to the presence of noise and reverberation. When the source activity is not controlled artificially, some methods rely on a VAD system as a preprocessing step before localization. It is also possible to simultaneously estimate the source activity *and* perform localization, as in [YNO17]. In this work, an additional neuron is appended to the network output, and used to estimate whether the source is active or not. Another way of estimating the NoS alongside localization is to adopt a thresholding method, notably when using a classification paradigm (see Section 4.2.2).

Localizing multiple sources is a much harder problem than single-source localization, especially when the activity of the different sources overlaps in time, as we

illustrated in Chapter 1. Nowadays, more and more neural-based localization systems attempt to improve multi-source SSL performance in noisy and reverberant environments. As in the single-source case, many of these multi-source methods assume the NoS J (as described in Section 1.2.3) is known before estimating their locations [Hir15; CH17; ML18; Per+19], which is then used to estimate the right number of DoAs. In practice, J can be estimated by a dedicated source counting algorithm. An alternative, proposed in a few articles, is to jointly estimate the total number of sources J and their location, either from the localization output [HMO18b; Moi+20; Sun+20], or by designing a multi-task network trained to also explicitly estimate the NoS [Ngu+20]. Note that in all these works, the sources are supposed to be static and the NoS is constant, *i.e.*, $J(t) = J, \forall t$.

Input features

Many types of input features have been used in the neural SSL literature. Some systems are inspired by signal representations from conventional methods. For instance, GCC-PHAT features have been employed in [Xia+15; Ves+16; HMO18a; Com+20], while SRP-PHAT-based acoustic maps have been used in [SDF18; DGMB21]. Other features based on cross-correlation functions have been proposed in [Gro+19; ML18]. Ideas from subspace methods have also been exploited in several works. For instance, the eigenvectors of the SCM are fed into neural networks in [TK16; Tak+18], while in [Ngu+20] the authors exploit the spatial pseudo-spectrum from the MUSIC algorithm.

Other classical types of features, usually employed in conventional methods, have been reused as input for neural networks. In [Cha+19; BGG20], the authors proposed to compute the relative transfer function (RTF) obtained from all microphone pairs and fed it into the neural network. Other neural SSL system systems were designed and used in a binaural set-up, which is a two-microphone system designed to mimic human listening conditions. They thus used classical binaural cues as input features of the network: inter-aural level differences [YAZ13; Rod+15; Zer+16], inter-aural time differences [YAZ13; Rod+15], and inter-aural phase differences [PS19; Ngu+18; SVF18; Shi+20; Sub+21].

Low-level representations have also been investigated as neural network inputs, letting the model learn to extract from them the relevant information for localization during the training phase. A number of SSL neural networks proposed in the literature rely on (multi-channel) STFT spectrograms. The network can use only the STFT magnitude [YNO17; PC17], only the STFT phase [Sub+21; ZZQ19], or both [Gui+21a; KPK21; Mar+19; Sch+21a]. Some systems use the decomposition of complex-valued spectrograms into real and imaginary parts [HMO18b; Moi+20]. Finally, a few *end-to-end* neural networks have been designed to estimate the source location directly from the raw multi-channel waveforms. In [SDZ18], the waveforms are fed into 1D convolutional layers, while in other systems [VDPMG18; Vec+19; PBG21] 2D convolutional layers are preferred.

Finally, many authors chose to take benefit of the Ambisonics format (see Chapter 2) for neural-based SSL. Some of them proposed to feed the network with an Ambisonics spectrogram [APV19; Gui+21a; Sch+21b], while in [Com+19] such spectrogram is considered as quaternion-valued and the authors adapted the neural network to operate on such features. The intensity vector is another Ambisonics-based representation that has proven effective for neural-based SSL, according to several articles [Per+18b; Per+19; Ngu+21]. Regarding the Ambisonics order, most of these methods work with the FOA format, but we can find some systems based on the HOA features [VGH20; Pos+21].

Architectures

Neural network architectures are probably the most explored aspect of DL-based SSL systems. The early deep learning SSL approaches employed simple feedforward neural networks [KL11; YAZ13; Xia+15; Ves+16; Rod+15]. CNNs have also been applied early to SSL, having been proven very powerful for computer vision tasks. The first use of a CNN for SSL can be found in [Hir15], with the model based on 2D convolutional layers. Many other works followed this path [CH17; CH19; HMO18b; VDPMG18]. An architecture with 1D convolutions layers has been proposed in [BHM21], while 3D convolutions are used in [DGMB21]. Moreover, dilated convolutions have also been explored in several papers [CH19; PBG21; Gui+21a]. In [CH19] the authors interestingly show that using the dilated convolutional layers with the increasingly larger dilation rates allows to reduce the total number of layers. A comparison of several type of convolutional layers can be found in [KPK21].

While the architectures consisting only of recurrent layers are rare in the SSL literature, we find a lot of works which consider CRNNs, whose convolutional part is generally useful for feature extraction, and recurrent layers are employed for temporal analysis. Examples of CRNN-based SSL systems can be found in [APV19; Per+18b; Per+19; Mar+19; Com+19].

Inspired again by the architectures from the computer vision literature, some neural SSL models incorporate residual connections, such as the networks proposed in [YNO17; SDZ18].

Attention mechanisms, which impressively improved NLP models, have also been employed in a few SSL neural networks. In [Sch+21b; Pha+20], the authors added attention layers to the end of a CRNN, resulting in a better use of temporal information in DoA estimation. Self-attention has also been integrated after a series of convolutional layers in [Cao+21; Sch+21a; Wan+21].

Finally, the use of encoder-decoder architecture for SSL has been explored in several works, for example in [HWQ20; Moi+20; Wu+21].

Output strategies

When addressing SSL with neural networks, two ways of designing the output layer are essentially considered, corresponding to the two following formulations of the SSL problem: classification and regression.

When considering SSL as a multi-label classification problem, the analyzed space is divided into a grid with many subregions (corresponding to different classes), and the network is actually trained to detect the presence of a source in each subregion, by outputting a presence probability. Theoretically, a very large number of sources can be detected, depending on the grid resolution. The main advantage of this approach is that it is possible to localize any number of sources. From the recording position, a suitable way of describing the surrounding space is to use spherical coordinates (θ, ϕ, r), denoting the azimuth, elevation and distance (range) of a sound source. In the literature we can find a lot of neural SSL systems designed to estimate only the azimuth [Rod+15; Hir15; SDZ18; Vec+19; Xia+15; Cha+19], only the elevation [TGT18], or both [Per+18b; Per+19; APV19], while only few works addressed distance estimation [Rod+15; BHM21]. Cartesian coordinates (x, y, z) have also been considered, though more rarely, using a classification paradigm, however limited to the estimation of (x, y) only [Moi+20; ML18].

Regression is another paradigm with which the network is trained to directly estimate the coordinates of a certain number of sources. To do so, each source coordinate is represented by one neuron whose value directly encodes the considered coordinate. One advantage of this approach is to not relying on a grid to represent the sound space. However a limitation occurs when considering multiple sources because of the source permutation problem [Sub+21], which deals with the ambiguity in the association between target and actual output. Despite this drawback, regression has been widely used in neural-based SSL. With spherical coordinates, some systems estimate only the azimuth [Ngu+18; Opo+19], while others estimate both azimuth and elevation [Mar+19; Sun+20]. However, most regression-based methods are trained to estimate cartesian coordinates, for example in [VDPMG18; KPK21; APV19; Com+19].

Data

When dealing with deep learning methods, the choice for training and testing data is very important. While the ideal case would be to train a neural network with a large amount of real-world data, in practice only a few real-world datasets annotated with the source locations are available, and the amount of such labelled data remains limited. That is why simulated data are employed in most neural systems during the training phase.

The most common approach to generate somewhat realistic multi-channel signals is by using artificial room impulse responses. These take into account the room acoustics as well as the position of the sources and microphone array in the environment. While several methods exist to simulate such IRs [SK02], the image source method

(ISM) [AB79] is undoubtedly the most employed in the neural SSL literature. It has been implemented in several publicly available frameworks, such as RIR generator [Hab06], SMIR generator [Jar+12], Pyroomacoustics [SBD18] and McRoomSim [Wab+10]. Such frameworks have been employed in [CH17; Per+18b; Ngu+20; VGH20; SDF18] to name a few. Other simulation methods have been explored, for instance in [Hir15] in which a diffuse reverberation model is added to the ISM, or in [Gel+21] where the authors compare several synthesis algorithms.

When an IR is simulated, it is then convolved with a "dry" speech signal (clean, monophonic and obtained with close-mike recording in a low reverberation environment) in order to obtain a realistic signal which encodes the room acoustics and the propagation between the signal source and the microphone array. Among the speech signal datasets used in the SSL literature, one can cite TIMIT [Gar+93], BREF [LGE91] or WSJ [Gar+07].

Regarding real-world data, a few datasets are available and are generally used to evaluate the neural systems. Recorded IR datasets [Cri+14; Fra17; Had+14] have been collected to further generate more realistic signals. A few other databases of signals recorded in real environments along with the source locations are also publicly available [Pol+21; Eve+20; Gui+21b].

Learning strategies

Another important aspect of DL-based methods which varies among the SSL literature is the choice of a learning strategy. When a sufficient amount of labelled data is available, a neural network can be trained with supervised learning. It is the most employed training strategy in the neural SSL literature, despite the fact that the amount of labelled real-world recordings is limited, owing to the use of simulated data. Examples of SSL systems relying on supervised learning can be found in [Per+18b; YAZ13; Hir15; Cha+19; CH19].

Semi-supervised learning has also drawn interest in a few works on neural SSL systems. Such a learning scheme relies on an initial supervised training phase (using a limited amount of labelled data), followed by another training phase using (a possibly larger amount of) unlabelled data. For instance, in [Tak+18; Moi+21] the unlabelled data are used to adapt a neural network, pre-trained with labelled data, to unseen conditions.

Another learning strategy, termed weakly supervised training, aims to train a neural network with weak labels, *i.e.*, the labels that can be inaccurate, imprecise or containing "coarse" meta-information. In [HMO19], the NoS is used as weak labels to further train the network using an adapted loss function. Another example of weakly supervised learning can be found in [Opo+19], in which the authors proposed to use a triplet loss function, which relies on adding two other examples to an usual example: a *positive* example which is close in the localization space to the usual example, and a *negative* example which is further in the space. The interest of this scheme is that it

can be used with only a few labelled data, providing that we can control the proximity of unlabelled data in the target space.

4.2.3 Thesis position

As for speaker counting, DL-based systems are more and more often employed in the SSL literature, as they show to be more robust to challenging conditions, such as noise, reverberation or the presence of multiple sources, than traditional methods. This thesis work also focused on using neural networks for SSL, based on the research initiated in the earlier PhD thesis [Per19]. At the time of our source localization experiments, single-source localization using neural networks on real-world data was already quite efficient. Using the versatility of the Ambisonics format, particularly the intensity vector, in this thesis we focused on the multi-source localization problem, which was still poorly addressed compared to the single-source configuration. We took an interest in rethinking several architecture blocks, in order to improve the localization performance. Also, in the same vein as our effort to reduce the temporal resolution for speaker counting models, we also focused on reducing the computation time of SSL neural networks. Finally, in a series of exploratory experiments, we tried improving single-source localization with a novel Ambisonics representation, which has never been addressed in the neural-based SSL literature.

Chapter 5

Speaker counting using neural networks

In this chapter, we present our speaker counting system and the experiments that we carry out to demonstrate and improve its robustness. Inspired by a pioneering work on speaker counting with neural networks [St19], we design a CRNN that is capable of counting up to 5 speakers in a multi-channel mixture containing noise and reverberation. We describe the input representation adopted to feed the neural network and how we address speaker counting as a classification problem. We detail the generation of the dataset used for training the network, as well as the testing datasets, the baseline systems and the metrics employed for assessing speaker counting performance. Finally, we present the different experiments we conduct with this system, and report and comment the results. The first series of experiments focus on assessing the use of multi-channel over single-channel signals, the second one compares the use of different convolution kernel sizes, and the last one is a short analysis which examines the network prediction accuracy depending on the considered frame in a given input sequence.

5.1 Overall methodology

5.1.1 Input features

As one can intuit, spectral information is important to distinguish between several overlapping speakers, and thus, for counting how many they are. This is why in [St19] the authors chose to represent the single-channel input signal with a time-frequency representation, in the STFT domain, leading to the use of the magnitude spectrogram. In our case, we want to add spatial information to our representation, which we conjecture to be useful for the network to better distinguish multiple speakers. This is why we represent the input signal with the multi-channel Ambisonics format, limited to order 1 (FOA). Recalling (2.31), an FOA signal in the STFT domain is encoded with four (complex-valued) STFT representations, from which we extract the magnitude information to obtain a 4-channel magnitude spectrogram (we discard the phase information as it was done in [St19]).

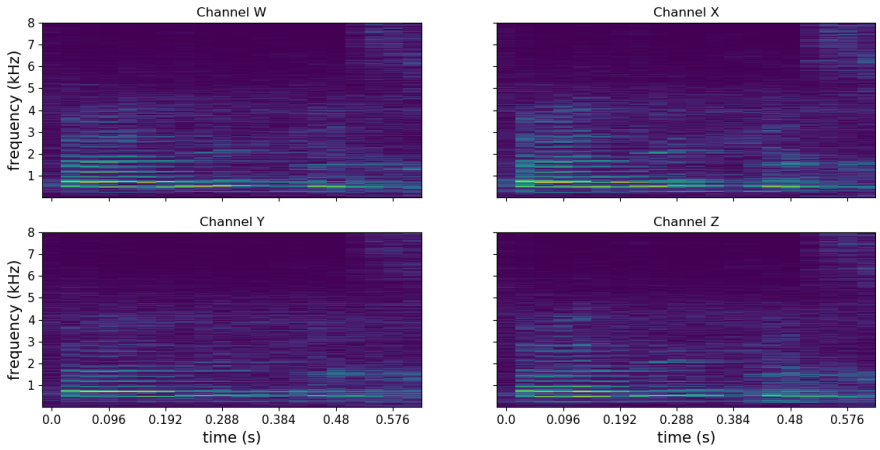

Figure 5.1: Example of an input signal represented with a FOA magnitude spectrogram. In this example, $T = 20$, and the number of speakers (which is not really possible to estimate visually) goes from 1 to 2 speakers around frame 12. For a better visualization, we apply a log function to these spectrograms, but in practice it is not done during the experiments.

Since a magnitude spectrogram is TF representation, it is generally represented in the form of 2D matrices of size $T \times F$, where T is the number of frames and F the number of frequency bins. In our representation, the four channels of the FOA magnitude spectrogram are stacked together in a third dimension leading to a 3D input tensor $\mathbf{X} \in \mathbb{R}^{T \times F \times 4}$. Fig. 5.1 shows an example of the 4-channel magnitude spectrogram obtained for an input signal.

As it is usual in deep learning, we normalize these spectrograms per frequency band over the entire training dataset, so that the mean and variance for each frequency band (including all frames and channels) are 0 and 1, respectively. The same mean and variance values from the training dataset are used to normalize the test data.

5.1.2 Speaker counting as a classification problem

We consider speaker counting as a multi-class classification problem, as it was shown to be more efficient than regression [St18]. Each class represents a number of speakers, and the network is trained to evaluate the probability of the input feature to belong to that class. More specifically, we limit our speaker counting system to count between 0 and 5 speakers, leading to 6 potential classes c_i, $i \in \{0, 1, 2, 3, 4, 5\}$. Then, for each input frame, the neural network is trained to estimate the probability $P(t, c_i \mid \mathbf{X})$ that the frame belongs to class c_i, and for $i \in \{0, 1, 2, 3, 4, 5\}$ (*i.e.*, it output 6 values in $[0, 1]$), as illustrated in Fig. 5.2. As detailed further, we design the network output layer so that all outputs sum to 1, acting as a discrete probability distribution. Finally, the number of speakers for the considered frame is estimated by selecting the class

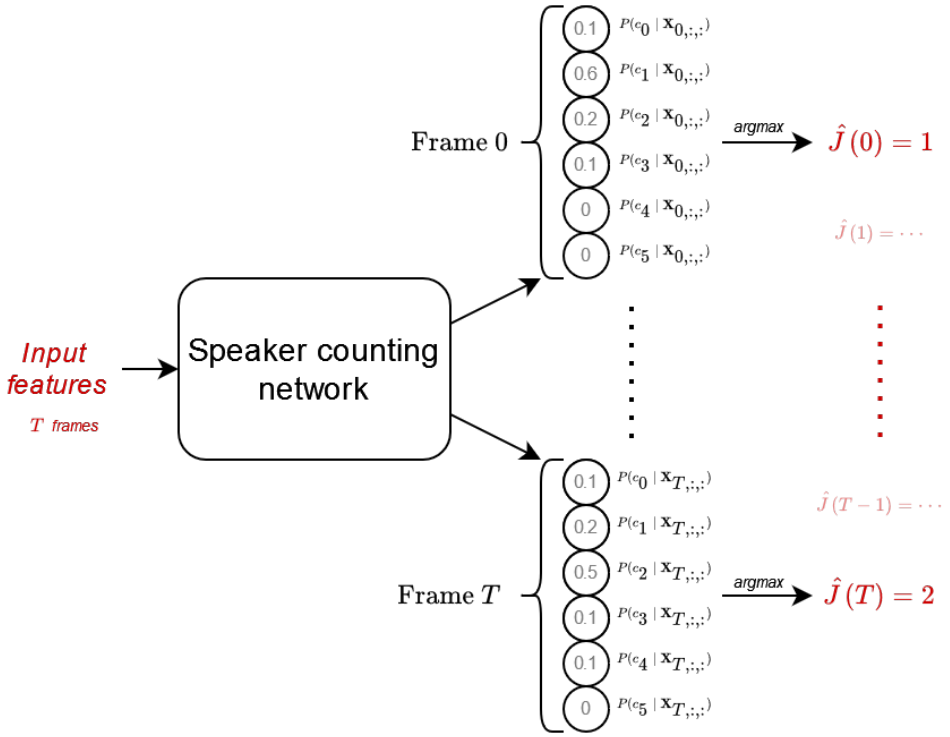

Figure 5.2: Speaker counting as a classification problem. Each candidate number of speakers is considered as a class, and the neural network is trained to estimate the probability that the input feature belongs to each class. The neural network is forced to output the set of probabilities for each frame in the input feature.

with the highest probability:

$$\hat{J}(t) = \arg\max_i P(t, c_i \mid \mathbf{X}), \tag{5.1}$$

Note that in our method, a probability for each class is computed for each frame, leading to a frame-wise resolution for our counting system. This is the main difference with [St18], in which the authors proposed to calculate a single probability distribution for the whole 5-s long input sequence.

5.1.3 Neural network global architecture

The neural network architecture we adopt for speaker counting is inspired by [St19], and is illustrated on Fig. 5.3.

A first series of convolutional layers processes the input tensor of shape $T \times 513 \times 4$ (the value 513, which is the number of frequency bins, comes from the chosen STFT analysis window size, see next section), where T is an hyperparameter in our experiments, and performs a feature extraction. This convolutional block first consists of two 2D convolutional layers with 64 and 32 convolution kernels of size $K \times K$, respectively, applied on the temporal and frequency axes, where K is another hyperparameter in our experiments. Then, a max-pooling layer with a pooling size of 1×3 is used, in

order to preserve the information along the temporal axis. Next, two other 2D convolutional layers with respectively 128 and 64 convolution kernels of size $K \times K$ are used, followed by another max-pooling layer of size 1×3. In all convolutional layers, we use a stride of 1 as well as zero-padding in order to preserve the shape of the input tensor. The important change compared to [St19] is that we use a max-pooling 1×3 instead of 3×3, allowing us to preserve the temporal dimension for a prediction at a frame-wise resolution.

The new features extracted by the convolutional module consist of 64 feature maps of size $T \times 57$. In order to proceed to a temporal analysis with recurrent layers, we reshape the obtained feature by stacking the feature maps along its second dimension, leading to a reshaped feature of size $T \times 3648$. In all convolutional layers, ReLU activations are used. Batch normalization is also applied before each max-pooling layer to make the neural network faster and more stable.

The temporal processing is then done using a single LSTM layer with a hidden state vector size of 40. This LSTM layer is used in a sequence-to-sequence mode, *i.e.*, the hidden state of the LSTM cell is output at each timestep, so that we obtain a new vector for each item of the input sequence (which is of length T). The activation functions used in the LSTM cells are the same as described in Section 3.3.3, *i.e.*, σ_h is the hyperbolic tangent function and σ_s is the sigmoid function.

Finally, each vector from the output sequence of the LSTM layer is processed independently by the 6-neuron output feedforward layer, whose activation is set to the softmax function. This ensures that a probability distribution over the 6 classes is produced for each timestep.

5.2 Experimental protocol

5.2.1 Audio parameters

In our experiments, the audio signals are sampled at 16 kHz, which is the frequency range of the Eigenmike® array for which the FOA channels exhibit acceptable directivity distortion [Baq17]. The STFT is computed using a sinusoidal window of length 1 024 (64 ms) with an overlap of 50%, thus a frame is computed every 32 ms. The FFT size is also 1 024, leading to 513 frequency bins.

5.2.2 Training parameters

The loss function used for training is the categorical cross-entropy. The Adam optimizer [KB14] is used with a starting learning rate of 10^{-3}, $\beta_1 = 0.9$, $\beta_2 = 0.999$, $\epsilon = 10^{-7}$. During the training phase, a dropout is used before the reshape layer, with a dropout rate of 0.25. During training, we monitor the categorical accuracy on the validation set, and we stop the training if the accuracy has not improved for 20 epochs, keeping the model with the best accuracy so far. The maximum number of

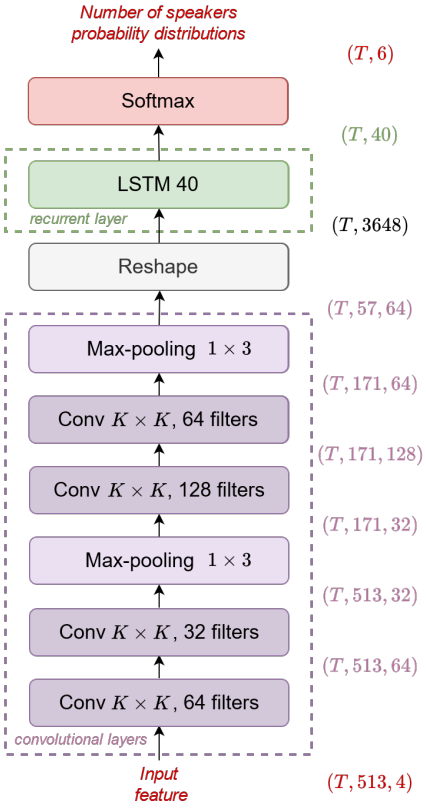

Figure 5.3: Neural network architecture for speaker counting. It is composed of a series of 2D convolutional layers, with max-pooling layers in-between, followed by an LSTM layer and a feedforward layer acting as the output layer. Max-pooling is applied only on the second axis (corresponding to the frequency dimension) to preserve temporal dimensionality and the LSTM is used in a sequence-to-sequence mode. The convolution kernel size $K \times K$ and the number of frames T in the input features are hyperparameters in our experiments.

epochs is set to 300. When the validation accuracy has not improved for 10 epochs, we divide the learning rate by a factor 2.

5.2.3 Training data

Our speaker counting CRNN is trained on simulated data. The simulation can be decomposed into two phases: the generation of RIRs and the training signals.

The RIRs are simulated with the image-source method [AB79], by adapting an existing framework [Hab06] to generate FOA RIRs. A large number of RIRs are generated in a variety of random conditions, such as the room dimensions and absorption coefficients, the microphone and source positions. First, we randomly set the dimension of the room, which is simplified to be parallelepipedic (usually referred to as a *shoebox*), within $[2, 10]$ m, $[2, 10]$ m and $[2, 3]$ m, for the length, width and height, respectively. The room RT60 is randomly chosen between 200 and 800 ms. Next, an ideal (open sphere) spherical microphone is randomly positioned in the room so that it is at least at a distance of 0.5 m from the walls. Then, 5 source positions

are randomly picked within the room dimensions. The protocol is repeated for 10 000 rooms, so that we end up with 50 000 RIRs.

To generate the speech mixtures, we use 16-kHz speech excerpts from the TIMIT dataset [Gar+93]. To match realistic conditions, we want to generate conversation-like mixtures, with the instantaneous number of speakers (in between 0 and 5) varying over time. The speech mixtures also need to be generated as if the speakers were in the same room (hence the 5 generated RIRs per room). To create such a realistic signal, we first fix a total number of speakers J which will participate in the current speech mixture (between 1 and 5). To create the mixture, a single-speaker 15 s dry signal is first generated by concatenating several sentences from a unique random speaker in the TIMIT database (it is crucial in this step not to mix sentences from different speakers to ensure the continuity of one speaker's frequency content) and alternating actual speech content with silence segments. More specifically, a preliminary silence with a random length in $[0.5, 1]$ s first initializes the signal. Then a random sentence from the chosen speaker is concatenated with the signal, followed by a silence of random length in $[0.5, 2]$ s. This last step is repeated for random sentences until a 15 s signal is obtained.[1] The obtained single-speaker 15 s dry signal is then convolved with one RIR of a randomly picked room to create a wet signal. This process is repeated for the J speakers of the current mixture, using the J distinct RIRs from the same room. Then, we mix all the single-speaker wet signals together to create a speech mixture with an instantaneous number of speakers varying from 0 to J speakers. The signal-to-interference ratios (SIR) used between the first single-speaker signal and the other signals is randomly chosen in $[0, 10]$ dB. The last step is to add a diffuse noise to this mixture to make it a step further more realistic. We randomly choose a noise signal among those in the noise database (including crowd, traffic, engine, nature sounds, etc.), which we convolve with a diffuse field generated by averaging the diffuse parts of two random RIRs measured in a real reverberant room. A random SNR is picked in $[0, 20]$ dB with respect to the first speech signal.

In the TIMIT dataset, each speech sentence is annotated with the pronounced word timestamps, at a sample precision. We use these annotations to automatically label voice activity vs silence for each speaker and thus label the 15 s mixtures with the ground-truth number of speakers at the sample resolution. When these signals are transformed into the STFT domain, we consider that a speaker is active in a frame if it is active for more than half of the samples in that frame.

Fig. 5.4 illustrates three examples of a 15 s mixture with a varying number of speakers. Because each speaker randomly starts and stops uttering small sentences, the number of speakers varies several times along the sequence.

We recall that each (train or test) input feature to our network is a sequence of T consecutive 4-channel FOA STFT magnitude frames, with T an hyperparameter that we set experimentally. These sequences are extracted from these 15 s mixtures with

[1] If the last concatenated sentence is too long so that the signal will be longer than 15 s, it is cropped and faded out in the last 100 ms.

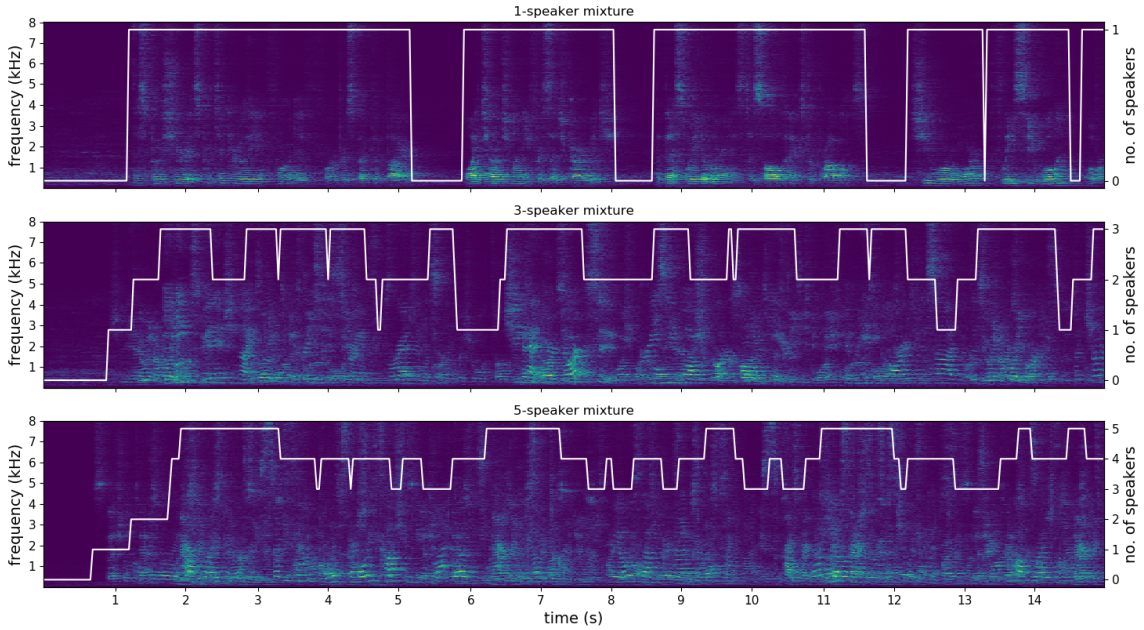

Figure 5.4: Example of spectrograms (W channel only) of 15 s long training signals with varying number of speakers. The white lines represent the varying (ground-truth) number of speakers in each mixture. The maximum number of speakers in these mixture are 1 (top), 3 (middle) and 5 (bottom). As we can see, the instantaneous number of speakers "continuously" varies along the 15 s of mixture, as each speaker starts and stops uttering a small sentence all along the signal.

basic segmentation, without any overlap between the sequences. The first version of our training dataset consisted of 5 J-speaker 15-s mixtures, for $J \in \{1, 2, 3, 4, 5\}$, for each room, leading to the same number of training/test sequences for each number of speaker J. However this strategy actually raises the famous *class imbalance problem* [BMM18], which happens when the number of examples is very different for each class. As we can see in the plots on Fig. 5.4, in each mixture the instantaneous number of speakers fluctuates around certain values and rarely reaches others. For example, in the 3-speaker mixture, the number of speakers is most often 2 or 3, while in the bottom plot we see that there barely are 5-speaker frames. Globally, generating the exact same number of J-speaker mixtures for all values of J would unbalance the cardinality of each class, with more training data towards the low-valued classes. To avoid this problem, we decide not to systematically generate all 5 speech mixtures for each room, but rather setting a probability that a J-speaker mixture will actually be generated. Table 5.1 shows these probabilities, set empirically to attain a more balanced training dataset. To illustrate this process, let us assume we already selected a certain room configuration, which comes with 5 generated SRIRs. We first consider a 1-speaker mixture, which probability of generation is 0.2 as indicated in Table 5.1. Whether the draw leads to the actual mixture generation or not, we then consider the

J	**1**	**2**	**3**	**4**	**5**
Probability to generate a J-speaker mixture	0.2	0.3	0.4	0.5	1

Table 5.1: Probabilities of generating a J-speaker mixture during the creation of the training dataset.

generation of a 2-speaker mixture, this time with a probability of 0.3. We continue in this process until considering the generation of a 5-speaker mixture, which is actually always done because of the probability 1. In that manner, we have actually generated 20% of the potential 1-speaker mixtures, 30% of the potential 2-speaker mixtures, etc.

The validation dataset, used to monitor the neural network training, is created exactly with the same methodology. Only 100 rooms are considered for this dataset, and we took care not to use generation data already used for the training dataset (speech sentences, speaker identities, rooms, noise signals).

Finally, we end up with about 100 hours of training data and 1 hour of validation data.

5.2.4 Testing data

We use several test datasets to assess the performance of our speaker counting neural network. The dataset is a simulated dataset created in the same manner as the training and validation datasets. For the test, we generated 500 RIRs in 100 different rooms. Again, the speakers and noise signals used for the test signals have not been used for the training and validation datasets. The obtained test dataset contains 1 hour of data.

5.2.5 Baseline

As our speaker counting system is partly inspired by the classification-based CRNN proposed in [St19], we consider this method as a baseline for the experiment in which we compare the use of single- and multi-channel signals. We nevertheless adjust this baseline to ensure having a fair comparison to to our method. First, we employ the recurrent layer in a sequence-to-sequence manner so that a prediction is made for every frame in the input feature.[2] This choice constraints us to use max-pooling of size 1×3 instead of 3×3 to preserve the temporal dimension.

This single-channel baseline id used to assess the benefit of multi-channel signals for speaker counting. In the following experiments of this chapter, our multi-channel speaker counting CRNN will act as the baseline system.

[2] In [St19], the authors designed their network to produce only one prediction for the whole input feature, as their goal was to predict the maximum number of speakers present in a 5-s single-channel mixture.

5.2.6 Evaluation metrics

To measure the performance of our speaker counting system we use several metrics. The classification accuracy A_{ii} for one class c_i is defined by the percentage of frames correctly classified with class c_i, among all frames belonging to class c_i. While it is a usual metric in a classification problem, we also extend this metric to measure the percentage of frames that are classified with class c_j among all frames belonging to class c_i. Hereafter, A is referred as the confusion matrix. Mathematically, by noting T_i the set of all test frames indices with the ground-truth number of speakers equal to i, A_{ij} is expressed as:

$$A_{ij} = \frac{\mathsf{card}(\{t \in T_i \mid \hat{J}(t) = j\})}{\mathsf{card}(T_i)}, \tag{5.2}$$

where $\mathsf{card}(T_i)$ denotes the cardinality of the set T_i. This accuracy metric calculated according to two indices (each representing a NoS) will be useful to assess how far the estimated number of speakers deviates from the ground-truth value.

We also measure the mean absolute error M_i per class, which is defined as:

$$M_i = \frac{1}{\mathsf{card}(T_i)} \sum_{t \in T_i} |\hat{J}(t) - J(t)|. \tag{5.3}$$

5.3 Experiments

In this section, we report and discuss the results of our speaker counting CRNN evaluation. We conduct several experiments in which we assess the values of some hyperparameters: the benefit of using multi-channel signals, the number of frames in the input sequence, the convolution kernel sizes. We also propose an analysis of the accuracy of the network depending on the frame position within the input sequence.

5.3.1 Single-channel against multi-channel features, with several sequence lengths

Experiment objective

The preliminary objective of our speaking counting CRNN is to assess the benefit of using multi-channel signals over single-channel ones, such as the one proposed in [St19]. As explained above, we adapt this baseline network to our problem of estimating the instantaneous number of speakers. Therefore, the baseline in this experiment is the same speaker counting architecture we adopt, presented in Section 5.1.3, but we limit the input features to only one channel. Instead of using the 4 channels obtained from the FOA representation, only the W channel is considered for the baseline. The W channel encodes the recorded signal as if it was recorded by an omnidirectional microphone, which can be adequately considered as a single-channel representation.

The intuition behind using multi-channel features is to provide the neural network with a means to better discriminate between spatially distinct sources. As it is done

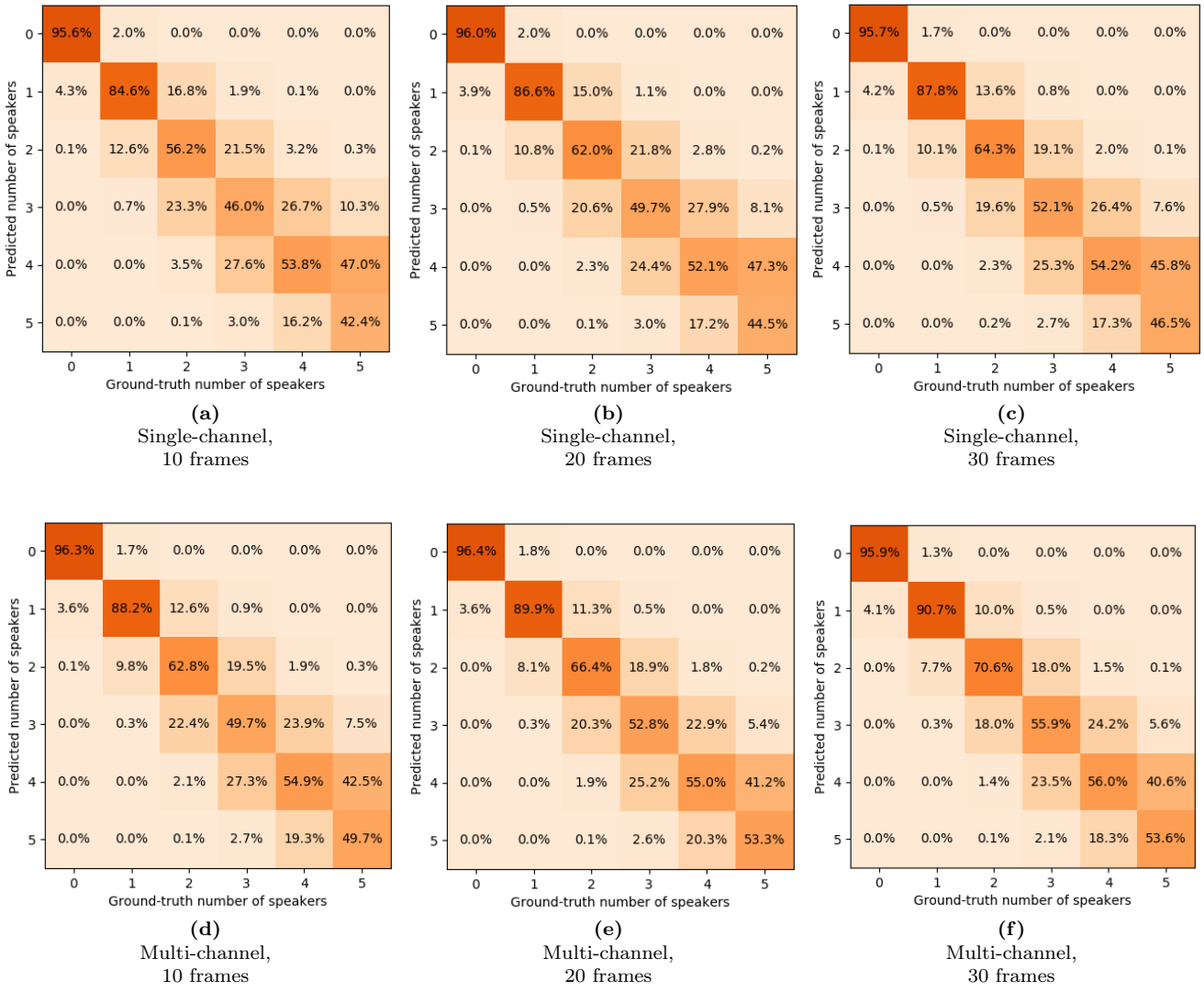

Figure 5.5: Confusion matrix A_{ij} of the single-channel (top) and multi-channel (bottom) speaker counting CRNNs on the test dataset with simulated SRIRs, for $T = 10, 20, 30$ frames (left to right).

in source localization (see Chapter 7), feeding multi-channel features to the neural network supplies it with multiple transformed versions of the same signal (due to the different microphone types and orientations). Depending on the source location, the original signal is not transformed the same way, which should be reflected in the magnitude spectrogram. We conjecture that the neural network can learn these characteristics to better discriminate the different speech sources.

To compare the use of single- and multi-channel features in several conditions, we also vary the length of the input sequence, *i.e.*, the number of frames T in the input features. We experimented with $T = 10$ (320 ms), $T = 20$ (640 ms), and $T = 30$ (≈ 1 s). In this experiment, the convolution kernel size is $K = 3$ (see Section 5.3.2 for an experiment on this hyperparameter).

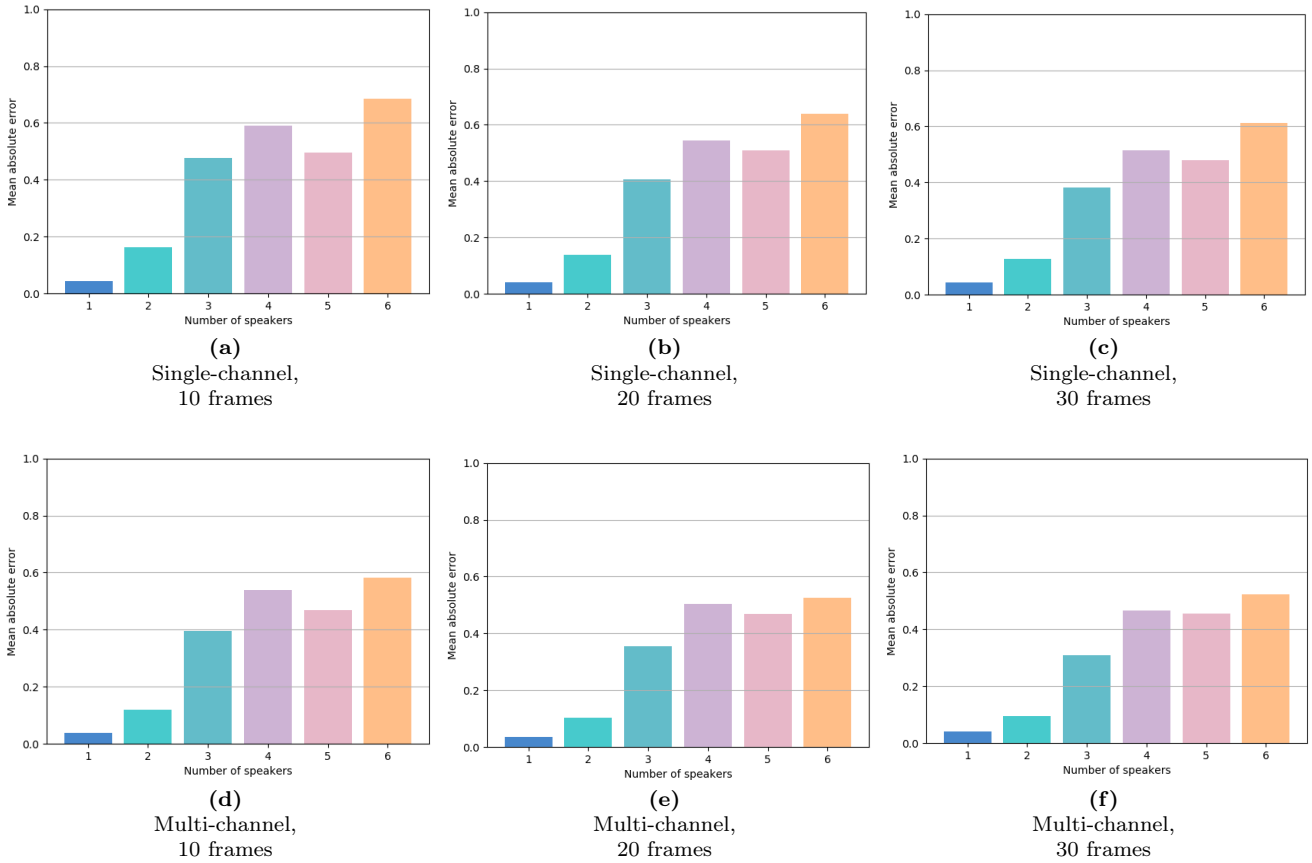

(a) Single-channel, 10 frames

(b) Single-channel, 20 frames

(c) Single-channel, 30 frames

(d) Multi-channel, 10 frames

(e) Multi-channel, 20 frames

(f) Multi-channel, 30 frames

Figure 5.6: Mean absolute errors M_i of the single-channel and multi-channel speaker counting CRNNs on the test dataset with simulated SRIRs, for $T = 10, 20, 30$ frames (left to right).

Results

We report the detailed accuracy results for all 6 experiments in the form of confusion matrices, which display the percentage of j-speaker frames (on the x-axis) which are estimated to contain j speakers (on the y-axis). These confusion matrices are shown in Figure 5.5. We also report graphics of the mean absolute errors in Figure 5.6. We recall that we compare the use of single-channel features to multi-channel features, for 3 values of T: 10, 20 and 30 frames.

First, we notice that both single- and multi-channel networks are very effective to detect the absence of speech in the signal, with over 95% of correct silent detection in all settings. It can therefore act as a robust VAD system. Then, the classification accuracy gradually decreases when the number of speakers increases, which is anticipated since the task becomes more complex. While the classification accuracy for 1-speaker signals is around 85% for the single-channel network, it reaches around 44% accuracy when 5 speakers are present in the signal, which is still an acceptable performance compared to a random guessing accuracy (16%).

While the mean absolute error is almost zero for zero-speaker signals in all configurations, it remains under 0.8 when one or more speakers are active, which means that

when the neural network predicts a wrong number of speakers, the error is ± 1 speaker in average. This behavior can be clearly noticed in the confusion matrices. When the network's prediction is wrong it is almost always done with an absolute error of 1, which is visualized around the matrix diagonal. For example, in Fig. 5.5e, we see that when the ground-truth number of speakers is 3, the neural network predicts wrongly 2 speakers 18.9% of the time and 4 speakers 25.2%, while it estimates 0, 1 or 5 only 3.1% of the time in total. Regarding the class $J = 5$ speakers, there seems to be an *edge effect*, so that the number of prediction for $J - 1$ speakers is surprisingly high compared to the other values of J, but this can be explained because of the absence of the class $J = 6$.

When comparing the effectiveness of the single- and multi-channel settings, we clearly see an increase in accuracy when multiple channels are taken into account, for all values of T. The gain in accuracy of the multi-channel network becomes larger when the number of speakers increases. We see in Fig. 5.5 that, when $T = 10$, the accuracy goes from 84.6% to 88.2% for 1-speaker signals ($\approx 4\%$ gain), from 46.0% to 49.7% for 3-speaker signals ($\approx 8\%$ gain) and from 42.4% to 49.7% for 5-speaker signals ($\approx 17\%$ gain). When $T = 30$, the accuracy goes from 87.8% to 90.7% for 1-speaker signals ($\approx 3\%$ gain), from 52.1% to 55.9% for 3-speaker signals ($\approx 7\%$ gain) and from 46.5% to 53.6% for 5-speaker signals ($\approx 15\%$ gain). These gains seem to confirm our preliminary conjecture which stated that the neural network takes benefit of the spatial characteristics present in the input multi-channel magnitude spectrogram, because the source locations are distinct enough. When looking at Fig. 5.6, we also notice an improvement in terms of mean absolute error for all multi-channel settings.

Regarding the input sequence length T, we notice that the more frames in the spectrogram, the more accurate is the neural network. It also seems to confirm our intuition that more temporal context is benefit for the neural network since it can process more successive frames. Due to how we generated our dataset, with simulated conversation-like signals, each frame has a number of speakers close to that of the neighboring frames: it is often the same number of speakers, sometimes it is shifted by ± 1 speaker. As we will see in more details in Section 5.3.3, another important factor to explain this gain in accuracy when T is larger is the nature of the LSTM layer to process past data to improve its prediction.

Finally, we can conclude that the multi-channel CRNN surpasses the single-channel model in all configurations, showing the usefulness of a multi-microphone inputs. The multi-channel CRNN is able to predict the instantaneous number of speakers of simulated data with an accuracy of at least 50% for all NoS, even with a short signal snapshot (320 ms), which is very interesting for online systems.

5.3.2 Convolution kernel sizes

Experiment objective

Now that we have demonstrated the benefit of the spatial information for speaker counting, we explore how the neural network performance varies when we change other parameters. In particular, in this experiment, we analyse the performance of the neural network as a function of the size of the convolution kernels. We have tested the increase of the kernel size from 3×3, as employed in the previous series of experiments, to 5×5 and 7×7. The goal is to make the convolutions span over more values during the feature extraction step, and see if it can provide the network a more flexible way to process the temporal and frequency dimensions.

Results

The confusion matrices and mean absolute error plots obtained from this new experiment are shown in Fig. 5.7 and 5.8, respectively. The first remark is that the same effect can be observed regarding the length of the input sequence, that is the speaker counting accuracy increases when T gets larger.

Regarding the evolution of the performance according to the size of the convolution kernels, it seems that the overall accuracy is higher when the kernel size increases, although it decreases for some values. To give some numbers, for $T = 10$, A_{55} is 49.7% for $K = 3$ whereas it reaches 58.6% for $K = 7$. However, for $T = 20$, A_{55} is equal to 53.3% for $K = 3$, largely increases to 63.4% for $K = 5$ but falls down to 53.0% for $K = 7$. Due to the fluctuations of the evolution of A_{ij} it is not straightforward to conclude with the confusion matrices. It is more apparent when looking at the mean absolute error plots on Fig. 5.8, where we see that the mean absolute error decreases in almost all cases when the kernel size expands. It is a bit more noticeable for higher number of speakers.

It thus seems that the neural network benefits, to some extent, from a larger span over the frames and frequency bins. Regarding the frequency dimension, one can think that the feature extraction with larger kernels would help the network to better gather the frequency content of distinct speakers. On the temporal axis, it can be beneficial to have access to more past or future frames in order to integrate the frequency content of several speakers with respect to time. This can be even more advantageous due to the intermittent nature of speech, however it is not clear if this has more to do with the LSTM layer than the other network's components.

To conclude this experiment, we see that the expansion of the convolution kernel helps increasing the accuracy of the counting network, although the gain is quite limited. An explanation of this increase could be that the network is able to access more frequency and temporal contents during the feature extraction, which can be beneficial to better weight the respective contribution of each speaker in the input features.

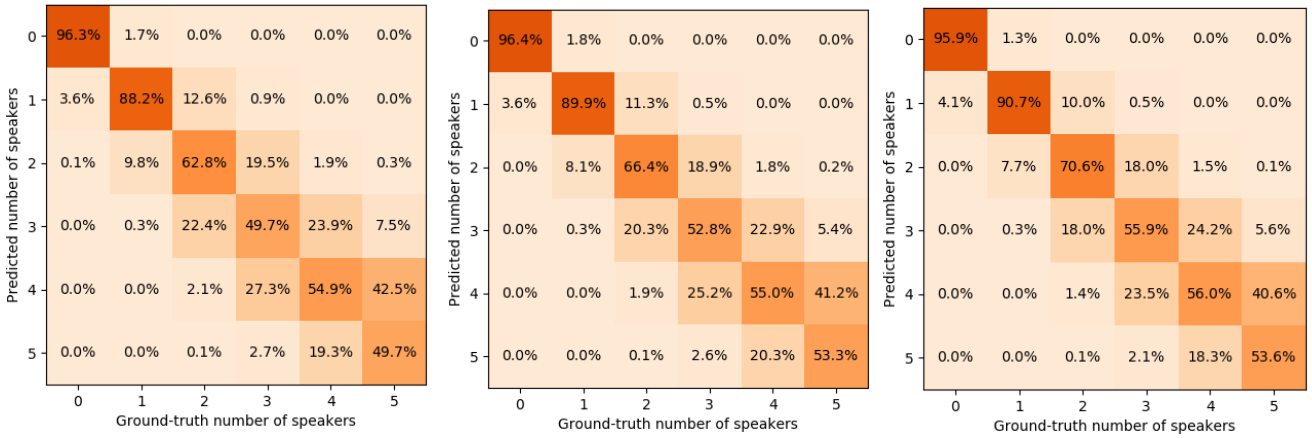

(a) Kernels 3×3, 10 frames

(b) Kernels 3×3, 20 frames

(c) Kernels 3×3, 30 frames

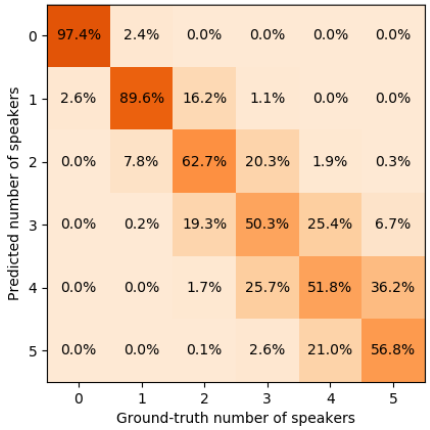

(d) Kernels 5×5, 10 frames

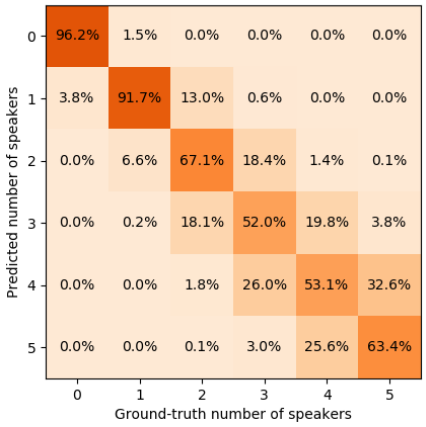

(e) Kernels 5×5, 20 frames

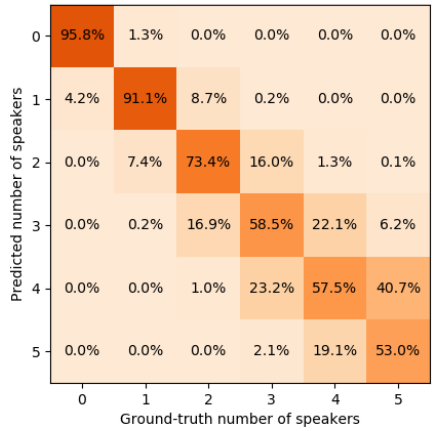

(f) Kernels 5×5, 30 frames

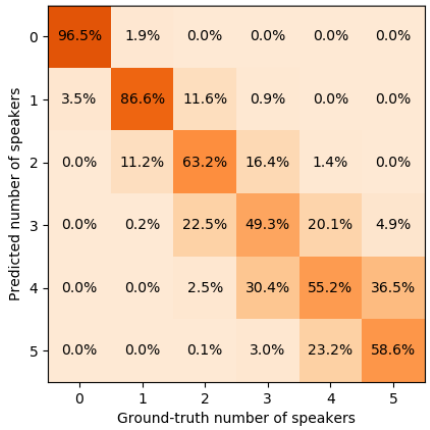

(g) Kernels 7×7, 10 frames

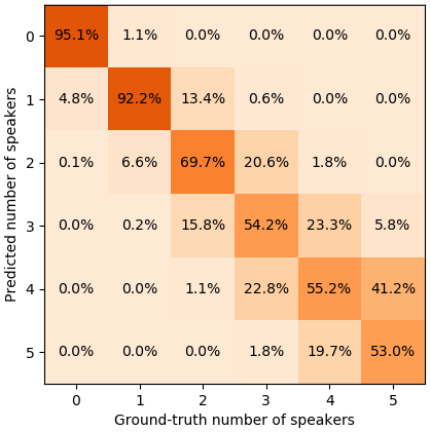

(h) Kernels 7×7, 20 frames

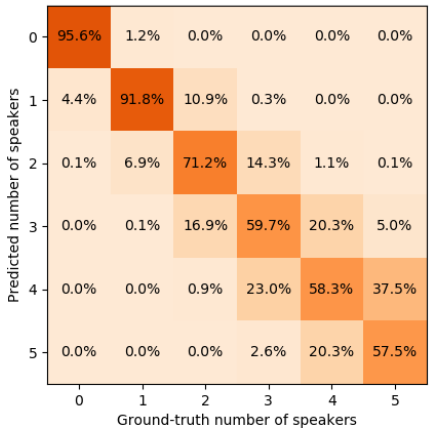

(i) Kernels 7×7, 30 frames

Figure 5.7: Confusion matrices of the accuracy A_{ij} of the proposed speaker counting multi-channel CRNN, evaluated on the test dataset, for convolution kernels of size 3×3 (top), 5×5 (middle row), and 7×7 (bottom), and for an input sequence length $T = 10$ frames (left), 20 frames (middle column), and 30 frames (right).

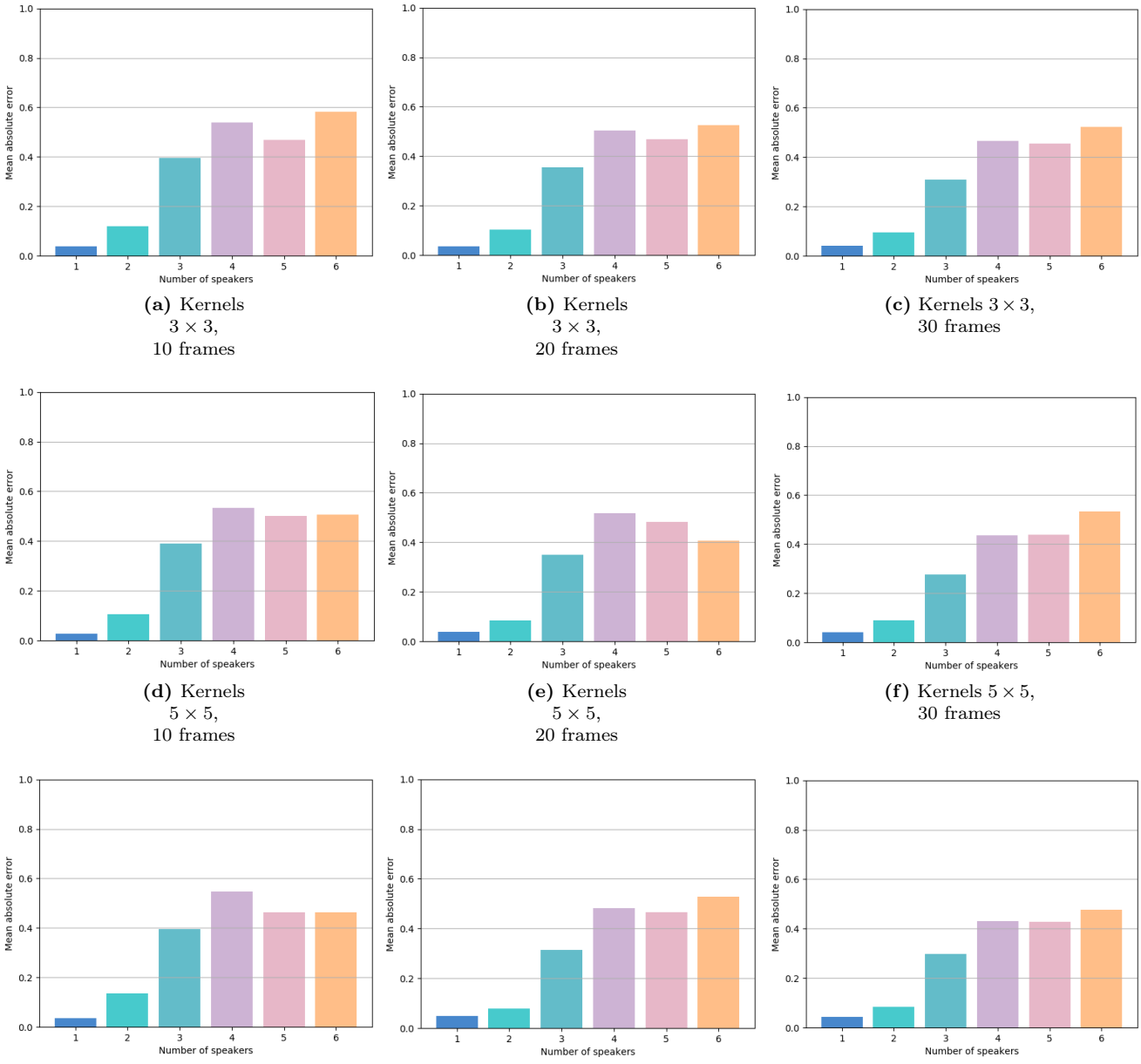

(a) Kernels 3×3, 10 frames

(b) Kernels 3×3, 20 frames

(c) Kernels 3×3, 30 frames

(d) Kernels 5×5, 10 frames

(e) Kernels 5×5, 20 frames

(f) Kernels 5×5, 30 frames

(g) Kernels 7×7, 10 frames

(h) Kernels 7×7, 20 frames

(i) Kernels 7×7, 30 frames

Figure 5.8: Mean absolute errors M_i of the multi-channel speaker counting CRNN on the test dataset, for several values of $(K \times K)$.

5.3.3 Counting accuracy profile along the sequence

Experiment objective

After analyzing the effect of the sequence length T and noticing that the network performance is better when T increases, we concluded that the LSTM layer makes better predictions if it can rely on more past frames. Moreover, we recall the reader that we use the LSTM in a sequence-to-sequence manner (*i.e.*, the LSTM makes a prediction at each timestep, using the processing of the previous timesteps). Therefore, one can legitimately think that making a prediction in the beginning of the input sequence will generally be less accurate than a prediction at the end of the sequence.

To verify this idea, we measure the overall categorical accuracy A regardless of the class, for an estimate at each frame position in the sequence. This frame-wise accuracy is defined by:

$$A(\tau) = \frac{\sum_{i=0}^{6} |T_i| A_{ii}(\tau)}{\sum_{i=0}^{6} |T_i|}, \tag{5.4}$$

where $A_{ii}(\tau)$ is the accuracy calculated only from the estimates for frames τ in a sequence. That is, for all test sequences, we only keep the prediction for the frame position τ to compute the accuracy $A(\tau)$. We do that for all $\tau \in [1, T]$ and end up with the accuracy $A(\tau)$ as a function of the frame position τ. To perform a fair evaluation on all frames of all test sequences, instead of extracting non-overlapping sequences of T frames from the 15 s test signals as we did in our previous experiment, here we actually extract the input features with an overlap of $T - 1$ (*i.e.*, we shift the input sequence by one frame at a time).

The evaluation of $A(\tau)$ is done for several values of $T \in \{10, 20, 30, 50\}$. We also vary the convolution kernel size, with values 3×3, 5×5 and 7×7, which has been shown to be very interesting for the analysis.

Results

Fig. 5.9 displays the accuracy $A(\tau)$ as a function of the frame position τ in the input sequence of size T, for several values of $T \in \{10, 20, 30, 50\}$ (represented with different colors) as well as three convolution kernel sizes $K \in \{3, 5, 7\}$ (corresponding to the three subplots). The overall accuracy, averaged over all frame positions, is also represented with the horizontal dashed lines for the reference.

The first observation we can make is that all curves present a similar shape, with first a rise of the accuracy $A(\tau)$ when τ increases from 0, then $A(\tau)$ reaches a maximum, and possibly a plateau in the middle values of τ, and finally $A(\tau)$ decreases when τ gets close to T. Part of this shape can be explained as an expected behavior from the LSTM layer. The increase in accuracy for the first values of τ can be interpreted as the fact that the LSTM needs a certain amount of past information to make a correct prediction. This rise is indeed quite important for the first values of τ. When $K = 3$ and $T = 10$, the accuracy goes from 62.5% for $\tau = 0$ to 70% for $\tau = 6$. For $K = 5$ and $T = 50$, $A(\tau)$ goes from 62.5% for $\tau = 0$ to around 74% at $\tau = 20$, and

then we observe a plateau for the accuracy. This plateau is noticeable (and possibly large) only for high values of T, and seems to indicate the convergence of the LSTM. For small T, one can think that the LSTM does not reach this convergence when the accuracy starts decreasing, due to another phenomenon, detailed below. To sum up, we can conclude that the LSTM needs a certain amount of past information for a good prediction, leading to a notable increase in prediction accuracy.

Whether the accuracy reaches a plateau (for large enough values of T) or a local maximum (for small T), we always see an important decrease when τ gets close to T. This means that the network predictions for the last frames of the input sequence are less accurate that for the middle frames, however better than for the very first frames. For instance, for $K = 3$, we notice that the accuracy starts decreasing for $\tau = T - 5$ for all T, except for $T = 10$ where the accuracy starts decreasing at $\tau = T - 3$. For $K = 5$, the accuracy decrease happens for $\tau = T - 9$ except for $T = 10$. For $K = 7$ the drop is less similar depending on T: we observe it for $\tau = T - 10$ when $T = 30$ and for $\tau = T - 16$ when $T = 50$. So it seems that the position where the accuracy starts decreasing is correlated to the size of the convolution kernels. In fact, we conjecture that it is due to the use of zero-padding in the convolutional layers. This technique, used to preserve the shape of the input feature, adds frames of zeroes before and after the input sequence (and zero-valued frequency bins also) so that the kernels can be applied at the edge of the spectrogram. It results in a convolution operation done on the edge regions where part of the processed data does not contain any information (*i.e.*, filled with zeroes), so the resulting vectors would contain less information for the next layer. As this effect happens for all convolutional layers, the number of zero-valued frames added at the beginning and end of the input features is related to the number of convolutional layers and the corresponding kernel sizes K. In our case, as there are 4 convolutional layers in our CRNN, $4 \times \frac{K-1}{2} = 2K - 2$ zero-valued frames are added before and after the input feature. Thus we can expect a decrease in accuracy, due the LSTM process on vectors with less information, starting from the frame at position $2K - 2$ before the end of the sequence.

Finally, due to the LSTM behavior and the use of zero-padding in all 4 convolutional layers, an empirical formula can be draw to express the optimal position τ_{opt} for a frame in the sequence, to obtain the best prediction (a sequence starts at $\tau = 0$):

$$\tau_{opt} = T - 2K + 1. \tag{5.5}$$

This empirical optimal position is showed in darker color in Fig. 5.9.

To conclude, this simple performance analysis shows that the use of LSTM layers and zero-padding in convolutional layers results in an asymmetrical prediction accuracy depending on the position of the analyzed frame in the input sequence. We notice that a gain of 10% in accuracy can be obtained by choosing the optimal frame position, which we try to justify by inspecting the behavior of neural network components. To illustrate the prediction power of our speaker counting system, we show

in Fig. 5.10 the predicted and ground-truth NoS of three 15-s mixtures, with 1, 3 and 5 speakers, respectively. We use the neural network with $K = 5$, and a sequence length $T = 30$. Using an overlap of $T - 1$, we successively extract the input features from the 15-s mixtures and keep only the prediction for the frame $\tau = \tau_{opt}$.[3] We therefore estimate the NoS for all frames in the mixtures. In the top plot of Fig. 5.10, (1-speaker signal), the prediction is almost perfect, but we notice that the network failed to capture a short speech break around frame 300, and seems to be sometimes a bit early or late by a few frames in its prediction (*e.g.*, around frames 75 and 360). In the middle plot (3-speaker signal), the predictions are less accurate than with 1 speaker but still relatively precise. We also notice a few predictions time-shifted from the ground-truth (*e.g.*, around frame 80 and sometimes the network does not detect a new speaker (*e.g.*, around frame 160). Moreover, in different frame regions (*e.g.*, around frames 210 and 330), the network overestimates the number of speakers. In the bottom plot (5-speaker signal), the prediction performance is degraded, as expected due to the increasing complexity of the task. Still, we see that the predictions lie around the ground-truth.

[3] As we do not use zero-padding, for the input feature extracted at the very beginning of the mixture we keep all predictions for $\tau < \tau_{opt}$, and for the input feature extracted at the very end we keep all predictions for $\tau > \tau_{opt}$.

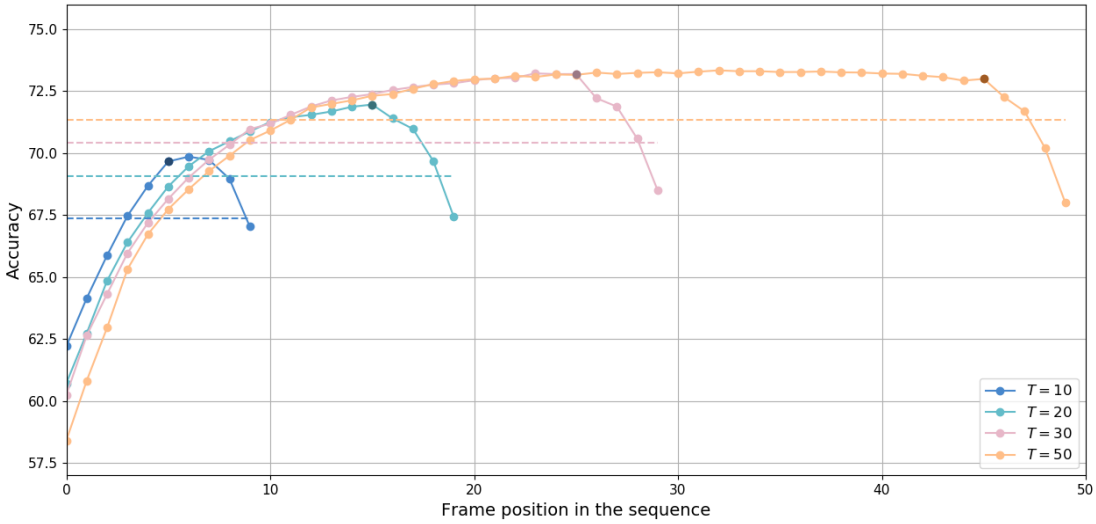

(a) $K = 3$

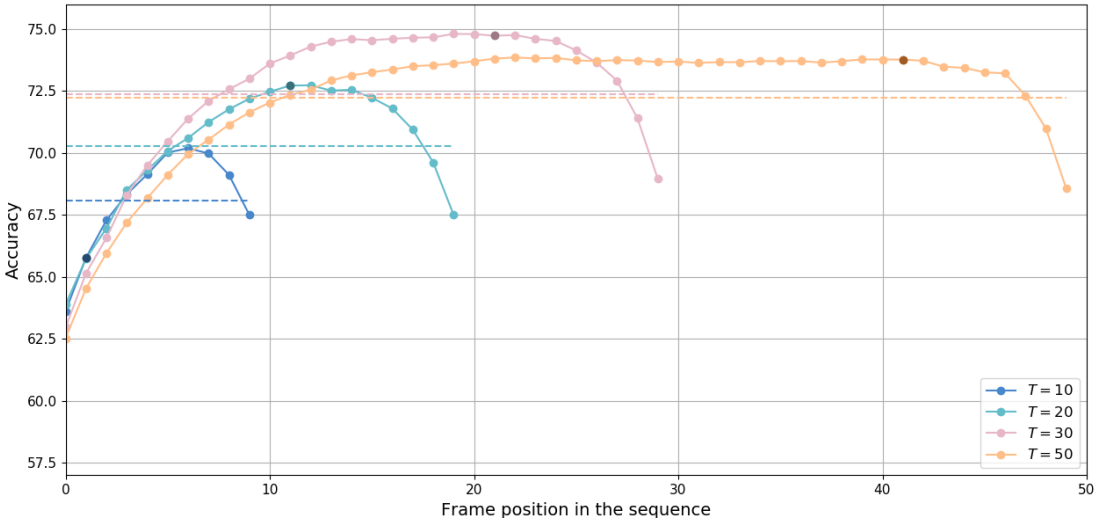

(b) $K = 5$

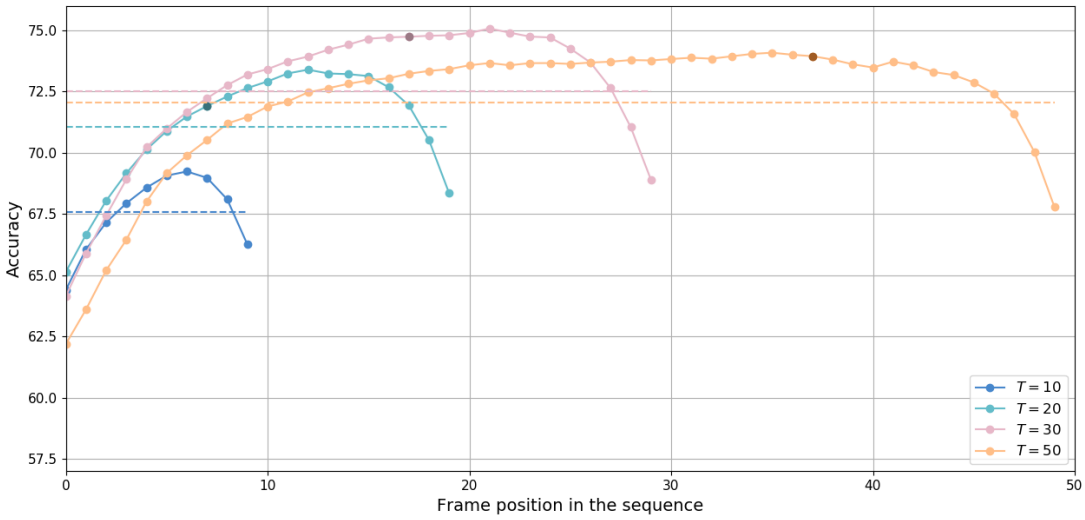

(c) $K = 7$

Figure 5.9: Overall accuracy according to the predicted frame position in the input sequence, for $K = 3$ (top), $K = 5$ (middle) and $K = 7$ (bottom). On each plot we show the frame-wise accuracy for different sequence length T, with a darker value representing the empirical optimal frame position. In horizontal dashed lines are represented the average accuracy on all frame positions.

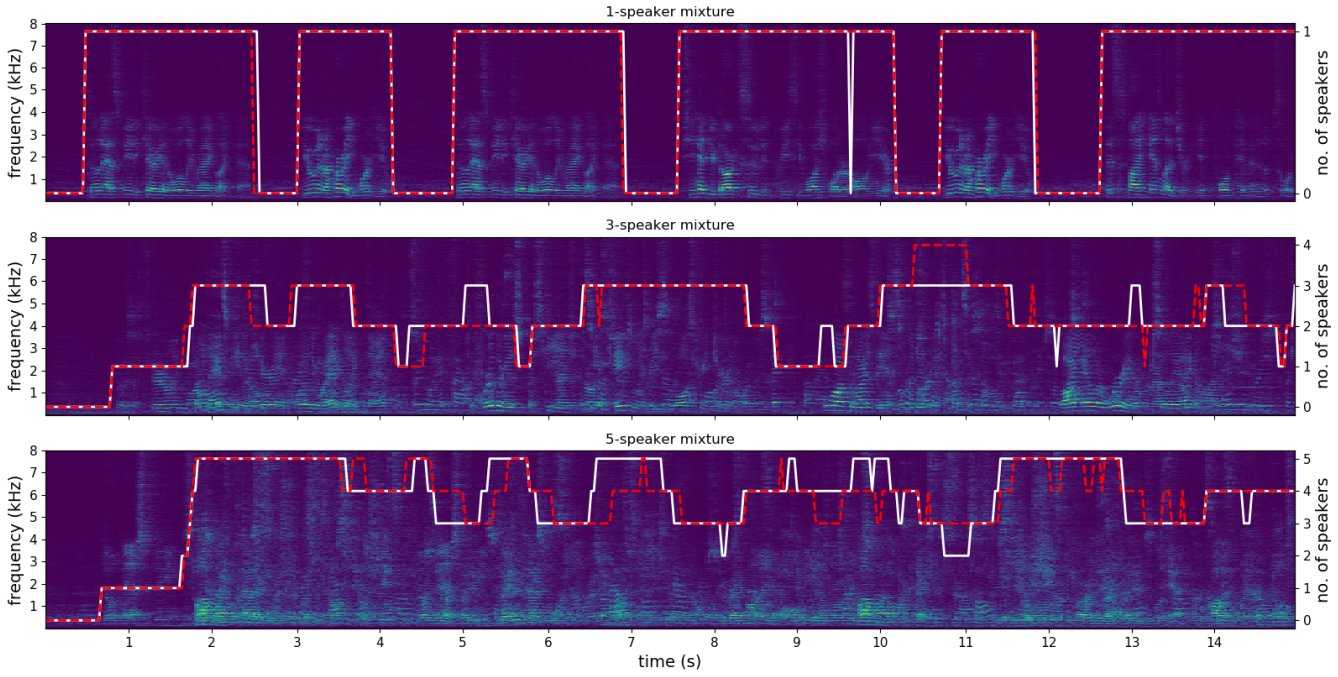

Figure 5.10: Spectrograms of the W channels of three test signals (with 1, 3 and 5 speakers), with the ground-truth NoS (in white) and the NoS predicted by the proposed multi-channel CRNN (in red). The prediction is based on the result provided by the network at frame τ_{opt} (see text).

5.4 Conclusion and perspectives

In this chapter, we have introduced a CRNN which is capable of counting up to 5 speakers in a FOA signals, with a frame-wise resolution. This latter point is a notable difference with the existing state-of-the-art at the time of the presented study. The best speaker counting system available at that time [St19] was providing the maximum NoS over 5s-mixtures.

Our CRNN, trained on FOA magnitude spectrogram is composed of several convolutional layers, which are designed to extract spectral and spatial information while preserving the temporal dimension, followed by a sequence-to-sequence LSTM layer and an output feedforward layer. The 6 softmax neurons of the output layer estimate a probability distribution over the NoS (from 0 to 5) for each frame in the input spectrogram. The evaluation of this speaker counting CRNN on simulated data showed that it can classify a multi-channel signal as being non-speech with almost perfect accuracy, and is able to estimate the presence of 1 speaker around 90% precision. When the number of speakers is greater or equal to 2, the accuracy is still greater than 50%.

We conducted several experiments in order to assess the benefit of certain hyperparameters. First, we showed the superiority of using multi-channel features over single-channel ones, suggesting the benefit of spatial information for speaker counting. We noticed that the network accuracy increased when the length of the input sequence was larger, and it seemed that augmenting the convolution kernel sizes slightly helped for better predictions but this was not fully conclusive. Finally, we carried out a performance analysis which showed that the network prediction accuracy was uneven for all frames in a given sequence, due to the LSTM behavior and the use of zero-padding in the convolutional layers. Based on an empirical investigation, we concluded that the best counting accuracy is obtained for the last frames in the sequence which are not affected by zero-padding.

Although some design efforts have been made to improve the counting accuracy, as well as an analysis to assess the network performance, there is still room for future investigation in many aspects. While only a small number of convolutional layers has been used here, we believe that the feature extraction stage could be easily improved, based on one experiment we conducted for DoA estimation 7.3.2. Regarding this, several aspect could be investigated, such as the number of convolutional layers, the convolutional shapes (2D, 3D), the use of dilated kernels, or even the addition of residual connections which might help if numerous layers are used. A better feature extraction could lead to a better discrimination between sources, thus leading to a more accurate speaking counting. One may also think of bidirectional layers for an improved temporal analysis. Regarding speaker discrimination, the use of phase information, as well as considering HOA features could further improve the network performance, which was already shown to benefit from spatial information. We think that increasing the Ambisonics order and improving feature extraction are the most

promising options for improving the speaker counting performance. Another perspective is to explore a more suitable loss function such as the earth-mover distance [HYS16], as it could make a better benefit of the inter-class relationships.

Chapter 6

Single-speaker localization

This exploratory chapter presents a series of experiments geared towards the use of the time domain velocity vector, which was presented in Section 2.4.3, for single-source localization. As a novel representation, analyzed from a theoretical point of view in a recent paper [DK20], the TDVV had never been applied to SSL with neural networks. Due to its promising characteristics, we explore the benefit of using the TDVV as the input feature for SSL, compared to using the FO-PIV, which is a state-of-the-art representation for neural-based multi-source localization [Per+18b]. Before addressing the multi-source scheme, we attempte to improve the single-source localization performance by designing and evaluating a variety of neural network architectures.

As in the previous chapter, we first explain how we employ the TDVV as a network input feature, then we present the output paradigm we used for localization and the overall network architecture. Then, we detail the adopted audio and training parameters, the nature of the training and test data, the baseline, and the metrics. In the first experiment, we directly compare the TDVV input features against the FO-PIV, using the same (baseline) neural network. Then we attempt to improve the network feature extraction module, so that it can make better use of the TDVV, with dilated convolutional layers and residual connections.

As the reader will realize throughout this chapter, this thesis part is very exploratory and experimental. The obtained results are not as good as excepted, and to find a cause of it is not a trivial task, due to the lack of theoretical understanding of the behavior of neural networks. Despite the somewhat disappointing results of the many experiments we conduct, we think that presenting this research it still relevant.

6.1 Overall methodology

6.1.1 Input features

As mentioned earlier, in this chapter we explore the use of the TDVV as a novel input features for a localization neural network. For a given frame of signal, we have seen in Section 2.4.3 that it is computed as the IFT of the FDVV, which itself is derived

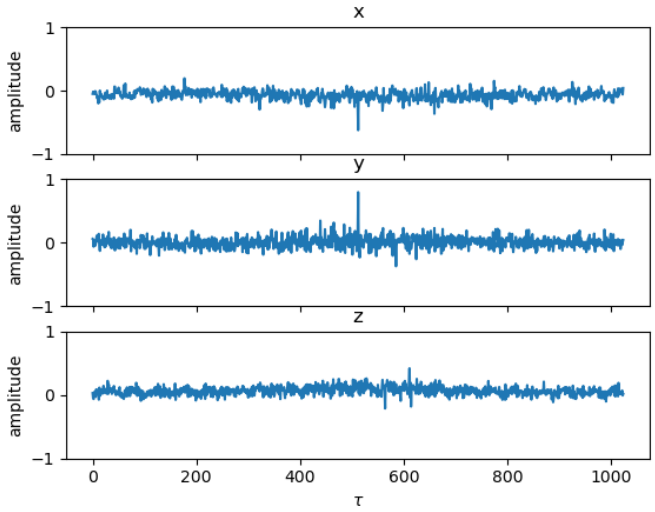

Figure 6.1: Plot of a TDVV for one frame of a training example, decomposed into the x-, y- and z- dimensions.

as the FO-PIV divided by the power of the channel W:

$$\mathbf{V}(\tau) = IFT(\mathbf{V}(f)) = IFT\left(\frac{\mathbf{I}(f)}{|W(f)|^2}\right) = IFT\left(\frac{1}{W(f)}\begin{bmatrix} X(f) \\ Y(f) \\ Z(f) \end{bmatrix}\right). \tag{6.1}$$

For each τ, the quantity $\mathbf{V}(\tau)$ is a vector with 3 coordinates x, y, z. The TDVV is then computed for several frames, which leads to a 3D input tensor $\mathbf{X} \in \mathbb{R}^{T \times N \times 3}$, where N is the IFT size.

When computing this quantity, we add a small value $\epsilon = 10^{-5}$ to $|W(f)|^2$ in order to avoid dividing by zero. An example of TDVV computed from the training dataset (see Section 6.2.3 below) is shown in Fig. 6.1, with one subplot for each of its channel dimensions. We see that this practical TDVV example does not fully resemble the theoretical TDVV illustrated in Fig. 2.6 but rather seems to be a very noisy version of it. We can still observe a few prominent peaks, theoretically corresponding to the contributions of one or more reflections (or the direct path for $\tau = 0$). This motivates us to rely on neural networks which we hope to be robust enough to cope with the noise.

6.1.2 Speaker localization as a classification problem

As for speaker counting, we consider speaker localization as a classification problem, similarly to [Per+18b]. Fig. 6.2 illustrates the general classification approach we take for speaker localization, with an arbitrary NoS. From the microphone array point of view, and with the microphone array center taken as the origin of a spherical coordinate system, the DoA space is represented as a unit sphere. This 2D sphere is discretized into several regions, which will act as the classes, with the following

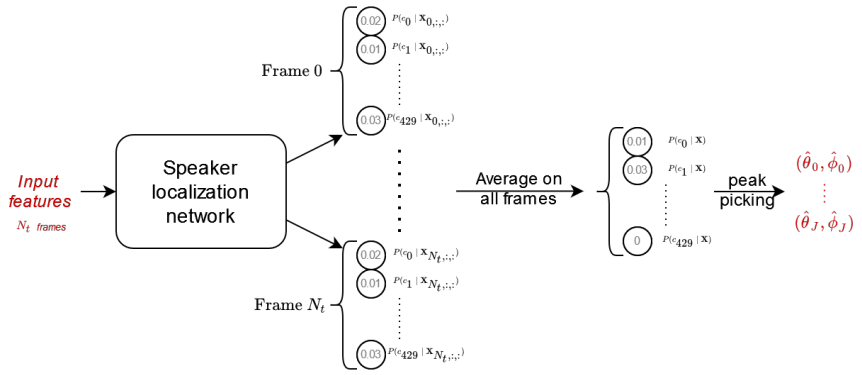

Figure 6.2: Illustration of a speaker localization system addressed as a classification problem.

discrete values for the source azimuth $\theta \in [-180°, 180°]$ and the source elevation $\phi \in [-90°, 90°]$:

$$\begin{cases} \phi_p = -90° + \dfrac{p}{P} \times 180°, \text{ for } p \in \{0, ..., P\} \\ \theta_q^p = -180° + \dfrac{q}{Q_p + 1} \times 360°, \text{ for } q \in \{0, ..., Q_p\} \end{cases}, \tag{6.2}$$

where $P = \lfloor \frac{180}{\alpha} \rfloor$, $Q_p = \lfloor \frac{360}{\alpha} cos\phi_p \rfloor$ and α is the grid resolution in degrees [1]. In all our experiments, we set $\alpha = 10°$, so that we end up with 429 DoA regions, each one represented as a class $c_i, i \in \{1, ..., 429\}$ for the network.

The neural network is trained to estimate a probability $P(\theta_q^p, \phi_p \mid \mathbf{X}_{t,:,:})$ that a sound source is present in region (θ_q^p, ϕ_p), for each region, and for each frame from an input feature $\mathbf{X}$. We then average the probability distributions over all frames in the input sequence to obtain one final distribution $P(\theta_q^p, \phi_p \mid \mathbf{X})$. As we consider the single-source scheme in this chapter, the peak-picking stage simplifies as extracting the direction with the highest probability to be the estimated DoA:

$$(\hat{\theta}, \hat{\phi}) = \underset{(\theta_q^p, \phi_p)_{p \in [0,P], q \in [0,Q_p]}}{\arg\max} P(\theta_q^p, \phi_p \mid \mathbf{X}). \tag{6.3}$$

6.1.3 Neural network architecture

Many neural network architectures are explored to improve the single-source localization accuracy. An illustration of the generic architecture can be found in Fig. 6.3. The input feature $\mathbf{X}$ presented above is fed into the input layer of the neural network. After a feature extraction module which will change according to the experiment, a recurrent module made of two bidirectional LSTM layers is used. These LSTM layers are used in a sequence-to-sequence manner so that each input frame leads to a new vector. In these layers, we use the same activation functions as described in Section 3.3.3. Then, each output vector of the second LSTM layer goes into a first

[1] Note that we also used the notation p to design the acoustic pressure and Q for the number of Ambisonics channels, however we believe that it does not lead to confusion.

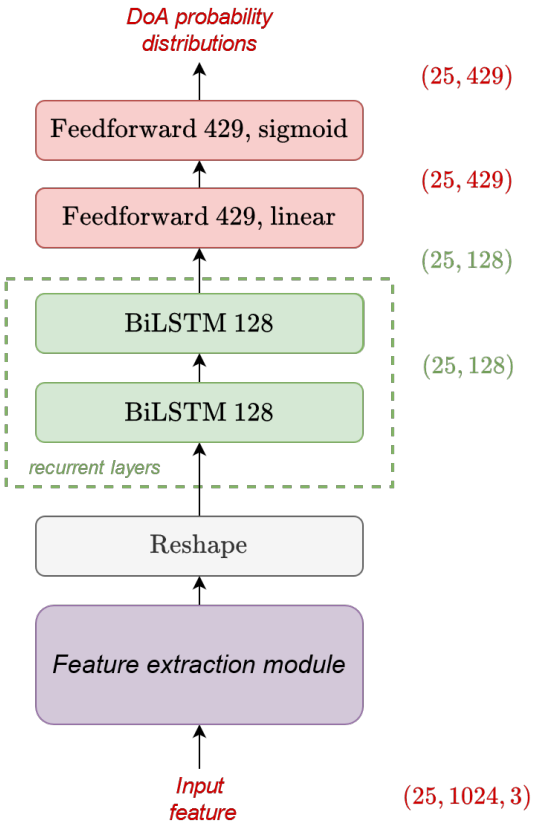

Figure 6.3: General architecture of the neural network used for single-speaker localization. The input feature is fed into a feature extraction module whose components change according to the experiment. A recurrent module with 2 bidirectional LSTM layers is then used in a sequence-to-sequence manner, and the LSTM output vector corresponding to each frame is fed into a block of two feedforward layers, the last one acting as the output layer. At the end, we end up with a probability distribution over the discretized DoA space for each input frame.

feedforward layer with 128 units and linear activation. Finally, another feedforward layer is used as the output layer, with 429 units (one for each DoA region) and a sigmoid activation function.

6.2 Experimental protocol

6.2.1 Audio parameters

We use the same audio parameters as in Chapter 5. The audio signals are sampled at 16 kHz. Both STFT and inverse STFT are computed with a Tukey window ($\alpha = 0.5$) of length 1 024 samples and an overlap of 50%. The motivation for this choice of the window function is to reduce the signal distortion within the frame, so that the derived TDVV features remain accurate.

6.2.2 Training parameters

The neural networks are trained using the binary cross-entropy as the loss function and the Adam optimizer with a starting learning rate of 10^{-3}, $\beta_1 = 0.9$, $\beta_2 = 0.999$, and $\epsilon = 10^{-7}$. During training, a dropout layer is used between the feedforward layers, with a dropout rate of 0.3. We also monitor the network accuracy on the validation dataset during the training phase. If the accuracy does not improve for 10 epochs, the learning rate is reduced by a factor 2, and if it does not improve for 20 epochs, we stop the training and keep the best performing model. The maximum number of epochs is set to 300.

6.2.3 Training data

The training dataset is generated in a similar way as for the speaker counting network, presented in 5.2.3, except that we do not aim to generate conversation-like mixtures. We instead create 1-s mixtures with a continuous speech coming from a static source.

We first generate a set a SRIRs with the image-source method [AB79] using an adaptation of the RIR generator [Hab06] to the Ambisonics format. The SRIRs are generated with the following protocol. In order be sure that every class is well represented, *i.e.*, every DoA is present with the same amount in the training phase, we first select a random DoA. Then, we pick random room dimensions in the range $[2, 10]$ m, $[2, 10]$ m and $[2, 3]$ m, for the width, length, and height, respectively, as well as the reverberation time RT60 between 200 and 800 ms. Next, the microphone array is randomly positioned somewhere in the room so that it is at least at 0.5 m from the walls. The first source position is randomly picked at a distance between 1 and 3 m from the microphone array with respect to the DoA selected at the beginning of the procedure. If such a constraint is not applicable (*i.e.*, it forces the first source to be outside of the room), we restart the algorithm with new room dimensions. We generate a total of 128 700 SRIRs.

To generate the speech signals, we use the TIMIT corpus [Gar+93], as in Chapter 5. For each generated SRIR, we extract speech excerpts containing 1 s of continuous speech, which we convolve with the SRIR to create a reverberant speech signal. A diffuse noise is added to the convolved speech signal with a random SNR between 0 and 20 dB. The diffuse noise is created by first picking a random noise signal in the same noise dataset as in Chapter 5, and convolving it with the average of the diffuse parts of two random measured SRIRs.

The validation dataset is generated in the exact same way, based on 1 287 SRIRs. We took care of using different speech and noise signals, as well as new random seeds to unmatch from the random pick used in the generation of the training dataset.

The overall process results in a total of around 35 hours of training data and 22 minutes of validation data.

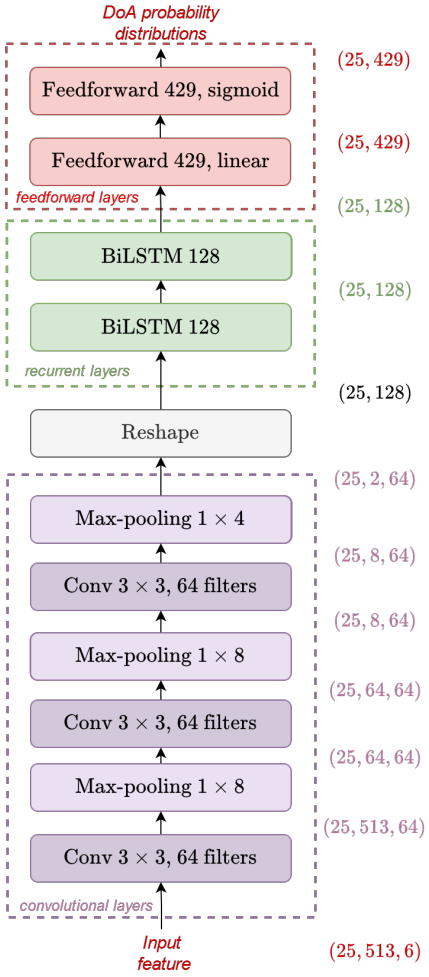

Figure 6.4: Baseline localization CRNN adopted in [Per+18b].

6.2.4 Testing data

To evaluate our neural networks, we use two testing datasets, one with simulated SRIRs and another with recorded SRIRs.

The first one is created using the same procedure as the training and validation sets. As for validation data, we take care of using new seeds for random picking, new speech signals and new noise signals to generate the data. We thus create a total of 22 minutes of testing data with simulated SRIRs. The speech signals in the second dataset are created in the same way as the first one, but using real SRIRs recorded with an EigenMike in a real reverberant room. The room is 4 m long, 7 m wide and 2.5 m high, and the RT60 is around 500 ms. The microphone array are placed in 36 positions, and for each one 16 loudspeakers emitted a sweep signal to gather a total of 576 SRIRs.

6.2.5 Baseline

As a baseline, we use the CRNN proposed by Perotin *et al.* in [Per+18b], from which we draw inspiration when designing several networks during the experiments. The

Input features	Accuracy (%)		Angular error (°)	
	<10°	<15°	Mean	Median
FO-PIV	**95.3**	**99.2**	**5.0**	**4.5**
TDVV	77.2	90.9	8.1	6.3

(a) Simulated SRIRs

Input features	Accuracy (%)		Angular error (°)	
	<10°	<15°	Mean	Median
FO-PIV	**67.1**	**83.9**	**11.5**	**7.3**
TDVV	53.9	71.2	16.3	9.1

(b) Real SRIRs

Table 6.1: Results of the localization of a single speech source with the baseline CRNN, for the FO-PIV vector and the TDVV as input feature. Best results are shown in bold.

baseline architecture is illustrated in Fig. 6.4. The main difference with our approach is that the input feature was composed of the real and imaginary parts of the FO-PIV (see Section 2.4.1). The feature extraction module is composed of 3 convolutional layers, with 64 convolution kernels of size 3×3, and each one is followed by a max-pooling layer with pooling sizes 1×8, 1×8 and 1×4, respectively. Dropout layers are used after each max-pooling layer during the training phase.

6.2.6 Evaluation metrics

We use two metrics to evaluate the localization performance. First, we compute the mean and median angular error (which is the angular distance between the estimated DoA and the ground-truth DoA) on the whole test dataset. On a sphere, the angular distance is defined on the unit sphere between two points (θ_1, ϕ_1) and (θ_2, ϕ_2) by:

$$\delta((\theta_1, \phi_1), (\theta_2, \phi_2)) = \arccos\big(\sin\phi_1 \sin\phi_2 + \cos\phi_1 \cos\phi_2 \cos(\theta_1 - \theta_2)\big). \tag{6.4}$$

We also measure the classification accuracy on the test set, which is the percentage of test examples with an angular error below a certain tolerance threshold. Considering that the minimum angle between two points in the grid defined in Section 6.1.2 is 7°, we evaluate the classification accuracy for a tolerance threshold of 10° and 15°.

6.3 Experiments

6.3.1 TDVV against FO-PIV

Experiment objective

The first experiment we conduct is a direct comparison of the use of the TDVV and FO-PIV as input features of the same neural network. For a fair comparison, we train the baseline CRNN, one with the TDVV and with the FO-PIV as input feature.

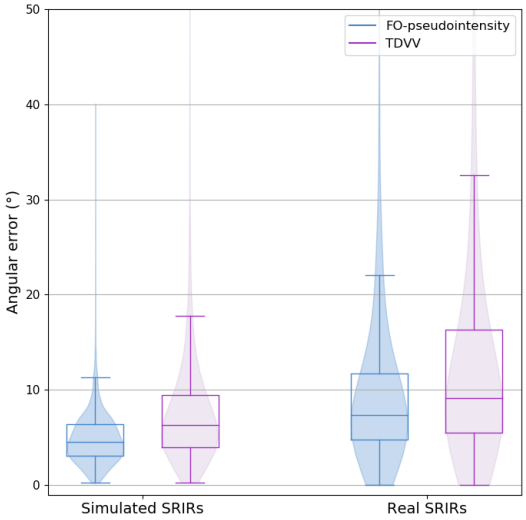

Figure 6.5: Distribution statistics on the angular error of the CRNN with TDVV and the baseline on both testing datasets. Boxplots show the first and third quartiles as well as the median value. Superposed to each boxplot is shown the corresponding violin plot, which is an estimation of the probability density function of the statistical distribution.

We use the exact same training, validation and test datasets, as well as the training parameters, so that only the input features differ between the two systems.

Results

The classification accuracy and the mean and median angular errors on the two test datasets (with simulated SRIRs and real SRIRs) are shown in Table 6.1. The angular error statistics are illustrated with boxplots and violin plots in Fig. 6.5.

On the dataset created with simulated SRIRs, we see that the CRNN using the TDVV as input underperforms the baseline, with a notable decrease in performance. The baseline proves to be very accurate for single-source localization [Per+18b] with 99.2% accuracy with an angular tolerance of 15°and 95% accuracy for a tolerance of 10°. The CRNN using the TDVV as input only achieves 90.9% and 77.2% in these metrics, respectively. We also see on the boxplots and violin plots that the angular errors for the TDVV are more scattered than for the FO-PIV.

Regarding the dataset with real SRIRs, the observations are similar, with a drop in accuracy by around 13% for the TDVV in comparison to the FO-PIV, for both 10° and 15°tolerances. By using the TDVV as input feature, we increase the mean angular error by almost 5°. The violin plots suggest that both CRNNs provide less consistent results on data generated with the real SRIRs, compared to the data generated with the simulated SRIRs.

All these results show that replacing the FO-PIV with the TDVV as neural network input feature leads to a notable decrease in localization performance. Whereas this new representation was shown to be meaningful on a theoretical point of view, it

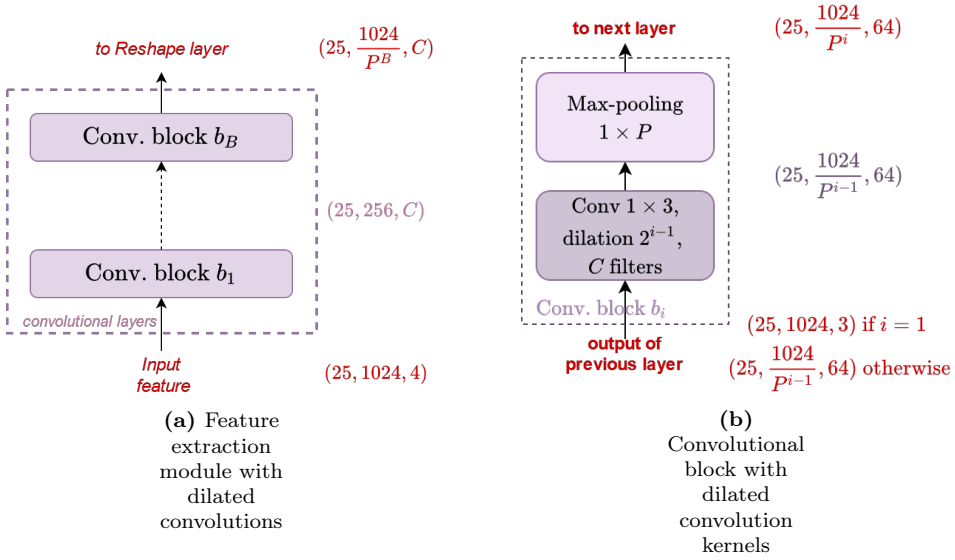

(a) Feature extraction module with dilated convolutions

(b) Convolutional block with dilated convolution kernels

Figure 6.6: Feature extraction module with B convolutional blocks consisting of a convolutional layer with increasing dilation factor followed by a max-pooling layer.

seems that the CRNN has more difficulties to extract the relevant information for DoA estimation than with the FO-PIV. This motivates us to conduct further experiments to improve the architecture, in order to give the neural network more capability to extract more relevant features.

6.3.2 CRNN with dilated convolutions

Experiment objective

The previous experiment showed us that the CRNN from [Per+18b] makes better use of the FO-PIV than the TDVV as input feature. One reason might be because the baseline architecture has been tuned for the use of FO-PIV and thus is not suitable for feature extraction from the TDVV. We then might need a more adapted neural network for this new representation. Recalling the theorical derivation of the TDVV in Section 2.4.3, we see that it contains information about certain reflections at some specific delay τ. One idea is then to give the network more flexibility during the feature extraction stage in order to process the relevant reflection components, indexed by several τ which are sometimes far from each other in the TDVV.

Dilated convolutions seem to be good candidates for that purpose because they can process data points which are not contained in a neighbouring area, without taking the in-between points into account. For this reason, we decide to replace the classical 3×3 convolution kernels with dilated kernels of size 1×3 so that the process is done only along the TDVV delay axis, separately for each frame. In that way, the TDVV information is not mixed across the frames in the convolutional layers, the temporal analysis being reserved for the subsequent layers. Fig. 6.6a shows an illustration of the network architecture we adopt. We replace all the convolution layers

Model label	B	P	C	# parameters
Baseline	/	/	/	578 927
Dil-B2-P0-C32*	4	0	32	17 155 951
Dil-B2-P2-C32		2	32	2 475 887
Dil-B2-P4-C32		4	32	640 879
Dil-B2-P4-C64		4	64	921 839
Dil-B3-P0-C32*	3	0	32	17 159 155
Dil-B3-P2-C32*		2	32	1 430 515
Dil-B3-P4-C32		4	32	447 475
Dil-B3-P4-C64		4	64	541 075
Dil-B4-P0-C32*	4	0	32	17 162 259
Dil-B4-P2-C32*		2	32	1 433 619
Dil-B4-P4-C32		4	32	450 579
Dil-B4-P4-C64		4	64	553 427

Table 6.2: Summary of all tested configurations of hyperparameter values with the resulting number of parameters constituting the neural network. Note that the baseline number of parameters is also given whereas it is not based on dilated convolutional blocks. Model labels marked with an asterisk are those which do not manage to train properly, resulting in random predictions.

from the baseline architecture with a series of B dilated convolution blocks illustrated in Fig. 6.6b where B is an hyperparameter in our experiments. These blocks are made of one convolutional layer with C convolution kernels of size 1×3 and a dilation factor which doubles at each additional block, starting with $l = 1$, and then followed by a max-pooling layer of size $1 \times P$. The idea behind this increasing dilation factor is borrowed from the WaveNet architecture [Oor+16], whose authors showed that it increases the receptive field of the convolutional layer. In our case the receptive field spans the τ axis.

We train this neural network for several hyperparameter values. We stack up from $B = 2$ (thus with dilation factors $l = 1, 2$) to $B = 4$ ($l = 1, 2, 4, 8$) convolutional blocks with $C = 32$ kernels and pooling sizes $P = 0, 2, 4$ (when $P = 0$ we do not use any max-pooling layers at all). For $P = 4$ (which gives the most conclusive results as we will see below), we also try using $C = 64$ kernels. Table 6.2 summarizes the different tested configurations with the resulting number of parameters constituting the neural networks, along with the baseline for comparison.

Results

For reasons that are not yet well identified, several sets of hyperparameters lead to an erratic network training (even after we retrain them again to make sure it is not a bug). Fig. 6.7 shows the validation accuracy evolution during such a training, as an example for model *Dil-B2-P0-C32*. Models that we are not able to train properly are indicated with an asterisk after their label in Table 6.2. Looking at the number of parameters of these wrongly trained model, there seems to be a correlation between a high number of parameters and an erratic training. As these models do not employ a

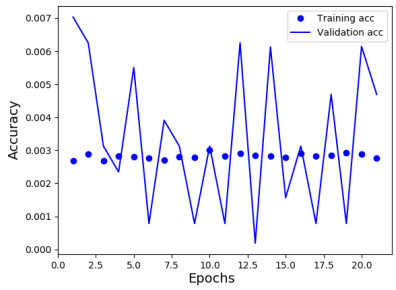

Figure 6.7: Training and validation accuracy evolution of the erratic training of model Dil-B2-P0-C32. We clearly see that the network does not learn, which leads to non-increasing accuracy on the validation set. Note that the accuracy is bounded by 100%.

lot of pooling in the convolutional blocks, the second tensor dimension at the output of the reshape layer is quite large, implying that most of the network parameters are used to map this dimension to the BiLSTM dimension of size 64. For example, for $B = 2$, $C = 32$, and no pooling, the shape at the output of the reshape layer is $(T, 32\,768)$, resulting in 16 810 496 parameters only for the first BiLSTM layer. This high number of parameters at one specific layer of the network could be the reason why it is hard to train. However, this problem happens also for relatively small models such as *Dil-B3-P2-C32* and *Dil-B4-P2-C32* (about 1.5 M parameters); we still miss a fully satisfying explanation of this issue.

Due to these still open problems, we present only the results for a portion of our experiments. We do not consider all the experiments leading to a functional network training. Instead, we limit the results to a subset of all configurations which allows us to rigorously compare several hyperparameter values. Therefore, since the pooling size seems to be important for a successful training, we evaluate only the models with $P = 4$, which allow us to compare the different numbers of convolutional blocks and kernels.

As we can see in Table 6.3 and Fig. 6.8, the performance of the dilated CRNNs is still far from the baseline. We even lose in performance compared to the baseline architecture with the TDVV as input feature (see Table 6.1). Using simulated SRIRs, the localization accuracy for this architecture was 90.9% for a tolerance of 15°, while it drops between 70.5 and 87.7% .when considering the best-performing dilated CRNN. With real SRIRs, the accuracy decrease a bit less pronounced, going from 71.2% with the baseline architecture to between 55.7% and 70.3%.

When comparing the dilated CRNNs with each other, we see that using $C = 64$ convolution kernels instead of $C = 32$ leads to better results in all cases. For instance with real SRIRs, the mean angular error goes from 26.8° to 21.8° when $B = 2$, or from 35.2° to 21.2° when $B = 4$. Moreover, there is a tendency that the performance increases when B increases, *i.e.*, using more convolutional blocks results in a more accurate network.

Model label	Accuracy (%)		Angular error (°)	
	<10°	<15°	Mean	Median
Baseline	**95.3**	**99.2**	**5.0**	**4.5**
Dil-B2-P4-C32	58.4	75.4	15.4	8.6
Dil-B2-P4-C64	69.3	85.2	10.3	7.3
Dil-B3-P4-C32	47.9	70.5	19.8	10.3
Dil-B3-P4-C64	70.9	87.1	9.6	7.1
Dil-B4-P4-C32	61.8	79.3	16.1	8.2
Dil-B4-P4-C64	68.1	85.5	10.5	7.3

(a) Simulated SRIRs

Model label	Accuracy (%)		Angular error (°)	
	<10°	<15°	Mean	Median
Baseline	**67.1**	**83.9**	**11.5**	**7.34**
Dil-B2-P4-C32	42.4	61.4	26.8	11.9
Dil-B2-P4-C64	50.7	68.1	21.8	9.8
Dil-B3-P4-C32	35.8	55.7	35.2	13.2
Dil-B3-P4-C64	49.1	67.4	18.4	10.1
Dil-B4-P4-C32	47.0	62.9	28.6	10.7
Dil-B4-P4-C64	52.0	70.3	21.2	9.6

(b) Real SRIRs

Table 6.3: Accuracy and angular errors of the dilated CRNNs with TDVV and the baseline on the testing datasets. Best results are in bold.

It is not clear why we observe a drop in performance with this new feature extraction module. In the baseline architecture, only 3 convolutional layers with 64 kernels are used, and the pooling size is larger. In our proposal, even with $C = 64$ and $P = 4$, we witness a decrease in accuracy. One important change we made is the replacement 3×3 max-pooling block by 1×3 pooling, which could be the cause of this decline, although it seems surprising to be the only explanation. It could be instructive to evaluate these models with 3×3 max-pooling to assess this idea, however we did not have time to do it.

To conclude this experiment, the proposed feature extraction module does not allow to improve over the baseline performance. It even further deteriorates compared to using the baseline architecture with the TDVV as input feature. However, we learn that using a relatively large max-pooling is necessary to avoid having too many parameters and an untrainable network, and that using $C = 64$ kernels in the majority of convolutional blocks leads to better results.

6.3.3 CRNN with dilated convolutions and residual connections

Experiment objective

In order to improve the feature extraction module, we try adding residual connections to the CRNN to help stabilising the training of a network. The idea is that each feature map is reused in the next layers, to hopefully allow the network more flexibility in

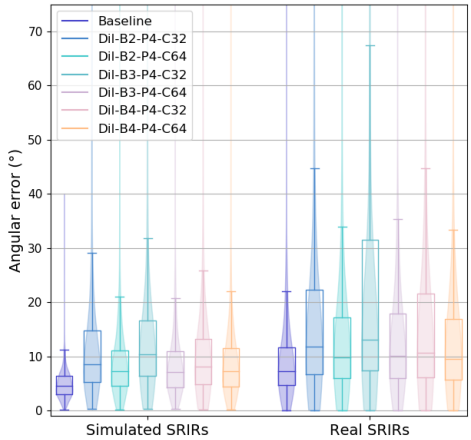

Figure 6.8: Distribution statistics on the angular error of the dilated CRNNs with TDVV and the baseline on both testing datasets.

producing an informative representation for the localization task. We use a similar architecture as before, with the difference that each convolutional block contains two convolutional layers with a residual connection, as illustrated in Fig. 6.9. As we can see, the output of the first convolutional layer is concatenated with the output of the second one, leading to a total of $2C$ feature maps. Again, the second dimension of the resulting tensor is reduced using a max-pooling layer. We experimente with different numbers of such blocks ($B = 1, 2, 3, 4, 5$). This results in more convolutional layers (10 when $B = 5$), therefore, we modify the dilation factor progression with all successive integer values; that is, in the first block we have $l = 1$ for the first convolutional layer and $l = 2$ for the second one, then for the second block we have $l = 3$ and $l = 4$, and so forth. We set the remaining hyperparameter values to the values that produces the best results in the previous experiment ($C = 64$, $P = 4$). Table 6.4 sums up the tested configurations.

Model label	B	P	C	**# parameters**
Baseline	/	/	/	578 927
Res-B1-P4-C64*	1	4	64	17 162 315
Res-B2-P4-C64*	2	4	64	4 616 595
Res-B3-P4-C64*	3	4	64	1 508 059
Res-B4-P4-C64	4	4	64	535 043
Res-B5-P4-C64	5	4	64	599 403

Table 6.4: Summary of all tested configurations of hyperparameter values with the resulting number of parameters constituting the residual CRNN. Model architectures marked with an asterisk are those which do not managed to train properly, resulting in random predictions.

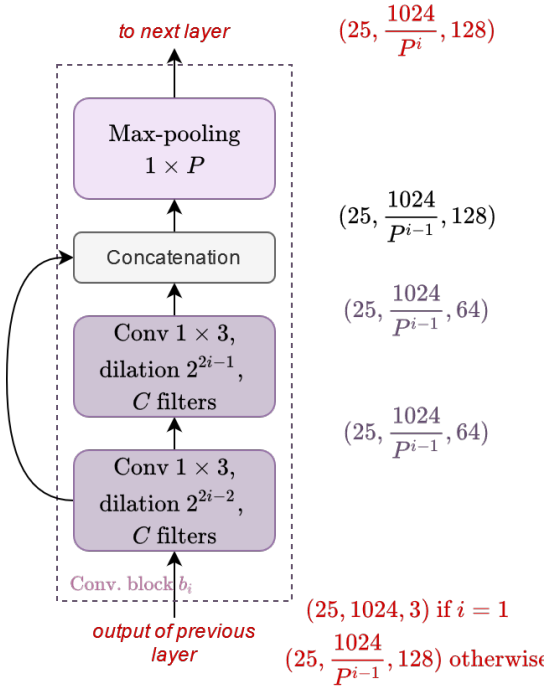

Figure 6.9: Convolutional block with two convolutional layers and with a residual connection propagating the output of the first block to the output of the second one. They are both concatenated before fed into a max-pooling layer.

Results

The residual connections fail to stabilise training, since the models with too many parameters (for $B = 1, 2, 3$) do not train properly, leading to random results. We thus present the results for $B = 4, 5$ in Table 6.5 and Fig. 6.10.

As we can see, the results are even worst than all other experiments. While the model labelled *Res-B4-P4-C64* reaches a reasonable performance slightly below the dilated CRNNs with $C = 64$, the model *Res-B4-P4-C64* results in poor performance, with only 45.2% accuracy with a tolerance of 15° with simulated SRIRs.

Although we keep the best hyperparameter values found in the previous experiment, we do not manage to improve the results by adding residual connections, and we even surprisingly worsen the localization performance. Compared to the previous models, we only change the design of the convolutional block by adding a second convolutional layer with a residual connection. Intuitively, such a modification should have a positive impact on localization performance, since it improves the flexibility of feature extraction. Unfortunately, we fail to explain the outcome of this experiment.

Model label	Accuracy (%)		Angular error (°)	
	<10°	<15°	Mean	Median
Baseline	**95.3**	**99.2**	**5.0**	**4.5**
Res-B4-P4-C64	61.3	80.3	13.0	8.2
Res-B5-P4-C64	26.4	45.2	21.1	16.8

(a) Simulated SRIRs

Model label	Accuracy (%)		Angular error (°)	
	<10°	<15°	Mean	Median
Baseline	**67.1**	**83.8**	**11.5**	**7.3**
Res-B4-P4-C64	47.5	65.4	23.2	10.3
Res-B5-P4-C64	22.7	40.4	29.8	17.8

(b) Real SRIRs

Table 6.5: Accuracy and angular errors of the residual CRNNs with TDVV and the baseline on the testing datasets. Best results are in bold.

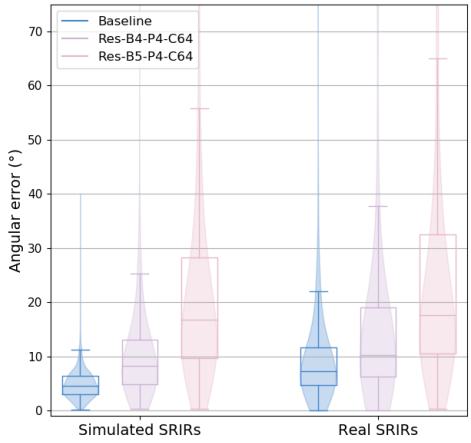

Figure 6.10: Distribution statistics on the angular error of the residual CRNNs with TDVV and the baseline on both testing datasets.

6.4 Conclusion and perspectives

In this chapter we presented a series of experiments to assess the capabilities of combining neural networks with the TDVV. While many information including the DoA can be extracted from the theoretical TDVV, we saw that, in practice, the extraction of such a feature is very noisy, which motivated us to rely on the expressive power of neural networks. Throughout numerous experiments, of whom we only presented those giving interesting results, we attempted to improve single-source localization with the TDVV as input feature, compared to the use of the FO-PIV. Although the use of TDVV resulted in a fair localization accuracy, the baseline was never outperformed. We made a lot of efforts to redesign the network feature extraction module to be adapted to this new kind of input feature, without success.

The most interesting, yet difficult part of these experiments, is to understand why we did not manage to improve localization with these new features. Concerning the models that we were not able to train properly, we speculated that this was due to the too large number of parameters accumulated in one specific layer, resulting from the network design. However, the reason why using dilated convolutions and residual connections decreased the performance is not clear. While the inconclusiveness of several attempts could allow to avoid repeating the same mistakes, we believe that these ideas could lead to interesting future works due to the promising possibilities of using the TDVV with neural networks.

As we were not able to successfully exploit the TDVV's nature despite the effort of finding an adapted feature extraction module, the issue could lie in the TDVV estimation itself. In these experiments, we extracted the TDVV in a somehow *naive* manner, by incorporating an *epsilon* value to avoid dividing by zero, which had the effect of emphasizing noise in low SNR conditions. More elaborate estimation algorithms could be employed beforehand to help the network for better feature extraction. For example, as the TDVV is related to the relative transfer function, one could adapt RTF estimation algorithms such as [SW96; Coh04; GBW01].

Furthermore, applying the self-attention mechanism across the delay dimension of TDVV, could be a viable alternative to (dilated) convolutions. This raises concerns with regards to computational complexity, hence an efficient implementation (*e.g.*, [Kat+20]) is a prerequisite.

While the inconclusiveness of all the presented attempts could allow to avoid repeating the same mistakes, we believe that these ideas could lead to interesting future works due to the promising possibilities of using the TDVV with neural networks. We still think that these ideas could really benefit source localization and that the effort should continue towards a robust TDVV estimation algorithm, as well as a neural network design conceived with the theoretical TDVV properties in mind.

Chapter 7

Multi-speaker localization

In the previous chapter, we explored single-speaker localization with a novel type of input feature called TDVV. We now focus on multi-speaker localization. However, TDVV assumes a single sound source, hence we will rely on the pseudointensity vector (which way, anyhow, shown to outperform the former even in the single-source scenario). We base our research on the same baseline [Per+19] as in the previous chapter. Therefore, in the present chapter, the NoS is supposed to be known by the the localization system.

After describing the neural network input features, the output paradigm and overall architecture, we present different parameters used in our system, the employed training and testing data, the baseline and evaluation metrics. Then, we detail the various experiments we conduct to improve the multi-speaker localization performance over the baseline. The first experiment aims at finding the best order of feeding the training data to the network, considering that the training signals contains between 1 and 3 speakers. In the second experiment, we design a new feature extraction module, and in the third, we consider replacing the recurrent layers with a self-attention mechanism. In the last experiment, we assess the use of HOA features.

7.1 Overall methodology

7.1.1 Input features

As in [Per+19], we use the pseudointensity vector as input feature for the multi-speaker localization neural network. This type of input features proved to be more robust than spectrograms for FOA signals [Per+18b]. In [Per+19], the input feature was obtained by computing the normalized active and reactive FO-PIV $\bar{\mathbf{I}}_a(t, f)$ and $\bar{\mathbf{I}}_r(t, f)$ from (2.37) and (2.38) and stacking them into the third dimension to obtain a 3D tensor of shape $T \times F \times 6$, with T the number of frames, F the number of frequency bins.

Fig. 7.1 shows the input feature extracted from a training example. Here we have $T = 25$ frames, and $F = 512$ frequency bins corresponding to the bandwidth $0-8$ kHz.

An extension of this input feature is assessed in an experiment presented in Section 7.3.4, in which we evaluate the benefit of using the HO-PIV over the FO-PIV.

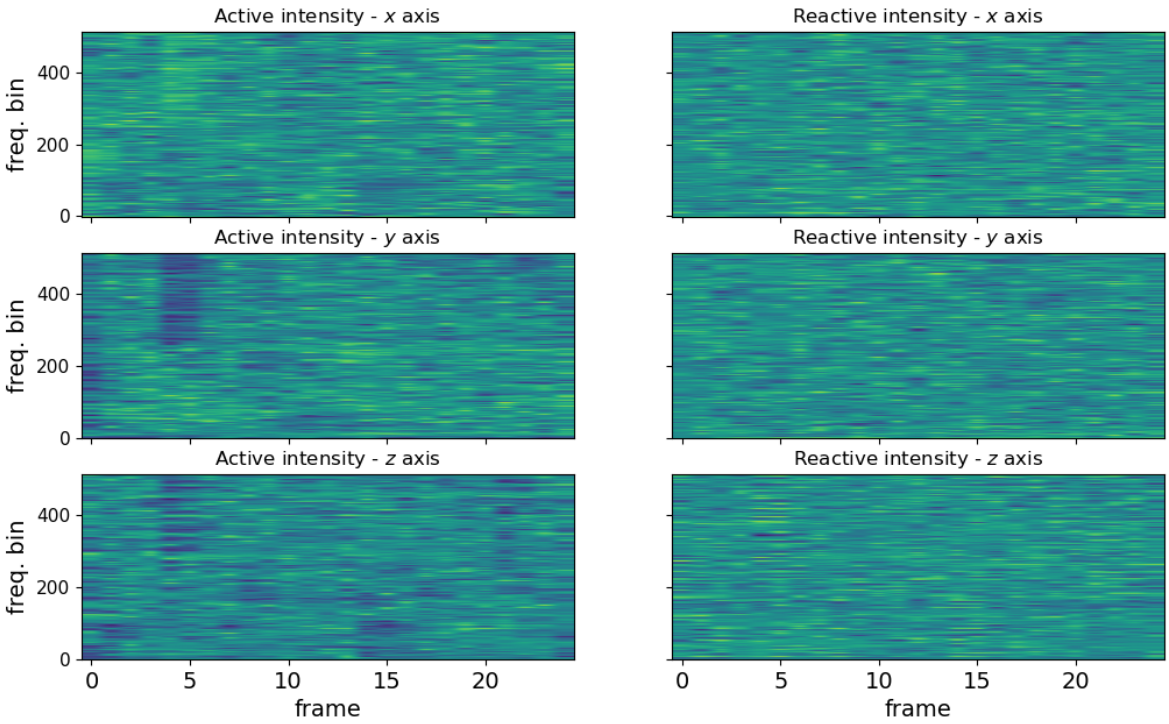

Figure 7.1: Plot of the 6 channels of a FO-PIV input feature extracted from a training example of 25 frames. From top to bottom: the x, y, z coordinates. Left: active intensity. Right: reactive intensity.

The HO-PIV feature is computed at order 2, leading to an input tensor of shape $T \times F \times 16$.

7.1.2 Multi-speaker localization as classification

We consider the multi-speaker localization problem with the same classification approach as that described in Chapter 6 and illustrated in Fig. 6.2. The same unit sphere discretization is used, leading to 429 possible DoA directions, considered as classes. We extend SSL to the multi-speaker case by directly extracting the J highest peaks in the output probability distribution, where J is the number of speakers. Note that, after averaging the probability distribution over the T frames (which leads us to consider the total NoS J instead of the instantaneous NoS $J(t)$), we do not smooth this probability distribution within a neighborhood like in [Per+19], as we found out it deteriorated the results.

When training and evaluating the network with generated data (using simulated and real SRIRs), we consider that J is known. For the evaluation on real signals from the LOCATA dataset [Eve+20], we use a thresholding method with a fixed threshold $\beta = 0.2$ for peak extraction.

When a certain number of DoAs are extracted from the localization network output, we employ the Hungarian algorithm [Kuh55] to assign the estimated DoAs with the ground-truth speaker positions. This algorithm minimizes the total assignment cost, as a sum of the costs obtained by the different assigned pairs. In the present case, it minimizes the total angular error obtained between all assigned pairs {predicted source DoA, ground-truth source DoA}.

7.1.3 Neural network architecture

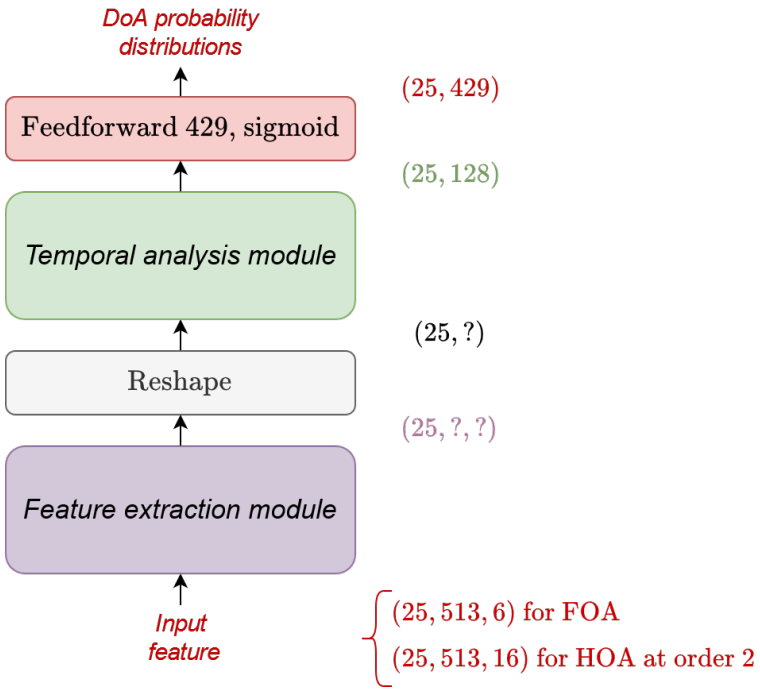

Figure 7.2: General architecture of the multi-speaker localization neural network. The design of the feature extraction and temporal analysis modules are part of the experiments.

The general architecture for our multi-speaker localization system is shown in Fig. 7.2. The input feature is first fed into a feature extraction module, whose design is addressed our the second experiment in Section 7.3.2 (in our first experiment in Section 7.3.1, the feature extraction module architecture is the same as in the baseline). Then, the new extracted feature is reshaped and sent through the temporal analysis module. The temporal analysis module design is addressed in our third experiment in Section 7.3.3. Then, each vector of the output sequence of this temporal analysis module finally goes separately into the output feedforward layer, which produces a probability distribution over the DoA space. Note that throughout the whole architecture, the temporal dimension is preserved, so that the output sequence is of the same length as the input sequence.

7.2 Experimental protocol

7.2.1 Audio and training parameters

The same audio parameters as in Chapter 6 are used, except that the STFT is computed with a sinusoidal window, as in [Per+19]. The training parameters are exactly the same. We consider $T = 25$ frames for each input sequence. To train the network, we use the binary cross-entropy as in the previous chapter.

7.2.2 Training data

The training dataset is generated in the same manner as the training data for the single-speaker localization system described in Chapter 6.2.3. The difference is that, when a first random DoA is picked, and the room configuration and microphone position are drawn, two other source DoAs are randomly picked so that the sources are in the room and their positions are at least 10°apart from one another. We thus obtain 3 SRIRs per room configuration and microphone position. This enables us to create 3 distinct training datasets T_1, T_2, and T_3, which contain training signals with 1, 2, and 3 speakers, respectively. This method follows the same protocol as in [Per+19], but is extended to 3 speakers instead of 2 as proposed by the authors of this study. For the training datasets T_2 and T_3, 1-s single-speaker signals are first generated as in Section 6.2.3, by picking a distinct random SRIRs in the same room. They are then mixed together using random SIR in $[0, 10]$ dB with respect to the first source (of course, we mix 2 signals for T_2, and we mix 3 signals for T_3).

At the end of this dataset generation process, the training datasets T_1, T_2, and T_3 contain 257, 400 signals of duration 1-s, resulting in a total of 772, 200 training mixtures (about 172 hours of signals).

7.2.3 Test data

To evaluate our models, we use three sets of test data, each one of different nature. The first set is made of three datasets, labelled E_1^{Sim}, E_2^{Sim} and E_3^{Sim}, which contain 1-, 2- and 3-speaker signals, respectively. These signals are generated using the same simulated SRIRs as in Section 6.2.4, and are created in the same manner as for the training data with several speakers. The second set is also made of three datasets, named E_1^{Real}, E_2^{Real} and E_3^{Real}, whose signals are generated using the same real SRIRs as in Section 6.2.4 and the same process as the previously described multi-speaker mixtures. The third test dataset is the datasets of four tasks of the LOCATA Challenge [Eve+20]. These data are used to assess our model on real data. Focusing on the EigenMike signals of all these LOCATA datasets, we use 13 signals of task 1 (single static loudspeaker), 13 signals of task 2 (multiple static loudspeakers), 5 signals of task 3 (single moving human talker) and 5 signals of task 4 (multiple moving human talkers). Although we do not focus on moving speakers and our model is not trained for this scenario, we still perform an evaluation on task 3 and 4 to assess the robustness

of our system to moving sources. These 4 test datasets are referred as E_1^{Rec}, E_2^{Rec}, E_3^{Rec} and E_4^{Rec}, for task 1, 2, 3 and 4, respectively.

7.2.4 Baseline

As a baseline, we use the same architecture as proposed in [Per+19], which is illustrated in Fig. 6.4. For fair comparison, we extend this model by training it with 3-speaker signals, whereas the authors of [Per+19] limited the training to 2-speaker mixtures. For the last experiments, which assess the benefit of using HOA features, we also compare our system to an adaptation of a DL-free algorithm [KG18], called *TRAMP*, to the same feature format. This method is based on the histogram of the DoAs derived from the pseudointensity vector over all considered frames and frequencies in the sequence.

7.2.5 Evaluation metrics

We use the same metrics as in Chapter 6: the localization accuracy with an angular tolerance of 10° and 15°, as well as a tolerance of 20° for the LOCATA dataset, and the mean and median angular errors.

7.3 Experiments

7.3.1 Training scheme

Experiment objective

As mentioned above, in the baseline study [Per+19], the experiments are limited to two speakers (thus, two training datasets), and during the training phase, the signals are fed into the network in a random order, regardless the number of speakers. This choice raises the question if there is an "optimal" order to present the training data to the neural network. One could think that the network is flexible enough to learn with all data mixed together, or on the contrary one could believe that it would be better for the network to be trained in an increasing order of complexity; that is, starting with signals with 1 speaker, then 2 speakers, and ending with 3 speakers, which can be thought as fine-tuning. Another possibility is to train the network with 3-speaker signals only (the most complex task), which may be enough to make the network robust for the easier tasks, *i.e.*, localizing 1 or 2 speakers. This idea is actually linked to the concept of curriculum training [Ben+09; Jia+15].

In the present experiment, we assess these ideas by training the baseline neural network of [Per+19] multiple times, using several training schemes and evaluating the obtained models on the test datasets E_j^{Sim} and E_j^{Real} for $j \in 1, 2, 3$. The different training schemes we evaluate are the following:

- The training is done with only one of the three training datasets T_1, T_2, or T_3. This enables us to determine how the neural network is able to adapt to simpler

Model label	E_1^{Sim}				E_2^{Sim}				E_3^{Sim}			
	Accuracy (%)		Angular error (°)		Accuracy (%)		Angular error (°)		Accuracy (%)		Angular error (°)	
	<10°	<15°	Mean	Median	<10°	<15°	Mean	Median	<10°	<15°	Mean	Median
M_{T_1}	**95.2**	99.1	**5.0**	**4.5**	29.5	40.1	41.4	23.1	16.4	26.3	45.2	34.0
M_{T_2}	91.8	98.6	5.8	5.2	76.3	87.0	12.0	6.4	45.9	60.3	25.6	11.2
M_{T_3}	89.9	98.1	6.1	5.4	77.3	**87.9**	11.8	6.4	**61.5**	**75.6**	**18.5**	**8.0**
$M_{T_1 \bigcup T_2}$	94.9	99.0	5.2	**4.5**	**78.4**	87.1	**10.7**	**5.9**	52.3	65.3	21.4	9.4
$M_{T_1 \bigcup T_2 \bigcup T_3}$	94.6	**99.2**	5.2	4.7	**78.4**	87.3	11.3	**5.9**	57.8	70.1	20.2	8.4
$M_{T_1 \to T_2}$	93.3	98.7	5.5	4.9	73.4	84.8	12.7	6.6	43.4	56.6	27.5	12.1
$M_{T_1 \to T_2 \to T_3}$	92.9	98.4	5.5	4.9	71.5	84.0	13.2	6.7	46.5	59.8	25.4	11.0

(a) Simulated SRIRs

Model label	E_1^{Real}				E_2^{Real}				E_3^{Real}			
	Accuracy (%)		Angular error (°)		Accuracy (%)		Angular error (°)		Accuracy (%)		Angular error (°)	
	<10°	<15°	Mean	Median	<10°	<15°	Mean	Median	<10°	<15°	Mean	Median
M_{T_1}	72.0	88.5	8.4	6.7	24.3	34.9	45.1	27.0	13.5	21.7	48.5	37.0
M_{T_2}	73.7	91.6	8.6	6.7	57.5	74.9	17.6	8.6	35.9	49.9	31.7	15.1
M_{T_3}	75.0	91.6	8.3	6.5	**60.5**	**77.5**	18.2	**8.2**	**48.4**	**63.8**	26.7	**10.3**
$M_{T_1 \bigcup T_2}$	74.6	90.9	8.3	**6.3**	57.2	74.0	**16.5**	8.6	39.1	53.4	26.4	13.5
$M_{T_1 \bigcup T_2 \bigcup T_3}$	**75.2**	**91.9**	8.3	**6.3**	59.8	75.2	16.7	8.3	44.2	58.4	**26.2**	11.9
$M_{T_1 \to T_2}$	74.6	91.1	**7.9**	6.6	53.7	71.3	19.9	9.2	33.1	46.8	31.0	16.6
$M_{T_1 \to T_2 \to T_3}$	75.0	91.0	**7.9**	6.5	53.3	70.3	21.0	9.2	35.8	49.3	31.5	15.3

(b) Real SRIRs

Table 7.1: Accuracy and angular errors of the baseline CRNN for different training schemes (different lines of the table), evaluated on the test datasets E_1^{Sim}, E_2^{Sim}, and E_3^{Sim} (top), and E_1^{Real}, E_2^{Real}, and E_3^{Real} (bottom).

situations (*e.g.*, when training on T_3 and evaluated on E_1^{Sim}) or more complex ones (*e.g.*, when training on T_1 and evaluated on E_3^{Sim}). The models trained on T_1, T_2, and T_3 are labelled M_{T_1}, M_{T_2}, and M_{T_3}, respectively.

- The training is done with several datasets mixed together, as in [Per+19]. In that case, the training examples are drawn randomly from all datasets. More specifically, we evaluate the model trained using T_1 and T_2, labelled as $M_{T_1 \bigcup T_2}$, and the one trained with all three datasets, labelled as $M_{T_1 \bigcup T_2 \bigcup T_3}$.

- The training is done in a sequential way, with the datasets presented one after another. The model is first trained with T_1 in a conventional manner (*i.e.*, using early stopping by monitoring the validation accuracy and using a decreasing learning rate). When this first training is done, we refine the model by training it on T_2, starting with the weights from the training with T_1 (in short, training with T_1 and fine-tuning with T_2). Then, training is done with T_3. This method is intuited by the fact that the neural network is forced to learn the task from the easier to the most complex one. The model trained with T_1 then T_2 is labelled $M_{T_1 \to T_2}$, and the model trained with T_1, then T_2, and then T_3 is labelled $M_{T_1 \to T_2 \to T_3}$.

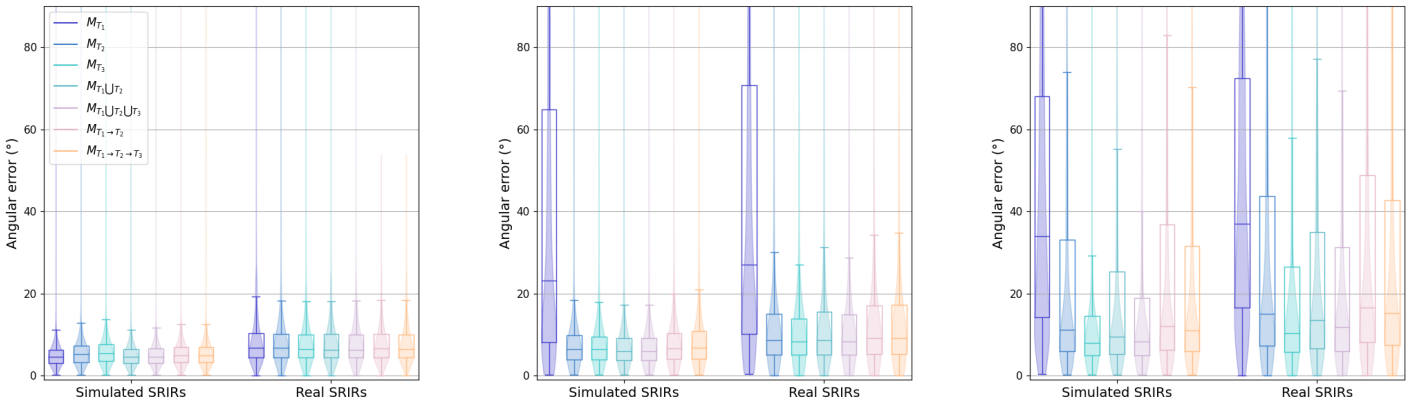

(a) 1-speaker signals **(b)** 2-speaker signals **(c)** 3-speaker signals

Figure 7.3: Boxplots of the angular errors of the baseline CRNN for different training schemes (different colors, see the legend) and evaluated on the test datasets E_1^{Sim} and E_1^{Real} (left), E_2^{Sim} and E_2^{Real} (middle), and E_3^{Sim} and E_3^{Real} (right).

Results

The results are displayed in Table 7.1 and Fig. 7.3. First, we see that all models perform accurately and approximately the same on 1-speaker signals: We obtain at least 90% and 98% accuracy on E_1^{Sim} for a tolerance of 10° and 15°, respectively, and more than 72% and 88% on E_1^{Real}. While this is not surprising for the models M_{T_1}, $M_{T_1 \bigcup T_2}$, $M_{T_1 \bigcup T_2 \bigcup T_3}$, $M_{T_1 \to T_2}$ and $M_{T_1 \to T_2 \to T_3}$, which are trained with 1-speaker signals, the good accuracy obtained by models M_{T_2} and M_{T_3} shows that we can train the network only with 3-speaker signals (and thus less training examples than for other models) and it will still be good at localizing 1 or 2 speakers. However, note that in this experiment the NoS is assumed known, so we do not take an interest in the network output variations depending on how it has been trained (*e.g.*, a possible observation is that a network trained only on 3-speakers signals may always output 3 prominent peaks even on 2-speaker mixtures). A last interesting observation is that M_{T_1} is the best performing model on E_1^{Sim}, which was somewhat expected, but is the worst performing one on E_1^{Real}, even if the metrics are still quite high.

Next, when looking at the results on 2-speaker signals for E_2^{Sim} and E_2^{Real}, we immediately notice that the model M_{T_1} is less accurate in localizing 2 simultaneous speakers than the models that have been purposely trained with 2- or 3-speaker mixtures. For simulated SRIRs, the angular error for M_{T_1} is more than 23° while for other models it is about 6–7°. This strengthens the intuition that the network cannot perform well a task that is harder than what he encountered during training. We also observe that the models $M_{T_1 \to T_2}$ and $M_{T_1 \to T_2 \to T_3}$ are less accurate that the models M_{T_2} and $M_{T_1 \bigcup T_2}$, and M_{T_3} and $M_{T_1 \bigcup T_2 \bigcup T_3}$,, respectively, suggesting that fine-tuning might not be optimal for multi-speaker localization, perhaps because the pretraining

on 1-speaker signals reaches local optimum from which it becomes difficult for fine-tuning to generalize to 2- and 3- speaker conditions. The best performing models on 2-speaker mixtures are those trained without fine-tuning and including 2- or 3-speaker signals during the training, *i.e.*, models M_{T_2}, M_{T_3}, $M_{T_1 \bigcup T_2}$ and $M_{T_1 \bigcup T_2 \bigcup T_3}$.

Finally, the results on the 3-speaker datasets confirm the analysis done in the previous paragraph. We see that the models M_{T_1} and M_{T_2} struggle to localize 3 speakers as they never encounter such signals during their learning. Similarly, we remark that the fine-tuned model $M_{T_1 \rightarrow T_2 \rightarrow T_3}$ is less accurate than models M_{T_3} and $M_{T_1 \bigcup T_2 \bigcup T_3}$, probably for the same reasons as explained above. On these datasets, the best performing model is M_{T_3}.

To sum up, these results indicate that a network trained on signals with few speakers is not able to localize many speakers, whereas, in contrast, a network trained on signals with many speakers is also able to predict the DoAs of fewer speakers. We also find out that fine-tuning is not the best option, presumably because the first training has already reached a local optimum in the network capabilities. It seems that the best option is one of the two schemes: training the network on mixtures with the highest NoS encountered in the test data, or training it with various mixtures, containing all the different considered NoS. For the remaining of this chapter, we choose the training scheme in which all the data are mixed together, as for model $M_{T_1 \bigcup T_2 \bigcup T_3}$ and as in [Per+19], except for the experiment presented in Section 7.3.4 as we will explain later.

7.3.2 Design of the feature extraction module

Experiment objective

In this experiment we focus on the design of the feature extraction module, which is directly fed with the input feature as illustrated in Fig. 7.2. In [Per+19], feature extraction is done using three convolutional layers, each followed by a max-pooling layer of size 1×8, 1×8 and 1×4, respectively (see Fig. 6.4). The relatively large pooling size leads to an important loss of information between each pair of successive convolutional layers. This choice might have been guided by the necessity to reduce the second dimension before the reshape layer (possibly for the same reasons why some networks did not train properly in Chapter 6). Losing such information could be detrimental for a proper feature extraction. In parallel, we believe that increasing the number of convolutional layers could help the network to find a better feature representation before the reshape layer.

For these reasons, we explore two changes to the baseline architecture: more convolutional layers and smaller pooling sizes. The newly proposed feature extraction module is illustrated in Fig. 7.4a. It is composed of B successive convolutional blocks, where B is a hyperparameter in this experiment. Each convolutional block b_i consists of 2 successive convolutional layers with 64 filters of size 3×3 followed by a max-pooling layer of size $1 \times P_i$, where P_i is another hyperparameter of this experiment

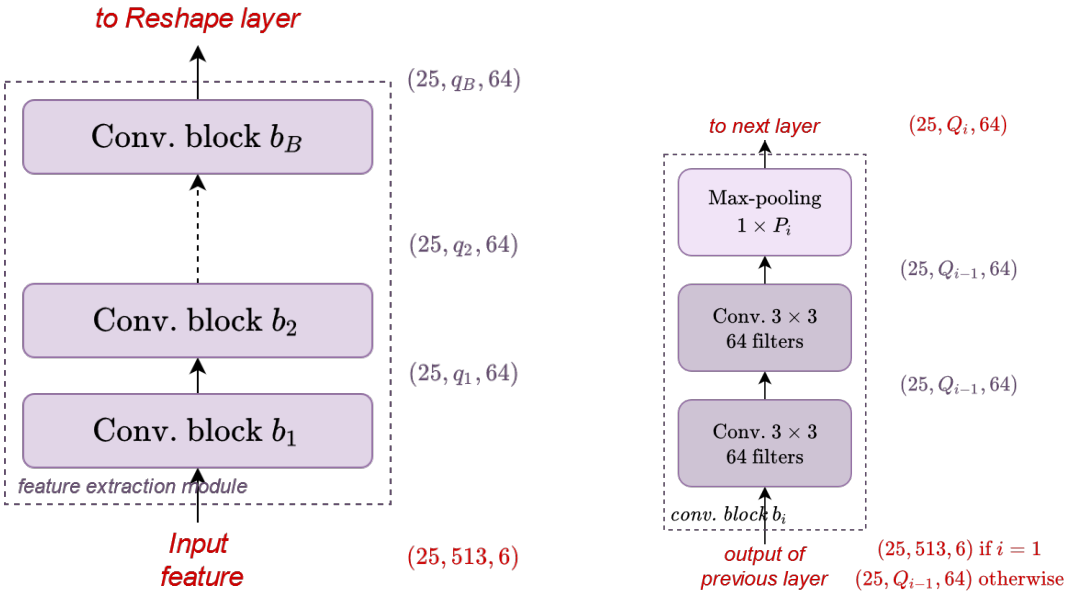

(a) Feature extraction module

(b) Convolutional block

Figure 7.4: Architecture of the feature extraction module and of an elementary convolutional block.

and varies according to the convolutional block b_i. In Fig. 7.4b, Q_i denotes the second dimension of the operated tensors and is computed as $Q_i = \frac{Q_{i-1}}{P_i}$.

Whereas in [Per+19] the authors used a max-pooling layer after each convolutional layer, in this new design, we use only one max-pooling layer after two successive convolutional layers in each convolutional block, so that the network has more information to extract useful features before downsampling the second dimension. In order to assess this idea, we try several combinations of hyperparameters B and $P_i, i \in 1, ..., B$. The max-pooling sizes P_i are chosen so that the second dimension just before the reshape layer is 2, 4 or 8. Table 7.2 summarizes the tested configurations, along with the resulting number of parameters in the network for fair comparison. We label the models M_{B,Q_B}, where B is the number of convolutional blocks and Q_B the second dimension of the output of the last convolutional block.

Results

Table 7.3 shows the results of all models on the test datasets with simulated and real SRIRs, as well as those from the various tasks of the LOCATA challenge. Fig. 7.5 and Fig. 7.6 display the corresponding boxplots and violin plots of the angular error distributions on the simulated datasets and the LOCATA dataset, respectively.

When looking at the results in Table 7.3, we see that all models surpass the baseline on the simulated datasets, and most of them lead to a better performance than the baseline on real recordings. Regarding 1-speaker signals, the gain in performance in small compared to the baseline, for the datasets with simulated and real SRIRs. For

Model label	# parameters	P_1	P_2	P_3	P_4	P_5	P_6	P_7
$M_{4,2}$	700 259	8	4	4	2	-	-	-
$M_{4,4}$	765 795	4	4	4	2	-	-	-
$M_{4,8}$	896 867	4	4	2	2	-	-	-
$M_{5,2}$	774 315	4	4	4	2	2	-	-
$M_{5,4}$	839 851	4	4	2	2	2	-	-
$M_{6,2}$	848 371	4	4	2	2	2	2	-
$M_{6,4}$	913 907	4	2	2	2	2	2	-
$M_{7,2}$	922 427	4	2	2	2	2	2	2
$M_{7,4}$	987 963	2	2	2	2	2	2	2

Table 7.2: Max-pooling sizes of the successive convolutional blocks b_i of the proposed feature extraction module with the number of parameters in the corresponding neural network.

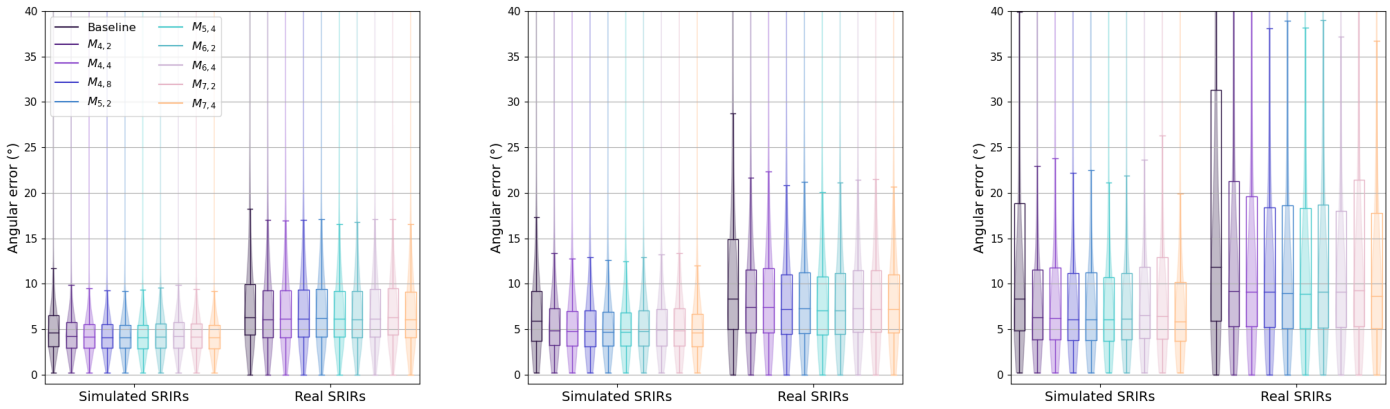

(a) 1-speaker signals **(b)** 2-speaker signals **(c)** 3-speaker signals

Figure 7.5: Distribution of the angular errors of the models with the redesigned feature extraction module and the baseline, evaluated on the test datasets E_1^{Sim} and E_1^{Real} (left), E_2^{Sim} and E_2^{Real} (middle) and E_3^{Sim} and E_3^{Real} (right).

the dataset E_1^{Sim}, the mean angular error for the baseline is 5.2° and at most 4.7° for our models, while for the dataset E_1^{Real} it reaches 8.3° and at most 8.1°, respectively. Looking at the accuracy is not very demonstrative since on simulated SRIRs the baseline already reached 99.2%. However, we see on the corresponding boxplots in Fig 7.5a that the angular errors are slightly less dispersed for our proposed models than for the baseline, which indicates that these models are less prone to large errors than the baseline. When looking at the results on the LOCATA datasets of task 1 (single static speaker), our models are not always better than the baseline, although some of them lead to a lower median. The baseline architecture thus seems quite well designed for localizing a single static source. However, regarding LOCATA task 3 signals (single moving speaker) our proposed feature extraction module leads to a significantly improved performance, with an accuracy ($< 15°$) of at least 70.0% and a mean error smaller than 13.7° (except for $M_{7,2}$) for the new models compared to

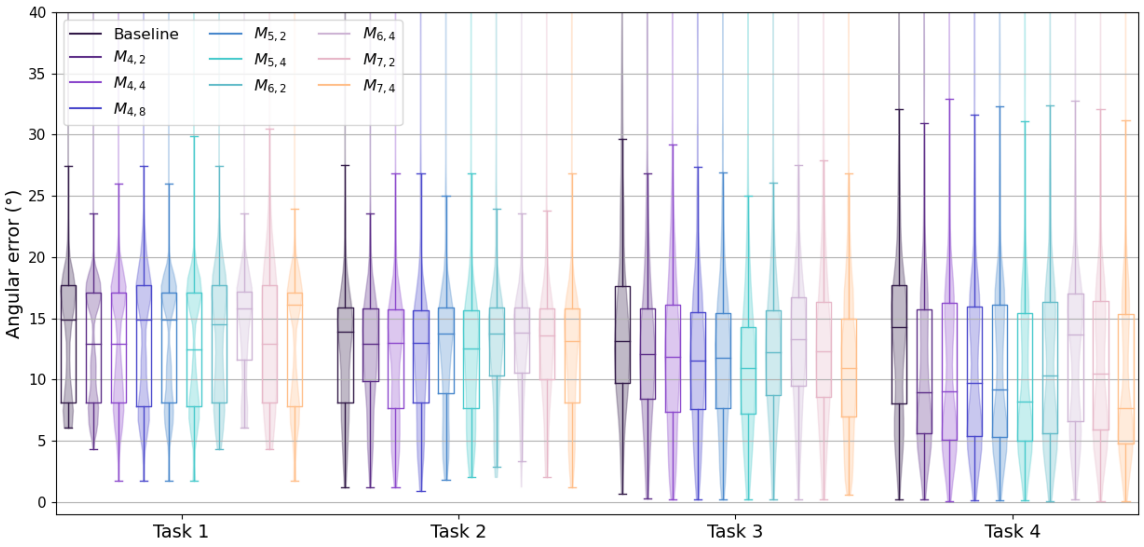

Figure 7.6: Distribution of the angular errors of the models with the redesigned feature extraction module and the baseline, evaluated on the test datasets E_1^{Rec} (left), E_2^{Rec} (middle left), E_3^{Rec} (middle right) and E_4^{Rec} (right).

66.9% and 14.1° for the baseline. This gain in performance is a bit surprising since none of these models are trained for moving speakers. These results could indicate that new models generalize better to unseen acoustic conditions than the baseline.

The results on 2- and 3-speaker signals clearly show that our proposed feature extraction module enables the network to be much more accurate than the baseline, in the multiple source scenario. With simulated SRIRs, the performance gain is conclusive: on E_2^{Sim}, the accuracy ($< 15°$) goes from 85.7% to at least 92.0% and the mean angular error is reduced to at most 8.6°, compared to 15.3° for the baseline. On E_3^{Sim}, the accuracy is increased from 68.1% for the baseline to at least 77.4% for the new models, with a mean error decrease from 27.2°to at most 16.3°. This improvement is slightly less notable on real SRIRs, where the gain in accuracy is between 8 and 11% for 2-speaker mixtures, and between 8 and 15% for 3-speaker mixtures. We also notice on the boxplots of Fig. 7.5b and 7.5c that the error dispersion is greatly reduced, which indicates a more robust model. When looking at the results on the LOCATA datasets task 2 (multiple static speakers), the same observations as for task 1 can be made, *i.e.*, the improvement is not really noticeable, and the models performance is on par with the baseline. Regarding task 4 (multiple moving speakers), the same conclusions as for task 3 can be drawn, which are that the new models seem to be slightly more efficient on these recorded signals. In particular, with regards to the $< 10°$ accuracy metric, most models outperform baseline with a margin larger than 20%.

Therefore, the results on all multi-speaker mixtures clearly demonstrate the superiority of the improved feature extraction over the one of the baseline architecture. While the performance gain is small for 1-speaker signals, the improvement is substantial for 2- and 3-speaker mixtures and prove that this new feature extraction module is much more robust in multi-speaker environments. The results on LOCATA datasets reinforce this remark, and also exhibit that our proposal interestingly leads to a more robust localization performance for moving sources. It is noteworthy that the tasks 3 and 4 of the LOCATA challenge involve human talkers, as opposed to tasks 1 and 2 where loudspeakers are used as sound sources. The latter are less accurately represented by point sources, which is the type of sources the networks are trained on. As intuited, using more convolutional layers and less drastic max-pooling provides more flexibility to the neural network, while it does not increase the number of parameters more than twice that of the baseline.

Now, when we compare the new models with each other, there is a little tendency that the use of deeper architectures (more convolutional layers) leads to better performance (the highest metrics are most often obtained with the model $M_{7,4}$). However, more investigation is needed to support this claim, since the observed results are insufficient to draw a firm conclusion on this aspect. Furthermore, when comparing models with the same number of convolutional blocks B, we notice that the best results are obtained by those with $Q_B = 4$, emphasizing the fact that downsampling information degrades the performance, although it allows a smaller number of parameters.

Model label	E_1^{Sim}				E_2^{Sim}				E_3^{Sim}			
	Accuracy (%)		Angular error (°)		Accuracy (%)		Angular error (°)		Accuracy (%)		Angular error (°)	
	<10°	<15°	Mean	Median	<10°	<15°	Mean	Median	<10°	<15°	Mean	Median
Baseline	94.6	99.2	5.2	4.7	77.6	85.7	15.3	6.0	57.1	68.1	27.2	8.3
$M_{4,2}$	97.6	99.6	4.7	4.2	86.7	92.5	8.3	4.9	71.4	79.9	15.0	6.3
$M_{4,4}$	98.3	**99.7**	4.5	**4.1**	87.9	92.7	8.5	4.8	71.2	79.5	15.4	6.2
$M_{4,8}$	98.2	99.6	4.5	**4.1**	88.0	92.6	8.4	4.8	72.2	80.7	14.7	6.1
$M_{5,2}$	98.3	**99.7**	4.6	**4.1**	87.9	92.8	8.0	4.7	72.5	80.5	14.6	6.1
$M_{5,4}$	98.4	**99.7**	4.6	**4.1**	88.8	93.1	8.1	4.7	73.3	81.0	14.9	6.1
$M_{6,2}$	98.4	99.5	4.7	**4.1**	88.7	93.2	8.1	4.8	72.2	80.7	14.4	6.1
$M_{6,4}$	**98.6**	**99.7**	**4.4**	**4.1**	88.3	93.3	**7.7**	4.7	**74.7**	**83.4**	**12.8**	5.9
$M_{7,2}$	97.8	99.5	4.7	**4.1**	86.3	92.0	8.6	4.8	68.6	77.4	16.3	6.5
$M_{7,4}$	98.4	**99.7**	**4.4**	**4.1**	**89.2**	**93.5**	7.8	**4.6**	74.4	81.3	14.1	**5.8**

(a) Simulated SRIRs

Model label	E_1^{Real}				E_2^{Real}				E_3^{Real}			
	Accuracy (%)		Angular error (°)		Accuracy (%)		Angular error (°)		Accuracy (%)		Angular error (°)	
	<10°	<15°	Mean	Median	<10°	<15°	Mean	Median	<10°	<15°	Mean	Median
Baseline	75.2	91.9	8.3	6.3	59.8	75.2	16.7	8.3	44.3	58.4	26.2	11.9
$M_{4,2}$	77.7	92.9	8.1	**6.1**	67.5	83.6	12.9	7.4	53.3	67.5	21.3	9.2
$M_{4,4}$	77.7	93.2	7.9	**6.1**	66.7	83.4	12.9	7.5	54.0	69.2	20.4	9.1
$M_{4,8}$	77.8	92.7	8.1	**6.1**	69.2	84.1	12.5	7.2	54.8	69.7	20.5	9.1
$M_{5,2}$	77.0	93.6	7.9	6.2	68.1	84.1	12.1	7.3	55.3	69.6	18.7	8.9
$M_{5,4}$	78.7	**93.8**	**7.6**	6.2	**70.2**	86.0	12.0	**7.0**	55.4	70.9	19.7	8.9
$M_{6,2}$	78.1	93.6	**7.6**	**6.1**	68.5	84.8	11.9	7.1	53.9	69.3	19.7	9.1
$M_{6,4}$	79.0	93.7	**7.6**	**6.1**	68.2	84.7	11.9	7.2	56.8	**73.3**	**17.3**	8.7
$M_{7,2}$	76.6	93.4	7.7	6.3	68.0	83.7	12.2	7.2	53.3	66.8	20.9	9.3
$M_{7,4}$	**79.8**	93.6	7.7	**6.1**	68.6	**86.2**	**11.7**	7.2	**56.9**	70.7	19.6	**8.6**

(b) Real SRIRs

Model label	E_1^{Rec}					E_2^{Rec}					E_3^{Rec}					E_4^{Rec}				
	Accuracy (%)			Angular error (°)		Accuracy (%)			Angular error (°)		Accuracy (%)			Angular error (°)		Accuracy (%)			Angular error (°)	
	<10°	<15°	<20°	Mean	Median	<10°	<15°	<20°	Mean	Median	<10°	<15°	<20°	Mean	Median	<10°	<15°	<20°	Mean	Median
Baseline	35.8	50.7	96.6	13.5	14.9	30.5	68.2	91.8	13.9	14.1	29.5	66.9	86.9	14.1	12.7	30.3	56.7	85.6	15.1	14.1
$M_{4,2}$	40.0	51.7	99.2	13.0	13.0	26.9	71.7	91.9	14.0	12.9	36.0	71.2	88.5	13.4	12.0	55.2	73.1	89.9	12.5	8.6
$M_{4,4}$	40.9	50.6	98.8	13.3	13.0	**34.5**	69.7	91.6	13.4	13.0	40.1	70.0	88.4	12.4	11.8	53.9	71.0	91.2	12.2	8.4
$M_{4,8}$	36.4	51.5	91.0	13.5	14.9	29.1	73.3	91.5	14.0	13.0	41.3	72.3	91.7	12.0	11.5	52.2	70.9	90.8	11.9	9.3
$M_{5,2}$	39.2	49.7	99.0	13.5	16.1	27.0	70.1	93.1	13.6	13.6	40.2	72.5	91.7	11.9	11.7	52.0	70.1	91.6	11.8	9.2
$M_{5,4}$	**46.5**	51.2	98.4	**12.4**	**12.0**	32.8	**73.4**	92.5	13.4	**12.5**	45.3	**77.7**	91.3	11.8	**10.8**	56.2	73.6	91.7	11.7	8.1
$M_{6,2}$	35.3	52.5	95.8	13.7	14.5	22.4	67.4	90.4	14.6	13.7	35.8	71.7	90.9	13.7	12.1	49.7	68.1	89.2	12.7	10.1
$M_{6,4}$	23.5	49.4	98.3	14.4	15.8	19.1	66.5	92.4	14.5	13.7	28.7	62.6	88.4	13.7	13.3	38.2	59.8	88.3	13.8	13.6
$M_{7,2}$	32.9	**55.5**	91.6	16.0	13.0	23.2	69.3	91.3	14.7	13.6	35.8	71.0	86.9	15.7	12.2	48.8	69.0	89.3	12.8	10.3
$M_{7,4}$	43.6	49.4	**99.4**	12.7	16.1	32.0	71.5	**93.8**	**13.0**	13.0	**45.6**	75.3	**92.5**	**11.3**	**10.8**	**58.8**	**74.0**	**92.0**	**11.1**	**7.6**

(c) Real recordings

Table 7.3: Accuracy and angular errors of the models with the redesigned feature extraction module and the baseline. Best results are in bold.

7.3.3 Self-attention mechanism

Experiment objective

In the previous experiment, we managed to greatly improve the capability of the CRNN to localize multiple speakers in a multi-channel mixture based on the redesign of the feature extraction module. Now, we focus on the temporal analysis module, which is fed with the reshaped extracted feature as illustrated in Fig. 7.2. In most neural network architectures proposed in the neural-based SSL literature, and particularly in [Per+19], such a temporal analysis module generally relies on recurrent layers, generally implemented with LSTM or GRU units (see Section 3.3). The advantage of such layers is their capacity of processing relatively long sequences and in the case of SSL, they can potentially learn the evolution of a speech sentence characteristics in order to improve the localization performance. However, this comes with the limitation of processing the temporal dimension in a sequential way, while some crucial information for localization likely lie in specific and isolated frames anywhere in the sequence, *e.g.*, frames with transients as pointed out in [Per19]. Another limitation of such recurrent layers, due to their processing following a temporal order, is that it is not possible to parallelize the computation of the output sequence. This computational cost can be an important constraint towards real-time devices.

We therefore propose to replace the BiLSTM layers, as used in the previous experiments and the baseline, with multi-head self-attention encoders introduced in [Vas+17]. In this new experiment, we employ the feature extraction module of the model $M_{6,4}$ [1]. Therefore, the model $M_{6,4}$, which includes recurrent layers (as do all models discussed in the previous sections), is the baseline in this new experiment. As illustrated in Fig. 7.7, the temporal analysis module contains L Transformer encoders, as represented in Fig. 3.11, where L is an hyperparameter in this experiment. In each encoder, we either employ multi-head or cross-multi-head self-attention, with H heads, H being another hyperparameter.

Table 7.4 details the different values of hyperparameters we try in this experiment. We first evaluate the benefit of using classical multi-head self-attention using 1 encoder and H heads, with $H \in \{1, 2, 3, 10\}$. These models are labelled MH-1enc-HH. Then, we compare the use of cross-multi-head self-attention over multi-head self-attention for 1 encoder with $H = 3$ or 10 heads. Finally we assess the addition of another encoder ($L = 2$), first with $H = 10$ to directly compare with $L = 1$, and also with $H = 5$ to compare the performance of 2 encoders with 5 heads against 1 encoder with 10 heads.

Results

The results of this experiment are reported in Table 7.5 and Figures 7.8 and 7.9.

[1] Although the previous section showed that this model does not gives the best results, we chose to base the current study on this model at a time when we did not collected all the evaluation data.

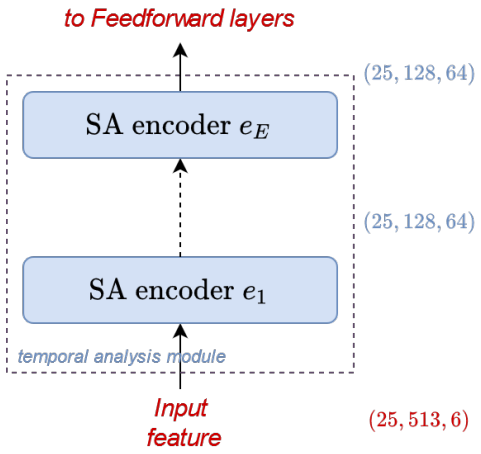

Figure 7.7: Architecture of the temporal analysis module of the proposed CNN including a series of self-attention encoders.

Model label	# parameters	SA type	L	H
$M_{\text{MH-1enc-1H}}$	796 125	MH	1	1
$M_{\text{MH-1enc-2H}}$	862 045	MH	1	2
$M_{\text{MH-1enc-3H}}$	927 965	MH	1	3
$M_{\text{MH-1enc-10H}}$	1 389 405	MH	1	10
$M_{\text{CMH-1enc-3H}}$	927 965	CMH	1	3
$M_{\text{CMH-1enc-10H}}$	1 389 405	CMH	1	10
$M_{\text{CMH-2enc-5H}}$	1 653 341	CMH	2	5
$M_{\text{CMH-2enc-10H}}$	2 312 541	CMH	2	10

Table 7.4: Values of hyperparameters experimented in each encoder of the temporal analysis module using self-attention.

First, we can see that the performance of the self-attention-based neural networks are on par with the CRNN performance, either on simulated data or real recordings. This shows that it is possible to replace the BiLSTM layers with self-attention encoders without losing in performance. Some models leads to a slightly lower performance, while others outperform the baseline. On real recordings, the improvement over the baseline is quite significant, which can be clearly observed in the boxplots in Fig. 7.9. We see that the use of self-attention encoders globally reduces the median angular error, but slightly increase the variance. Moreover, Table 7.6 shows that the inference time of all self-attention-based models is significantly lower than the CRNN baseline, *i.e.*, 44% lower in real-time percentage when using 1 encoder (and 33% lower when using 2 encoders). This inference time does not seem to be correlated to the number of parameters but rather to the number of encoders. This was expected, since such an architecture leads to the processing of each encoder one after another. In contrast, increasing the number of heads does not lengthen the inference time since the matrix operations can be done in parallel in the graphical processing units (GPU) that we use in our experiments.

Second, when assessing the use of different number of heads H with classical MH

Model	1 source				2 sources				3 sources			
	Acc. <10°	Acc. <15°	Mean	Med.	Acc. <10°	Acc. <15°	Mean	Med.	Acc. <10°	Acc. <15°	Mean	Med.
Baseline ($M_{6,4}$)	**98.6**	99.7	**4.4**	**4.1**	88.3	93.3	7.7	**4.7**	74.7	83.4	12.8	5.9
$M_{\text{MH-1enc-1H}}$	98.3	99.7	4.5	4.2	87.9	93.6	7.9	4.9	71.6	81.5	13.5	6.5
$M_{\text{MH-1enc-2H}}$	98.1	99.7	4.7	4.2	87.1	93.0	8.7	4.9	72.2	80.6	15.8	6.2
$M_{\text{MH-1enc-3H}}$	98.1	99.6	4.7	4.2	87.7	92.7	8.8	4.8	72.9	80.7	16.2	6.0
$M_{\text{MH-1enc-10H}}$	98.5	99.6	4.5	**4.1**	**90.4**	94.5	7.4	**4.7**	77.3	84.7	12.3	**5.6**
$M_{\text{CMH-1enc-3H}}$	98.5	**99.8**	**4.4**	**4.1**	89.3	94.1	7.6	4.8	75.9	84.1	12.7	5.9
$M_{\text{CMH-1enc-10H}}$	98.4	99.5	4.5	**4.1**	89.9	94.5	**6.8**	**4.7**	**78.2**	**85.7**	**11.3**	**5.6**
$M_{\text{CMH-2enc-5H}}$	98.5	99.6	4.6	4.2	**90.4**	94.7	7.0	**4.7**	75.6	84.2	12.4	6.0
$M_{\text{CMH-2enc-10H}}$	97.9	99.3	4.8	4.2	88.7	**94.9**	7.3	5.0	72.8	83.7	13.0	6.5

(a) Simulated SRIRs

Model	1 source				2 sources				3 sources			
	Acc. <10°	Acc. <15°	Mean	Med.	Acc. <10°	Acc. <15°	Mean	Med.	Acc. <10°	Acc. <15°	Mean	Med.
Baseline ($M_{6,4}$)	**79.0**	**93.7**	7.6	**6.1**	68.2	84.7	11.9	**7.2**	56.8	73.3	17.3	8.7
$M_{\text{MH-1enc-1H}}$	77.0	93.5	**7.5**	6.2	67.4	83.5	11.5	**7.2**	53.8	69.9	18.9	9.1
$M_{\text{MH-1enc-2H}}$	76.8	93.4	7.6	6.3	67.9	83.8	12.7	7.5	53.6	68.5	22.5	9.1
$M_{\text{MH-1enc-3H}}$	76.2	92.7	8.1	6.3	67.4	84.9	12.3	7.3	54.6	68.3	21.8	9.1
$M_{\text{MH-1enc-10H}}$	77.3	93.0	8.3	6.2	68.2	86.3	11.2	7.3	57.8	74.0	16.9	**8.5**
$M_{\text{CMH-1enc-3H}}$	77.5	92.6	8.0	6.3	68.6	85.6	10.7	7.3	56.4	72.3	18.2	8.9
$M_{\text{CMH-1enc-10H}}$	77.0	92.6	8.0	6.2	68.6	85.8	10.5	7.3	**58.2**	**74.8**	**15.2**	**8.5**
$M_{\text{CMH-2enc-5H}}$	75.7	92.6	8.4	6.3	**70.0**	**87.1**	**10.4**	**7.2**	57.7	74.2	16.3	8.6
$M_{\text{CMH-2enc-10H}}$	75.7	91.1	8.8	6.2	69.0	86.9	10.6	**7.2**	56.3	73.3	17.1	8.9

(b) Real SRIRs

Model label	E_1^{Rec}					E_2^{Rec}					E_3^{Rec}					E_4^{Rec}				
	Accuracy (%)			Angular error (°)		Accuracy (%)			Angular error (°)		Accuracy (%)			Angular error (°)		Accuracy (%)			Angular error (°)	
	<10°	<15°	<20°	Mean	Median	<10°	<15°	<20°	Mean	Median	<10°	<15°	<20°	Mean	Median	<10°	<15°	<20°	Mean	Median
Baseline ($M_{6,4}$)	35.8	50.7	96.6	13.5	14.9	**30.5**	68.2	**91.8**	13.9	14.1	29.5	66.9	86.9	14.1	12.7	30.3	56.7	85.6	15.1	14.1
$M_{\text{MH-1enc-1H}}$	29.3	55.4	96.2	13.4	14.5	27.3	69.9	88.4	**13.7**	**12.9**	42.5	73.2	90.6	12.5	11.3	41.7	64.7	87.7	13.8	12.3
$M_{\text{MH-1enc-2H}}$	33.6	49.3	98.9	13.2	13.7	22.2	59.6	77.1	14.2	13.0	39.8	70.6	**91.4**	**12.1**	11.7	46.6	64.2	85.2	12.4	10.2
$M_{\text{MH-1enc-3H}}$	29.5	**57.7**	98.9	13.2	13.7	19.0	59.2	80.2	14.6	13.7	34.5	69.4	90.6	13.0	12.3	48.8	**67.0**	87.6	**11.7**	9.7
$M_{\text{MH-1enc-10H}}$	37.3	50.1	**99.5**	**12.9**	**11.9**	23.4	66.1	88.0	14.5	13.6	**44.9**	**75.9**	90.9	12.3	**10.9**	**50.9**	66.7	88.2	12.8	**9.6**
$M_{\text{CMH-1enc-3H}}$	**41.7**	51.1	92.9	13.0	14.9	21.3	64.6	86.7	14.6	13.8	38.9	67.4	88.0	12.5	12.2	48.1	66.3	88.8	12.9	10.6
$M_{\text{CMH-1enc-10H}}$	35.2	49.4	98.1	13.5	16.1	25.3	66.8	87.7	13.9	**12.9**	42.2	72.8	89.9	12.3	11.3	48.5	65.6	87.3	13.8	10.4
$M_{\text{CMH-2enc-5H}}$	35.2	49.2	99.3	13.4	16.1	25.2	**70.3**	87.6	15.4	13.0	35.2	63.4	86.9	13.7	12.5	49.6	66.3	87.9	14.0	10.4
$M_{\text{CMH-2enc-10H}}$	39.8	54.6	98.0	13.5	14.2	25.7	68.7	88.0	14.5	13.6	27.2	62.9	86.9	14.7	13.4	39.6	64.6	**90.6**	14.3	13.4

(c) Real recordings

Table 7.5: Accuracy and angular errors of the models with the temporal analysis module based on self-attention and the baseline. Best results are in bold.

self-attention, we see that using self-attention with $H = 1, 2, 3$ heads gives performance that is slightly lower than the baseline. However, the model $M_{\text{MH-1enc-10H}}$, with $H = 10$ heads, is more accurate than the baseline. This improvement is also more pronounced when there are many speakers in the analyzed signal. For instance, on 3-speaker mixtures with synthetic SRIRs, the accuracy ($< 10°$) for this model is 77.3% while it is 74.7% for the baseline. Increasing the number of self-attention heads may thus be beneficial for multi-source localization. We postulate that this is due to multiple "views" of the same input sequence, *i.e.*, the diversity provided by multiple self-attention heads.

Next, when we compare the performance for multi-head against cross-multi-head self-attention, we see that CMH leads to better results than MH, and even better results than the baseline. For example, the mean average error on 3-speaker signals with simulated SRIRs is lowered by 3.5° when using CMH with $H = 3$ heads, and by 1.0° with $H = 10$. The same gain in performance can be observed on mixtures generated with real SRIRs: on 2-speaker signals, the CMH-based model with 10 heads leads to a mean average error of 10.5° vs. 11.2° for the MH-based model, whereas for

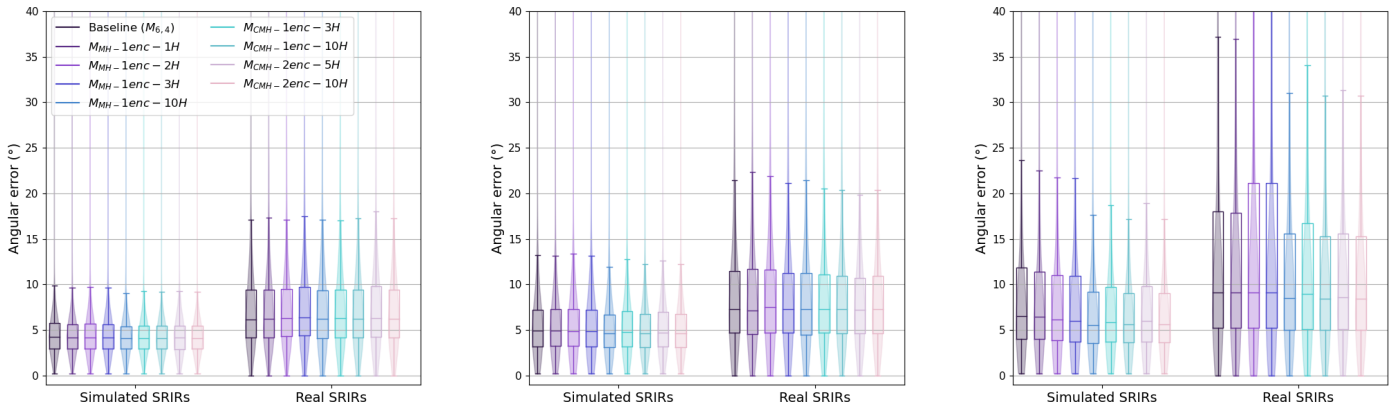

(a) 1-speaker signals **(b)** 2-speaker signals **(c)** 3-speaker signals

Figure 7.8: Distribution of the angular errors of the models with the temporal analysis module based on self-attention and the baseline, evaluated on the test datasets E_1^{Sim}, E_2^{Sim}, E_3^{Sim}, E_1^{Real}, E_2^{Real} and E_3^{Real}.

Model	real-time %	# parameters
Baseline ($M_{6,4}$)	437	913,907
$M_{\text{MH-1enc-1H}}$	244	796,125
$M_{\text{MH-1enc-2H}}$	244	862,045
$M_{\text{MH-1enc-3H}}$	244	927,965
$M_{\text{MH-1enc-10H}}$	244	1,389,405
$M_{\text{CMH-1enc-3H}}$	244	927,965
$M_{\text{CMH-1enc-10H}}$	244	1,389,405
$M_{\text{CMH-2enc-5H}}$	281	1,653,341
$M_{\text{CMH-2enc-10H}}$	281	2,312,541

Table 7.6: Real-time percentage for inference and number of parameters for the different tested models (in our experiments, frame length = 0.032 s).

3-speaker mixtures it is lower by 1.7°. Regarding real recordings, the superiority of CMH over MH is less visible, especially because the model $M_{\text{MH-1enc-10H}}$ is one of the best performing models on real data.

Furthermore, the results when adding another self-attention encoder to the temporal analysis module are less conclusive. Model $M_{\text{CMH-2enc-5H}}$, which uses 5 heads, is better than Model $M_{\text{CMH-2enc-10H}}$ with 10 heads for 2-speaker mixtures, but it loses performance for 3-speaker mixtures. Also the first one shows a better performance on real recordings with mobile sources but has worse results when the sources are static. When comparing the use of 1 and 2 encoders with $H = 10$ heads, the results are slightly lower for Model $M_{\text{CMH-2enc-10H}}$. This shows that stacking more encoders does not necessarily improve the performance. However, we believe that further experiments are needed for a more convincing conclusion.

To conclude this experiment, we show that it is possible to replace BiLSTM layers

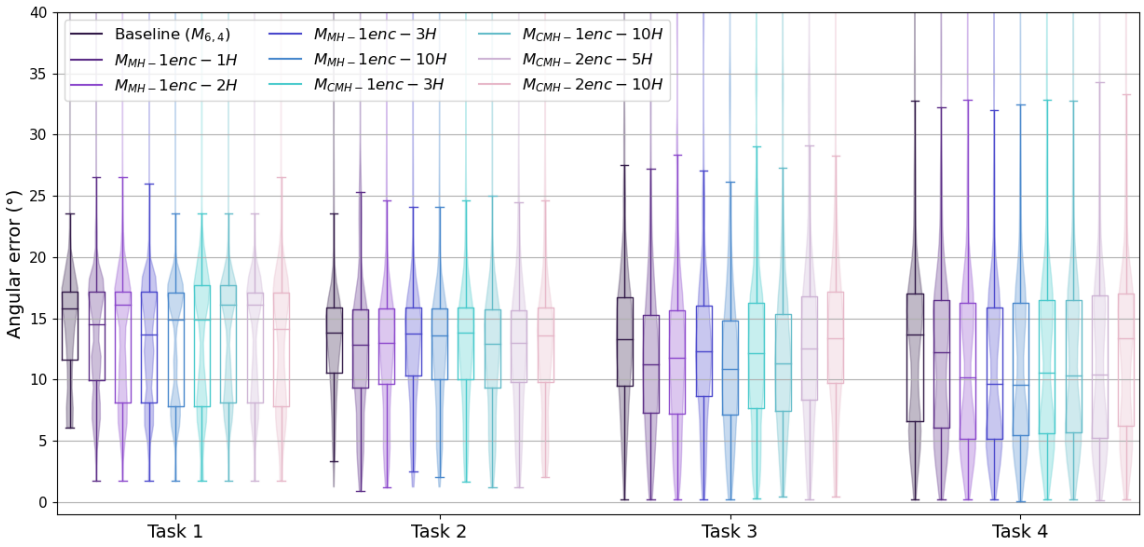

Figure 7.9: Distribution of the angular errors of the models with the temporal analysis module based on self-attention and the baseline, evaluated on the test datasets E_1^{Rec}, E_2^{Rec}, E_3^{Rec} and E_4^{Rec}.

with self-attention encoders without losing in performance, which can greatly decrease the network inference time. We see that using more attention heads seems to increase the localization accuracy, but stacking encoders does not necessarily have the same effect. However, we manage to improve the overall performance using cross-multi-head self-attention, which is especially pronounced in a multi-speaker context.

7.3.4 HO-PIV *v.s.* FO-PIV

Experiment objective

In this last experiment, we propose to evaluate the use of higher-order Ambisonics for the input signal. With higher Ambisonics orders, the spatial resolution is increased and therefore it provides a suitable representation, especially when the sources are spatially close to each other [ZF19]. With this property, one can expect to improve the overall localization performance. For that matter, we use the extension of the normalized pseudointensity vector to the higher-order Ambisonics, namely the HO-PIV $\bar{\mathbf{I}}^N$, as presented in Section 2.4.1. For practical reasons, this experiment is more limited than the previous ones in terms of data. First, we only assess the use of HO-PIV at order $N = 2$, *i.e.*, with 9 Ambisonics channels, leading to input tensors of shape $25 \times 513 \times 16$ since we still stack the real and imaginary parts in the third dimension. Also, we limit the training data to T_3 only (*i.e.*, we work with 3-speaker mixtures) since this proved to be also quite robust on 1- and 2-speaker signals.[2]

[2]To give some insights, each dataset T_n with FO-PIV is about 80 GB big, resulting in a total of 240 GB of training data. Such data quantity reaches $240 \times \frac{16}{6} = 640$ GB at order 2 and $240 \times \frac{30}{6} = 1\,200$ GB at order 3. The time necessary to process such an amount of data is prohibitively long.

Model label	E_1^{Sim}				E_2^{Sim}				E_3^{Sim}			
	Accuracy (%)		Angular error (°)		Accuracy (%)		Angular error (°)		Accuracy (%)		Angular error (°)	
	<10°	<15°	Mean	Median	<10°	<15°	Mean	Median	<10°	<15°	Mean	Median
$M_{6,4}$	95.3	99.1	5.2	4.7	85.3	92.9	9.0	5.3	71.0	81.5	14.6	6.2
$M_{6,4}^{HO}$	**98.8**	**99.7**	**4.5**	**4.2**	**91.5**	**95.0**	**7.2**	**4.5**	**82.4**	**87.3**	**11.6**	**4.8**

(a) Simulated SRIRs

Model label	E_1^{Real}				E_2^{Real}				E_3^{Real}			
	Accuracy (%)		Angular error (°)		Accuracy (%)		Angular error (°)		Accuracy (%)		Angular error (°)	
	<10°	<15°	Mean	Median	<10°	<15°	Mean	Median	<10°	<15°	Mean	Median
$M_{6,4}$	74.3	92.4	8.0	7.0	61.5	80.3	16.0	8.3	48.9	66.2	22.9	10.1
$M_{6,4}^{HO}$	**76.1**	**93.5**	**7.9**	**6.3**	**67.1**	**84.6**	**13.4**	**7.3**	**56.2**	**72.4**	**20.0**	**9.0**

(b) Real SRIRs

Model label	E_1^{Rec}					E_2^{Rec}					E_3^{Rec}					E_4^{Rec}				
	Accuracy (%)			Angular error (°)		Accuracy (%)			Angular error (°)		Accuracy (%)			Angular error (°)		Accuracy (%)			Angular error (°)	
	<10°	<15°	<20°	Mean	Median	<10°	<15°	<20°	Mean	Median	<10°	<15°	<20°	Mean	Median	<10°	<15°	<20°	Mean	Median
Baseline (TRAMP)	**39.9**	**58.3**	**99.8**	12.5	**13.0**	31.4	57.6	69.4	**13.4**	**10.5**	35.7	70.2	87.0	12.4	12.1	29.1	50.1	70.6	16.3	14.1
Baseline ($M_{6,4}$)	39.8	49.9	99.5	**12.2**	16.1	**32.2**	70.3	88.3	13.9	12.2	**45.6**	**74.3**	**92.4**	**10.9**	**11.1**	**44.1**	**63.6**	**88.0**	**13.8**	**12.1**
$M_{6,4}^{HO}$	34.5	55.8	91.4	15.0	**13.0**	22.5	**73.1**	**94.8**	16.5	13.9	24.6	61.4	83.0	15.8	13.5	31.3	60.0	86.7	16.7	14.0

(c) Real recordings

Table 7.7: Accuracy and angular errors of the model with HOA features and the baseline with FOA features. Best results are in bold.

As previously, we use odel $M_{6,4}$ trained with FO-PIV input feature as the baseline in this experiment. We then train the exact same neural network with HO-PIV input features as described above, leading to a model labelled $M_{6,4}^{HO}$. As we showed in the first experiment that limiting the training on 3-speaker signals still gives satisfying results on 1- and 2-speaker mixtures, we evaluate this model on all testing datasets.

Results

The results of this experiment are reported in Table 7.7 and Fig. 7.10 and 7.11. We can see that the model using HOA features surpasses the baseline with FOA features on the simulated datasets, however on real recordings the improvement is not conclusive. On the datasets E_j^{Sim} and E_j^{Real}, the improvement is quite significant: the accuracy ($< 10°$) is increased from 95.3% (FOA features) to 98.8% (HOA features) on E_1^{Sim}, from 85.3% to 91.5% on E_2^{Sim} and from 71.0% to 82.4% on E_3^{Sim}. On the datasets with real SRIRs, the improvement is similar (with all scores that are of course worse than on simulated data). We also observe that the gain in accuracy is better when there are more speakers, partly because the performance was already very high on 1-speaker signals and quite good on 2-speaker signals, but surely thanks to the better spatial resolution granted by the use of a HOA representation. This should give the network more information to better spatially separate the sources, therefore the benefit is emphasized when more sources are active. On real recordings, it is more difficult to assess the superiority of the HOA model. First, we see that the DNN-free baseline is better on E_1^{Rec}, which is not surprising since it is known to be performant on single-speaker signals. We observe a small improvement of the HOA model over the

Since we do not want to decrease the number of room configurations in the training dataset, we limit the training to the dataset T_3 with HO-PIV at order 2.

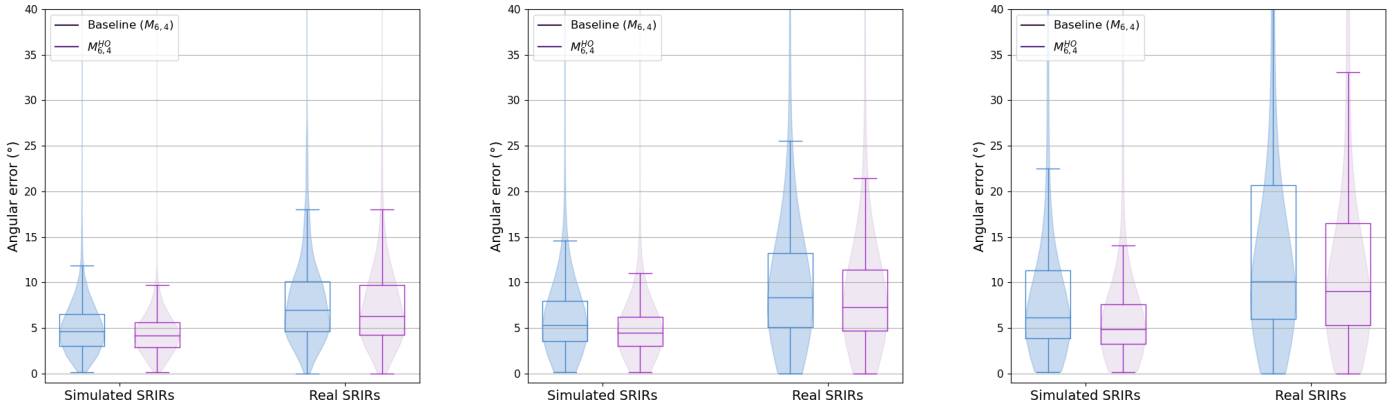

(a) 1-speaker signals **(b)** 2-speaker signals **(c)** 3-speaker signals

Figure 7.10: Distribution of the angular error of the model with HOA features and the baseline with FOA features, evaluated on the test datasets E_1^{Sim}, E_2^{Sim}, E_3^{Sim}, E_1^{Real}, E_2^{Real} and E_3^{Real}.

Scenario	E_1^{Sim}				E_2^{Sim}				E_3^{Sim}			
	Accuracy (%)		Angular error (°)		Accuracy (%)		Angular error (°)		Accuracy (%)		Angular error (°)	
	<10°	<15°	Mean	Median	<10°	<15°	Mean	Median	<10°	<15°	Mean	Median
FOA components only	6.4	13.6	50.9	36.0	6.2	13.1	49.7	38.2	6.1	12.3	49.2	38.8
HOA components only	40.8	48.5	87.8	18.8	31.7	41.5	57.9	36.7	27.0	36.8	52.0	34.8

(a) Simulated SRIRs

Scenario	E_1^{Real}				E_2^{Real}				E_3^{Real}			
	Accuracy (%)		Angular error (°)		Accuracy (%)		Angular error (°)		Accuracy (%)		Angular error (°)	
	<10°	<15°	Mean	Median	<10°	<15°	Mean	Median	<10°	<15°	Mean	Median
FOA components only	4.5	15.3	51.9	34.8	5.3	12.9	50.6	38.8	5.6	12.2	51.3	39.5
HOA components only	31.6	43.8	86.3	33.4	25.3	36.0	63.6	41.8	23.2	33.8	58.1	43.1

(b) Real SRIRs

Table 7.8: Accuracy and angular errors of the HOA model evaluated on signals with FOA components only and HOA components only

FOA model on the dataset E_2^{Rec}, with an accuracy of 73.1% against 70.3%, although the mean and median angular errors are higher. however, on the other multi-speaker dataset E_4^{Rec}, the HOA network shows worse results worse than the DL-based baseline.

Fig. 7.12 shows an example of the outputs of the deep-learning-free baseline and the HO model $M_{6,4}^{HO}$ for one sequence of the test set E_2^{Rec}. We see that the baseline method leads to more scattered peaks than the neural network model, which could be detrimental to the localization performance if the sources are too close from each other. We notice that the network model outputs much more sparse values, however we notice a sort of ghost source, around $\theta = -100$ and $\phi = -40$, whose presence leads us to think that training the network only on T_3 forces it to output 3 prominent peaks.

For further analysis, we evaluate the model $M_{6,4}^{HO}$ on the test datasets for two additional configurations: when only the FOA components of the HO-PIV are kept, *i.e.*, the other channels are forced to zero values, and when only the HOA components

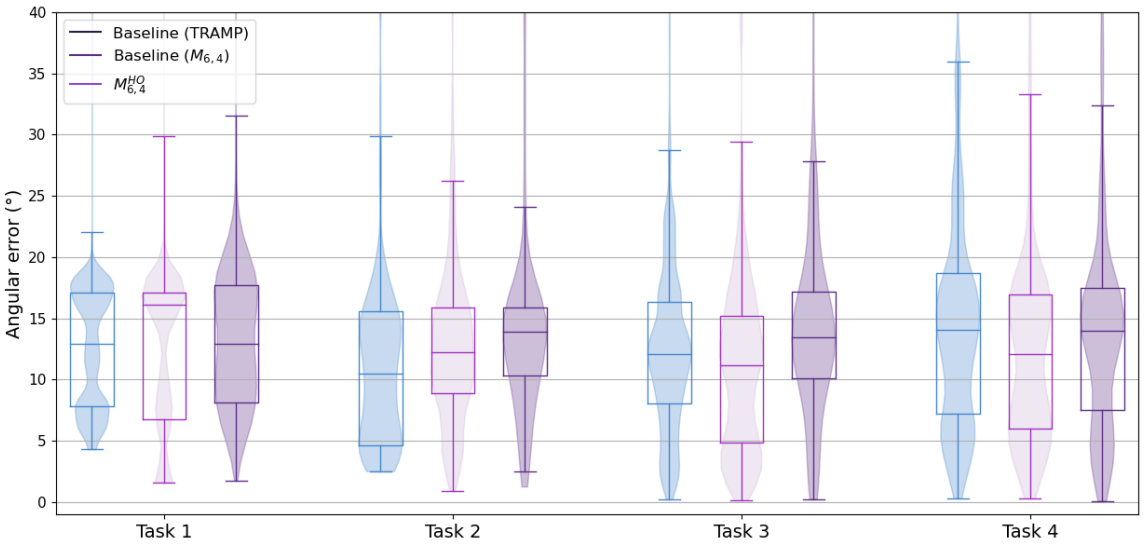

Figure 7.11: Distribution of the angular error of the model with HOA features and the baseline with FOA features, evaluated on the test datasets E_1^{Rec}, E_2^{Rec}, E_3^{Rec} and E_4^{Rec}.

(order 2 in our case) are kept, *i.e.*, the FOA channels are forced to zero values. The motivation for these experiments is to gain some insight in the way the network is using the Ambisonic features. Indeed, under certain hypothesis, the components of orders 1 and 2 can be used independently from one another to obtain an analytic DoA estimate. The very low results in the first row of Table 7.8 first show that the network is not capable of relying only on FOA components when it has been trained with HOA features. This underlines that network characteristics of processing the features in its own specific manner to perform the learnt task. Moreover, we see that the results on the test datasets using only the HOA components are not as low as with FOA components only, it seems that the network finds more useful information in the components of order 2, than the FOA components. However, since the performance is much worse than when using all components, it is evident that the network has learnt how to efficiently combine features of all orders to perform the DoA estimation. This impressive combination capacity, which is not easily feasible analytically, underlines the general *black box* characteristics of the neural networks, which we still have difficulties to fully understand today.

7.4 Conclusion and perspectives

In this chapter, we addressed source localization when several speakers overlap in a noisy and reverberant mixture, and with the assumption of a known NoS. Based on the CRNN model proposed in [Per+19], we first questioned the optimal order in which we need to present the training examples to the network, which are made of 1-, 2-

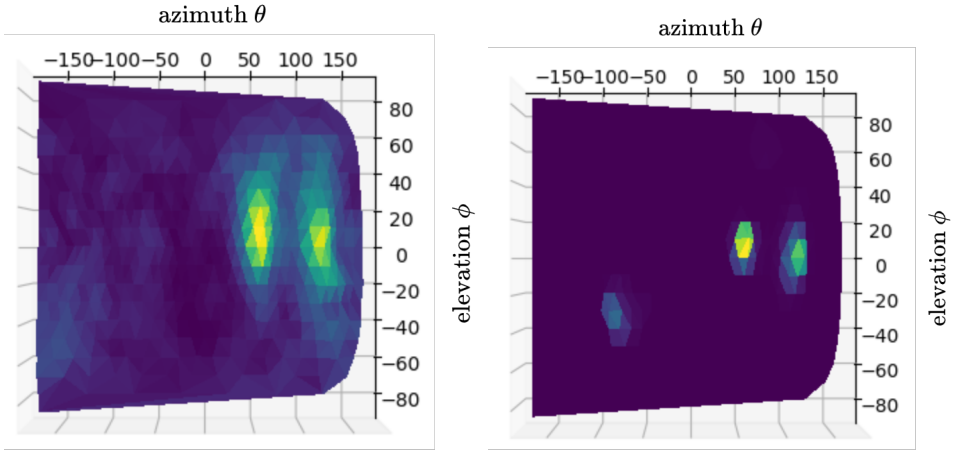

(a) TRAMP output **(b)** $M_{6,4}^{HO}$ output

Figure 7.12: Output DoA probability distributions of the TRAMP baseline (left) and the HOA network (right) on a sequence of the dataset E_2^{Rec}. Low values are represented with blue colors and high values with yellow colors.

and 3-speaker signals, to obtain the best performance. We found out that relying only on signals with 3 speakers makes the network robust enough to perform well on mixtures with 1 and 2 speakers, whereas – not surprisingly – it is not capable of performing multi-speaker localization when trained only on 1-speaker signals. Also, we understood that pretraining a localization network, followed by fine-tuning manner, *i.e.*, with 1-speaker signals first, then with 2-speaker signals and finally with 3-speaker signals, is not the best training scheme. We concluded that a good choice is to feed all examples randomly during the training phase, as it is done in most neural-based SSL systems.

Next, we proposed a redesign of the feature extraction module, made of convolutional and max-pooling layers, in an attempt to improve the multi-source localization performance of the baseline CRNN [Per+19]. To give the network more capacity to extract its own meaningful features, we employed more convolutional layers and less aggressive max-pooling, leading to significantly more layers in total. We tried many models for a large set of hyperparameter values, and the results showed a significant improvement for all these models over the baseline, especially on mixtures with multiple speakers.

Then, we focused on replacing the recurrent layers usually employed in localization CRNNs with multi-head self-attention mechanism. The motivation was to dispose of recurrent layers, which are not parallelizable (and thus, *e.g.*, limit the use of neural networks on embedded devices), as well as providing more flexibility in the temporal analysis with the self-attention mechanism. Using classical MHSA encoders, we managed to reach a similar localization performance as the CRNN baseline, with an inference time reduced by 44%. Furthermore, we improved the localization accuracy, especially in a multi-speaker context, by proposing a more general way of using several

heads in the self-attention encoder.

Finally, we assessed the benefit of using a HO-PIV as an input feature for a CRNN. We obtained a substantial improvement on simulated datasets over the use of FO-PIV features, which was actually expected. However, on real recordings this improvement has not been observed, for reasons we do not understand. We also showed that such a network needs to use the components of all orders to successfully perform localization.

While significant improvements have been made over the baseline CRNN with the redesign of several neural modules, many aspects have not been treated in this research. First, the lack of in-depth analysis of our contributions makes it difficult to fully understand the obtained results. Regarding the new feature extraction module, although we intuit that more layers implies more network flexibility, it would be insightful to apply visualization techniques to interpret the behavior of convolutional layers. Among the available techniques to interpret the network computation, we can think of visualizing convolutional filter responses [Cho17, p 167], intermediate feature maps [Cho17, p. 160] or using more advanced methods such as layer-wise propagation [Bac+15] as employed in [Per19]. In the same vein, analyzing the conduct of the self-attention mechanism and comparing it to the BiLSTM layers could give interesting insights on how the network processes a sequence in the temporal analysis module. Regarding these self-attention layers, it would also be interesting to apply these mechanisms in the frequency dimension, with the intuition that the attention heads could focus on the relation between specific frequency bins which contains the information of a specific speaker. This might gives more flexibility to the neural network to discriminate the different speakers using their spectral characteristics. Moreover, our last experiment on HOA features could be carried on by first including all training data as done in the other methods, which would probably lead to better results not only on simulated data and but also on real recordings. Also, increasing the Ambisonics order, higher than 2 as experimented here, should lead to an improvement in the localization performance, at the cost of much more data. Relying on a training dataset with directive sources could also be of interest [Gel+21]. Again, an analysis on the network process over HO-PIV features could be very interesting, since it seems that the network has learnt some specific way of exploiting the first and second order features, different from analytical approaches. Finally, an idea we did not have time to experiment with is to think of a loss function which incorporates the NoS, as it is supposed to be known in these methods, in order to encourage the network to estimate the right number of DoAs. Practically, this could be done by forcing the network to output a spatial spectrum with the right number of peaks by penalizing it when additional high peaks are present in the output. This last idea is a first step towards combining speaker counting and localization, which brings us to the next chapter, which deals with this topic.

Chapter 8

Hybrid methods for speaker counting and localization

In Chapters 6 and 7, the number of speakers in the test mixtures was supposed to be known. This is also the case in most neural-based SSL systems presented in the literature, as explained in Section 4.2.2. When estimating the speakers DoA with a classification paradigm, we knew the exact number of peaks to extract at the output of the neural network, which allowed us to solely focus on the localization performance. However, in real-life scenarii, the number of sources is unknown, and practical methods must include a speaker counting system beforehand to extract the right number of peaks, or must apply a thresholding method to the peak distribution.

In this chapter, we explore several methods to circumvent the strong assumption of the known NoS, using the results of our studies on speaker counting presented in Chapter 5. The outline of this chapter differs from the previous ones in which all experiments were grouped in the same section because of their common methodology. Here, the explored solutions are relatively different from each other, therefore each section of this chapter is dedicated to one considered method. In the first section, we assess the benefit of using our speaker counting network to estimate the NoS before localization and employ it to extract the right number of DoAs. We compare this method to the application of a classical thresholding method, and to the use of the ground-truth NoS to evaluate its robustness. In the second section, we investigate the contribution of the NoS as an additional input feature to a localization network to figure out if it can make use of this supplementary piece of information. Finally, in the last section, we study the possibility of jointly estimating the NoS and the DoAs in the same multi-task network.

8.1 NoS estimation for speaker localization

As explained above, usual methods to estimate the DoA of several sources are based on the assumption of a known NoS, or sometimes employ a thresholding method when a classification paradigm is used. In this section, we propose to circumvent these limitations by estimating the NoS using our counting system presented in Chapter 5, before estimating the speakers location with the localization network.

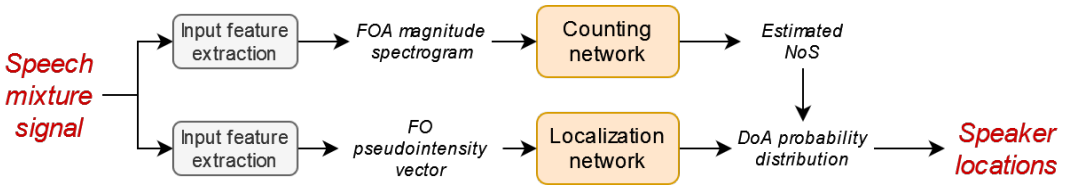

Figure 8.1: Processing pipeline of an SSL system using the estimated NoS of a counting network.

8.1.1 Method

System pipeline

The processing pipeline of the proposed system is illustrated in Fig. 8.1. An input speech mixture is first transformed into the input features of the counting and localization networks; that is, the FOA magnitude spectrograms and the FO-PIV, respectively. Then each network processes its respective input feature to generate the output: a NoS probability distribution from the counting network, and a DoA probability distribution from the localization network. The estimated NoS is first obtained as the class with the highest probability of the counting network output, as in Chapter 5. This estimated NoS then determines the number of peaks to extract from the localization network DoA distribution output. Note that for the evaluation of the system, the estimated DoAs are associated with the ground-truth labels using the Hungarian algorithm [Kuh55], as already done in Section 7.1.2.

Counting and localization networks

The counting network adopted in this experiment is the same as in Chapter 5, with $T = 20$, $K = 3$ and using the optimal frame position as derived in Section 5.3.3 to maximize the counting accuracy. However, we retrain this network for a maximum number of sources $J = 3$. The first reason for choosing this setting here is that we localize at most 3 speakers simultaneously. We thus retrain the network to include the 3-source constraint, as we conjecture that it would perform better than the 5-source variant. The second reason is to provide a fair comparison of detection and counting metrics with the multi-task networks described in the last section of this chapter.

For the localization network, we use Model $M_{5,2}$ detailed in Section 7.3.2.[1] We recall that this model is composed a feature extraction module made of 5 convolutional blocks, then 2 BiLSTM layers followed by 2 feedforward layers.

[1]We use here Model $M_{5,2}$ instead of $M_{6,4}$ as in the previous chapter because the experiments on the feature extraction module were not concluded yet at the time of the study presented in the present chapter.

8.1.2 Experimental protocol

Training and testing data

As we consider here speaker counting in addition to localization, we employ a training dataset that is similar to the one described in Section 5.2.3. The generated signals are 15-s long reverberant and noisy conversation-like mixtures, with a varying number of speakers. We limit the maximum number of speakers to 3 (instead of 5 in Chapter 5) to be consistent with the previous chapter on multi-speaker localization. Simulated SRIRs are used to create the mixtures, along with TIMIT [Gar+93] excerpts.

We evaluate our model on generated test sets that are similar to the ones described in Section 5.2.4 (*i.e.*, with simulated SRIRs and real SRIRs, and up to 3 simultaneous speakers).

Baselines

To assess the interest of using the estimated NoS provided by the counting network, we compare it with the use of the ground-truth NoS (referred as the *oracle* method) and the NoS estimated using a thresholding method (we test several threshold values $\beta = 0.1, 0.2, 0.5$). To do that, we simply replace the estimated NoS from the counting network with the other considered NoS estimates.

Metrics

To measure the performance of the proposed joint speaker counting and localization system, we calculate counting, detection and localization metrics. Regarding counting metrics, we compute the accuracy A_{ij} and the mean absolute error M_i, as in Chapter 5. We also consider the detection precision, which is defined as the ratio between the number of true positives (*i.e.*, estimated DoAs actually corresponding to a source) and the number of estimated DoAs, and the detection recall, which is defined as the ratio between the number of true positives and the number of sources to be localized. For the localization metrics, we consider only the true positives, *i.e.*, the DoA estimations actually assigned to one label, and we calculate the localization accuracy (for angular error tolerance of 10° and 15°) and the mean and median angular errors, as in Chapters 6 and 7.

8.1.3 Results

The counting metrics are showed in Table 8.1 and displayed in Fig. 8.2 and 8.3 as confusion matrices and M_i bar charts, respectively. The prediction precision and recall are shown in Fig. 8.4. Note that these metrics are not provided for the oracle method since they are all maximal. Table 8.2 presents the localization results (again, only for correctly detected sources).

When we look at the counting metrics, we can see the benefit of using a neural-based counting system over the traditional thresholding method. In the detection

Counting method	Simulated SRIRs				Real SRIRs			
	Detection		Counting		Detection		Counting	
	Prec.	Rec.	Acc. (%)	Mean abs. error	Prec.	Rec.	Acc. (%)	Mean abs. error
Network	0.96	**0.92**	**82.5**	**0.2**	0.96	**0.82**	70.3	**0.3**
Thres. ($\beta = 0.1$)	0.96	0.83	74.1	0.3	0.95	0.81	**70.6**	**0.3**
Thres. ($\beta = 0.2$)	0.98	0.75	68.2	0.4	0.97	0.71	64.3	0.5
Thres. ($\beta = 0.5$)	**0.99**	0.55	55.1	0.7	**0.99**	0.47	47.9	0.8

Table 8.1: Detection and counting results of the counting network and the thresholding methods on test datasets with simulated and real SRIRs. Best results are in bold.

Counting method	Simulated SRIRs				Real SRIRs			
	Accuracy (%)		Angular error (°)		Accuracy (%)		Angular error (°)	
	<10°	<15°	Mean	Median	<10°	<15°	Mean	Median
Oracle	75.2	81.5	15.5	5.2	56.2	72.9	18.3	9.3
Neural network	78.7	84.8	12.9	5.1	62.8	81.1	13.2	8.8
Threshold ($\beta = 0.1$)	86.2	92.1	8.4	4.5	66.2	85.2	10.5	8.4
Threshold ($\beta = 0.2$)	88.9	94.0	7.4	4.2	68.6	87.3	10.0	8.2
Threshold ($\beta = 0.5$)	**93.3**	**96.4**	**6.0**	**3.9**	**72.9**	**90.0**	**9.2**	**7.9**

Table 8.2: Localization accuracy and angular errors for several counting methods. Best results are in bold.

and counting results of Table 8.1, we can first observe the quite high performance of the counting network on the dataset with simulated SRIRs, with at least 0.90 of detection precision and recall and a mean absolute error of 0.2 only. On the dataset with real SRIRs, the results are less favorable, especially regarding the detection recall with reaches 0.82 and the counting accuracy which is 70.3%, emphasizing that in real conditions the counting network sometimes underestimates the NoS, thus missing to localize occasional speakers. Regarding the detailed counting metrics in Fig. 8.2 while the accuracy for classifying no-speech frames is almost perfect for all counting methods (*i.e.*, with more than 95% accuracy), for speech frames the counting network clearly allows for a better speaker counting performance. On the dataset with simulated SRIRs, 75.8% of the 2-speaker frames are correctly classified by the counting network where using a thresholding method leads to an accuracy of about 62%; for 3-speaker frames, the accuracy reaches more than 55% for the neural network against only 27.5% using a threshold. We observe the same tendencies on the dataset with real SRIRs, except that the thresholding method with $\beta = 0.1$ is slightly more accurate than the neural-based system for 1- and 3-speaker mixtures. The mean absolute error M_i for every NoS is always lower for the network model than for the other methods. For instance, the M_i for the counting network are lower than 0.5 on signals with simulated SRIRs, meaning that the error committed by the network quite never exceeds 1 source (confirmed by the confusion matrices). Thresholding methods are less precise, especially when facing numerous simultaneous sources: for instance, M_3 for $\beta = 1$ almost reaches 1. On signals with real SRIRs, the mean absolute error for the thresholding method with β is closer to that of the neural network, but it is still slightly higher. A reason why the thresholding method leads to close performance to the network's one could be because the localization network (on the output of which

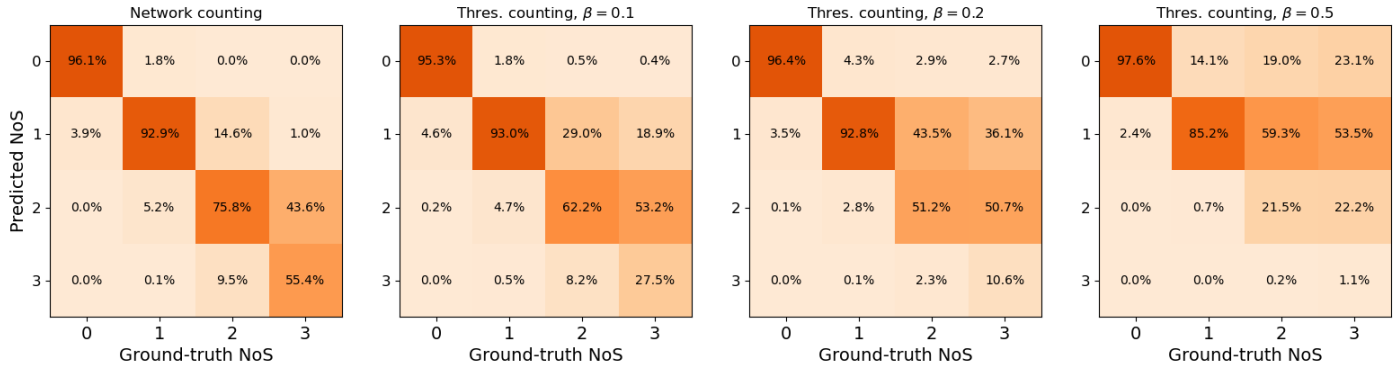

(a) Simulated SRIRs

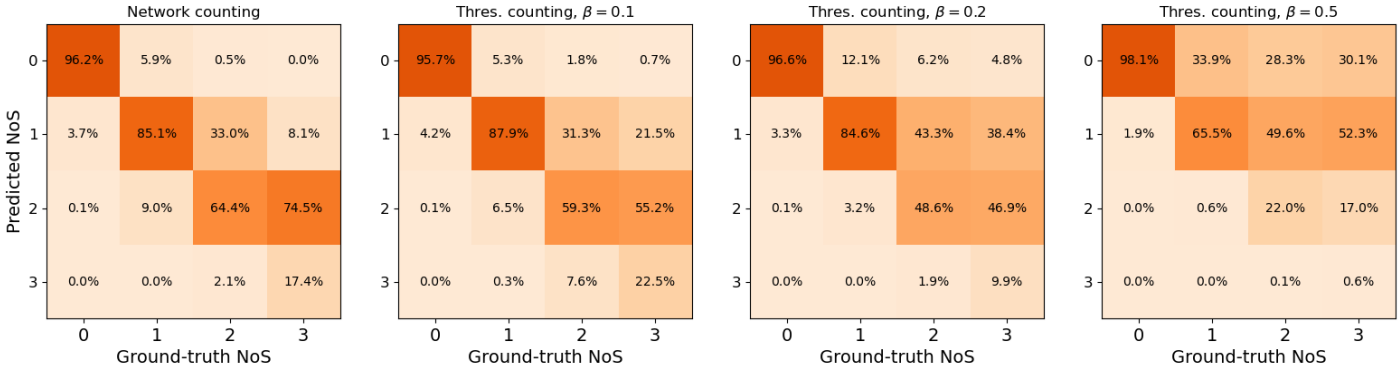

(b) Real SRIRs

Figure 8.2: Confusion matrices of the accuracy A_{ij} for several counting methods: a neural network counting method and a thresholding method for several values of the threshold β.

the thresholding method is applied) is more robust on signals with real SRIRs than the counting network.

The detection metrics in Fig. 8.11 confirm the advantage of using a neural network for speaker counting. The detection recall of the network on both test datasets clearly surpasses that of all thresholding methods, while the precisions are about the same. By using a counting network, we miss only 10% and 20% of the sources, for the datasets with simulated and real SRIRs, respectively, while for the thresholding methods almost 20% of the sources are missed on signals with simulated SRIRs for $\beta = 0.1$, and we even miss more half of the speakers for real SRIRs when $\beta = 0.5$. This highlights the fact that the thresholding methods often fail to detect some sources due to occasional too small peaks in the localization network output, even if the consecutive precision is almost perfect.

Finally, let us take a look at the localization metrics in Table 8.6 and Fig. 8.12 while recalling that they are calculated by taking into account only the true positives. The thresholding method with the highest threshold value leads to the best localization metrics, but this is obtained at the cost of not detecting a lot of sources that are more difficult to localize, as shown by the detection results. On the contrary, we see that using the counting network allows to correctly detect sources that are not well localized, which leads to a two-digit mean angular error, whereas it remains under

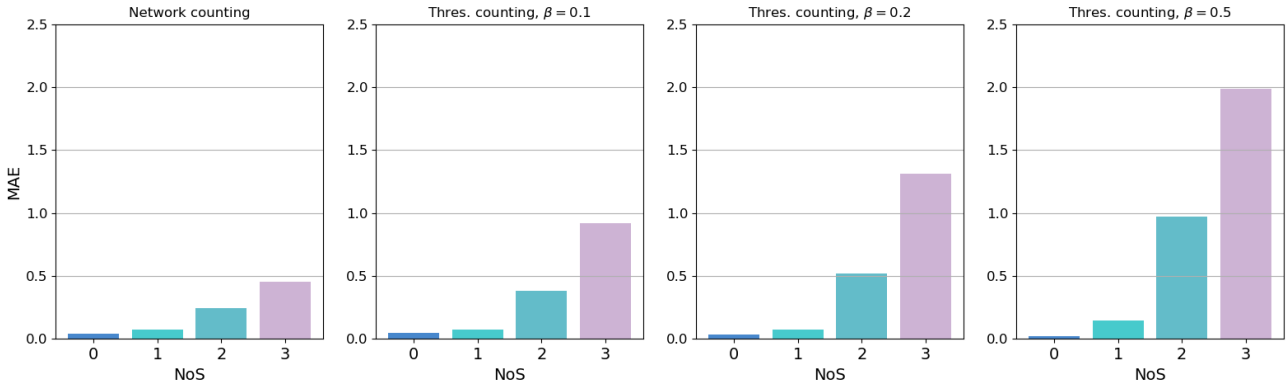

(a) Simulated SRIRs

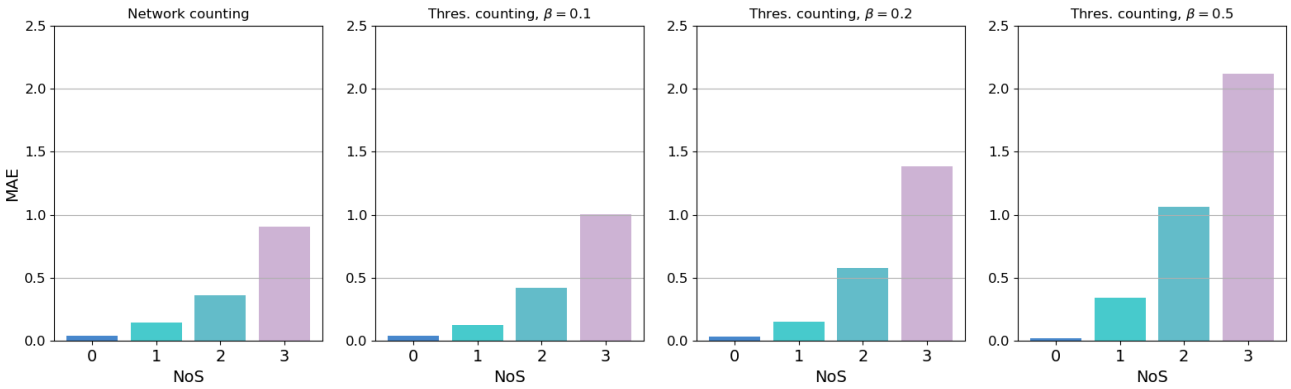

(b) Real SRIRs

Figure 8.3: Mean absolute errors M_i for several counting methods: a neural network counting method and a thresholding method for several values of the threshold β.

10° with thresholding methods. The localization results with the counting network are relatively close to those using the ground-truth NoS, which are, by definition, optimal with respect to the source detection.

To conclude this study, the results show that using our speaker counting neural network allows to relax the strong assumption of knowing the NoS in advance. This counting network provides fairly accurate NoS estimations that can be used to localize speakers. This method has shown better detection performance over a thresholding method, which often leads to missing sources. Moreover, it can be observed that the localization performance using a speaker counting network closely approaches the one using the ground-truth NoS.

8.2 NoS injection in a localization neural network

8.2.1 Method

In this section, we present a series of experiments in which we attempt to improve the localization network by injecting the NoS as an additional input information. The goal is to provide the network with an additional information hoping that it can improve

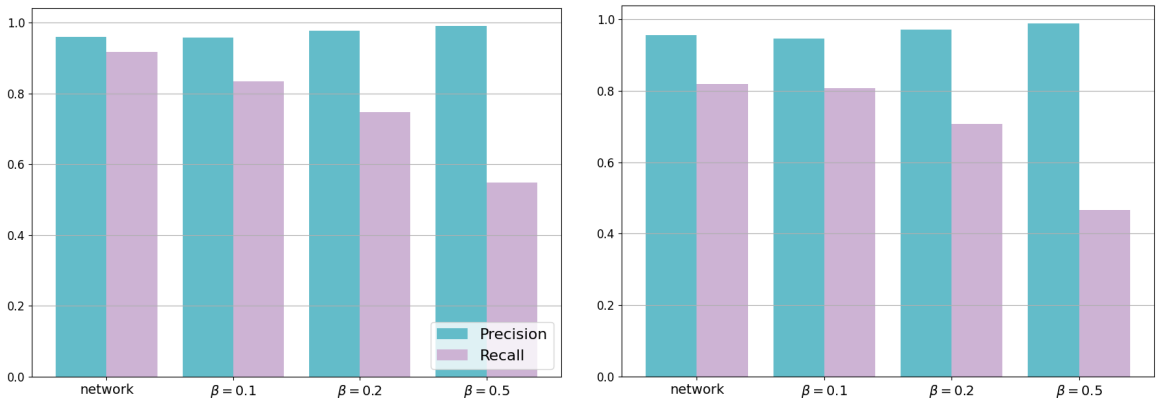

(a) Simulated SRIRs **(b)** Real SRIRs

Figure 8.4: Detection precision and recall for several counting methods: a neural network counting method and a thresholding method for several thresholds β.

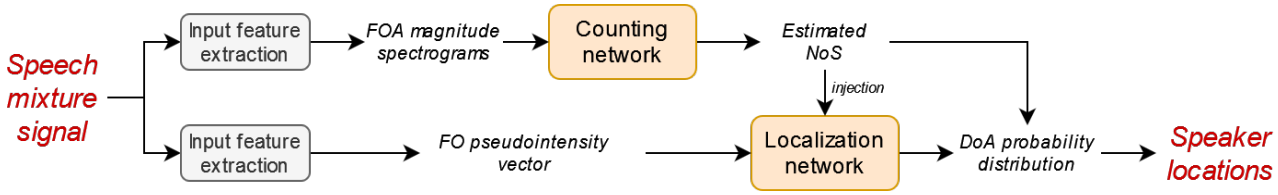

Figure 8.5: Processing pipeline of a localization system with NoS injection.

the localization performance, with the intuition that it could help the network to output a cleaner DoA peak distribution.

The proposed localization system with NoS injection is illustrated in Fig. 8.5. The NoS is injected as an input feature into the localization network, in addition to the FO-PIV features. At this stage, we name it the *injection NoS*. The NoS is also used further for peak-picking on the localization network output. We refer to this second use of the NoS as the *prediction NoS*. The need for a distinction between the injection NoS and the prediction NoS will be made clear in the following.

We propose and test different ways to inject the NoS into the localization network, as illustrated in Fig. 8.6 and commented below. As in the previous section, we opt for base model $M_{5,2}$ as proposed in Section 7.3.2. Note that, unlike in Chapter 6 and 7, here we do not average the DoA distribution over all frames of a sequence in the network output. Instead, we go back to a frame-wise prediction to demonstrate the usefulness of the counting DNN at high temporal resolution. Throughout several experiments, we try injecting the NoS in several positions in the neural network:

- alongside the input features;
- after the feature extraction (and reshape) module;
- after the temporal analysis module;
- both after the feature extraction module and after the temporal analysis module;

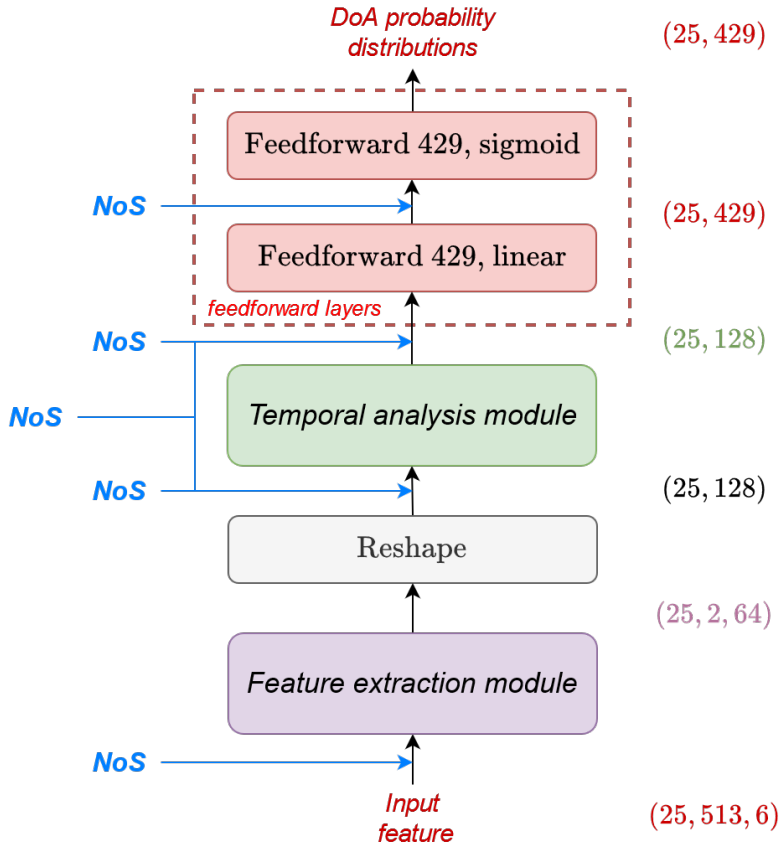

Figure 8.6: Tested positions for the NoS injection in the localization network.

- after the first feedforward layer.

The injection is done by concatenating the NoS feature with the feature tensor present at the place of injection. For each frame t, the NoS feature corresponding to the instantaneous NoS $J(t)$ is represented as a one-hot encoded vector $\mathbf{z}(t)$ of size $J+1$ where J is the maximum number of speakers considered in the mixtures. This vector encodes the NoS information by setting $z_i(t) = 1$ if $i = J(t)$ and $z_i(t) = 0$ otherwise. The injection is done for each frame in the considered tensor, which is possible since the temporal dimension is preserved through all layers. The concatenation is carried out on the second dimension (akin to the input frequency dimension) for all frames. For instance, if the injection is done alongside the input feature of shape $(25, 513, 6)$, the tensor obtained after the concatenation is of shape $(25, 513 + J + 1, 6)$; if the injection is performed after the temporal analysis module, the new tensor shape is $(25, 128 + J + 1)$.

The different options for the injection position are motivated by different intuitions. Mixing the NoS feature with the FO-PIV feature seems odd since the convolutional layers will treat all this data at once, but this practice has proved to be beneficial in another audio task [Vog+17]. Concatenating the NoS to the extracted feature after the convolutional layers seems a bit more reasonable since it can accompany the data modelled by the feature extraction module to help during the temporal

analysis process, as the instantaneous NoS can vary in each frame. In the same vein, injecting the NoS feature just after the BiLSTM layers gives an additional cue for the network classification task performed by the two feedforward layers. We also tried adding the NoS feature just before the output, again with the idea of providing such an information alongside higher-level features. Injecting the NoS both before and after the temporal analysis module has been experimented afterwards based on the obtained results, as detailed below.

8.2.2 Experimental protocol

Training and testing data

To train these neural networks, we used the same training and testing datasets as in the previous section (*i.e.*, obtained by generating 15-s long reverberant and noisy speech mixtures, with an instantaneous NoS varying from 0 to 3). Simulated SRIRs are used to generate the training signals, while for testing, we used the datasets of both simulated and recorded SRIRs.

During training, we use the ground-truth NoS both as the injection NoS and the prediction NoS. However, during inference in a practical use-case, we use the estimated NoS from the speaker counting network both for injection and prediction. In that manner, we train the network in an optimal way hoping that it will be robust enough when an imperfect NoS information is provided.

Baselines

To assess the benefit of NoS injection, we compare the proposed model with the base model $M_{5,2}$ (see Section 7.3.2 for more details) without injection. Moreover, to gauge the robustness of such a network in real conditions, *i.e.*, when the ground-truth NoS is not available, we evaluate the networks on the test datasets for different versions of the injection NoS and the prediction NoS independently:

- The injection and prediction NoS are both the ground-truth NoS. This allows us to directly compare our proposed system with the oracle condition.
- The injection NoS is the ground-truth NoS and the prediction NoS is estimated by the speaker counting network. We evaluate the robustness of using an estimated NoS for the DoA prediction while the NoS input data is the ground-truth.
- The injection NoS is estimated by the neural network, and the prediction NoS is the ground-truth NoS. This last configuration allows to assess the network capacity to cope with the injection of an imperfect NoS, while being in an optimal condition for peak picking.

In the following, using the ground-truth NoS for injection or for DoA peak-peaking is referred to as *oracle* injection NoS and *oracle* prediction NoS, respectively. Using the NoS provided by the counting neural network is referred to as *estimated* injection NoS and *estimated* prediction NoS.

Metrics

We use the same metrics as in the previous section. In this series of experiments, we either use the ground-truth NoS, which leads perfect counting and detection scores, or the estimated NoS using the counting network, whose performance have been shown in Table 8.1 and discussed in the previous section. Besides, we show the localization results which are the main interest in these experiments.

8.2.3 Results

Table 8.3 shows the localization results of the model with all considered injection positions, and for the four different combinations of oracle/estimated NoS and injection/prediction.

First, let us clarify that the results when no injection is used are obtained with a peak-picking of the DoA output distribution based on the ground-truth NoS for Tables 8.3a and 8.3b, and on the estimated NoS for Tables 8.3c and 8.3d, for a fair comparison with the models with NoS injection. Globally, we observe that most results with NoS injection are better than without injection. In all four tables, we notice that some injection positions almost always lead to better results than the model without injection. Particularly, this is the case when the injection is done after the temporal analysis module only, and both after the feature extraction and the temporal analysis modules. To give some numbers, when the only estimated NoS is used (Table 8.3d), the localization accuracy ($< 10°$) for simulated SRIRs is increased from 78.7% without injection to 83.8% with injection after the temporal analysis module, and the median angular error is decreased from 5.1° to 4.5°. On real SRIRs, the gain in performance is less noticeable, with an accuracy increase of only 1.6% and a median error decrease of 0.6° when injecting the NoS both after the feature extraction and temporal analysis modules. We can hence conclude that estimated NoS injection actually helps the localization network to achieve a better performance.

If we look at Table 8.3a, where only the ground-truth NoS is used for injection and DoA extraction, which can be considered as the optimal configuration, we also observe a gain in performance when injecting the NoS in several positions, such as after the temporal analysis module of after the feature extraction module. This confirms the interest of NoS injection. Now, when looking at Table 8.3b, whose difference with Table 8.3a is that we inject an estimated (thus imperfect) NoS instead of the ground-truth NoS (but still using the oracle prediction NoS), we observe than the results are almost as good as in the fully optimal conditions of Table 8.3a. This suggests that the counting network provides an estimated NoS with high enough accuracy, so that the injection of the estimated NoS is beneficial for the localization network. The loss in accuracy is around 1% when using an estimated injection NoS, while the median angular error is almost unaffected.

Focusing on Table 8.3c for which the ground-truth NoS is injected and the estimated NoS is used for DoA peak picking, we observe the common raise in localization

performance due to the miss detection of certain sources, which surely corresponds to the difficult cases, with a bad localization accuracy. This observation is identical when comparing the results model without injection between Tables 8.3a, 8.3b and Tables 8.3c, 8.3d. Then, as above, comparing Table 8.3d with Table 8.3c allows us to assess the use of an estimated NoS for the injection instead of the ground-truth NoS. Again, we can see that the results are almost the same, and are even closer than when comparing the numbers of Tables 8.3a and 8.3b. This indicates that when an estimated NoS is used for DoA peak extraction, using the same estimated NoS for injection is almost as effective as using the ground-truth NoS. This also shows that the use of inexact (estimated) NoS is more detrimental for peak-picking, than it is when used for injection.

Finally, the boxplots and violin plots in Fig. 8.7 underline the interest of NoS injection on data with simulated SRIRs, however the results are less convincing on real-world data. On the dataset with simulated SRIRs, we clearly observe the advantage of NoS injection as it allows to reduce the angular error variance, although the median angular error almost remains unchanged. This figure confirms that the best injection location seems to be both after the feature extraction and temporal analysis modules. Regarding the dataset with real SRIRs, we notice that when the ground-truth NoS is used for DoA extraction, the injection leads a higher error variance, especially with an estimated NoS injection. With a DoA extraction based on an estimated NoS, the boxplots indicate that the injection results are on par with the model without injection.

To conclude this study, we observe a certain interest of injecting the NoS as an additional input feature into the localization network. While injecting it directly alongside the intensity-based input features, or just before the output layer, has not been beneficial, we notice than NoS injection after the feature extraction module, after the temporal analysis module or after both modules leads to a clear gain in localization performance on the dataset with simulated SRIRs. On the dataset with real SRIRs, the interest of injection is slightly more moderate but several figures confirm its usefulness. Throughout a careful analysis, we manage to show the robustness of relying on an estimated NoS instead of the ground-truth NoS at both the injection and the prediction levels.

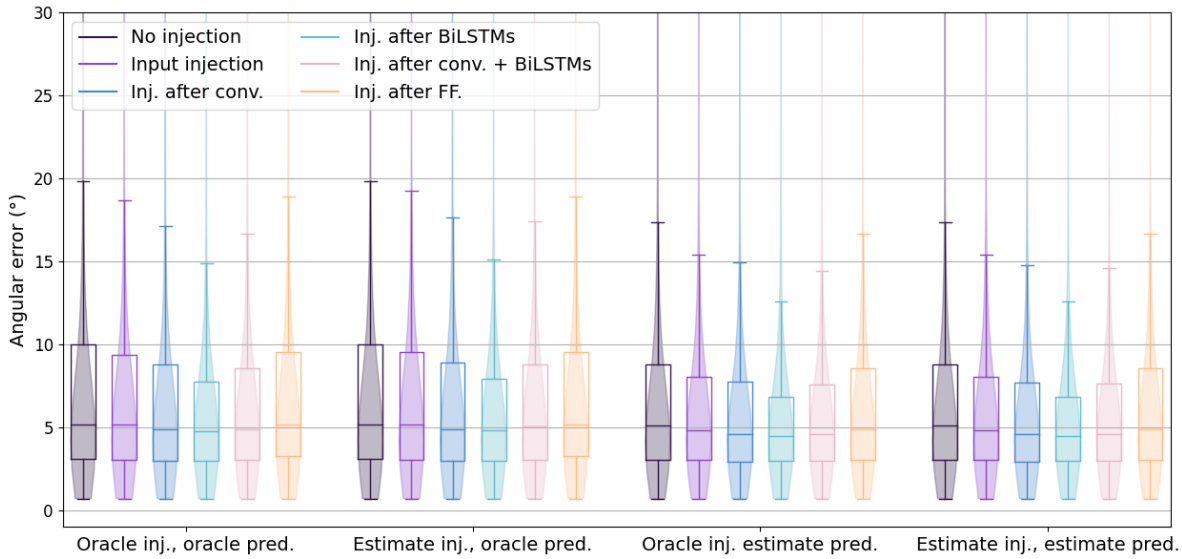

(a) Simulated SRIRs

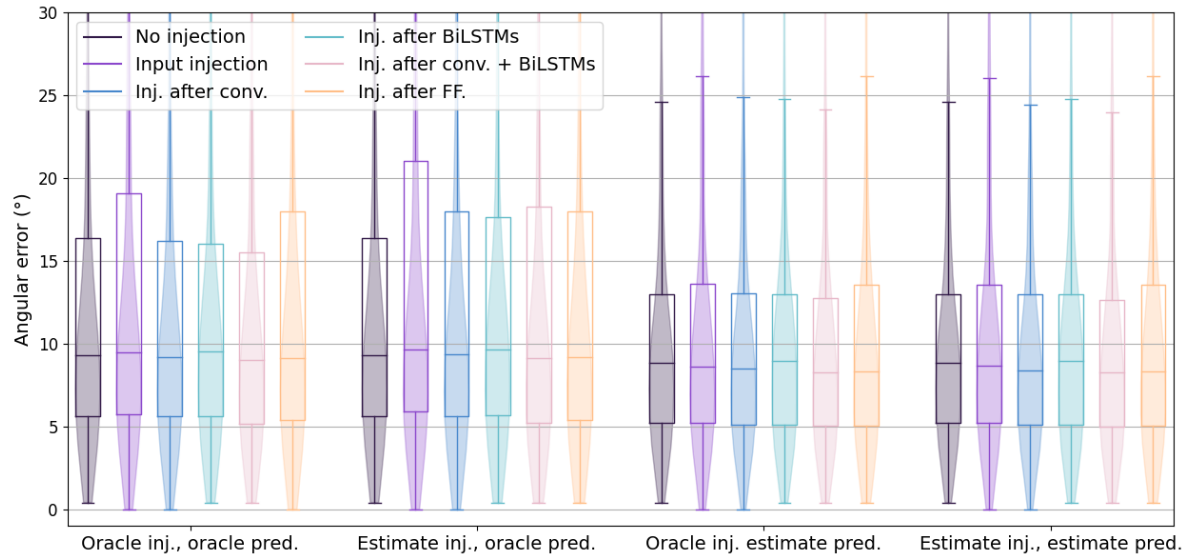

(b) Real SRIRs

Figure 8.7: Boxplots of the angular errors of the localization network for several injection positions, and considering several NoS derivation configurations.

Injection position	Simulated SRIRs				Real SRIRs			
	Accuracy (%)		Angular error (°)		Accuracy (%)		Angular error (°)	
	<10°	<15°	Mean	Median	<10°	<15°	Mean	Median
No injection	75.2	81.5	15.5	5.2	56.2	72.9	18.3	9.3
Input	75.9	81.9	15.7	5.1	52.7	70.4	19.8	9.5
After feature extraction	78.4	83.3	14.7	**4.8**	56.0	73.4	17.3	9.2
After temporal analysis	**80.1**	**84.4**	**13.7**	**4.8**	53.9	73.3	18.2	9.6
After feature extrac. & temp. analysis	78.4	83.4	14.2	**4.8**	**57.9**	**74.3**	**16.9**	**9.0**
After feedforward layer	76.1	82.3	14.9	5.2	55.5	71.4	19.7	9.1

(a) Oracle injection NoS, oracle prediction NoS

Injection position	Simulated SRIRs				Real SRIRs			
	Accuracy (%)		Angular error (°)		Accuracy (%)		Angular error (°)	
	<10°	<15°	Mean	Median	<10°	<15°	Mean	Median
No injection	75.2	81.5	15.5	5.2	56.2	**72.9**	**18.3**	9.3
Input	75.5	81.6	16.1	5.2	51.4	69.0	20.7	9.6
After feature extraction	77.6	82.2	15.4	**4.8**	54.9	71.4	18.9	9.3
After temporal analysis	**79.5**	**83.9**	**14.2**	**4.8**	52.7	71.9	19.5	9.6
After feature extrac. & temp. analysis	77.5	82.2	15.1	5.0	**56.8**	72.5	19.0	**9.1**
After feedforward layer	76.1	82.6	14.9	5.2	55.4	71.3	19.8	9.2

(b) Estimated injection NoS, oracle prediction NoS

Injection position	Simulated SRIRs				Real SRIRs			
	Accuracy (%)		Angular error (°)		Accuracy (%)		Angular error (°)	
	<10°	<15°	Mean	Median	<10°	<15°	Mean	Median
No injection	78.7	84.8	12.9	5.1	62.8	81.1	13.2	8.8
Input	79.6	85.4	13.3	4.8	59.0	78.4	14.8	8.6
After feature extraction	81.9	86.5	12.4	4.6	61.5	80.7	**12.7**	8.5
After temporal analysis	**83.8**	**87.8**	**11.5**	**4.5**	60.1	81.1	13.5	9.0
After feature extrac. & temp. analysis	82.3	86.7	11.9	4.6	**63.9**	**82.1**	12.8	**8.3**
After feedforward layer	79.6	85.9	12.6	4.8	61.6	79.4	14.5	**8.3**

(c) Oracle injection NoS, estimated prediction NoS

Injection position	Simulated SRIRs				Real SRIRs			
	Accuracy (%)		Angular error (°)		Accuracy (%)		Angular error (°)	
	<10°	<15°	Mean	Median	<10°	<15°	Mean	Median
No injection	78.7	84.8	12.9	5.1	62.8	81.1	13.2	8.8
Input	79.5	85.5	13.3	4.8	59.0	78.7	14.6	8.7
After feature extraction	82.0	86.3	12.4	4.6	62.3	81.1	**12.6**	8.4
After temporal analysis	**83.8**	**87.7**	**11.5**	**4.5**	59.9	81.1	13.5	9.0
After feature extrac. & temp. analysis	82.3	86.5	12.1	4.6	**64.4**	**82.4**	12.7	**8.2**
After feedforward layer	79.7	86.0	12.6	4.8	61.7	79.4	14.5	8.3

(d) Estimated injection NoS, estimated prediction NoS

Table 8.3: Accuracy and angular errors of the localization network with NoS injection, for different injection positions and the four combinations of oracle/estimated NoS for injection and prediction. Best results are in bold.

8.3 Multi-task speaker counting and localization network

In a last series of experiments, we propose to consider a multi-task neural network scheme that directly estimates both the NoS and the speaker locations at the same time. Multiple designs are tested, inspired by the architectures of the speaker counting and localization networks.

8.3.1 Method

Input feature

In this new approach of the joint counting and localization system, we use as input features a combination of both input features employed in the previously presented separate counting and localization networks (*i.e.*, the magnitude FOA spectrograms and the FO-PIV feature).

As explained in Section 8.3.1 below, in a first design of multi-task network, we combine both input features in the same input tensor. Using the same parameterization as before, the magnitude FOA spectrograms consists of a tensor of size $(25, 513, 4)$ and the normalized FO-PIV feature size is $(25, 513, 6)$. Therefore, the combined features at the input of the multi-task network are obtained by concatenating these two tensor features along the third dimension, leading to a new tensor of size $(25, 513, 10)$. Indeed, these features are of a very different nature, and simple concatenation may seem ad-hoc. However, we deem that the network is capable of learning how to extract the useful information from such an input.

We also designed a multi-task network in which the two input features are fed into two separate input branches, corresponding to two similar feature extraction modules (see Section 8.3.1). In this system, these input features are obtained identically as in the separate counting and localization networks: normalization is employed across the whole training dataset for the magnitude spectrograms, and the normalized version of the FO-PIV is used.

Multi-task network architectures

During our experiments, we consider several multi-task network architectures, which are illustrated in Fig. 8.8.

The first multi-task network we propose, shown in the left of Fig. 8.8, is made of a common feature extraction module for both input features, which are concatenated into a single feature tensor as explained in Section 8.3.1 above. The overall architecture is still based on the model $M_{5,2}$ presented in Section 7.3.2, except for the feedforward layers. After the temporal analysis module, the output tensor is fed into two distinct branches, one for the counting task and the other for the localization task. Each branch contains the same number of feedforward layers D, which is a hyperparameter in this experiment. In our counting network architecture presented in Chapter 5, a single feedforward layer –which is also the output layer– is used after the LSTM layer,

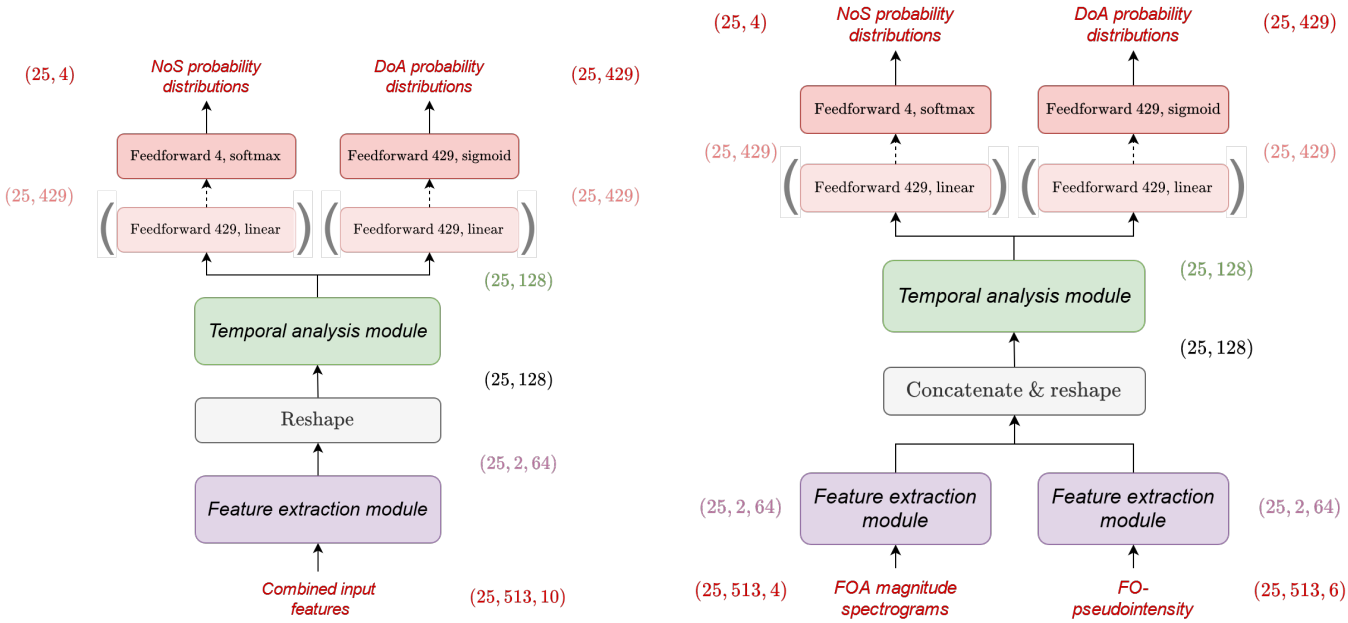

(a) Architecture with combined input features

(b) Architecture with separated input features

Figure 8.8: Architectures of the proposed multi-task counting and localization neural networks.

whereas in Model $M_{5,2}$ there are two feedforward layers after the temporal analysis module. We therefore experiment with $D = 1$ and $D = 2$. For all D values, the feedforward output layer of the counting branch consists of 4 neurons with a softmax activation, and the feedforward output layer of the localization branch is made of 429 neurons with a sigmoid activation. When $D = 2$, the layer after the temporal analysis module contains 429 neurons with a linear activation.

The second proposed multi-task network is similar to the first one explained above, except than the input features are not combined into a single tensor before the feature extraction module. Instead, each feature goes into a separate but identical feature extraction module which is trained to find a suitable representation for each input feature. The two extracted feature are then concatenated and reshaped before being fed into a common temporal analysis module. The other parts of the network are the same as above and we also experiment this second architecture with $D = 1$ and $D = 2$.

The multi-task model with combined input features is referred to as M_D^{Comb} and the one with separated input features is referred to as M_D^{Sep}, with D being the number of feedforward layers. Table 8.4 sums up the trained models and indicates the resulting number of parameters.

As we can see, parts of the neural network are shared for both tasks, which is thought under the assumption that both counting and localization are two tasks that are sufficiently tied to take benefit of a share representation learned by the neural network.

Model label	Input features	D	# parameters
M_1^{Comb}	Combined	1	778 339
M_2^{Comb}	Combined	2	833 680
M_1^{Sep}	Separated	1	1 177 291
M_2^{Sep}	Separated	2	1 232 632

Table 8.4: Multi-task neural network configurations for joint speaker counting and localization, and corresponding number of parameters.

Inference scheme

As we have seen above, counting and localization are handled with two separated output layers. Each of these layers outputs a probability distribution over the task-wise classes, *i.e.*, the NoS (from 0 to 3) and the DoA regions (unit sphere discretized in 429 zones). During the inference, for each frame, the estimated NoS is first retrieved from the counting branch output as the class with the highest probability, in the same way as in Chapter 5. We then use this estimated NoS to extract the right number of peaks from the localization branch output to estimate the speaker DoAs for each frame.

8.3.2 Experimental protocol

Training and testing data

The training and testing datasets are the same as in the two previous subsections. As before, we use the ground-truth NoS and DoAs during the training phase.

Training parameters

The loss function $\mathcal{L}$ used to train the multi-task network is a combination of the loss functions used in the counting and localization networks: the categorical cross-entropy $\mathcal{L}_{count}$ and the binary cross-entropy $\mathcal{L}_{loc}$. We define $\mathcal{L} = \lambda\mathcal{L}_{loc} + (1-\lambda)\mathcal{L}_{count}$, where λ is the weight. $\mathcal{L}_{count}$ is calculated only on the counting branch output and $\mathcal{L}_{loc}$ is calculated only on the localization branch output. The weight λ can be tuned in order to balance the performance between counting and localization, according to the user needs. Several values of λ are tried to find a good trade-off: $\lambda \in \{0.9, 0.99, 0.995\}$. This choice have been done empirically, by observing that the localization task leads to much greater loss values than counting.

Baseline and metrics

We compare these multi-task models with model $M_{5,2}$ evaluated only with the estimated NoS from the counting network (see Section 8.1.3), to compare the different approaches in a practical configuration without relying on the NoS knowledge assumption. We also compare them with the best performing model with NoS injection, *i.e.*, the injection is done after both the feature extraction and temporal analysis modules (see Section 8.2.3). Recall that the counting network was retrained for a maximum

Loss weight	Counting		Detection		Localization			
λ	Accuracy (%)	Mean abs. error	Precision	Recall	Accuracy (%) <10°	Accuracy (%) <15°	Angular error (°) Mean	Angular error (°) Median
0.9	**94.3**	**0.1**	**0.97**	**0.99**	45.3	56.3	28.6	11.9
0.99	91.7	**0.1**	0.95	**0.99**	**82.1**	85.1	14.2	**4.2**
0.995	90.0	**0.1**	0.94	**0.99**	81.1	**85.2**	**12.8**	4.6

(a) Simulated SRIRs

Loss weight	Counting		Detection		Localization			
λ	Accuracy (%)	Mean abs. error	Precision	Recall	Accuracy (%) <10°	Accuracy (%) <15°	Angular error (°) Mean	Angular error (°) Median
0.9	**93.7**	**0.1**	**0.97**	**0.97**	32.4	49.1	30.0	15.4
0.99	90.0	**0.1**	0.95	**0.97**	**60.7**	**76.6**	**16.9**	**8.5**
0.995	88.6	**0.1**	0.95	**0.97**	53.5	71.3	17.4	9.4

(b) Real SRIRs

Table 8.5: Counting, detection and localization results of the multi-task network for several loss combination weight values and for the datasets generated with simulated SRIRs (a) and real SRIRs (b). Best results are in bold.

NoS of 3, so that we can directly compare the multi-task network counting performance with the counting-only network.

In this new experiment, we measure the counting, detection and localization metrics, as described in Section 8.1.2.

8.3.3 Results

Loss combination weights assessment

Table 8.5 reports the counting, detection and localization results on the datasets with simulated and real SRIRs. We clearly observe the contribution of the chosen values for the weight λ: when $\lambda = 0.9$, the counting and precision metrics are the highest, reaching 94.3% and 93.7% in counting accuracy for simulated and real SRIRs, respectively, and almost perfect detection scores for both datasets. However the localization performance is quite poor, attaining only 56.3% accuracy ($< 15°$) for simulated SRIRs and 49.1% for real SRIRs. When setting $\lambda = 0.99$, the results become more satisfactory: the counting accuracy is above or equal to 90% for both datasets, while the localization accuracy ($< 10°$) is 82.1% and 60.7% on simulated and real SRIRs, respectively. The localization mean and median angular errors are also almost divided by two when using these weights values. When setting $\lambda = 0.995$, the counting performance is further slightly decreased but the localization performance globally does not increase significantly (it can even decrease, especially with the real SRIRs). This seems to indicate a limit in the trade-off between the counting and localization loss functions. In this experiment, $\lambda = 0.99$ clearly seems the best choice.

This study clearly highlights the importance of carefully choosing the weights of the counting and localization loss functions when training the multi-task neural network. A relatively small change in the weight values can have a large impact on the network learning, whose ability will definitely be biased towards one of the two

Model label	Counting		Detection		Localization			
	Accuracy (%)	Mean abs. error	Precision	Recall	Accuracy (%) <10°	Accuracy (%) <15)	Angular error (°) Mean	Angular error (°) Median
$M_{5,2}$	82.5	0.2	0.96	0.92	78.7	84.8	12.9	5.1
$M_{5,2}$ with inj.	82.5	0.2	0.96	0.92	82.3	**86.5**	**12.1**	4.6
M_1^{Comb}	91.6	**0.1**	0.95	**0.99**	82.1	85.1	14.2	**4.2**
M_2^{Comb}	91.6	**0.1**	0.95	**0.99**	**83.1**	86.1	12.3	**4.2**
M_1^{Sep}	**93.7**	**0.1**	**0.97**	**0.99**	81.3	84.8	13.4	4.3
M_2^{Sep}	92.2	**0.1**	0.96	**0.99**	79.5	84.1	13.6	5.1

(a) Simulated SRIRs

Model label	Counting		Detection		Localization			
	Accuracy (%)	Mean abs. error	Precision	Recall	Accuracy (%) <10°	Accuracy (%) <15)	Angular error (°) Mean	Angular error (°) Median
$M_{5,2}$	70.3	0.3	**0.96**	0.82	62.8	81.1	13.2	8.8
$M_{5,2}$ with inj.	70.3	0.3	**0.96**	0.82	**64.4**	**82.4**	**12.7**	**8.2**
M_1^{Comb}	90.0	**0.1**	0.95	**0.97**	60.8	76.6	16.9	8.5
M_2^{Comb}	91.0	**0.1**	**0.96**	**0.97**	57.7	72.4	17.9	9.1
M_1^{Sep}	**91.3**	**0.1**	**0.96**	**0.97**	56.4	73.4	16.7	9.1
M_2^{Sep}	90.9	**0.1**	**0.96**	**0.97**	54.8	74.3	17.1	9.2

(b) Real SRIRs

Table 8.6: Counting, detection and localization results of the multi-task neural networks and the model $M_{5,2}$ with and without injection, for the datasets generated with simulated SRIRs (a) and real SRIRs (b). Best results are in bold.

considered tasks. For the following experiment, we opt to keep the values $\lambda = 0.99$ to compute the multi-task loss function, which seem a good trade-off between a good counting and localization performance.

Multi-task architectures comparison

Table 8.6 reports the counting, detection and localization results of the multi-task networks as well as the baseline model $M_{5,2}$ with and without NoS injection, evaluated using the estimated NoS from the counting network (therefore, the counting and detection performance reported in the two first lines of Table 8.6 (a) and (b) are the ones of the counting network). Fig. 8.9 and 8.10 show the counting confusion matrices and mean absolute error, respectively. Fig. 8.11 exhibits the detection metrics and Fig. 8.12 displays the boxplots and violin plots of the localization angular errors.

Focusing on Table 8.6, we clearly see that the multi-task neural network provides a substantial gain in counting accuracy, and therefore in detection performance, compared to the counting network results. On simulated SRIRs, the counting accuracy goes from 82.5% for the counting network to more than 90% for all configurations of the multi-task network. On real SRIRs, the increase in performance is even larger: 70.3% for the counting network against, again, more than 90% for all multi-task networks. This important boost in counting performance leads to an great improvement in terms of detection recall. On real SRIRs, it reaches 0.97 whereas it is only at 0.82 for Model $M_{5,2}$. This means that the multi-task networks are capable of detecting almost all localizable speakers, even in real-world conditions.

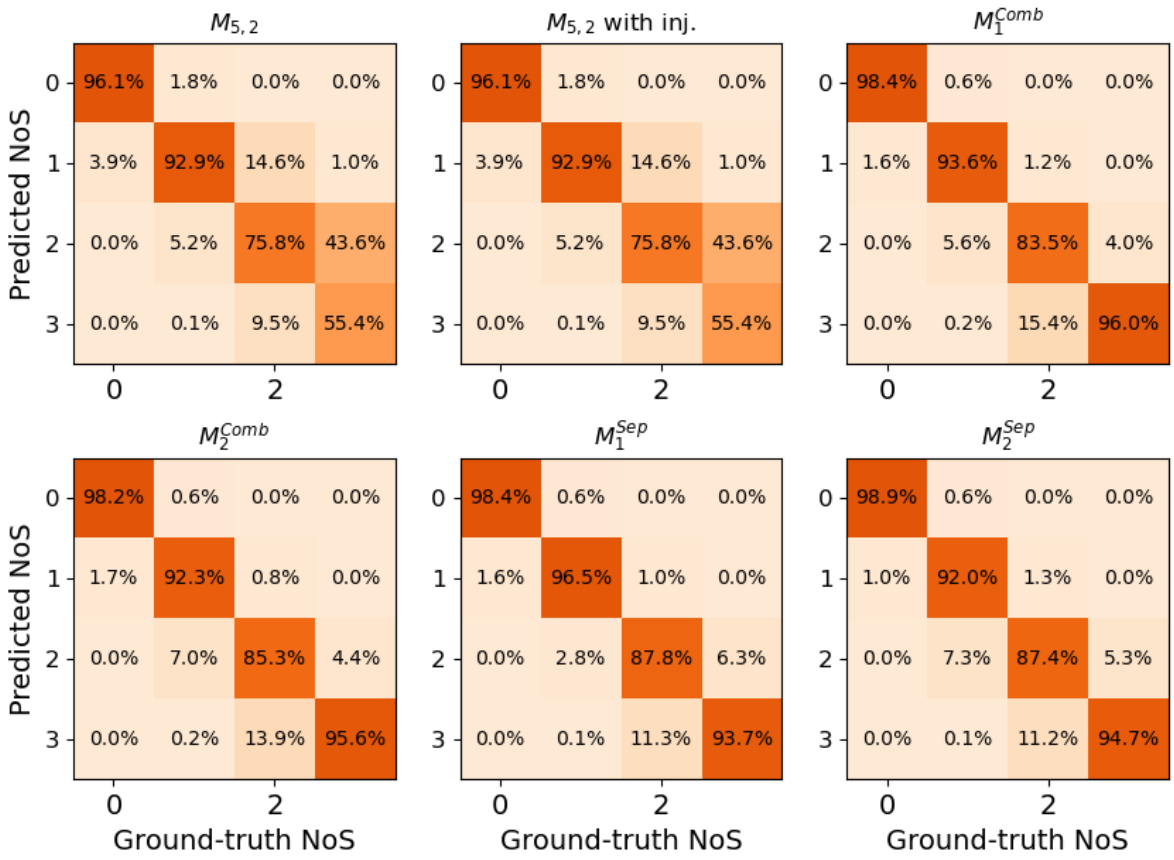

(a) Simulated SRIRs

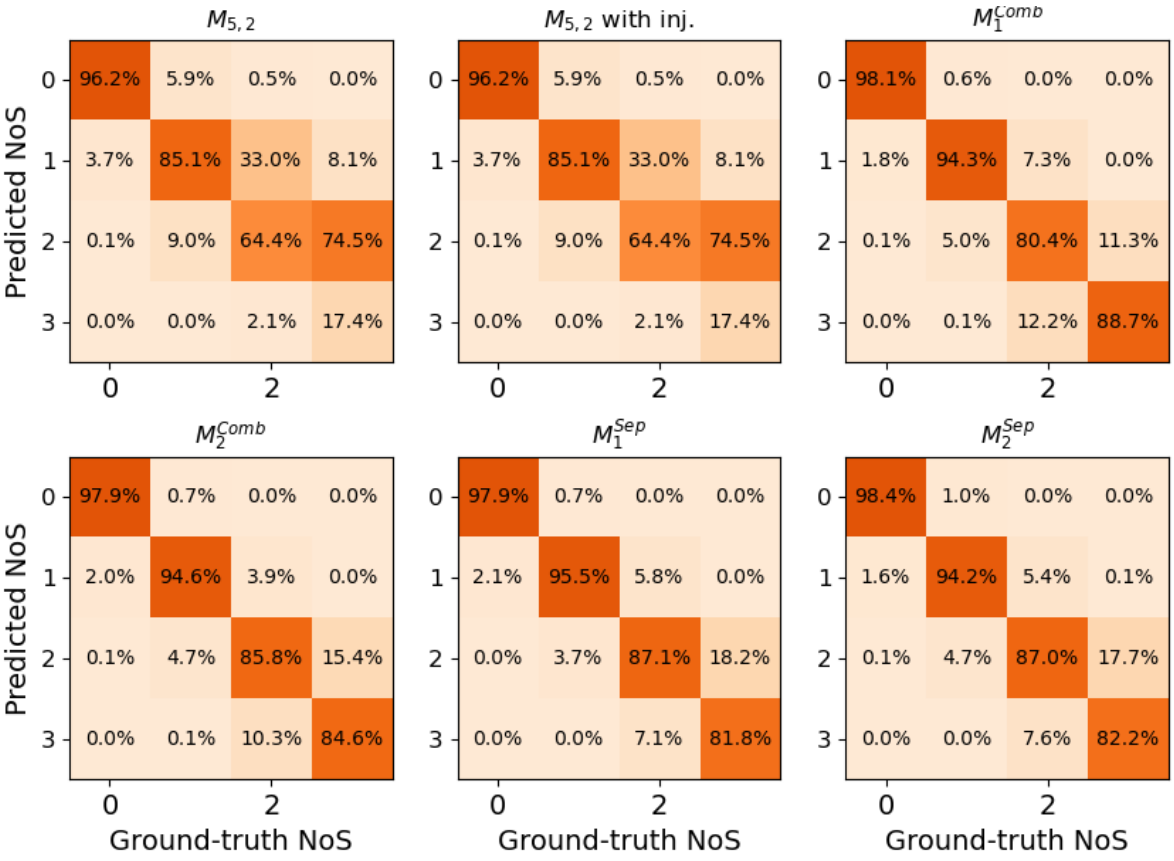

(b) Real SRIRs

Figure 8.9: Confusion matrices of the accuracy A_{ij} for the multi-task neural networks and the model $M_{5,2}$ with and without NoS injection.

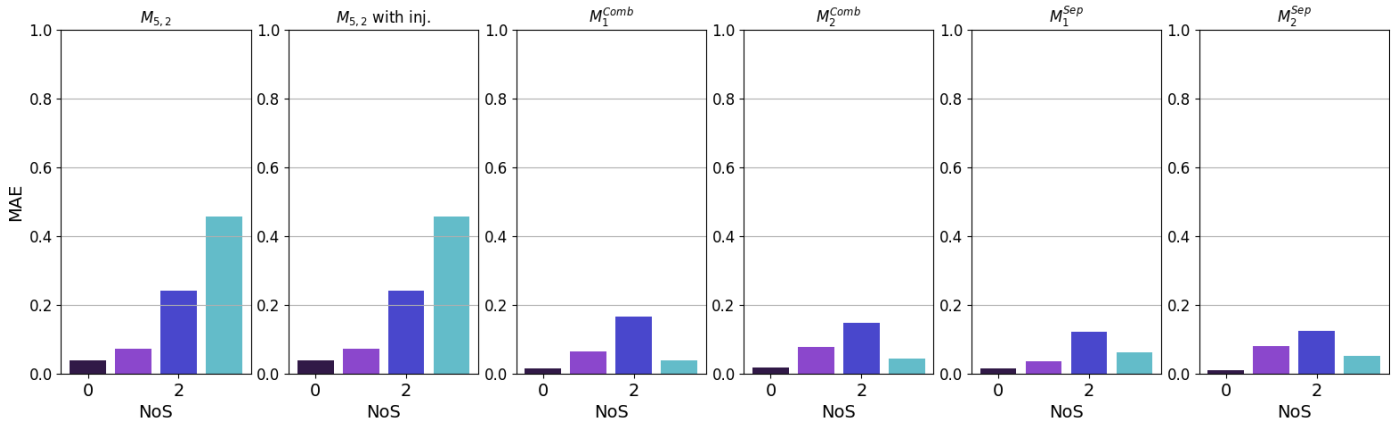

(a) Simulated SRIRs

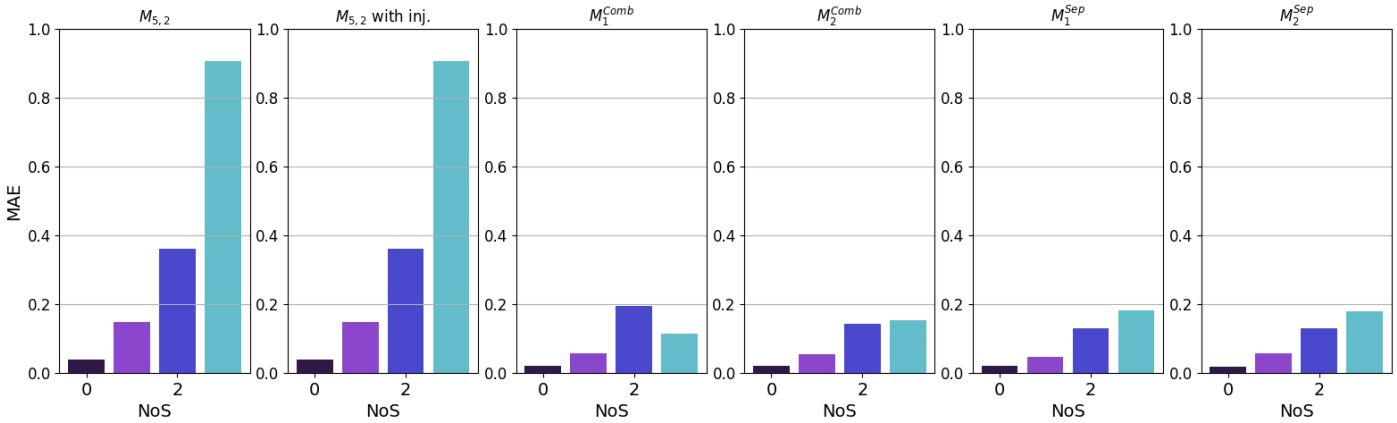

(b) Real SRIRs

Figure 8.10: Mean absolute errors M_i for the multi-task neural networks and the model $M_{5,2}$ with and without NoS injection.

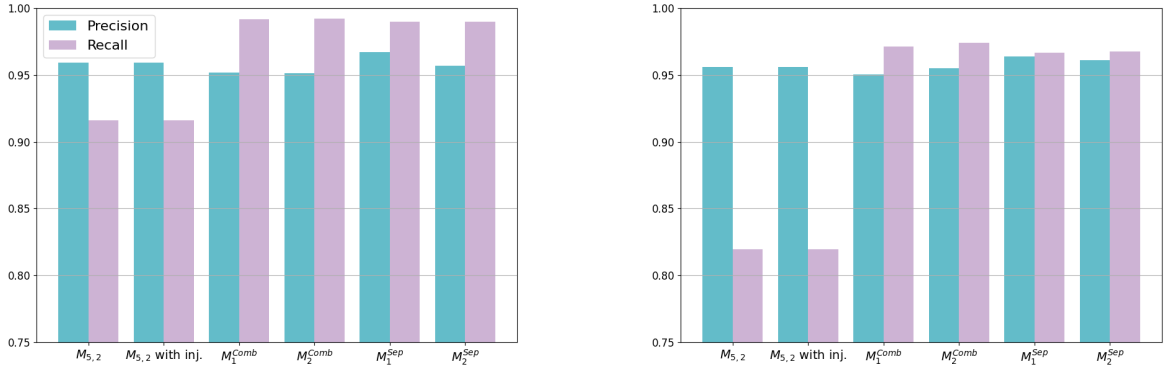

(a) Simulated SRIRs **(b)** Real SRIRs

Figure 8.11: Detection precision and recall for the multi-task neural networks and the model $M_{5,2}$ with and without NoS injection.

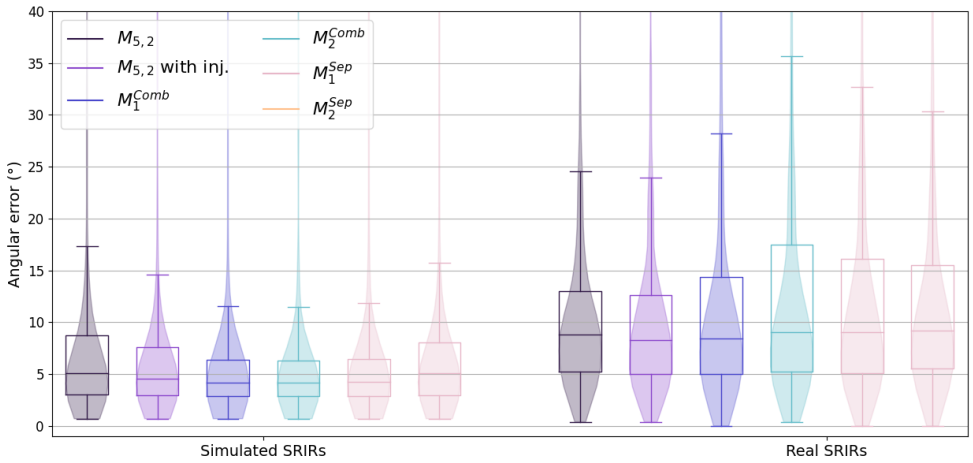

Figure 8.12: Boxplots of the angular errors of the localization network for the multi-task neural networks and the model $M_{5,2}$ with and without NoS injection.

When looking at the confusion matrices in Fig. 8.9, we can appreciate the robustness of the multi-task networks to count up to 3 speakers, with more than 80% accuracy for all NoS on both simulated and real SRIRs. This approach also allows to greatly reduce the mean absolute error, as showed in Fig. 8.10, especially for 2 and 3 speakers, which does not exceed 0.2 on both datasets. The detection metrics (see Fig. 8.11) confirms the great performance of multi-task models over the baselines, with a source detection rate (recall) greater than 95% on real SRIRs in parallel with a relatively low false positive rate denoted by a precision of more than 95%, whereas for the counting-only network these metrics reached 96% and 82%, for precision and recall, respectively.

Regarding the localization results showed in Table 8.6 and Fig. 8.12, the multi-task networks are below the model $M_{5,2}$ with NoS injection on simulated SRIRs but are on par with the baseline $M_{5,2}$. On real SRIRs, we see that the multi-task networks leads to worse localization performance than the model $M_{5,2}$ with and without injection. However, recalling that the localization metrics are computed only for true positives, the results for the multi-task networks are in fact quite impressive given the very high detection recall. On simulated SRIRs, the multi-task networks are capable of detecting more speakers with an localization precision that remains at the level of the best baseline, although we can expect that some of the additional detected speakers are difficult to localize. Regarding the results on real SRIRs, they are below the baselines. Here, the effect of detecting more sources (and thus more sources that are difficult to localize and that lead to a quite high angular error) is probably more important, because of the larger difference in accuracy and recall with the baselines, compared to simulated SRIRs. For a more fair assessment, we can compare the localization results of the multi-task networks with those of the $M_{5,2}$ model when the latter uses

an oracle counting system, leading to a comparable detection performance, as shown in Table 8.2. We see that the localization accuracy ($< 10°$) for the baseline $M_{5,2}$ is here 56.2% for real SRIRs, whereas it reaches 60.8% for the model M_1^{Comb}. Therefore, this seems to indicate that, for a similar counting/detection performance, the multi-task approach is performing better in localization compared with the baseline.

When comparing the different configurations of the multi-task neural network, we notice that for models M^{Sep}, adding a second feedforward layer tends to reduce the localization performance while not necessarily increasing the network counting and detection capability. For separate input features, the multi-task network with two feedforward layers performs 1.8% less in localization accuracy ($< 10°$) than the same model with one feedforward layer, for simulated and real SRIRs, respectively. However the inverse observation can be made for models M^{Comb}, where M_2^{Comb} is the one with the best localization results. Hence it is not straightforward to conclude about the interest of adding a second feedforward layer. Furthermore, it is not clear that separating the input features with a dedicating feature extraction module for each of them presents an advantage in such a multi-task system. The results on all multi-task networks are globally on par, whereas using two separate feature extraction modules leads to an important increase in the number of parameters (around 51% more). Finally when looking at the boxplots in Fig. 8.12, we see can appreciate the fact that the multi-task networks detect more sources at the cost of a higher localization angular error variance, which seems to highlight the detection of sources more difficult to localize.

To conclude, the multi-task networks present quite impressive results in terms of counting and detection, compared to the use of a dedicated counting network as previously. The gain in counting performance is remarkable, especially on signals with real SRIRs. Regarding the localization performance, we can say that they almost reach the performance of the baseline model $M_{5,2}$ using an estimated NoS, which is quite impressive because of the high detection recall whereas the baseline's localization accuracy drastically drops when detecting more sources. It seems that the multi-task neural networks are capable of extracting high-level features that are relevant for both counting and localization. Feeding the input features separately in two different feature extraction modules or in combination in a single one has not provided convincing differences in performance. It seems that the overall improvement is due to the use of both input features and the network multi-task training.

8.4 Conclusion and perspectives

In this chapter, we have explored several ways of combining the counting and localization networks. In a first study, we assessed the benefit of using a separate counting network to estimate the NoS, before using this information to extract the right number of DoAs from a localization network output. We concluded that the speaker counting system is robust enough to be used in a practical use-case, as a replacement for the

traditional NoS knowledge assumption that is made in research studies. Next, we investigated the interest of injecting the NoS information as an additional input feature to the localization network, with the idea that this can help to shape a more accurate DoA probability distribution output. By comparing the localization performance with and without NoS injection, as well as evaluating the robustness of using an estimated NoS instead of the ground-truth NoS, we demonstrated that this additional piece of information is valuable for the localization network, even if the performance gain is not considerable. Finally, we proposed to combine the counting and localization tasks into a single multi-task neural network, designed with two separate output branches for each task. We appropriately tuned the combination of the counting and localization loss functions with dedicated tests. Then, we showed the superiority of this multi-task approach over the use of two separate task-wise networks. We were able to largely improve the counting and detection performance, while the localization performance were globally remaining at a level very close to the baseline. This is a quite satisfactory result, considering the high detection accuracy and the fact that sources that are difficult to detect (not detected by the baseline) may also be difficult to localize. The experiments dealing with the order of the combination module and the feature extraction module to combine the different input features have not been conclusive, since the results obtained with the two solutions were on par.

The research work presented in this chapter leads to several questions and perspectives. First, the proposal of injecting the NoS, based on the idea that a robust estimate NoS could help the localization network for a better output distributions, has not led to an important increase in localization accuracy, especially on real-world signals. A first idea would be to use the NoS probability distribution, estimated by the counting network, instead of a one-hot encoded vector which drops possibly precious information. A general perspective to address the issue of real-world data performance lies in the deep learning research effort to adapt neural network trained with simulated data on real-world data. In the specific context of this work, we believe that there might be a better manner to help the localization network with this precious NoS information. As we pointed out in other chapters, analyzing in depth how the neural network uses the NoS information could give some insights. Another intriguing interesting aspect gravitates around the proposed (variants of the) multi-task neural network, especially regarding the reason why the counting performance has been largely improved with this system compared to the baseline. Analyzing where does this improvement come from –which we did not have time to conduct– would help us understand what network aspect is crucial for source counting. Is it the feature extraction module? (we recall the proposed perspective at the end of Chapter 5), the combined input features? the benefit of jointly learning counting and localization? Also, it would be great to comprehend the way the multi-task network uses the same extracted feature –and the contents of this feature– for two tied but distinct tasks.

Chapter 9

Conclusion

9.1 Conclusion

In this thesis, we focused on estimating the number of speakers and their respective location from a multi-channel audio signal. We considered the challenging context of domestic environments, where reverberation and noise are present. We addressed these problems with deep neural networks, which were shown to be able to tackle the speaker counting and localization problems efficiently, with an emphasis on low-latency performance.

9.1.1 Speaker counting

In the first part, we trained a CRNN on simulated data to count the number of speakers in a multi-channel mixtures which is blurred by reverberation and diffuse noise. We showed that this counting system was capable of counting up to 5 speakers, at a frame-wise resolution, while the best speaker counting method at the time of this research was able to provide the maximum NoS in a 5-s audio segment. Our method proved to be quite robust, with a very high accuracy when estimating the NoS to be 0 to 2, while this accuracy is still above 50% for greater NoS. After showing the benefit of using multi-channel features over single-channel ones, we conducted several experiments to analyze the performance according to several sets of hyperparameters. Finally, we carried on an investigation to assess the importance of a frame position within the input sequence to maximize the corresponding output accuracy. We derived an empirical formula which gives the frame position in the input sequence having the most accurate NoS estimate, leading to an overall accuracy of more than 75%. This short analysis was not bound to our counting problem, but is rather generic, based on the intuition behind the functioning of convolutional and LSTM layers.

9.1.2 Speaker localization

In the second part, we addressed the speaker localization problem, under the assumption that the NoS is preliminary known. We first considered the simpler problem of localizing one speaker, in order to assess the interest of the TDVV, a novel input feature with promising theoretical perspectives. In order to improve the single-speaker localization performance over the use of the intensity-based input features, we explored

a number of neural network architectures, such as CRNNs, CRNNs with dilated convolutions and CRNNs with residual connections. Nevertheless, the results never showed an improvement over the baseline, and yet it is quite difficult to analyze the neural network to understand the reasons for this behavior. In spite of the efforts to derive an adapted feature extraction module for the TDVV, we concluded that the problem could lie into the TDVV estimation itself.

Then, we focused on estimating the DoAs of multiple overlapping speakers with intensity-based features. These had already proven to be quite robust for single-speaker localization, and are deemed promising for localizing multiple speakers as well. After evaluating the best way to train the localization neural network for multiple speakers, we redesign the feature extraction module of a state-of-the-art model in order to give more capacity to the network to derive effective representations. This new design has greatly improved the localization performance, especially in a multi-speaker context. Next, we proposed to replace the classical recurrent layers present in the CRNN with self-attention mechanism. The objective was to reduce the inference time while retaining similar localization performance, which was successfully accomplished. We further managed to improve the multi-speaker localization performance by proposing a new way of computing attention scores with multiple heads. Finally, we assessed the benefit of using the HOA-, instead of the FOA-based features. The obtained results indicated that the network trained using higher-order pseudointensity is performing better than its FOA counterpart, particularly in the presence of multiple speakers.

9.1.3 Joint speaker counting and localization

In the last part, we proposed to relax the assumption that the NoS needs to be known beforehand, by combining our speaker counting and speaker localization systems. First, we evaluated the robustness of using the speaker counting network to estimate the NoS instead of using the ground-truth. We demonstrated that the counting system is accurate enough so that the localization network leads to an estimate of most DoAs with sufficient efficiency. Then, we investigated the idea of injecting the NoS information as an additional input feature into the localization network. We observed that when the injection took place at specific layers, *i.e.*, after the feature extraction and temporal analysis modules, it helped the localization network to be more accurate. Finally, we jointly addressed speaker counting and localization with a common multi-task neural network. After evaluating the best way to combine the counting and localization loss functions, we designed several multi-task neural network architectures and compared them with the use of separate counting and localization systems. We demonstrated that these multi-task networks are more robust in terms of counting accuracy than our original speaker counting, and that the localization performance remained high. These last experiments suggested that a neural model can simultaneously perform speaker counting and localization, without the strong assumption of knowing the NoS in advance.

9.2 Perspectives

In this thesis, we focused on speaker counting and localization from many angles, especially regarding the design of several network modules with a goal of improving the overall performance. However, our experiments and the subsequent results showed some limitations which we did not have time to address. In the following paragraphs, we discuss a few perspectives and ideas which would be interesting to develop in order to improve the networks performance, and gain a better understanding of their inherent behavior.

9.2.1 Real-world data adaptation

In all our experiments we noticed a drop in performance when the neural networks, which had always been trained on simulated data, were tested against real-world signals. This effect is well-known in the deep learning research, and is quite usual in many tasks due to the lack of realistic training data. In our research, all training examples were generated using the "shoebox" acoustic simulations. Such geometry is rarely encountered is real-world environments. Moreover, the microphone array was allowed to be placed (almost) anywhere in the room, resulting in unrealistic positions (*e.g.*, floating in the air), whereas in reality a recording device is often positioned on a table, leading to strong reflections. A first approach is to consider a more sophisticated room acoustics simulator, capable of taking into account more complex room geometries and acoustic phenomena, such as scattering or diffraction. Such an idea, however, presents the limitation of a heavier computation cost, which should be balanced with the amount of data to be generated. Another idea would be to progressively train the network to more and more realistic signals, *e.g.*, first with signals generated with simulated SRIRs, then fine-tuning the network with signals generated with real SRIRs, then again fine-tuning it further using recorded data. Finally, one could lean towards the research effort on domain adaptation, which provides interesting methods to improve the performance of a network on a particular domain (*e.g.*, real-world data in our case) while it has been trained on another domain (*e.g.*, simulated data).

9.2.2 Neural networks process analysis

Although some efforts were made in this thesis to analyze the networks behavior and the influence of some hyperparameters, there is still room for in-depth analyses, which would certainly be profitable to understand why some models perform better than others, and how further improvements can be achieved. This analysis concern is at the core of recent deep learning research, because of the neural network's black box nature, and we hereby propose a few targeted points to be analyzed regarding our domain. A first perspective is to interpret the extracted features which allows the networks to perform quite well in a multi-speaker context, for example based on filter visualization techniques [Cho17; Bac+15]. Regarding the improvements obtained in Section 7.3.2, one can wonder what are the differences between the extracted feature

of the baseline and the one of the new module which leads to such a performance gain. Also, the small variations in the results for the different proposed feature extraction modules push us into looking into the networks behavior when another convolutional block is added or less max-pooling is employed. In the same vein, it could be very instructive to study the contents of the extracted feature in the multi-task networks, since it proved to be suitable not only for localization but also for counting. While it is obvious that these two tasks are bound in a certain way, the networks seem to extract meaningful patterns in the input features which are somehow beneficial for counting and localization altogether, which is not straightforward to do with our human-crafted algorithms.

Furthermore, it could be quite insightful to understand how the attention mechanism is able to make use of the inter-frame information. While the behaviors of LSTM layers are a bit more instinctive to understand due to their recurrent processing, it is more complicated to figure out how self-attention scores are computed, an why the emphasis is put on certain frames. A thorough investigation regarding the scores and the computed vectors could reveal interesting properties on the most informative frames for speaker localization. We believe that an extensive analysis effort should be pursued to definitely leverage the remarkable capabilities of neural networks. Not only could it allow to notably improve the accuracy of counting and localization systems, but it could more importantly provide us new considerations to progress in the audio research field.

9.2.3 Moving sources

In some experiments, we evaluated our localization network on the LOCATA dataset, which includes two sets of data with moving speakers. While we never consider this particular context, we saw that our localization system was able to follow the DoAs of several speakers with a fair accuracy, which is probably due to a relatively short temporal analysis window. However, the localization performance could be greatly improved with a dedicated tracking system. We could leverage our robust speaker counting system to provide an information about the sources "birth" or "death", alongside a neural-based tracking network, to improve the localization of moving sources. Furthermore, it could be interesting to incorporate speaker spectral signatures into a tracking system for even better performance, which would bring us at the intersection with speaker recognition and diarization.

9.2.4 Combination of deep learning and conventional signal processing techniques

In this PhD work, the exploitation of the spatial information contained in the mixture signal was done mostly "implicitly," by inputing a multichannel (Ambisonic) representation of the signal in the DNNs. Another perspective that we have not considered in this PhD work is in the "explicit" combination of deep learning with conventional

multichannel signal processing techniques, inspired by what has been done for speech enhancement and speech/audio source separation.

Deep-learning-based (single-channel) speech enhancement and separation are mostly based on the masking approach in the TF domain. Binary masks or soft masks (reminiscent of the well-known single-channel Wiener filter) are estimated with DNNs from the noisy signal and applied to it to obtain a cleaned version [WC17]. For multichannel speech enhancement and separation, it is possible to input the multichannel signal in the mask estimation network. But, it can been noted that the masking technique has also been combined with conventional (multichannel signal processing) approaches such as beamforming [VVB88], see for example [Erd+16], [HDHU16] and [Hig+17]. The authors of these three papers proposed a similar basic combination of DL-based single-channel speech enhancement (to extract/exploit the speech spectral information) and beamforming techniques (to extract/exploit the spatial information). DNNs are used to estimate masks in the TF domain, which are used to select speech-dominant against noise-dominant TF points. The speech-dominant and noise-dominant points are then used to estimate speech and noise spatial covariance matrices, respectively, which are then used to build beamforming filters. Those studies report better ASR scores than with direct TF masking or basic beamforming applied separately.[1] This approach was extended in [Per+18a] with an additional first stage of beamforming in the high-order ambisonics domain to improve the mask estimation.

In the same general idea, but an approach closer to source separation than to beamforming, the authors of [NLV16] combined a DNN trained to estimate a clean speech spectrogram from a noisy speech spectrogram with the source separation technique based on the spatial covariance matrix (SCM) model and Wiener filtering from [DVG10]. An unsupervised multichannel speech enhancement system combining a deep model (a variational autoencoder) for modeling the clean speech signal and the SCM model from [DVG10] for modeling the spatial characteristics was proposed in [LGH19].

All these work lead us to believe that there is room for combining DNNs and conventional models (especially for the modeling of spatial information) for source counting and localization, as well as for combining these tasks with speaker diarization, enhancement and separation. The connection between audio source separation and SSL is strong, reciprocal (audio source separation can help SSL and SSL can help audio source separation), and is already exploited in many studies [VVG18; Gan+17]. Obviously, a reliable NoS estimation is also useful for both SSL and separation. Therefore, a straighforward extension of our work presented in Section 8.3 could be to add the separation task at the output of the proposed speaker counting / speaker localization multi-task network. And beyond that, future works may consider jointly source counting, localization, diarization and separation/enhancement in an hybrid approach combining deep learning and conventional signal processing techniques.

[1] Note that, in parallel, more direct and brute-force approaches were also considered, with joint end-to-end optimization of the mask estimator, the beamformer, and possibly an ASR acoustic model, in the TF domain [Men+17; Hey+17], and in the time domain [Li+16].

Bibliography

[AB79] Jont B. Allen and David A. Berkley. "Image method for efficiently simulating small-room acoustics". en. In: *The Journal of the Acoustical Society of America* 65.4 (1979), pp. 943–950.

[ACB19] Valentin Andrei, Horia Cucu, and Corneliu Burileanu. "Overlapped speech detection and competing speaker counting—humans sersus deep learning". In: *IEEE Journal of Selected Topics in Signal Processing* 13.4 (Aug. 2019), pp. 850–862.

[AGB10] Simon Arberet, Rémi Gribonval, and Frédéric Bimbot. "A robust method to count and locate audio sources in a multichannel underdetermined mixture". In: *IEEE Transactions on Signal Processing* 58.1 (2010), pp. 121–133.

[Ang+12] Xavier Anguera, Simon Bozonnet, Nicholas Evans, Corinne Fredouille, Gerald Friedland, and Oriol Vinyals. "Speaker diarization: a review of recent research". In: *IEEE Transactions on Audio, Speech, and Language Processing* 20.2 (Feb. 2012), pp. 356–370.

[APV19] Sharath Adavanne, Archontis Politis, and Tuomas Virtanen. "Localization, detection and tracking of multiple moving sound sources with a convolutional recurrent neural network". en. In: *arXiv:1904.12769* (Apr. 2019).

[Ara03] Takayuki Arai. "Estimating number of speakers by the modulation characteristics of speech". en. In: *IEEE International Conference on Acoustics, Speech, and Signal Processing*. Vol. 2. 2003, pp. 197–200.

[Aro92] Barry Arons. "A review of the cocktail party effect". en. In: *Journal of the American Voice I/O Society* 12.7 (1992), pp. 35–50.

[AWH13] George B. Arfken, Hans-Jurgen Weber, and Frank E. Harris. *Mathematical methods for physicists: a comprehensive guide*. 7th. Elsevier, 2013.

[Bac+15] Sebastian Bach, Alexander Binder, Grégoire Montavon, Frederick Klauschen, Klaus-Robert Müller, and Wojciech Samek. "On pixel-wise explanations for non-linear classifier decisions by layer-wise relevance propagation". In: *PloS one* 10.7 (2015).

[Baq17] Mathieu Baque. "Analyse de scène sonore multi-capteurs : un front-end temps-réel pour la manipulation de scène". fr. PhD thesis. Le Mans: Université du Maine, 2017.

[BCB15] Dzmitry Bahdanau, Kyunghyun Cho, and Yoshua Bengio. "Neural machine translation by jointly learning to align and translate". In: *International Conference on Learning Representations*. May 2015.

[Ben+09] Yoshua Bengio, Jérôme Louradour, Ronan Collobert, and Jason Weston. "Curriculum learning". In: *International Conference on Machine Learning*. ICML '09. New York, NY, USA: Association for Computing Machinery, June 2009, pp. 41–48.

[BGG20] Michael J. Bianco, Sharon Gannot, and Peter Gerstoft. "Semi-supervised source localization with deep generative modeling". In: *IEEE International Workshop on Machine Learning for Signal Processing*. July 2020.

[BHM21] Giovanni Bologni, Richard Heusdens, and Jorge Martinez. "Acoustic reflectors localization from stereo recordings using neural networks". In: *IEEE International Conference on Acoustics, Speech and Signal Processing*. June 2021, pp. 1–5.

[Bla97] Jens Blauert. *Spatial hearing: the psychophysics of human sound localization*. en. MIT Press, 1997.

[Blu31] Alan D. Blumlein. "Improvements in and relating to sound-transmission, sound-recording and sound-reproducing systems". Pat. 394325. 1931.

[BMM18] Mateusz Buda, Atsuto Maki, and Maciej A. Mazurowski. "A systematic study of the class imbalance problem in convolutional neural networks". eng. In: *Neural Networks* 106 (Oct. 2018), pp. 249–259.

[BOV12] Charles Blandin, Alexey Ozerov, and Emmanuel Vincent. "Multi-source TDOA estimation in reverberant audio using angular spectra and clustering". en. In: *Signal Processing* 92.8 (Aug. 2012), pp. 1950–1960.

[Bre94] Albert S. Bregman. *Auditory scene analysis: the perceptual organization of sound*. en. MIT Press, 1994.

[Bro+20] Tom B. Brown, Benjamin Mann, Nick Ryder, Melanie Subbiah, Jared Kaplan, Prafulla Dhariwal, Arvind Neelakantan, Pranav Shyam, Girish Sastry, Amanda Askell, Sandhini Agarwal, Ariel Herbert-Voss, Gretchen Krueger, Tom Henighan, Rewon Child, Aditya Ramesh, Daniel M. Ziegler, Jeffrey Wu, Clemens Winter, Christopher Hesse, Mark Chen, Eric Sigler, Mateusz Litwin, Scott Gray, Benjamin Chess, Jack Clark, Christopher Berner, Sam McCandlish, Alec Radford, Ilya Sutskever, and Dario Amodei. "Language models are few-shot learners". en. In: *Conference on Neural Information Processing System*. 2020.

[Bro+21] Michael M. Bronstein, Joan Bruna, Taco Cohen, and Petar Veličković. "Geometric deep learning: grids, groups, graphs, geodesics, and gauges". In: *arXiv:2104.13478* (May 2021).

[Cao+21] Yin Cao, Turab Iqbal, Qiuqiang Kong, Fengyan An, Wenwu Wang, and Mark D. Plumbley. "An improved event-independent network for polyphonic sound event localization and detection". In: *IEEE International Conference on Acoustics, Speech and Signal Processing*. 2021.

[CH17] Soumitro Chakrabarty and Emanuël A. P. Habets. "Multi-speaker localization using convolutional neural network trained with noise". In: *arXiv:1712.04276* (2017).

[CH19] Soumitro Chakrabarty and Emanuël A. P. Habets. "Multi-speaker DoA estimation using deep convolutional networks trained with noise signals". en. In: *IEEE Journal of Selected Topics in Signal Processing* 13.1 (2019), pp. 8–21.

[Cha+19] Shlomo E. Chazan, Hodaya Hammer, Gershon Hazan, Jacob Goldberger, and Sharon Gannot. "Multi-microphone speaker separation based on deep DoA estimation". In: *European Signal Processing Conference*. Sept. 2019.

[Cho+14] Kyunghyun Cho, Bart van Merrienboer, Caglar Gulcehre, Dzmitry Bahdanau, Fethi Bougares, Holger Schwenk, and Yoshua Bengio. "Learning phrase representations using RNN encoder-decoder for statistical machine translation". In: *Conference on Empirical Methods in Natural Language Processing*. Oct. 2014.

[Cho17] François Chollet. *Deep learning with Python*. en. Simon and Schuster, 2017.

[Coh04] Israel Cohen. "Relative transfer function identification using speech signals". In: *IEEE Transactions on Speech and Audio Processing* 12.5 (Sept. 2004), pp. 451–459.

[Com+19] Danilo Comminiello, Marco Lella, Simone Scardapane, and Aurelio Uncini. "Quaternion convolutional neural networks for detection and localization of 3D sound events". en. In: *IEEE International Conference on Acoustics, Speech and Signal Processing*. 2019.

[Com+20] Luca Comanducci, Federico Borra, Paolo Bestagini, Fabio Antonacci, Stefano Tubaro, and Augusto Sarti. "Source localization using distributed microphones in reverberant environments based on deep learning and ray space transform". In: *IEEE/ACM Transactions on Audio, Speech, and Language Processing* 28 (2020), pp. 2238–2251.

[Cor+20] Samuele Cornell, Maurizio Omologo, Stefano Squartini, and Emmanuel Vincent. "Detecting and counting overlapping speakers in distant speech scenarios". en. In: *Interspeech*. Oct. 2020.

[Cri+14] Luca Cristoforetti, Mirco Ravanelli, Maurizio Omologo, Alessandro Sosi, and Alberto Abad. "The DIRHA simulated corpus". en. In: *LREC*. 2014, pp. 2629–2634.

[Dan01] Jerôme Daniel. "Représentation de champs acoustiques, application à la transmission et à la reproduction de scènes sonores complexes dans un contexte multimédia". French. PhD thesis. Paris: Paris VI, 2001.

[DBA07] Jacek P. Dmochowski, Jacob Benesty, and Sofiene Affes. "A generalized steered response power method for computationally viable source localization". In: *IEEE Transactions on Audio, Speech, and Language Processing* 15.8 (Nov. 2007), pp. 2510–2526.

[Dev+19] Jacob Devlin, Ming-Wei Chang, Kenton Lee, and Kristina Toutanova. "BERT: pre-training of deep bidirectional transformers for language understanding". en. In: *arXiv:1810.04805* (May 2019).

[DGMB21] David Diaz-Guerra, Antonio Miguel, and Jose R. Beltran. "Robust sound source tracking using SRP-PHAT and 3D convolutional neural networks". In: *IEEE/ACM Transactions on Audio, Speech, and Language Processing* 29 (2021), pp. 300–311.

[DK20] Jerome Daniel and Srdan Kitic. "Time domain velocity vector for retracing the multipath propagation". en. In: *IEEE International Conference on Acoustics, Speech and Signal Processing*. 2020, pp. 421–425.

[Dos+21] Alexey Dosovitskiy, Lucas Beyer, Alexander Kolesnikov, Dirk Weissenborn, Xiaohua Zhai, Thomas Unterthiner, Mostafa Dehghani, Matthias Minderer, Georg Heigold, Sylvain Gelly, Jakob Uszkoreit, and Neil Houlsby. "An image is worth 16x16 words: transformers for image recognition at scale". In: *International Conference on Learning Representations*. May 2021.

[DVG10] Ngoc QK Duong, Emmanuel Vincent, and Rémi Gribonval. "Under-determined reverberant audio source separation using a full-rank spatial covariance model". In: *IEEE Transactions on Audio, Speech, and Language Processing* 18.7 (2010), pp. 1830–1840.

[Erd+16] Hakan Erdogan, John R. Hershey, Shinji Watanabe, Michael Mandel, and Jonathan Le Roux. "Improved MVDR beamforming using single-channel mask prediction networks". In: *Interspeech*. 2016.

[Eve+20] Christine Evers, Heinrich W. Löllmann, Heinrich Mellmann, Alexander Schmidt, Hendrik Barfuss, Patrick A. Naylor, and Walter Kellermann. "The LOCATA Challenge: acoustic source localization and tracking". In: *IEEE/ACM Transactions on Audio, Speech, and Language Processing* 28 (2020), pp. 1620–1643.

[Fra17] Jon Francombe. "IoSR listening room multichannel BRIR dataset". In: *University of Surrey* (2017).

[Gan+17] Sharon Gannot, Emmanuel Vincent, Shmulik Markovich-Golan, and Alexey Ozerov. "A consolidated perspective on multimicrophone speech enhancement and source separation". In: *IEEE/ACM Transactions on Audio, Speech, and Language Processing* 25.4 (2017), pp. 692–730.

[Gar+07] John Garofolo, David Graff, Doug Paul, and David Pallett. "CSR-I (WSJ0)". In: *Linguistic Data Consortium*. 2007.

[Gar+93] John S. Garofolo, Lori F. Lamel, William M. Fisher, Jonathan G. Fiscus, David S. Pallett, Nancy L. Dahlgren, and Victor Zue. *TIMIT acoustic-phonetic continuous speech corpus*. Tech. rep. 1993.

[GBC16] Ian Goodfellow, Yoshua Bengio, and Aaron Courville. *Deep learning*. MIT Press, 2016.

[GBW01] Sharon Gannot, David Burshtein, and Ehud Weinstein. "Signal enhancement using beamforming and nonstationarity with applications to speech". In: *IEEE Transactions on Signal Processing* 49.8 (Aug. 2001), pp. 1614–1626.

[Gel+21] Femke B Gelderblom, Yi Liu, Johannes Kvam, and Tor Andre Myrvoll. "Synthetic data for DNN-based DoA estimation of indoor speech". en. In: *IEEE International Conference on Acoustics, Speech and Signal Processing*. 2021, p. 6.

[Ger73] Michael A. Gerzon. "Periphony: with-height sound reproduction". English. In: *Journal of the Audio Engineering Society* 21.1 (Feb. 1973), pp. 2–10.

[Gro+19] Francois Grondin, James Glass, Iwona Sobieraj, and Mark D. Plumbley. *Sound event localization and detection using CRNN on pairs of microphones*. Tech. rep. Oct. 2019.

[Gru+20a] Pierre-Amaury Grumiaux, Srdan Kitic, Laurent Girin, and Alexandre Guerin. "High-resolution speaker counting in reverberant rooms using CRNN with Ambisonics features". en. In: *European Signal Processing Conference*. Amsterdam, Netherlands, 2020.

[Gru+20b] Pierre-Amaury Grumiaux, Srdan Kitic, Laurent Girin, and Alexandre Guérin. "Multichannel CRNN for speaker counting: an analysis of performance". en. In: *Forum Acusticum*. 2020.

[Gru+21a] Pierre-Amaury Grumiaux, Srdan Kitic, Laurent Girin, and Alexandre Guérin. "Improved feature extraction for CRNN-based multiple sound source localization". en. In: *European Signal Processing Conference*. 2021.

[Gru+21b] Pierre-Amaury Grumiaux, Srdan Kitic, Prerak Srivastava, Laurent Girin, and Alexandre Guérin. "SALADnet: self-attentive multisource localization in the Ambisonics domain". en. In: *Accepted to IEEE Workshop on Applications of Signal Processing to Audio and Acoustics* (2021).

[Gru+21c] Pierre-Amaury Grumiaux, Srđan Kitić, Laurent Girin, and Alexandre Guérin. "A survey of sound source localization with deep learning methods". In: (Sept. 2021). Submitted.

[Gui+21a] Karim Guirguis, Christoph Schorn, Andre Guntoro, Sherif Abdulatif, and Bin Yang. "SELD-TCN: sound event localization & detection via temporal convolutional networks". en. In: *European Signal Processing Conference*. Jan. 2021, pp. 16–20.

[Gui+21b] Eric Guizzo, Riccardo F. Gramaccioni, Saeid Jamili, Christian Marinoni, Edoardo Massaro, Claudia Medaglia, Giuseppe Nachira, Leonardo Nucciarelli, Ludovica Paglialunga, Marco Pennese, Sveva Pepe, Enrico Rocchi, Aurelio Uncini, and Danilo Comminiello. "L3DAS21 challenge: machine learning for 3D audio signal processing". In: *arXiv:2104.05499* (Apr. 2021).

[Hab06] Emanuel A. P. Habets. *Room impulse response generator*. Tech. rep. Technische Universiteit Eindhoven, 2006.

[Had+14] Elior Hadad, Florian Heese, Peter Vary, and Sharon Gannot. "Multichannel audio database in various acoustic environments". en. In: *International Workshop on Acoustic Signal Enhancement*. Sept. 2014, pp. 313–317.

[HDHU16] Jahn Heymann, Lukas Drude, and Reinhold Haeb-Umbach. "Neural network based spectral mask estimation for acoustic beamforming". In: *IEEE International Conference on Acoustics, Speech and Signal Processing*. 2016.

[He+16] Kaiming He, Xiangyu Zhang, Shaoqing Ren, and Jian Sun. "Deep residual learning for image recognition". In: *IEEE Conference on Computer Vision and Pattern Recognition*. 2016, pp. 770–778.

[Hen+20] Romain Hennequin, Anis Khlif, Felix Voituret, and Manuel Moussallam. "Spleeter: a fast and efficient music source separation tool with pre-trained models". en. In: *Journal of Open Source Software* 5.50 (June 2020), p. 2154.

[Her+14] Juergen Herre, Johannes Hilpert, Achim Kuntz, and Jan Plogsties. "MPEG-H audio-The new standard for universal spatial/3D audio coding". In: *Journal of the Audio Engineering Society* 62 (Dec. 2014), pp. 821–830.

[Hey+17] Jahn Heymann, Lukas Drude, Christoph Boeddeker, Patrick Hanebrink, and Reinhold Haeb-Umbach. "Beamnet: End-to-end training of a beamformer-supported multi-channel ASR system". In: *IEEE International Conference on Acoustics, Speech and Signal Processing*. 2017.

[Hig+17] Takuya Higuchi, Keisuke Kinoshita, Marc Delcroix, Katerina Zmolkova, and Tomohiro Nakatani. "Deep clustering-based beamforming for separation with unknown number of sources". In: *Interspeech*. 2017.

[Hin+12] Geoffrey Hinton, Li Deng, Dong Yu, George E. Dahl, Abdel-rahman Mohamed, Navdeep Jaitly, Andrew Senior, Vincent Vanhoucke, Patrick Nguyen, Tara N. Sainath, and Brian Kingsbury. "Deep neural networks for acoustic modeling in speech recognition: the shared views of four research groups". In: *IEEE Signal Processing Magazine* 29.6 (Nov. 2012), pp. 82–97.

[Hir15] Toni Hirvonen. "Classification of spatial audio location and content using convolutional neural networks". en. In: *Audio Engineering Society Convention*. 2015.

[HMO18a] Weipeng He, Petr Motlicek, and Jean-Marc Odobez. "Deep neural networks for multiple speaker detection and localization". In: *IEEE International Conference on Robotics and Automation* (2018), pp. 74–79.

[HMO18b] Weipeng He, Petr Motlicek, and Jean-Marc Odobez. "Joint localization and classification of multiple sound sources using a multi-task neural network". en. In: *Interspeech*. 2018, pp. 312–316.

[HMO19] Weipeng He, Petr Motlicek, and Jean-Marc Odobez. "Adaptation of multiple sound source localization neural networks with weak supervision and domain-adversarial training". en. In: *IEEE International Conference on Acoustics, Speech and Signal Processing*. May 2019, pp. 770–774.

[HPN17] Gaëtan Hadjeres, François Pachet, and Frank Nielsen. "DeepBach: a steerable model for bach chorales generation". In: *International Conference on Machine Learning*. Aug. 2017, pp. 1362–1371.

[HS97] Sepp Hochreiter and Jürgen Schmidhuber. "Long short-term memory". In: *Neural Computation* 9.8 (Nov. 1997), pp. 1735–1780.

[HSW89] Kurt Hornik, Maxwell Stinchcombe, and Halbert White. "Multilayer feedforward networks are universal approximators". en. In: *Neural Networks* 2.5 (1989), pp. 359–366.

[Hua+17] Gao Huang, Zhuang Liu, Laurens Van Der Maaten, and Kilian Q. Weinberger. "Densely connected convolutional networks". In: *IEEE Conference on Computer Vision and Pattern Recognition*. July 2017, pp. 2261–2269.

[HWQ20] Yankun Huang, Xihong Wu, and Tianshu Qu. "A time-domain unsupervised learning based sound source localization method". In: *International Conference on Information Communication and Signal Processing*. Sept. 2020, pp. 26–32.

[HYS16] Le Hou, Chen-Ping Yu, and Dimitris Samaras. "Squared earth mover's distance-based loss for training deep neural networks". en. In: *arXiv:1611.05916* (Nov. 2016).

[Jac91] Finn Jacobsen. "A note on instantaneous and time-averaged active and reactive sound intensity". en. In: *Journal of Sound and Vibration* 147.3 (June 1991), pp. 489–496.

[Jar+12] Daniel P. Jarrett, Emanuel A. P. Habets, Mark R. P. Thomas, and Patrick A. Naylor. "Rigid sphere room impulse response simulation: Algorithm and applications". In: *The Journal of the Acoustical Society of America* 132.3 (Sept. 2012), pp. 1462–1472.

[JHN17] Daniel P. Jarrett, Emanuël A. P. Habets, and Patrick A. Naylor. *Theory and applications of spherical microphone array processing*. en. Vol. 9. Springer Topics in Signal Processing. Springer, 2017.

[Jia+15] Lu Jiang, Deyu Meng, Qian Zhao, Shiguang Shan, and Alexander G Hauptmann. "Self-Paced Curriculum Learning". en. In: *AAAI Conference on Artificial Intelligence*. 2015, p. 7.

[JJ13] Finn Jacobsen and Peter Moller Juhl. *Fundamentals of general linear acoustics*. en. John Wiley & Sons, July 2013.

[Jum+21] John Jumper, Richard Evans, Alexander Pritzel, Tim Green, Michael Figurnov, Olaf Ronneberger, Kathryn Tunyasuvunakool, Russ Bates, Augustin Žídek, Anna Potapenko, Alex Bridgland, Clemens Meyer, Simon A. A. Kohl, Andrew J. Ballard, Andrew Cowie, Bernardino Romera-Paredes, Stanislav Nikolov, Rishub Jain, Jonas Adler, Trevor Back, Stig Petersen, David Reiman, Ellen Clancy, Michal Zielinski, Martin Steinegger, Michalina Pacholska, Tamas Berghammer, Sebastian Bodenstein, David Silver, Oriol Vinyals, Andrew W. Senior, Koray Kavukcuoglu, Pushmeet Kohli, and Demis Hassabis. "Highly accurate protein structure prediction with AlphaFold". en. In: *Nature* (July 2021), pp. 1–11.

[Kat+20] Angelos Katharopoulos, Apoorv Vyas, Nikolaos Pappas, and François Fleuret. "Transformers are RNNs: fast autoregressive transformers with linear attention". en. In: *International Conference on Machine Learning*. PMLR, 2020, pp. 5156–5165.

[KB14] Diederik P. Kingma and Jimmy Ba. "Adam: A Method for Stochastic Optimization". en. In: *arXiv:1412.6980* (2014).

[KC76] Charles Knapp and Glifford Carter. "The generalized correlation method for estimation of time delay". In: *IEEE Transactions on Acoustics, Speech, and Signal Processing* 24.4 (Aug. 1976), pp. 320–327.

[KG18] Srdan Kitic and Alexandre Guérin. "TRAMP: TRacking by a realtime AMbisonic-based Particle filter". en. In: *LOCATA Challenge Workshop* (2018).

[Kin00] Lawrence E. Kinsler, ed. *Fundamentals of acoustics*. 4th ed. ZSCC: 0010654. New York: Wiley, 2000.

[Kin+20] Keisuke Kinoshita, Marc Delcroix, Shoko Araki, and Tomohiro Nakatani. "Tackling real noisy reverberant meetings with all-neural source separation, counting, and diarization system". In: *IEEE International Conference on Acoustics, Speech and Signal Processing*. May 2020, pp. 381–385.

[KL11] Youngwook Kim and Hao Ling. "Direction of arrival estimation of humans with a small sensor array using an artificial neural network". en. In: *Progress In Electromagnetics Research* 27 (2011), pp. 127–149.

[KPK21] Daniel Krause, Archontis Politis, and Konrad Kowalczyk. "Comparison of convolution types in CNN-based feature extraction for sound source localization". en. In: *European Signal Processing Conference*. Jan. 2021, pp. 820–824.

[Kuh55] Harold W. Kuhn. "The Hungarian method for the assignment problem". en. In: *Naval Research Logistics Quarterly* 2.1-2 (Mar. 1955), pp. 83–97.

[LeC+89] Yann LeCun, Bernhard Boser, John S. Denker, Donnie Henderson, Richard E. Howard, Wayne Hubbard, and Lawrence D. Jackel. "Backpropagation applied to handwritten zip code recognition". In: *Neural Computation* 1.4 (1989), pp. 541–551.

[LGE91] Lori F. Larnel, Jean-Luc Gauvain, and Maxine Eskénazi. "BREF, a large vocabulary spoken corpus for French". In: *Eurospeech*. 1991.

[LGH19] Simon Leglaive, Laurent Girin, and Radu Horaud. "Semi-supervised multichannel speech enhancement with variational autoencoders and non-negative matrix factorization". In: *IEEE International Conference on Acoustics, Speech and Signal Processing*. 2019, pp. 101–105.

[Li+16] Bo Li, Tara N. Sainath, Ron J. Weiss, Kevin W. Wilson, and Michiel Bacchiani. "Neural network adaptive beamforming for robust multichannel speech recognition." In: *Interspeech*. 2016.

[LPM15] Minh-Thang Luong, Hieu Pham, and Christopher D. Manning. "Effective approaches to attention-based neural machine translation". In: *Conference on Empirical Methods in Natural Language Processing*. Sept. 2015, pp. 1412–1421.

[LZL18] Qinglong Li, Xueliang Zhang, and Hao Li. "Online direction of arrival estimation based on deep learning". en. In: *IEEE International Conference on Acoustics, Speech and Signal Processing*. Apr. 2018, pp. 2616–2620.

[Mar+19] Hector A. Cordourier Maruri, Paulo Lopez Meyer, Jonathan Huang, Juan Antonio del Hoyo Ontiveros, and Hong Lu. *GCC-PHAT cross-correlation audio features for simultaneous sound event localization and detection (SELD) in multiple rooms*. en. Tech. rep. 2019.

[Men+17] Zhong Meng, Shinji Watanabe, John R. Hershey, and Hakan Erdogan. "Deep long short-term memory adaptive beamforming networks for multichannel robust speech recognition". In: *IEEE International Conference on Acoustics, Speech and Signal Processing*. 2017.

[Mer06] Juha Merimaa. "Analysis, synthesis, and perception of spatial sound - binaural localization modeling and multichannel loudspeaker reproduction". en. PhD thesis. Helsinki: Helsinki University of Technology, 2006.

[ML18] Wei Ma and Xun Liu. "Phased microphone array for sound source localization with deep learning". In: *Aerospace Systems* 2.2 (2018), pp. 71–81.

[Moi+20] Guillaume Le Moing, Phongtharin Vinayavekhin, Tadanobu Inoue, Jayakorn Vongkulbhisal, Asim Munawar, Ryuki Tachibana, and Don Joven Agravante. "Learning multiple sound source 2D localization". In: *IEEE 21st International Workshop on Multimedia Signal Processing*. Dec. 2020.

[Moi+21] Guillaume Le Moing, Phongtharin Vinayavekhin, Don Joven Agravante, Tadanobu Inoue, Jayakorn Vongkulbhisal, Asim Munawar, and Ryuki Tachibana. "Data-efficient framework for real-world multiple sound source 2D localization". In: *IEEE International Conference on Acoustics, Speech and Signal Processing*. 2021.

[Mor06] Sébastien Moreau. "Étude et réalisation d'outils avancés d'encodage spatial pour la technique de spatialisation sonore Higher Order Ambisonics : microphone 3D et contrôle de distance". fr. PhD thesis. Le Mans: Université du Main, 2006.

[MP43] Warren S. McCulloch and Walter Pitts. "A logicial calculus of the ideas immanent in nervous activity". en. In: *The Bulletin of Mathematical Biophysics* 5 (1943), pp. 115–133.

[Nas+19] Ali Bou Nassif, Ismail Shahin, Imtinan Attili, Mohammad Azzeh, and Khaled Shaalan. "Speech recognition using deep neural networks: a systematic review". In: *IEEE Access* 7 (2019), pp. 19143–19165.

[Neu+19] Thilo von Neumann, Keisuke Kinoshita, Marc Delcroix, Shoko Araki, Tomohiro Nakatani, and Reinhold Haeb-Umbach. "All-neural online source separation, counting, and diarization for meeting analysis". In: *IEEE International Conference on Acoustics, Speech and Signal Processing*. May 2019, pp. 91–95.

[Ngu+18] Quan Nguyen, Laurent Girin, Gérard Bailly, Frédéric Elisei, and Duc-Canh Nguyen. "Autonomous sensorimotor learning for sound source localization by a humanoid robot". en. In: *Workshop on Crossmodal Learning for Intelligent Robotics in conjunction with IEEE/RSJ IROS*. 2018.

[Ngu+20] Tho Thi Ngoc Nguyen, Woon-Seng Gan, Rishabh Ranjan, and Douglas L. Jones. "Robust source counting and DoA estimation using spatial pseudo-spectrum and convolutional neural network". In: *IEEE/ACM Transactions on Audio, Speech, and Language Processing* 28 (2020), pp. 2626–2637.

[Ngu+21] Thi Ngoc Tho Nguyen, Ngoc Khanh Nguyen, Huy Phan, Lam Pham, Kenneth Ooi, Douglas L. Jones, and Woon-Seng Gan. "A general network architecture for sound event localization and detection using transfer learning and recurrent neural network". In: *IEEE International Conference on Acoustics, Speech and Signal Processing*. June 2021, pp. 935–939.

[Nic10] Rozenn Nicol. "Sound spatialization by higher order Ambisonics: encoding and decoding a sound scene in practice from a theoretical point of view". en. In: *International Symposium on Ambisonics and Spherical Acoustics*. 2010, p. 9.

[NLV16] Aditya A. Nugraha, Antoine Liutkus, and Emmanuel Vincent. "Multichannel audio source separation with deep neural networks". In: *IEEE/ACM Transactions on Audio, Speech, and Language Processing* 24.9 (2016), pp. 1652–1664.

[Oor+16] Aaron van den Oord, Sander Dieleman, Heiga Zen, Karen Simonyan, Oriol Vinyals, Alex Graves, Nal Kalchbrenner, Andrew Senior, and Koray Kavukcuoglu. "WaveNet: a generative model for raw audio". en. In: *arXiv:1609.03499* (Sept. 2016).

[Opo+19] Renana Opochinsky, Bracha Laufer-Goldshtein, Sharon Gannot, and Gal Chechik. "Deep ranking-based sound source localization". en. In: *IEEE Workshop on Applications of Signal Processing to Audio and Acoustics*. 2019, pp. 283–287.

[Par+21] Tae Jin Park, Naoyuki Kanda, Dimitrios Dimitriadis, Kyu J. Han, Shinji Watanabe, and Shrikanth Narayanan. "A review of speaker diarization: recent advances with deep learning". In: *arXiv:2101.0962* (June 2021).

[Pas+17] Shahab Pasha, Jacob Donley, Christian Ritz, and Yue Xian Zou. "Towards real-time source counting by estimation of coherent-to-diffuse ratios from ad-hoc microphone array recordings". en. In: *Hands-free Speech Communications and Microphone Arrays*. San Francisco, CA: IEEE, 2017, pp. 161–165.

[PBG21] Hadrien Pujol, Eric Bavu, and Alexandre Garcia. "BeamLearning: an end-to-end deep learning approach for the angular localization of sound sources using raw multichannel acoustic pressure data". In: *The Journal of the Acoustical Society of America* 149.6 (Apr. 2021), pp. 4248–4263.

[PC17] Pasi Pertilä and Emre Cakir. "Robust direction estimation with convolutional neural networks based steered response power". In: *IEEE International Conference on Acoustics, Speech and Signal Processing*. Mar. 2017, pp. 6125–6129.

[PDMP18] Ville Pulkki, Symeon Delikaris-Manias, and Archontis Politis. *Parametric time-frequency domain spatial audio*. en. Wiley, 2018.

[Per+18a] Lauréline Perotin, Romain Serizel, Emmanuel Vincent, and Alexandre Guérin. "Multichannel speech separation with recurrent neural networks from high-order Ambisonics recordings". In: *IEEE International Conference on Acoustics, Speech and Signal Processing*. 2018.

[Per+18b] Lauréline Perotin, Romain Serizel, Emmanuel Vincent, and Alexandre Guérin. "CRNN-based joint azimuth and elevation localization with the Ambisonics intensity vector". In: *International Workshop on Acoustic Signal Enhancement*. Sept. 2018, pp. 241–245.

[Per19] Lauréline Perotin. "Localisation et rehaussement de sources de parole au format Ambisonique". French. PhD thesis. Université de Lorraine, Oct. 2019.

[Per+19] Lauréline Perotin, Romain Serizel, Emmanuel Vincent, and Alexandre Guérin. "CRNN-based multiple DoA estimation using acoustic intensity features for Ambisonics recordings". In: *IEEE Journal of Selected Topics in Signal Processing* 13.1 (Mar. 2019), pp. 22–33.

[Pha+20] Huy Phan, Lam Pham, Philipp Koch, Ngoc Q. K. Duong, Ian McLoughlin, and Alfred Mertins. "On multitask loss function for audio event detection and localization". In: *arXiv:2009.05527* (Sept. 2020).

[Pol+21] Archontis Politis, Sharath Adavanne, Daniel Krause, Antoine Deleforge, Prerak Srivastava, and Tuomas Virtanen. "A dataset of dynamic reverberant sound scenes with directional interferers for sound event localization and detection". In: *arXiv:2106.06999* (June 2021).

[Pos+21] Nils Poschadel, Robert Hupke, Stephan Preihs, and Jürgen Peissig. "Direction of arrival estimation of noisy speech using convolutional recurrent neural networks with higher-order Ambisonics signals". In: *arXiv:2102.09853* (Mar. 2021).

[PS19] Junhyeong Pak and Jong W. Shin. "Sound socalization based on phase difference enhancement using deep neural networks". In: *IEEE/ACM Transactions on Audio, Speech, and Language Processing* 27.8 (2019), pp. 1335–1345.

[Pur+19] Hendrik Purwins, Bo Li, Tuomas Virtanen, Jan Schlüter, Shuo-yiin Chang, and Tara Sainath. "Deep learning for audio signal processing". In: *IEEE Journal of Selected Topics in Signal Processing* 13.2 (Apr. 2019), pp. 206–219.

[PWQ20] Chao Peng, Xihong Wu, and Tianshu Qu. "Competing speaker count estimation on the fusion of the spectral and spatial embedding space". en. In: *Interspeech*. 2020, pp. 3077–3081.

[Raf05] B. Rafaely. "Analysis and design of spherical microphone arrays". en. In: *IEEE Transactions on Speech and Audio Processing* 13.1 (Jan. 2005), pp. 135–143.

[Raf19] Boaz Rafaely. *Fundamentals of spherical array processing*. en. Vol. 16. Springer, 2019.

[RB18] Mirco Ravanelli and Yoshua Bengio. "Speaker recognition from raw waveform with SincNet". en. In: *IEEE Spoken Language Technology Workshop*. 2018, pp. 1021–1028.

[RK89] Richard Roy and Thomas Kailath. "ESPRIT-estimation of signal parameters via rotational invariance techniques". In: *IEEE Transactions on Acoustics, Speech, and Signal Processing* 37.7 (July 1989), pp. 984–995.

[Rod+15] Reinhild Roden, Niko Moritz, Stephan Gerlach, Stefan Weinzierl, and Stefan Goetze. "On sound source localization of speech signals using deep neural networks". en. In: *Deutsche Jahrestagung für Akustik*. 2015.

[SBD18] Robin Scheibler, Eric Bezzam, and Ivan Dokmanić. "Pyroomacoustics: a Python package for audio room simulation and array processing algorithms". In: *IEEE International Conference on Acoustics, Speech and Signal Processing*. Apr. 2018, pp. 351–355.

[Sch+21a] Christopher Schymura, Benedikt Bönninghoff, Tsubasa Ochiai, Marc Delcroix, Keisuke Kinoshita, Tomohiro Nakatani, Shoko Araki, and Dorothea Kolossa. "PILOT: introducing Transformers for probabilistic sound event localization". In: *arXiv:2106.03903* (June 2021).

[Sch+21b] Christopher Schymura, Tsubasa Ochiai, Marc Delcroix, Keisuke Kinoshita, Tomohiro Nakatani, Shoko Araki, and Dorothea Kolossa. "Exploiting attention-based sequence-to-sequence architectures for sound event localization". en. In: *European Signal Processing Conference*. 2021.

[Sch86] Ralph Schmidt. "Multiple emitter location and signal parameter estimation". In: *IEEE Transactions on Antennas and Propagation* 34.3 (Mar. 1986), pp. 276–280.

[SDF18] Daniele Salvati, Carlo Drioli, and Gian Luca Foresti. "Exploiting CNNs for improving acoustic source localization in noisy and reverberant conditions". In: *IEEE Transactions on Emerging Topics in Computational Intelligence* 2.2 (Apr. 2018), pp. 103–116.

[SDZ18] Dmitry Suvorov, Ge Dong, and Roman Zhukov. "Deep residual network for sound source localization in the time domain". In: *arXiv:1808.06429* (Aug. 2018).

[Shi+20] Kazuki Shimada, Yuichiro Koyama, Naoya Takahashi, Shusuke Takahashi, and Yuki Mitsufuji. "ACCDOA: activity-coupled cartesian direction of arrival representation for sound event localization and detection". In: *IEEE International Conference on Acoustics, Speech and Signal Processing*. Oct. 2020.

[Sil+17] David Silver, Thomas Hubert, Julian Schrittwieser, Ioannis Antonoglou, Matthew Lai, Arthur Guez, Marc Lanctot, Laurent Sifre, Dharshan Kumaran, Thore Graepel, Timothy Lillicrap, Karen Simonyan, and Demis Hassabis. "Mastering chess and shogi by self-play with a general reinforcement learning algorithm". In: *arXiv:1712.01815* (Dec. 2017).

[SK02] Peter Svensson and Ulf R. Kristiansen. "Computational modelling and simulation of acoutic spaces". English. In: *AES International Conference on Virtual, Synthetic, and Entertainment Audio*. Audio Engineering Society, June 2002.

[SO10] Halim Sayoud and Siham Ouamour. "Proposal of a new confidence parameter estimating the number of speakers-an experimental investigation-". In: *Journal of Information Hiding and Multimedia Signal Processing* 1.2 (Apr. 2010).

[SP97] Mike Schuster and Kuldip K. Paliwal. "Bidirectional recurrent neural networks". In: *IEEE Transactions on Signal Processing* 45.11 (Nov. 1997), pp. 2673–2681.

[Sri+14] Nitish Srivastava, Geoffrey Hinton, Alex Krizhevsky, Ilya Sutskever, and Ruslan Salakhutdinov. "Dropout: a simple way to prevent neural networks from overfitting". en. In: *Journal of Machine Learning Research* 15.1 (June 2014), pp. 1929–1958.

[St18] Fabien-Robert Stöter, Soumitro Chakrabarty, Bernd Edler, and Emanuel A. P. Habets. "Classification vs. regression in supervised learning for single channel speaker count estimation". In: *IEEE International Conference on Acoustics, Speech and Signal Processing*. 2018, pp. 436–440.

[St19] Fabian-Robert Stöter, Soumitro Chakrabarty, Bernd Edler, and Emanuel A. P. Habets. "CountNet: estimating the number of concurrent speakers using supervised learning". en. In: *IEEE/ACM Transactions on Audio, Speech, and Language Processing* 27.2 (2019), pp. 268–282.

[Sub+21] Aswin Shanmugam Subramanian, Chao Weng, Shinji Watanabe, Meng Yu, and Dong Yu. "Deep learning based multi-source localization with source splitting and its effectiveness in multi-talker speech recognition". In: *arXiv:2102.07955* (Feb. 2021).

[Sun+20] Harshavardhan Sundar, Weiran Wang, Ming Sun, and Chao Wang. "Raw waveform based end-to-end deep convolutional network for spatial localization of multiple acoustic sources". In: *IEEE International Conference on Acoustics, Speech and Signal Processing*. May 2020, pp. 4642–4646.

[SVF18] Sunit Sivasankaran, Emmanuel Vincent, and Dominique Fohr. "Keyword-based speaker localization: localizing a target speaker in a multi-speaker environment". en. In: *Interspeech*. 2018.

[SW96] Ofir Shalvi and Ehud Weinstein. "System identification using nonstationary signals". In: *IEEE Transactions on Signal Processing* 44.8 (Aug. 1996), pp. 2055–2063.

[Tak+18] Ryu Takeda, Y. Kudo, K. Takashima, Y. Kitamura, and K. Komatani. "Unsupervised adaptation of neural networks for discriminative sound source localization with eliminative constraint". In: *IEEE International Conference on Acoustics, Speech and Signal Processing*. 2018, pp. 3514–3518.

[TGT18] Etienne Thuillier, Hannes Gamper, and Ivan J. Tashev. "Spatial audio feature discovery with convolutional neural networks". en. In: *IEEE International Conference on Acoustics, Speech and Signal Processing*. 2018, pp. 6797–6801.

[TK16] Ryu Takeda and Kazunori Komatani. "Discriminative multiple sound source localization based on deep neural networks using independent location model". In: *IEEE Spoken Language Technology Workshop*. 2016, pp. 603–609.

[TR06] S.E. Tranter and D.A. Reynolds. "An overview of automatic speaker diarization systems". In: *IEEE Transactions on Audio, Speech, and Language Processing* 14.5 (Sept. 2006), pp. 1557–1565.

[Vas+17] Ashish Vaswani, Noam Shazeer, Niki Parmar, Jakob Uszkoreit, Llion Jones, Aidan N. Gomez, Lukasz Kaiser, and Illia Polosukhin. "Attention is all you need". en. In: *Conference on Neural Information Processing System*. Dec. 2017, pp. 5998–6008.

[VDPMG18] Juan Manuel Vera-Diaz, Daniel Pizarro, and Javier Macias-Guarasa. "Towards end-to-end acoustic localization using deep learning: from audio signal to source position coordinates". In: *Sensors* 18.10 (2018), p. 3418.

[VDPMG21] Juan Manuel Vera-Diaz, Daniel Pizarro, and Javier Macias-Guarasa. "Towards domain independence in CNN-based acoustic localization using deep cross correlations". en. In: *European Signal Processing Conference*. 2021, pp. 226–230.

[Vec+19] Paolo Vecchiotti, Ning Ma, Stefano Squartini, and Guy J. Brown. "End-to-end binaural sound localisation from the raw waveform". en. In: *IEEE International Conference on Acoustics, Speech and Signal Processing*. 2019, pp. 451–455.

[Ves+16] Fabio Vesperini, Paolo Vecchiotti, Emanuele Principi, Stefano Squartini, and Francesco Piazza. "A neural network based algorithm for speaker localization in a multi-room environment". In: *IEEE International Workshop on Machine Learning for Signal Processing*. 2016, pp. 1–6.

[VGH20] Vishnuvardhan Varanasi, Harshit Gupta, and Rajesh M. Hegde. "A deep learning framework for robust DoA estimation using spherical harmonic decomposition". In: *IEEE/ACM Transactions on Audio, Speech, and Language Processing* 28 (2020), pp. 1248–1259.

[Vog+17] Richard Vogl, Matthias Dorfer, Gerhard Widmer, and Peter Knees. "Drum transcription via joint beat and drum modeling using convolutional recurrent neural networks". en. In: *Conference of the International Society for Music Information Retrieval*. 2017, pp. 150–157.

[VVB88] Barry D. Van Veen and Kevin M. Buckley. "Beamforming: A versatile approach to spatial filtering". In: *IEEE ASSP Magazine* 5.2 (1988), pp. 4–24.

[VVG18] Emmanuel Vincent, Tuomas Virtanen, and Sharon Gannot. *Audio source separation and speech enhancement*. John Wiley & Sons, 2018.

[Wab+10] Andrew Wabnitz, Nicolas Epain, Craig Jin, and André Van Schaik. "Room acoustics simulation for multichannel microphone arrays". In: *International Symposium on Room Acoustics*. 2010, pp. 1–6.

[Wan+20] Wei Wang, Fatjon Seraj, Nirvana Meratnia, and Paul J.M. Havinga. "Speaker counting model based on transfer learning from SincNet bottleneck layer". In: *IEEE International Conference on Pervasive Computing and Communications*. Mar. 2020, pp. 1–8.

[Wan+21] Qing Wang, Jun Du, Hua-Xin Wu, Jia Pan, Feng Ma, and Chin-Hui Lee. "A four-stage data augmentation approach to ResNet-Conformer based acoustic modeling for sound event localization and detection". en. In: *arXiv:2101.02919* (Jan. 2021).

[WC17] DeLiang Wang and Jitong Chen. "Supervised speech separation based on deep learning: an overview". In: *arXiv:1708.07524* (2017).

[WC18] DeLiang Wang and Jitong Chen. "Supervised speech separation based on deep learning: an overview". In: *IEEE/ACM Transactions on Audio, Speech, and Language Processing* 26.10 (Oct. 2018), pp. 1702–1726.

[WK18] Haoran Wei and Nasser Kehtarnavaz. "Determining number of speakers from single microphone speech signals by multi-label convolutional neural network". In: *Annual Conference of the IEEE Industrial Electronics Society*. Oct. 2018, pp. 2706–2710.

[WM00] Earl G. Williams and J. Adin Mann. "Fourier acoustics: sound radiation and nearfield acoustical holography". en. In: *The Journal of the Acoustical Society of America* 108.4 (Oct. 2000), pp. 1373–1373.

[Wu+21] Yifan Wu, Roshan Ayyalasomayajula, Michael J. Bianco, Dinesh Bharadia, and Peter Gerstoft. "SSLIDE: sound source localization for indoors based on deep learning". In: *IEEE International Conference on Acoustics, Speech and Signal Processing*. Feb. 2021.

[Xia+15] Xiong Xiao, Shengkui Zhao, Xionghu Zhong, Douglas L. Jones, Eng S. Chng, and Haizhou Li. "A learning-based approach to direction of arrival estimation in noisy and reverberant environments". In: *IEEE International Conference on Acoustics, Speech and Signal Processing*. 2015, pp. 2814–2818.

[Xu+13] Chenren Xu, Sugang Li, Gang Liu, Yanyong Zhang, Emiliano Miluzzo, Yih-Farn Chen, Jun Li, and Bernhard Firner. "Crowd++: unsupervised speaker count with smartphones". en. In: *ACM International Joint Conference on Pervasive and Ubiquitous Computing*. 2013, pp. 43–52.

[XZ20] Yiming Xiao and Haijian Zhang. "Improved source counting and separation for monaural mixture". In: *arXiv:2004.00175* (Mar. 2020).

[YAZ13] Karim Youssef, Sylvain Argentieri, and Jean-Luc Zarader. "A learning-based approach to robust binaural sound localization". In: *IEEE/RSJ International Conference on Intelligent Robots and Systems*. 2013, pp. 2927–2932.

[YH21] Midia Yousefi and John H L Hansen. “Real-time speaker counting in a cocktail party scenario using attention-guided convolutional neural network”. en. In: *Interspeech*. 2021.

[YK16] Fisher Yu and Vladlen Koltun. “Multi-scale context aggregation by dilated convolutions”. In: *International Conference on Learning Representations*. 2016.

[YLP17] Bing Yang, Hong Liu, and Cheng Pang. “Multiple sound source counting and localization based on spatial principal eigenvector”. en. In: *Interspeech*. ISCA, 2017, pp. 1924–1928.

[YNO17] Nelson Yalta, Kazuhiro Nakadai, and Tetsuya Ogata. “Sound source localization using deep learning models”. In: *Journal of Robotics and Mechatronics* 29.1 (2017), pp. 37–48.

[Zer+16] Alfredo Zermini, Yingfu Yu, Yong Xu, Wenwu Wang, and Mark D. Plumbley. “Deep neural network based audio source separation”. In: *IMA International Conference on Mathematics in Signal Processing*. 2016.

[ZF19] Franz Zotter and Matthias Frank. *Ambisonics: a practical 3D audio theory for recording, studio production, sound reinforcement, and virtual reality*. en. Springer Nature, 2019.

[ZZQ19] Wangyou Zhang, Ying Zhou, and Yanmin Qian. “Robust DoA estimation based on convolutional neural network and time-frequency masking”. en. In: *Interspeech*. Sept. 2019, pp. 2703–2707.